

Routes for the Formation of Thin Oil Shelled Microbubbles towards Hydrophobic Drug Delivery

Adam Henry Churchman

The University of Leeds
School of Physics and Astronomy
School of Electronic and Electrical Engineering
September 2017

Submitted in accordance with the requirements for the degree of
Doctor of Philosophy

The candidate confirms that the work submitted is his own and that appropriate credit has been given where reference has been made to the work of others.

This copy has been supplied on the understanding that it is copyright material and that no quotation from the thesis may be published without proper acknowledgement.

The right of Adam Henry Churchman to be identified as Author of this work has been asserted by him in accordance with the Copyright, Designs and Patents Act 1988.

Acknowledgments

To anyone who has known me during my time as a PhD student, I am sure that it will not come as a surprise to hear that it was, unequivocally, not smooth sailing. It was tough, but here I am, now at the end, in large part due to those people.

I would like to thank my PhD supervisor, Prof Stephen Evans. It took quite a while for me to get into my stride, but with his continued support I was able to realise what I had to do. I am certain that without his encouragement and pushing I would not have been able to achieve what I have.

A large thank you must go to Dr Sally Peyman. She was not only a great friend during my time here, but took on a far more supervisory role than she had to. She deserves a huge amount of credit for the time and effort she has put in to my PhD. Sal - I cannot thank you enough.

The success of this project could not have been achieved without a large amount of work that was performed by Dr Victoria Mico. It would be wrong of me not to acknowledge that. But, Victoria has meant much more to me during my PhD. She was my ever-present bubble buddy ready to talk at the drop of a hat about our science – more often than not our frustration at it – or just about life. Bubble buddies for life. I will miss you.

I would also like to take the time to thank Dr Radwa Abou-Saleh El Moursi who has been fully supportive throughout the entire PhD process and ready to talk or help whenever asked.

Special thanks should go to Dr James McLaughlan and Dr Tony Evans for their assistance with ultrasound experiments, to Julia Gala De Pablo for her designs and work towards the microfluidic trapping experiments as well as other experiments not shown in this thesis, and to Fern Armistead and Liam Hunter for their help with microfluidic device production. For assistance with thesis correction, I would like to thank Andrew Harvie (along with Stephen Evans, Sally Peyman, Victoria Mico, and Fern Armistead).

I would like to spread my acknowledgments to Prof Steven Freear, my secondary supervisor, and the Leeds Microbubble Consortium for their advice and discussion during this project.

Everyone in Molecular and Nanoscale Physics had contributed to this thesis in some way, be it from help with experiments, to talk about science, or even just keeping me sane. I would not have been able to get this far without a supportive group behind me. So a thank you goes to you to each one of you.

Dr James William Cooper has been a pillar of support for me over this last year. I do not know what I would have done without him or where I would be now. I imagine in a puddle of self-doubt. You have been amazing. I finally understand, and the pain is real!

Lastly, I want to give a special thank you to my family. To my mum, my dad, and my brother. I would never have been able to achieve as much in my life as I have without knowing that you were always behind me, supporting me every step of the way. In the end, cultivating my competitive streak was always the right way to go, thanks Simon. I have written this thesis knowing that part of it should belong to each of you.

Abstract

Advances in drug development and screening protocols have lead to a dramatic increase in the number of candidate drugs for clinical application. Many of these drugs show strong *in vitro* effects, however *in vivo* they suffer from off-site toxicity, reduced bioavailability, and poor water solubility. Drug delivery systems have been developed to encapsulate these drugs, only releasing them at target sites. This has led to a greater bioavailability at the target site, reducing the total drug dosage required for delivery, whilst increasing the concentration and potency of these drugs where they are required. However, one of the growing challenges for drug delivery systems is drug hydrophobicity.

Microbubbles (MBs) have been used in medicine for over 30 years as ultrasound contrast enhancing agents. More recently, they have been shown to enhance drug delivery through co-delivery and ultrasound exposure. For improved delivery, a number of MB-drug composites have been developed, with many showing a high degree of success for hydrophilic drugs. The effective delivery of primarily hydrophobic drugs remains a challenge. A number of research groups have looked into forming MBs with the inclusion of an oil layer for drug encapsulation into the MB shell, giving an Oil Layer Inside MB (OLI-MB). Problems arose in each study ranging from; polydispersity, low stability, clinically unviable size distributions, ultrasound requirements for drug release outside of clinical application, and a general lack of control over the formation and the oil layer thickness per OLI-MB.

This project aimed to develop a reliable and simple route for the formation of OLI-MBs with thin oil layers, at clinically relevant sizes and concentrations. Three formation routes were tested; oil nanodroplet self-assembly and spreading at MB surfaces, three-phase flow through a single microfluidic flow focused nozzle, and activation of liquid perfluorocarbon-oil droplets into OLI-MBs. With the use of microfluidics, the first formation route was found to produce OLI-MBs of 2.4 μm at 10^6 OLI-MBs/ml, with oil layers 10s of nanometres thick, which showed ultrasound response. As such, this formation route is of further clinical interest.

Publications

- **A. H. Churchman**, V. Mico, J. Gala de Pablo, S. A. Peyman, S. Freear, and S. D. Evans. *Combined Flow-Focus and Self-Assembly Routes for the Formation of Lipid Stabilised Oil-Shelled Microbubbles*. *Microsystems & Nanoengineering – Nature*. [Accepted for publication]
- **A. H. Churchman**, V. Mico, J. Gala de Pablo, S. A. Peyman, and S. D. Evans. *Forming oil layer inside microbubbles through single step microfluidics, towards hydrophobic drug delivery*. 20th International Conference on Miniaturized Systems for Chemistry and Life Sciences, MicroTAS 2016. 750-751 (2016). [Conference proceedings]
- **A. H. Churchman**, **V. Mico**, S. A. Peyman, and S. D. Evans. *Single step microfluidic production of microbubble architectures for hydrophobic drug delivery*. 18th International Conference on Miniaturized Systems for Chemistry and Life Sciences, MicroTAS 2014. 1265-1267 (2014). [Conference proceedings]

List of abbreviations

3C1	Three-phase FF microchip with 3 Channels at the nozzle, version 1
3C2	Three-phase FF microchip with 3 Channels at the nozzle, version 2
3C3	Three-phase FF microchip with 3 Channels at the nozzle, version 3
5C1	Three-phase FF microchip with 5 Channels at the nozzle, version 1
AAL	Acoustically Active Lipospheres
ADV	Acoustic Droplet Vapourisation
BB	Bubble Buffer
C5	Perfluoropentane
C6	Perfluorohexane
Ca	Capillary number
DC	Duty Cycle
DLS	Dynamic Light Scattering
ESP	Equilibrium Spreading Pressure
FF	Flow Focused/Focusing
fps	frames per second
FRET	Fluorescence/Förster Resonance Energy Transfer
FWHM	Full Width Half Maximum
IC	Inertial cavitation
LB	Langmuir-Blodgett
LOND	Lipid Oil Nanodroplet
MB	Microbubble
OLI-MB	Oil Layer Inside Microbubble
PDMS	Polydimethylsiloxane
PEG	Polyethylene glycol
PFC	Perfluorocarbon
prf	peak repetition frequency
Q	Volumetric flow rate
QCM-D	Quartz Crystal Microbalance with Dissipation monitoring
Re	Reynolds number
R_{ϕ}	Resistance to flow
S	Spreading coefficient
SD	Standard Deviation
US	Ultrasound
UV-Vis	Ultraviolet-Visible spectrometer
We	Weber number

For chemical abbreviations see Experimental Chapter 4.1, Table 4.1, p57.

Table of Contents

Acknowledgments.....	iii
Abstract	v
Publications.....	vi
List of abbreviations	vii
Table of Contents.....	viii
List of Figures.....	xii
1. Introduction	1
1.1. Microbubbles – Combining theranostic properties with controlled, externally activated release of payloads.....	4
1.2. Microbubble-drug composites.....	6
1.2.1. Hydrophilic drug-MB composites.....	9
1.2.2. Hydrophobic drug-MB composites	10
1.3. Aims of this project and outline of the thesis.....	13
2. Context and background to the three OLI-MB formation techniques.....	17
2.1. Destabilising oil droplets to produce thin oil layer films	17
2.2. Three phase microfluidic production of microbubbles	21
2.3. Activation of liquid perfluorocarbon droplets to gas bubbles.....	26
3. Theory and Background.....	32
3.1. Microfluidics	32
3.1.1. Fluid flow in micrometre scale channels.....	32
3.1.2. Microfluidic droplet and bubble pinch-off formation.....	35
3.2. Microbubbles and ultrasound.....	37
3.2.1. Echogenicity	37
3.2.2. Resonant frequency, f_0	41
3.2.3. MB life-time	44
3.3. Wettability	48
3.3.1. Droplets entering a stabilised interface.....	50
3.4. Fluorescence and Förster/Fluorescence Resonance Energy Transfer (FRET)	51
3.5. Activation of perfluorocarbon liquid droplets to gas bubbles.....	54
3.5.1. Droplet to MB size expansion.....	54
3.5.2. Vapourisation temperature as a function of droplet size.....	57

3.5.3. Vapourisation pressure as a function of droplet size	58
4. Experimental	60
4.1. Chemicals, solutions, and microscopy.....	60
4.2. Microfluidic microchips	63
4.2.1. Microchip fabrication.....	64
4.2.2. Microchip designs.....	66
4.2.3. Interfacing fluid phases to the microfluidic chips	72
4.3. Non-microfluidic imaging chambers	73
4.4. Non-oil MB production	75
4.5. Surface pressure measurement of air-aqueous interfaces by a Langmuir- Blodgett trough.....	76
4.5.1. Pressure-area isotherms	78
4.5.2. Equilibrium spreading pressure: Spreading of lipid from a volatile solvent..	78
4.5.3. Equilibrium spreading pressure: Spreading of lipid from a deposit on glass	79
4.6. Contact angle measurements and total surface energy calculations	80
4.7. Particle sizing and concentration measurements	82
4.8. US equipment calibration – transducer drive voltage to pressure at the target	87
4.9. Monitoring the mechanics of Lipid Oil Nanodroplet (LOND) rupture into an oil layer and the production of OLI-MBs from LOND precursors.....	88
4.9.1. LOND formation	88
4.9.2. Hydrophilic/hydrophobic treatment of surfaces	89
4.9.3. LOND interaction with hydrophobic/hydrophilic treated glass surfaces.....	91
4.9.4. Quartz crystal microbalance with dissipation monitoring.....	91
4.9.5. Changes to surface pressure due to interactions between LONDS and an air- lipid/aqueous surface	93
4.9.6. Production of OLI-MBs from LOND solution	95
4.9.7. Förster/Fluorescence resonance energy transfer (FRET) enabled LONDS	97
4.10. Microfluidic FF formation of OLI-MBs from bulk phases	101
4.10.1. Evaluating oils for the control of the oil layer thickness during on-chip co- flow	101
4.10.2. Evaluating on-chip pinch off mechanics of gas-in-oil and oil-in-aqueous..	102
4.10.3. Three-phase FF trials	103
4.11. Activation of double emulsion liquid perfluorocarbon (PFC)-in-oil-in- aqueous droplets into OLI-MBs	105
4.11.1. Single emulsion PFC droplet production	105
4.11.2. Double emulsion PFC droplet production.....	106

4.11.3.	Activation of single and double emulsion liquid PFC droplets.....	108
4.11.3.1.	Thermal activation methods	108
4.11.3.2.	Hypobaric activation and on-chip pressure drop	110
4.11.3.3.	US activation methods	113
4.12.	MB echogenicity	116
5.	Results: Surface Energy of an OLI-MB.....	118
5.1.	Pressure-area Isotherms and the Equilibrium Spreading Pressure of lipids at the air-water interface.....	118
5.2.	Surface Energy of oil, air, MilliQ/lipid structures.....	124
5.3.	Mechanical agitation of gas, oil and lipid solution	131
5.4.	Conclusion.....	133
6.	Results: Lipid Oil Nanodroplet (LOND) adsorption and spreading to form a thin oil film	135
6.1.	Size, concentration and lifetime of LONDS.....	135
6.2.	LOND interactions with functionalised glass surfaces.....	139
6.3.	QCM-D studies of LOND interactions with hydrophobic/hydrophilic surfaces.....	142
6.4.	Surface pressure changes to model MB surfaces on the addition of LONDS.....	147
6.4.1.	LOND interactions at a water/lipid-air interface.....	147
6.4.2.	Time dependence of LOND model MB interactions.....	152
6.5.	Formation of OLI-MBs from LOND solution.....	154
6.5.1.	Mechanical agitation formation and MB lifetime.....	155
6.5.2.	Microfluidic OLI-MB formation.....	158
6.5.2.1.	Squalane OLI-MBs	158
6.5.2.2.	Squalene OLI-MBs	163
6.5.2.3.	Tripropionin OLI-MBs	164
6.5.3.	Microfluidic spray production.....	168
6.6.	LOND introduction to stable MBs.....	169
6.7.	Using FRET to assess LOND rupture at a MB surface.....	171
6.7.1.	Assessment of FRET fluorophores	171
6.7.2.	FRET at model MB air-water interfaces.....	176
6.7.3.	FRET to confirm OLI-MB formation.....	177
6.8.	Native oil fluorescence as an alternative to fluorescent oil-loading.....	178
6.9.	Echogenicity of LOND formed OLI-MBs	180
6.10.	Conclusion	182
7.	Results: Co-flow controlled, three-phase FF pinch-off.....	186

7.1. Forming a thin oil layer under oil-aqueous co-flow	187
7.2. Mapping flow rate ratios to facilitate three-phase FF pinch-off.....	190
7.2.1. Oil droplet pinch-off in water/surfactant	191
7.2.2. MB pinch-off in oil	193
7.2.3. Combining two-phase pinch-off regimes to estimate three-phase pinch-off conditions	197
7.3. Three-phase FF trials	199
7.3.1. Lipid shelled OLI-MBs.....	201
7.3.2. Pluronic shelled OLI-MBs.....	202
7.3.3. Triton shelled OLI-MBs	204
7.3.4. BSA shelled OLI-MBs	206
7.4. Conclusion	207
8. Results: Activation of perfluorocarbon-in-oil-in-aqueous double emulsion droplets into OLI-MBs	211
8.1. Formation of single emulsion perfluorocarbon droplets.....	211
8.2. Formation of double emulsion perfluorocarbon-in-oil droplets.....	218
8.3. Activation of single and double emulsion droplets	227
8.3.1. Thermal activation	227
8.3.2. Activation by pressure drop	230
8.3.2.1. On-chip flow induced pressure drop	231
8.3.2.2. Hypobaric activation	233
8.3.2.3. Ultrasound activation.....	237
8.4. Conclusion	248
9. Conclusions	252
References	255

List of Figures

1.1	Schematic of a liposome loaded with hydrophilic and hydrophobic drugs	2
1.2	Schematic of MBs acting under ultrasound in vasculature	5
1.3	Schematic of MB composites for drug loading	8
1.4	Schematics of the three OLI-MB formation routes proposed in this project.....	15
2.1	TEM images of squalane and tripropionin LONDS [6]	18
2.2	Coalescence time for n-hexadecane lysozyme droplets to a n-hexadecane oil layer [91]	19
2.3	SEM images of whipped cream showing bubbles stabilised by fat [95, 99]	21
2.4	Three-phase FF device, Hettiarachchi <i>et al</i> (2012) [29]	22
2.5	Multi-layered gas lipospheres, Hettiarachchi <i>et al</i> (2012) [29]	23
2.6	Three-phase FF device, Kendall <i>et al</i> (2012) [73]	24
2.7	Three-phase FF device, Shih <i>et al</i> (2013) [35]	24
2.8	Triacetin-pluronic shelled MBs, Shih <i>et al</i> (2013) [35]	25
2.9	Ultrasound pressure threshold required to activate C_5F_{12} droplets into bubbles based on their initial diameter [105-107]	27
2.10	ADV and IC thresholds for C_5F_{12} droplets based on diameter and US frequency respectively [113]	29
2.11	C_5F_{12} -Soybean-BSA double emulsion droplets [116]	29
2.12	Schematic of set-up for ADV experiments, with C_5F_{12} -Soybean-BSA double emulsion droplets interacting with cells in an OptiCell [116]	30
3.1	Schematic to explain Re dependence on channel width to height	34
3.2	Schematic of pinch-off regimes characteristic for defined Ca values	36
3.3	Schematic graph to show increased ultrasound scatter from a resonating MB	38
3.4	Schematic of MB oscillation relative to an ultrasound wave [37]	40
3.5	Schematic of a drug loaded MB delivering payload in the vasculature.....	40
3.6	Schematic of an OLI-MB indicating the shell parameters due to the additional oil layer.....	41

3.7	Theoretical OLI-MB resonant frequency over diameter.....	42
3.8	Calculation of OLI-MB dissolution time due to oil layer thickness	47
3.9	Schematic of adhesion between two immiscible materials	48
3.10	Schematic of wetting, partial wetting, and dewetting	50
3.11	Jablonski diagram of FRET	53
3.12	Schematic of absorption-emission spectra for FRET fluorophores	53
3.13	Theoretical PFC droplet expansion on activation to gas.....	56
3.14	Vapourisation temperature of C_5F_{12} droplets over droplet diameter	58
3.15	Vapourisation pressure of C_5F_{12} droplets over droplet diameter.....	59
4.1	Schematic of PDMS microchip fabrication	64
4.2	Two-phase FF microchip	66
4.3	Microspray microchip	67
4.4	Three-phase 5C1, 3C1, 3C2, and 3C3 microchips.....	68
4.5	Microfluidic traps.....	69
4.6	Microfluidic traps optimised for 2-5 μm particles	70
4.7	Schematic of apparatus for microfluidic trap use	70
4.8	PDMS flow cell.....	72
4.9	Set-up for PMMA-SU8-PMMA microchips.....	72
4.10	Sample set-up for imaging; 50 μm deep chamber and droplet on glass	74
4.11	Non-microfluidic flow cell.....	75
4.12	Set-up and basic output for a LB trough	76
4.13	Apparatus used for the contact angle measurement	81
4.14	Schematic of an oil lens on a water/lipid-air surface	81
4.15	Schematic of the working area of a qNano pore	84
4.16	Optical method for measuring microscale particles.....	86
4.17	Schematic of LOND formation by tip sonication and emulsiflex.....	88
4.18	Apparatus and schematic of QCM-D.....	91

4.19	LB trough set-up for adding LONDS below a water/lipid-air monolayer.....	94
4.20	Concept of FRET loaded LONDS for OLI-MB formation	98
4.21	Method used to measure oil layer thickness in an oil-aqueous co-flow channel	102
4.22	Method used to measure double emulsion core to total droplet radius ratio	107
4.23	Set-up for thermal control of microchips/chambers	110
4.24	Schematic of hypobaric activation apparatus.....	111
4.25	3.5 MHz ultrasound, heat controlled set-up	115
4.26	Schematic of microbubble ultrasound scatter measurement.....	116
5.1	Compression-expansion isotherm of DPPC at different speeds	119
5.2	Compression-expansion isotherms and measurement of the collapse pressure....	119
5.3	Measurement of ESP by additions of lipid/solvent to an air-water interface	121
5.4	Measurement of ESP by pulling a lipid coated plate through an air-water interface	124
5.5	Contact angle measurement of oils at a water/lipid-air interface.....	125
5.6	Surface tension measured from surfaces coated with combinations of oil and lipid	127
5.7	Surface energy of configurations of air, oil, and water in the presence of lipid ...	129
5.8	Surface energy of the Figure 5.7 configurations, equivalent to a 2 μm OLI-MB with a thin oil layer	129
5.9	Schematic of OLI-MB shrinkage leading to monolayer compression, followed by oil and gas phase separation.....	131
5.10	Structures from mechanical agitation of C ₄ F ₁₀ , oil, and lipid solution	132
6.1	LOND emulsion size due to tip sonication time	136
6.2	Size comparison between multiple LOND stock solutions	137
6.3	Lifetime measurements of LOND solutions	138
6.4	Contact angle of functionalised glass	139
6.5	Interaction of LOND solution with functionalised glass	140
6.6	LOND solution spreading over 'fresh' glass surfaces	141

6.7	Contact angle of treated QCM-D crystals	143
6.8	Interaction of LOND solution with hydrophobic and hydrophilic QCM-D	144
6.9	Oil layer thickness formed from LOND spreading	146
6.10	Schematic of a LOND spreading to form an oil lens or oil layer	147
6.11	LOND entry by expanding a compressed monolayer	148
6.12	Expansion-compression cycles to assess LOND entry into the monolayer	150
6.13	Sketch of expected surface pressure recording during LOND entry	150
6.14	LOND introduction to static monolayers	152
6.15	Schematic of a surface after intact LOND entry and LOND spreading	154
6.16	Sizing of mechanical agitation OLI-MBs	155
6.17	Lifetime of mechanical agitation OLI-MBs	156
6.18	Washing of fluorescent mechanical agitation OLI-MBs	156
6.19	Washing of fluorescent mechanical agitation OLI-MBs, shell to background fluorescence	157
6.20	Washing of fluorescent mechanical agitation POPC-PEG LOND-MBs	158
6.21	Microfluidic squalane OLI-MB formation with 1 vol% glycerol	159
6.22	Microfluidic squalane OLI-MB formation with 10 vol% glycerol	160
6.23	Squalane OLI-MBs after trapping and washing	161
6.24	Squalane OLI-MB sizing	161
6.25	Squalane OLI-MB lifetime	162
6.26	Comparing the lifetime of mechanical agitation and microfluidic OLI-MBs	163
6.27	Microfluidic squalene OLI-MB formation	163
6.28	Microfluidic tripropionin OLI-MB formation	164
6.29	Tripropionin OLI-MBs in 50 μ m deep chambers and after washing	166
6.30	Tripropionin OLI-MB sizing	167
6.31	Tripropionin OLI-MB lifetime	168
6.32	Flowing LONDS past stable MBs	170

6.33	FRET fluorophores in squalane and tripropionin oils.....	171
6.34	Absorption-emission spectra from FRET Fluorophores in oil.....	172
6.35	Confocal images of FRET LOND solution mixes	173
6.36	White number comparisons from the confocal images of the FRET solutions ..	174
6.37	Emission spectra from FRET LOND solutions	175
6.38	FRET signal from LONDS at large bubble surfaces	176
6.39	FRET signal from microfluidically formed OLI-MBs due to LOND spreading	177
6.40	Intrinsic squalene fluorescence in squalene OLI-MBs	179
6.41	US response from OLI-MBs	180
7.1	Schematic of three-phase FF pinch-off.....	187
7.2	Oil layer thickness in the oil-aqueous co-flow channel	188
7.3	Oil layer thickness in the co-flow channel due to ratio of oil to aqueous phase flow rates	189
7.4	Oil layer dewetting in the co-flow channel.....	190
7.5	Schematic of how the three-phase pinch-off can be broken down into two two-phase pinch-off.....	190
7.6	Oil pinch-off in Triton solution.....	191
7.7	Mapping the oil-in-Triton pinch-off regime to the oil an Triton flow rates	192
7.8	C ₄ F ₁₀ pinch-off in dodecane oil	194
7.9	Schematic showing how a MB in a thin channel can be observed with an 'apparent' diameter.....	194
7.10	Plotting the apparent diameter over the gas and oil flow rate ratio	195
7.11	Regions for successful C ₄ F ₁₀ pinch-off in oils	196
7.12	Combining the C ₄ F ₁₀ -in-dodecane and dodecane-in-Triton pinch-off results	197
7.13	Lipid-squalane shelled OLI-MB formation in the three-phase 3C3 device.....	201
7.14	Pluronic-triacetin shelled OLI-MB formation in the three-phase 5C1 device....	203
7.15	Triton-dodecane shelled OLI-MB formation in the three-phase 3C3 device	205
7.16	BSA-soybean shelled OLI-MB formation in the three-phase 3C3 device.....	206

8.1	Liquid C ₅ F ₁₂ microfluidic microdroplet formation	212
8.2	C ₅ F ₁₂ phase change during microfluidic pinch-off	213
8.3	Sizing of microfluidic C ₅ F ₁₂ , C ₆ F ₁₄ , and C5:C6 microdroplets	214
8.4	Lifetime of C ₅ F ₁₂ microdroplets	215
8.5	Sizing and lifetime of C ₅ F ₁₂ nanodroplets	216
8.6	Mechanical agitation of C ₅ F ₁₂ in oils with surfactant.....	219
8.7	Microfluidic pinch-off of mechanical agitation oil-C ₅ F ₁₂ nanoemulsion.....	221
8.8	Mechanical agitation C ₅ F ₁₂ -oil-BSA double emulsion droplets.....	222
8.9	Sizing and radius ratio of C ₅ F ₁₂ -oil-BSA double emulsion droplets.....	225
8.10	C ₅ F ₁₂ -soybean-BSA double emulsion droplets formed for varied C ₅ F ₁₂ and BSA concentration	226
8.11	Heating of C ₅ F ₁₂ microdroplets	228
8.12	Heating of C ₅ F ₁₂ nanodroplets.....	229
8.13	C ₅ F ₁₂ microdroplets under flow for shear force activation.....	232
8.14	Hypobaric activation of C ₅ F ₁₂ , C ₆ F ₁₄ , and C5:C6 microdroplets.....	235
8.15	Hypobaric activation of C ₅ F ₁₂ -soybean-BSA double emulsion	236
8.16	45 kHz activation of C ₅ F ₁₂ microdroplets	238
8.17	45 kHz activation of C ₅ F ₁₂ nanodroplets	240
8.18	45 kHz activation of C ₅ F ₁₂ nanodroplets as a function of exposure time.....	241
8.19	45 kHz activation of C ₅ F ₁₂ -soybean-BSA double emulsion droplets.....	242
8.20	1.1 MHz, Ibidi chip activation of C ₅ F ₁₂ microdroplets and C ₅ F ₁₂ -soybean-BSA double emulsion	243
8.21	3.5 MHz, High Frame Rate Imaging activation of C ₅ F ₁₂ -soybean-BSA double emulsion droplets, DC 100%	245
8.22	3.5 MHz, High Frame Rate Imaging activation of C ₅ F ₁₂ -soybean-BSA double emulsion droplets, DC 10%	247
9.1	Thought experiment of OLI-MB formation and post-formation stabilisation by a lipid/diacetylene-oil shell	254

1. Introduction

Cancer is one of the leading health concerns worldwide. Globally it accounted for the deaths of 8.8 million people in 2015, and in Europe alone it causes the deaths of 1.9 million people per year (20% of all deaths in Europe).¹ In the UK, it is currently estimated that 1 in 2 people will get cancer in their lifetime.² While research into the large field of cancer treatment has in general improved survival rates of at least 10 years, from 25% in the early 1970s to 50% in 2014, the treatment of certain types of cancer and patient have remained poor. For example, people diagnosed with pancreatic or lung cancer still suffer survival rates of 1% and 5% respectively.² Progress has been made, but clearly improvements to diagnosis and treatment are still crucial. Treatment of cancer is commonly undertaken through a combination of surgery, radiation therapy, and chemotherapy. The latter of which forms the primary basis for treatment of advanced and metastatic tumours.^{3,4} All three of these methods have varying degrees of invasiveness, patient recovery time, and efficacy challenges. For the development of effective chemotherapy agents, the pharmaceutical industry faces a number of obstacles. Drugs can show high levels of toxicity towards healthy non-target tissue, a problem that is made worse when coupled with non-selective *in vivo* distribution. Many drugs also present poor aqueous solubility and stability issues.⁵⁻⁷ These can lead to irritant properties and damage to healthy, rapidly dividing tissue (e.g. bone marrow).^{3,5} In addition, these obstacles lead to a lower concentration of the drug at the target site, which decreases the desired effect from the drug whilst limiting the total dose the patient can receive. These problems often limit therapy and can lead to a higher chance for treatment failure. As such, recently there has been a wealth of study into the formation and use of drug delivery systems.^{4,5,8,9} The primary goals of these systems are to contain the drug safely until it is released and to enhance the selectivity of its distribution *in vivo*. This is to allow for a wider range of drugs to be administered to the patient, with a higher bioavailability of the drug at the target site, whilst reducing the negative side effects of off-site toxicity, enhancing patient treatment, recovery, and overall quality of life. Drug delivery systems are by no means limited only to chemotherapeutic drugs, but cancer treatment is often given as one of, if not the primary, driving forces for research into these systems.

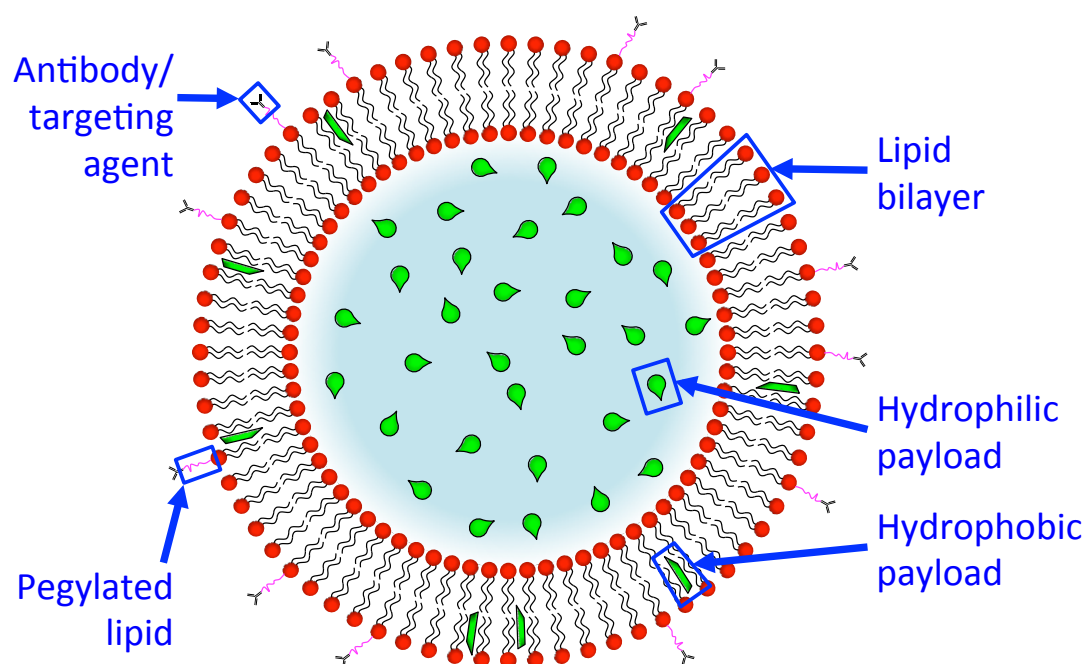


Fig. 1.1. Schematic of a liposome encapsulating (teardrop shape) hydrophilic and (trapezoid shape) hydrophobic drug payloads. Formed with pegylated lipid and targeting agent, for ‘stealth’ from the immune system and targeted delivery respectively. (Figure is not to scale. For example the PEG chains (pink) would realistically be far longer than the lipid tails (black)).

Many drug delivery systems have now been developed including, porous nanoparticles,^{10–12} micelles,^{9,13} lipid emulsions,⁹ and polymer microcapsules,^{8,14} but perhaps the most prevalent system is currently that of liposomes.⁵ Figure 1.1 shows a schematic of a liposome loaded with hydrophilic and hydrophobic drugs. Liposomes consist of a lipid bilayer surrounding an aqueous core. Since the carrier is formed primarily from lipid, the structure is biodegradable after it has delivered its payload. Further, they can be functionalised, for example with pegylated lipid for ‘stealth’ against the immune system,⁴ and target-specific surface molecules to aid delivery (for example antibodies).¹⁵ The first liposomal anti-cancer drug to reach clinical approval was Doxorubicin, with the successful encapsulation of almost all traditional anti-cancer drugs following after that.⁵ This has led to the clinical approval of a number of commercial liposomal anti-cancer drug agents including Myocet, Doxil, DepoCyte, and DaunoXome, with many clinical trials occurring for other agents and their drugs.⁵ Liposomal delivery has reduced the toxic effect of drugs in almost all studies, however there are drawbacks to liposomes as a drug delivery system. Liposome-specific side effects have been noted, for example, to cause skin reactions, most commonly hand-foot syndrome,¹⁶ and hypersensitivity, which can lead to cardiopulmonary distress.¹⁷ Meanwhile, whilst liposomal delivery has reduced off-site toxicity, no significant improvement has been shown to overall patient survival. Whilst the aqueous core can be

loaded with a high concentration of hydrophilic drug, the space for hydrophobic and amphiphilic drugs, within the bilayer shell, is far more limited. Due to combinatorial chemistry and high-throughput screening, the number of drug candidates that present hydrophobicity or poor aqueous solubility has risen in recent years. Estimates vary that this accounts for 30-70% of all drugs currently being developed.¹⁸⁻²² If these drugs are delivered as free-drug in the blood stream they tend to agglomerate, reducing their efficacy and potentially causing toxic effects.²⁰ As such there is a requirement for a system capable of safely transporting higher concentrations of these drugs into the body, and then delivering them efficiently to the target site.

There are three primary solutions to aiding the delivery of poorly aqueous soluble drugs; making physical or chemical modifications to the drug, delivering the free drug in a co-solvent, or loading the drug into particles with hydrophobic cores and hydrophilic exteriors.^{21,23} Each of these routes has associated problems. One of the most typical ways to modify hydrophobic drugs for better aqueous solubilisation is to form them into a salt.^{22,24} However, salts can undergo common-ion self-association, becoming supersaturated and precipitate out of solution. These can become the acidic or basic forms, becoming toxic, leading to epigastric distress.^{22,24} A co-solvent is made when a water- and fat-miscible solvent is mixed with water. This solution is able to solubilise hydrophobic drugs more effectively, with some examples seeing a 500-fold increase in solubility of the drugs, due to reducing the concentration of water in the solution and breaking up the water's hydrogen bonds.^{25,26} This can also allow poorly water stable drugs, which can rapidly degrade or transition through reactive states, to be placed in an environment to which they have increased stability.²⁶ However, drugs have been shown to distribute inhomogeneously throughout co-solvents.²⁷ The co-solvent itself must also be non-toxic, blood compatible, non-sensitising, non-irritating, and physically and chemically inert. However, most candidate co-solvents that show a clinically relevant increase to drug solubility do not follow all of the aforementioned requirements.^{26,27} The third possible solution given was that of loading drugs into or onto hydrophobic drug delivery structures.

This thesis deals with the prospect of forming hydrophobic structures for the loading and then delivery of drug payloads (more specifically oil coated microbubbles - this will be covered in greater detail in section 1.2). In recent years hydrophobic drug delivery systems have been the focus of a large amount of research. Oil emulsions, stabilised by a shell presenting a hydrophilic outside, remain one of the most simple and effective ways to transport hydrophobic drug into the body.^{6,28} Since these are typically similar in

structure to the liposomes described earlier, but with an oil core and a lipid monolayer shell as apposed to a liposome's water core and bilayer, oil emulsions typically have the same benefits of having a biodegradable, functionalisable shell.

The release mechanisms of most available drug delivery systems, which are covered by the above descriptions, can be either passive, e.g. due to drug leakage from the carrier, or active, due to environmental triggered release, e.g. in response to local temperature or pH.^{29,30} However, such mechanisms often lead to unpredictable drug release profiles when applied *in vivo*.³¹ Therefore, a hydrophobic drug delivery system with a controlled, externally activated, triggered release mechanism could offer a considerable advantage over existing technologies. Microbubbles (MBs) offer a promising solution to this problem.

1.1. Microbubbles – Combining theranostic properties with controlled, externally activated release of payloads

Over the past 35-45 years, MBs have become well established as the most powerful particulate for enhancing contrast in ultrasound (US) radiography.³² First generation MBs incorporated air cores, stabilised by human albumin shells.³³ Second generation MBs are often stabilised by lipid, protein, or polymer, and changed the gas cores to be high molecular weight, with low aqueous-solubility and diffusion rates, in order to extend lifetime and vasculature perfusion (most commonly perfluorocarbon gases are used).^{33,34} Wider research has formed MBs incorporating a number of other materials, including gas cores of nitrogen, oxygen, and carbon dioxide and shells formed from sugars and solid particles (often referred to as armoured MBs), and has seen their wider use in fields such as particle propulsion and the recovery of oil from wastewater.^{33,35-40} The compressibility of a MB's gas core, combined with its high acoustic impedance mismatch against surrounding blood plasma, leads to a large scattering cross-section, which gives MBs a high acoustic response.⁴¹ This response can be as high as the response from bone or air in lung, but the response is higher from MBs compared to tissue when imaging non-linear, or sub- or super-harmonic response, providing a higher contrast-to-tissue ratio.^{42,43} These properties make MBs a powerful tool in diagnostic US imaging of the cardiovascular system and organs. As an example, contrast-enhancement of US by MBs was recently evaluated to be a potential powerful tool for monitoring the success of liver cancer radio frequency ablation.⁴⁴ Since they are used in the bloodstream, an important limitation has been that MBs are at maximum 8 μm in diameter in order to prevent issues with blood flow such as arterial embolisms.⁴⁵

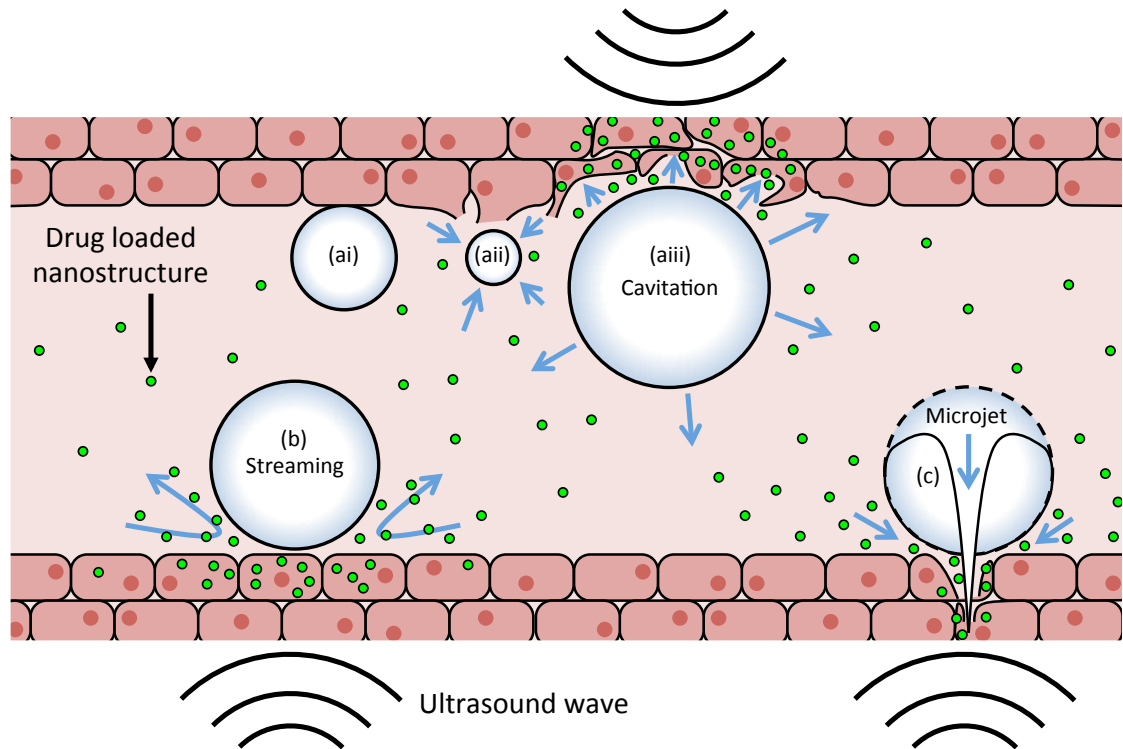


Fig. 1.2. Schematic showing MBs in the vasculature, and how US can drive MBs to (a) oscillate under stable cavitation [(aii) compressing and (aiii) expanding from their (ai) at rest size], (b) stream fluid, and (c) jet towards the vasculature, injecting surrounding contents into cells. The Figure presents how these effects can aid the penetration of drugs (green) into cells.

More recently, MBs have also been shown to be capable of enhancing the therapeutic delivery of drugs.⁴⁶ Figure 1.2 shows how MBs can interact with vasculature walls when undergoing exposure to an ultrasound wave, and how this can affect neighbouring drugs during MB-drug co-delivery. When a MB is exposed to an US wave, it oscillates with the wave, expanding and contracting.^{47,48} This oscillates any fluid in the surrounding area. As shown in Figure 1.2a, if this occurs near the boundary of a cell, the oscillations of the MB provide stresses on the cell wall, which induces holes to appear in the membrane. This effect is known as sonoporation.^{49–51} Stable cavitation of a MB can also lead to streaming of surrounding fluids (Figure 1.2b). Streaming increases the mobility of any drug-carrying fluid (for example in MB and drug co-delivery) and can contribute further to sonoporation, enhancing the chance for drug to cell uptake.^{32,48,50,52} Sonoporation has been shown to allow drugs easier access to cross the cell membrane through the short-lived pores it creates. After sonoporation stops the pores can be transient, where cell is able to rapidly repair the pores, or the pores can remain open and lead to cell death.⁴⁹ One factor that determines if pores become transient or lethal is MB mobility. Van Rooij *et al* (2016) found that limited

displacement of MBs during sonoporation led to the greatest enhancement of drug perfusion into cells whilst inhibiting cell death that would have occurred from static MBs.⁵³ For the method of sonoporation, pre-formed MBs can be injected into a patient's vasculature. However in the absence of pre-formed MBs, US can still induce sonoporation by firstly generating MBs through cavitation directly from the gasses dissolved in the liquid media (blood plasma *in vivo*).^{46,54} If a MB is driven to collapse near a wall, this can lead to the formation of a "microjet" (Figure 1.2c), which can provide momentum to surrounding fluid and drugs.^{50,55,56} The direction of the microjet depends upon the mechanical properties of the wall. Whilst microjets have been found to face towards cells mounted on a rigid substrate, microjets formed in *ex vivo* tissue were found to be directed away from the nearest vessel wall.^{55,57} Saleki-Haselghoubi and Dadvand (2018) gained a deeper understanding of bubble jet dynamics by simulating a bubble oscillating near a circular aperture made in a curved rigid plate. They found that dependant on the aperture's diameter and proximity to the bubble, a jet may not form, may form and face towards or away from the aperture, or jets towards and away may form simultaneously.⁵⁸ This could suggest that for drug delivery, where it is likely difficult to control individual MB proximity to defined vasculature on a large MB population, MB jet direction could be difficult to control and in multiple directions for clinically relevant MB populations. Due to the above, MBs have become very promising "theranostic" agents, with both 'diagnostic' and 'therapeutic' capabilities. However, since MBs can be site-specifically driven to destruction, they have also presented a promising solution to solve the issue that many drug delivery systems lack a controlled, externally activated, triggered release mechanism. As well as the co-delivery of drugs with MBs, MB composites can be made that act as a vehicle for drugs, encapsulating them into or adsorbing them onto their shells. US destruction pulses can then be used to trigger the release of the encapsulated or attached drug payload by destroying the MB vehicle at the target site. This would allow the drug to be safely transported around the body, targeted to problem sites via functionalisation of the commonly lipid MB shell, located in real-time via US, and then released controllably by a change in the US exposure.

1.2. Microbubble-drug composites

Figure 1.3 shows a number of different drug-MB composite designs that have been developed, which roughly fall into the following six categories:^{45,47,50,59–62}

Composite 1. Surface loaded MBs (Figure 1.3b)

Composite 2. Shell loaded MBs (Figure 1.3c)

Composite 3. MBs decorated with hydrophilic core nanoparticle (Figure 1.3d)

Composite 4. MBs decorated with hydrophobic core nanoparticle (Figure 1.3e)

Composite 5. Echogenic liposomes (Figure 1.3f)

Composite 6. Echogenic oil droplets (Figure 1.3g) - this is the structure focal to this thesis. This structure contains three key parts; a gas core, surrounded by an oil layer, surrounded by a shell. The materials of those key parts have been different for different groups, but the layout of the structure has remained the same. This composite has been given a number of different names including:

- Oil layer inside MBs (OLI-MBs) - the term used in this thesis
- Acoustically active lipospheres (AALs)
- Oil-filled polymer-shelled microcapsules

The odd numbered MB composites (1, 3, and 5) are able to hold both hydrophilic and hydrophobic drugs. However, they have a far greater capacity for hydrophilic drugs, which can be held in their large aqueous volumes, but a limited capacity for hydrophobic drugs, which can be held only in their shells. For each odd numbered MB, the following even numbered MB is better suited to the delivery of hydrophobic drugs.

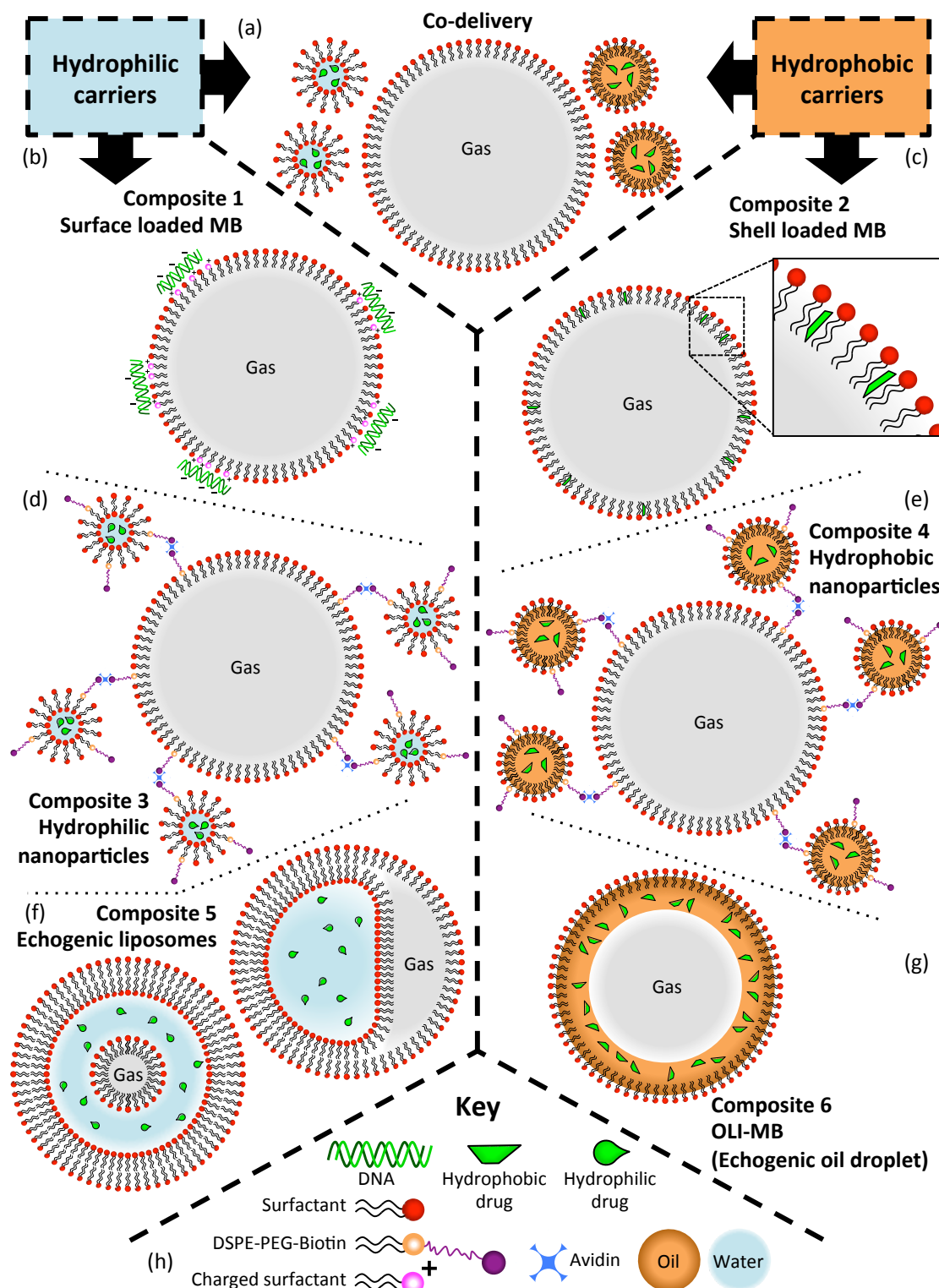


Fig. 1.3. Schematics of MB drug delivery systems. (a) Co-delivery of a drug-free MB with (green teardrop) hydrophilic drug loaded liposomes and (green trapezoid) hydrophobic drug loaded (orange) oil droplets is shown, followed by MB composites for loading with (b, d, and f) hydrophilic or (b, e, and g) hydrophobic drugs, and (h) a key to identify each structure.

1.2.1. Hydrophilic drug-MB composites

Surface loaded MBs (Figure 1.3b, *composite 1*) usually consist of a charged payload and a MB with an oppositely charged shell. Electrostatic attraction then holds the two components together. This structure has been a focus for the delivery of nucleic acids, though it has also been used for a wider range of drugs. Vannan *et al.* (2002) and Christiansen *et al.* (2003) formed this composite from MBs containing cationic lipids, loaded with plasmid DNA, and Taylor *et al.* (2007) formed a similar composite by loading MBs with envelope[protein]-deficient retrovirus.^{63–65} For the latter, it was found that roughly only 30 viral particles were loaded per MB, however this was enough to lead to a 100-fold higher gene expression than compared to co-delivery of the retrovirus with bare MBs. In order to load more payload onto a MB, the number of charged molecules in the shell needs to be increased. However, the percentage of charged lipid molecules in a MB's shell is restricted since higher amount lead to increases in the surface tension of the MB, which results in a lower MB stability and lifetime.⁶⁶ MBs decorated with hydrophilic nanoparticles (Figure 1.3d, *composite 3*) were first reported by Lum *et al.* (2006) where they attached polystyrene beads to MBs by the use of DSPE-PEG-biotin lipid and biotin-avidin attachment.⁶⁷ The same group then used this technique to form MB-liposome composites.⁶⁸ Typically, this leads to 10^5 liposomes per MB, which can be filled with high volumes of hydrophilic drug due to their large aqueous core. These composites have also been used for the delivery of sRNA and genes. However, injections of biotin-avidin links have been shown to cause immune system responses.^{45,66} Other groups have looked into coupling the liposomes and MBs directly. For example Geers *et al.* (2011) and Luan *et al.* (2012) used covalent thiol-maleimide links.^{69,70} It has been reported that whilst MBs with attached liposomes showed no significant difference in shell elasticity, the shell viscosity and the US pressure threshold (required for the onset of MB oscillations) were both increased over MBs without liposomes. Expansion-only behaviour, where MBs expand with little to no compression during US cycles, was found to occur at lower frequencies for MBs with attached liposomes over non-liposome attached MBs. This behaviour was attributed to the liposomes close packing during compression, inhibiting further compression.⁷⁰ Echogenic liposomes (Figure 1.3f, *composite 5*) are a liposomal structure with at least one bubble (regularly nanoscale) located within either the lipid bilayer or the aqueous core. As such, they have the drug delivery benefits of liposomes with the added capabilities of MBs as theranostic agents and a route for activated payload release. Echogenic liposomes have been formed at diameters comparable to typical MBs and the

other MB composites presented in this section (typically formed at 1-5 μm), with Raymond *et al.* (2016) and Shekhar (2017) forming them at 0.8-3 μm .^{71,72} However in addition, Huang *et al.* (2004) formed echogenic liposomes of ~ 800 nm, and Klegerman *et al.* (2016) formed monodisperse echogenic liposomes of ~ 100 nm.^{73,74} This potential for smaller size allows echogenic liposomes to extravasate in the body more efficiently.

1.2.2. Hydrophobic drug-MB composites

Shell loaded MBs (Figure 1.3c, *composite 2*) consist of a MB stabilised by an amphiphilic surfactant (lipid, polymer, or protein) shell, where drugs are loaded into the shell. Hydrophobic drugs and amphiphilic drugs can be loaded into the shell. However, adding payload molecules into the shell is likely to result in less stable MBs. Added to this, at least for lipid MBs, the hydrophobic regions available for drug loading are small, so it can be expected that shell loading is limited. Work using this construct has seen Teupe *et al.* (2002) load DNA into BSA MBs, Zhao *et al.* (2005) load therapeutic protein and hirudin into lipid MBs, Howard *et al.* (2006) form adenoviral MBs, and Phillips *et al.* (2011) load rapamycin into lipid MBs.⁷⁵⁻⁷⁸ Mico (2017) presented (Figure 1.3e, *composite 4*) MBs decorated with hydrophobic oil nanoparticles, termed lipid oil nanodroplets (LONDs), forming MB-LONDs.⁷⁹ The purpose of this work was to form the same biotin-avidin bound structure as seen for *composite 3*, but with the attached nanoparticles containing a core of oil rather than aqueous, to allow for a high volume of hydrophobic payload to be loaded inside. MB-LONDs were successfully formed from squalane and tripropionin oils, which are able to solubilise non-polar payloads, such as dodecanethiol-coated quantum dots, and partially-polar, hydrophobic payloads, such as combretastatin A4 and Calcein AM, respectively.⁷⁹

The main issues with the approaches described above are the low loading capacity in MB shells, and the immune response to the biotin-avidin bonds in the MB-LONDs. OLI-MBs (Figure 1.3g, *composite 6*), which can be thought of as echogenic oil droplets (in comparison to echogenic liposomes, Figure 1.3f, *composite 5*), and which have been referred to before as AALs, consist of a central gas core, surrounded by a layer of oil, with the oil-aqueous continuous phase interface stabilised by a lipid, protein, or polymer shell. Compared to the shell loaded MBs, the oil layer allows for a high volume of drug loading and foregoes the need to squeeze payload into the stabilising shell. Compared to the MB-LONDs, the outer shell is expected to give the same limited immune response as that of non-echogenic oil droplets. Unger *et al.* (1998) were the first to incorporate an

oil layer into MBs, giving them the name AALs.⁸⁰ Since then AALs have been reproduced and further characterised by other groups. AALs are produced through the mechanical agitation of lipid solution, oil (primarily soybean or triacetin), and a gas such as perfluorobutane (C_4F_{10}), resulting in MBs of 2.9 μm average diameter with a thick oil shell capable of high drug loading per MB.⁸⁰ However, large MB to MB variability has been observed, with sizes ranging from 1-10 μm and drug-loading being inconsistent between vehicles.^{81,82} Oil layers can range from 500-1000 nm and 300-700 nm for triacetin and soybean oil respectively, with some vehicles containing no gas at all.^{82,83} It is thought that this large MB to MB variability is due to the chaotic nature of the production method, and lack of control over gas encapsulation. In terms of their US capabilities, AALs' thick oil layer is thought to lead to viscous damping.⁸³ Compared to non-oil-MBs, AALs fragmentation by US is significantly more difficult, with a high mechanical index of 0.67-2.0, and a five-fold higher pulse length being required for MB destruction.^{81,83} During tests of AALs on cells, 30% of the cells were found to die from the US alone.⁴⁷ In 2007 Fang *et al.* claimed to be capable of forming AALs with further control over their average oil layer thickness by varying the relative concentrations of perfluorocarbon to oil. These AALs were repeatedly referred to as MBs. However their diameters ranged from 200 to 600 nm, their cores were perfluoropentane or perfluorohexane (bulk boiling points of 29 and 59 °C respectively, which increases with decreasing droplet size - see Theory Chapter, Figure 3.14), and thermal (37 °C) lifetime experiments showed that only 10% of AAL weight was lost over 12 h. It is far more likely that these AALs were fully liquid filled, with no gas core, so were double emulsion droplets, rather than MBs.⁸⁴ In 2009 Lentacker *et al.* concluded that it remained difficult to efficiently release drugs from any of these AALs using medically relevant US.⁴⁷ Clearly there was a need to be able to form OLI-MB like structures with a thinner and more consistent oil layer. During 2008-2009 Kooiman *et al.* formed polymer shelled OLI-MB like structures that showed an improved clinical application over that of AALs.^{81,85,86} They formed hexadecane OLI-MBs with fluorinated end-capped poly(L-lactic acid) polymer shells. These OLI-MBs showed a tighter size distribution than AALs, with a mean diameter of 1.3 μm , and US response at clinically relevant MI.^{47,81} When exposed to US of a higher MI to release of their payload, these MBs were found to crack, rather than collapse as would be expected for lipid shelled MBs. This was likely due to a stiffer shell supplied by the polymer. The differences between lipid and polymer shelled non-oil-MBs collapsing and cracking respectively has been presented before.⁴⁵ This may indicate that stable oscillations and the formation

of a shock wave on MB destruction could be smaller for these OLI-MBs. This would lead to a less efficient sonoporation effect for enhancing drug transport into target cells during release. During these studies Kooiman *et al.* were limited to forming OLI-MBs filled with ~90 vol% or 35 vol% oil, or MBs filled with no oil, meaning there was room for better control over the structure's gas to oil ratio.⁸¹ For gas-only MBs, resonant frequency is known to be inversely proportional to the MB size. Since the polymer OLI-MBs remained at a constant total diameter regardless of the oil loading, the more oil filled capsules contained smaller gas cores. However, the non-oil-MBs and both oil filled MBs were found to have resonance frequencies around 20 and 13 MHz respectively, meaning that the MBs with smaller gas cores had a lower resonance. Kooiman *et al.* attributed this to the higher shell volume (due to the added oil thickness) relative to the gas core for the oil filled capsules, leading to increased damping of the MB oscillations, which would lower the resonance, and the MBs being encapsulated by a polymer-hexadecane shell (rather than just polymer) where the presence of the oil would contribute to a less ridged shell. In the case of the latter, hexadecane-water has a lower interfacial tension (52 mN/m) than that of air-water (72.8 mN/m).⁸⁷ This would provide less of a driving force for the polymer to stabilise the MB-oil capsule, which could give a lower polymer concentration across the capsule surface, leading to a less rigid shell. To the best of this author's knowledge, to date, no further progress has been seen with these polymer-shelled OLI-MB like structures.

In order to overcome the lack of control presented in the above research, a number of groups have looked into forming OLI-MB like structures through the use of microfluidics. Microfluidic flow focusing (FF) geometries have been widely shown to form lipid MBs with high levels of size control. Typically, these MBs are formed at 1-5 μm with polydispersity indices as low as 2-5%.⁸⁸⁻⁹⁰ This control also extends to foams (architectures of highly close-packed MBs), where Andrieux *et al.* (2018) gained fine tuning over a foams' polydispersity and spatial organisation through FF formation.⁹¹ Ahmad *et al.* (2008) demonstrated the production of ~50 μm multi-layered OLI-MBs through the use of coaxially arranged needles, providing a high degree of monodispersity.⁹² However this method is in part limited by the needles' inner and outer diameters, often leading to MBs that are larger than that required for medical applications. Zhang *et al.* (2013) were able to form multi-layered MBs, of air-in-tween 80/water-in-paraffin, by using a system of two subsequent two-phase FF nozzles respectively.⁹³ However off-chip imaging showed their MBs to be ~50 μm , far above

the clinical size limit of 8 μm . Hettiarachchi *et al.* (2009), Kendall *et al.* (2012), and Shih *et al.* (2013) presented three linked publications that demonstrated methods for OLI-MB formation by using a three-phase FF nozzle system.^{31,94,95} Successful on-chip formation of OLI-MBs was presented, but off-chip imaging of the MBs was minimal, and it was claimed that collection of sufficient samples for post-production imaging and further use was not possible, providing evidence that the structures were unstable. Meanwhile, sizing data showed that the OLI-MBs formed were too large to be used clinically, at $\sim 15\ \mu\text{m}$, $18.6\text{--}22.3\ \mu\text{m}$, and controlled down to a minimum diameter of $8\ \mu\text{m}$ respectively. It was also assumed in all three papers that all of the oil flow was incorporated into the OLI-MBs. No work was done to assess the efficiency of oil loading, even though triacetin oil was used which is highly soluble in water ($70\ \text{g/l}$),⁹⁶ and could have solubilised away during or after OLI-MB formation. There was strong reason to suspect that, with a few further steps of progress, microfluidic FF formation would have been capable of forming OLI-MBs at clinically relevant sizes, but that the OLI-MBs formed needed to be assessed more thoroughly for oil loading and off-chip stability.

1.3.Aims of this project and outline of the thesis

The main aim of this project was to develop an effective, simply, and reliable technique for the formation of OLI-MBs with a thin oil layer, clinically relevant size ($1\text{--}5\ \mu\text{m}$, $< 8\ \mu\text{m}$), and a concentration that would allow for further study of the OLI-MBs' ultrasound and drug loading characteristics and be of clinical interest, all with the intent to enhance the delivery potential for therapeutic, hydrophobic drugs.

This work aimed to:

- (1) Improve upon and fill the gaps in the work already published on OLI-MB formation. Specifically by forming;
 - OLI-MBs with a thin oil layer, in order to decrease oscillation damping, leading to a higher ultrasound response within clinical ranges.
 - OLI-MBs that were stable enough for imaging, potentially through the transition from on-chip formation to off-chip collection.
- (2) After that was achieved;
 - Gain further control over the oil layer thickness in respect to the OLI-MB diameter.
 - Reliably assess the OLI-MBs for their oil content.

- Evaluate how the oil layer thickness affected the OLI-MBs' ultrasound and drug loading capabilities.

Control of three different phases on-chip is inherently difficult and often leads to poor MB yields. Therefore two objectives became apparent as different routes for OLI-MB formation, which were explored separately throughout this project:

- (1) In a two-phase FF system, evaluate the potential for an oil-in-water emulsion (LONDS) to be used as the continuous stabilising phase and as a precursor to oil layer formation at fresh MB surfaces (Figure 1.4a).
- (2) In a three-phase FF system, introduce the oil and aqueous phases upstream from the gas phase and nozzle, allowing the two phases to controllably co-flow, then allow them to be presented at the gas phase as an effective single liquid phase (Figure 1.4b).

Literature surrounding the clinical application of liquid perfluorocarbon droplets that can be activated into MBs led to a third possible route for the formation of OLI-MBs. Here, the objectives were to;

- (3) Controllably form double emulsion liquid perfluorocarbon-in-oil-in-aqueous droplets that after activation to OLI-MBs would be of a clinically appropriate size, and assess how the geometry changed during activation (Figure 1.4c).

In the chapter immediately following this one, the literature behind each of these three OLI-MB formation routes is described in greater depth.

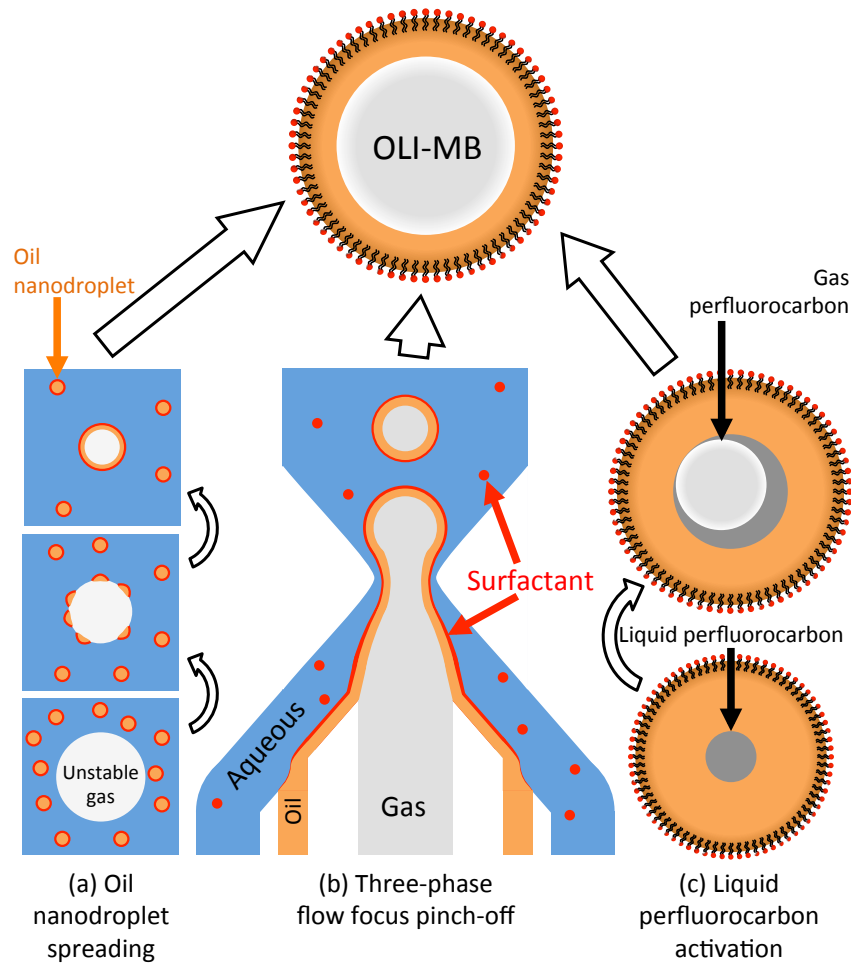


Fig. 1.4. Schematic of the three OLI-MB formation routes that were examined during this thesis project. (a) Oil nanodroplet self-assembly and spreading to form an oil layer at the MB surface. (b) Three-phase FF microfluidic pinch-off. (c) Liquid perfluorocarbon-in-oil double emulsion activation into gas perfluorocarbon-in-oil MBs.

This thesis is structured as follows:

- **Chapter 2** presents the literature background to the three OLI-MB formation techniques that were explored within this project. This covers; (1) Destabilising oil droplets to produce thin oil layer films. (2) Three-phase microfluidic FF formation of MBs. (3) Activation of single and double emulsion liquid perfluorocarbon droplets into gas MBs.
- **Chapter 3** describes the theory that underpins the techniques used and that were important to form and characterise the structures and surfaces formed in this project.
- **Chapter 4** provides the experimental methods that were used for the formation and characterisation of MBs and includes those used to help understand their formation.

- **Chapter 5** is concerned with studying the energetic favourability of potential configurations of gas, oil, and lipid/water phases. This was carried out to determine if the OLI-MB structure was expected to be formed either spontaneously or under controlled introduction of the three phases, and to give insight on the expected stability of the OLI-MB structure after formation.
- **Chapter 6** is concerned with forming OLI-MBs through destabilising LONs to form a thin oil layer at the MB surface. The work details the average OLI-MB diameter, estimations of the oil layer thickness, studies the lifetime and preliminarily ultrasound response, and evaluates the formation route for a number of oils towards extending the drug delivery potential.
- **Chapter 7** is concerned with three-phase FF formation of OLI-MBs controlled by upstream introduction and co-flow of the aqueous and oil phases.
- **Chapter 8** is concerned with forming double emulsion liquid perfluorocarbon droplets capable of activation into OLI-MBs. The work details formation of the lipid droplets from a number of oils, and then looks at the activation of the droplet both as a bulk sample and how the geometry changes during actions.
- **Chapter 9** summaries the main findings presented and discussed during this thesis, gives a final conclusion of the work as a whole, and provides an outlook to future studies in this field. This includes a discussion on which of the three formation techniques showed the most success and which should be taken forward in future work, including suggestions for how to move forward.

2. Context and background to the three OLI-MB formation techniques

The primary goal during this thesis was to develop a method that would allow for the formation of the OLI-MB structure within clinical size limits ($<8\ \mu\text{m}$) and concentrations. Three formation routes were studied; (1) the spreading of oil nanodroplets at the MB gas-water interface, (2) three-phase microfluidic FF pinch-off, and (3) the activation of double emulsion liquid core droplets into gas core OLI-MBs. This chapter serves as a literature review of studies that have previously been published that were integral to these three approaches.

2.1. Destabilising oil droplets to produce thin oil layer films

The first OLI-MB formation route studied the potential for oil nanodroplets to be used as precursors to the formation of an oil layer at MB surfaces. The literature of this section therefore focuses on oil-in-water emulsion formation and coalescence times at water-gas or –oil interfaces, and anti-foaming and stabilisation of foams and bubbles by oil droplet self-assembly.

Formation of oil droplet nanoemulsions is typically performed by ultrasonification or high-pressure homogenisation, both of which commonly lead to droplets under 300 nm in diameter.^{6,97–101} A wealth of studies have been undertaken on the use of nanoemulsions in the food industry, typically focusing on the conditions that affect droplet formation size.^{102,103} However, interest in their use as drug delivery systems in the pharmaceutical industry is growing, partially driven by their ability to penetrate through small capillaries and the high uptake seen across biological tissue barriers.¹⁰⁴ Nanoemulsions capable of therapeutic drug delivery have been developed from a number of biocompatible surfactants including Tween,¹⁰⁵ polyethylene glycol (PEG),¹⁰⁶ and a range of lipids.^{100,107–110} Lipid based emulsions are of particular promise to therapeutics due to being cheap, easy to handle, and their ability to be functionalised for targeted delivery.⁶ Droplet formation size has been found to be primarily dependant on the surfactant shell type, oil viscosity, and formation pressure. The effect from the surfactant shell stems from its ability to lower surface tension, change the shell stiffness, and geometrically control the shell curvature due to its packing parameter (ratio of head to tail size). For example, Hak *et al.* (2012) found that droplets stabilised by PEG were smaller with a higher PEG concentration.¹¹¹ The long PEG chain likely increased the

packing parameter, increasing shell curvature, giving smaller droplets. Lower viscosity oils have been found to result in smaller droplets due to a high deformability. A comparison by Wooster *et al.* (2008) of droplets formed from hexadecane and higher viscosity peanut oil found a 33% diameter difference between the two.¹¹² Lastly, Mico *et al.* (2017) found that higher pressures for homogenisation formation led to smaller droplets.⁶ This last study is of particular interest to this project as the formation protocol presented in that paper was used for emulsion formation during this project with some adaptations (for more information see Experimental Chapter 4.9.1). The work by Mico *et al.* (2017) evaluated high-pressure homogenisation formation of Lipid based Oil Nanodroplets (LONDS) towards medical application. They examined formation using a range of biocompatible oils; squalane, squalene, olive oil, triacetin, tripropionin, isoamyl acetate, and eicosapentaenoic acid, eventually choosing squalane and tripropionin as their successful model oils. Lipid shells consisted of POPC + 5 mol% DSPE-PEG(2000)-Biotin and DSPC + 20 mol% cholesterol + 5 mol% DSPE-PEG(2000)-Biotin for squalane and tripropionin respectively. Optimal formation was found to occur at 175 MPa, forming LONDS of average diameter 165 and 100 nm for squalane and tripropionin respectively, with polydispersity index of 0.1-0.3. Figure 2.1 shows example transmission electron microscopy images of these LONDS. The droplets were found to be stable (less than a 10% change to diameter) over 6 weeks at both 4 °C and 37 °C, with the latter result being of particular interest to clinical application. Tripropionin LONDS were loaded with Combretastatin A4 at 76% efficiency. SVR mouse endothelial cells were treated with these LONDS, resulting in microtubule disruption. This provided evidence for successful drug release and uptake into the cells.

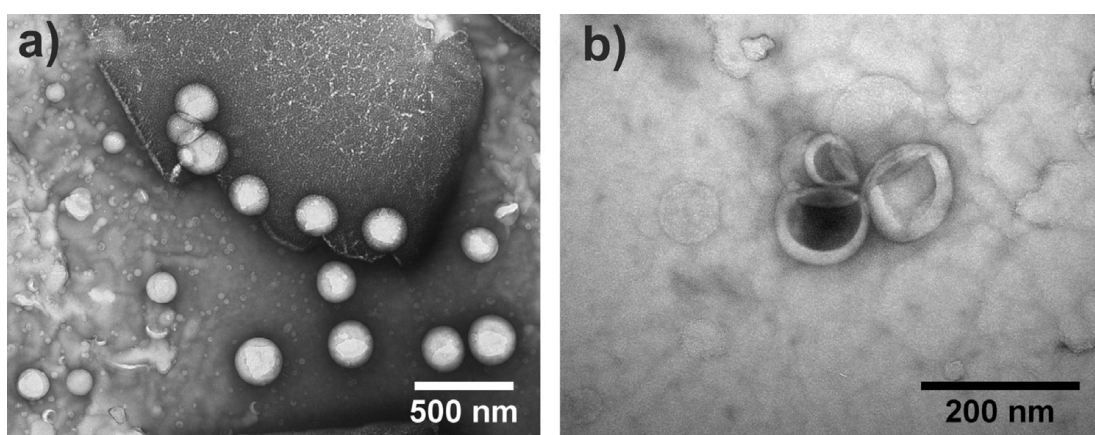


Fig 2.1. Transmission electron microscopy images of high pressure (175 kPa) homogenisation LONDS. (a) Squalane LONDS stabilised with POPC + 5 mol% DSPE-PEG2000-biotin. (b) Tripropionin LONDS stabilised with DSPC + 20% Cholesterol + 5% DSPE-PEG2000-biotin. This Figure has been taken from reference [6].

Once a lipid coated oil nanoemulsion is formed it is typically stable against droplet-to-droplet coalescence for hours, days, or months. However, the coalescence time of these droplets with a partially stable water-oil or water-gas surface can differ greatly. In terms of this project, the surface for droplet coalescence (later in this thesis referred to as adsorption, rupture, spreading, and merging) was that of a fully or only partially lipid stabilised MB. Dickinson, *et al.* (1988) looked at how protein surfactants extend the coalescence time of microscale oil-in-protein/water droplets to a water/protein-oil film.¹¹³ They studied n-hexadecane oil droplets with three different proteins β -casein, κ -casein and lysozyme. Figure 2.2 shows how the droplet size affected the coalescence time and shows an extension of the relationship into the nanoscale. These results showed that the average droplet coalescence time increased from 5 to 30 s with decreasing droplet size from 10 to 2 μm , and that a protein shell with a greater surface viscoelasticity led to further inhibition against coalescence. Oil nanodroplets used in this thesis project were on an order of magnitude smaller than those studied by Dickinson, *et al.* (1988), and so would be expected to take longer to coalesce. Extending the exponential relationship of Dickinson, *et al.* (1988) predicts that nanodroplets of 170 nm would take 80 ± 17 s for coalescence to occur. Since the oil and surfactant shells used in this thesis project were different, this cannot be used as a direct estimate for the coalescence time, however this information did give an indication that coalescence would be expected on the order of seconds to minutes rather than milli to microseconds or hours to days.

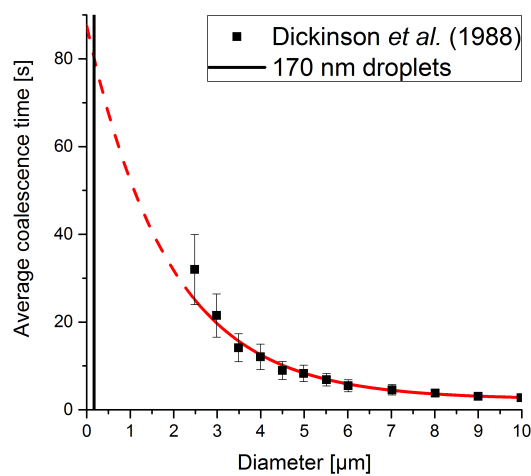


Fig 2.2. Average coalescence time of n-hexadecane lysozyme droplets, as a function of droplet diameter, against a 20 min old water/lysozyme-air surface. This Figure has been adapted from reference [113].

The stabilisation and destabilisation of single bubbles and bubble foams have both been reported by the introduction of oil emulsion droplets to the air-water interface.^{114–116} Most commonly, stabilisation is caused by droplets accumulating and adsorbing at the foam plateau borders or bubble surfaces.^{114,117} Koczó *et al.* (1992) claimed that the accumulation of a higher oil fraction of stable droplets between foam bubbles leads to a more stable overall foam.¹¹⁴ On the other hand, destabilisation usually occurs if droplets spread at the air-water surface, leading to an anti- or de-foaming effect by reducing surface elasticity.^{115,116} During de-foaming, oil locally penetrates a foam's film structure as a defect, displacing the stabilising surfactant. This lowers the surface tension at that point, presenting a 'weak' point. The pulling forces from the surface tension of neighbouring MBs then pull this weak film apart destroying the MBs in that area.¹¹⁶ However, stabilisation and destabilisation is not always as strict as defined above, with one of the primary and most extensively studied examples being the stabilisation process of whipped cream. When air is incorporated into an oil emulsion this often leads to an adsorption of the oil droplets at the fresh air-aqueous surfaces in order to minimise the total surface free energy of the system. Once droplets begin to adsorb, it is expected that flocculation and further coalescence will occur.¹¹⁷ Heller and Peters (1970) presented how flocculation of insoluble droplets at air-water interfaces occurs at a far higher rate than flocculation in the bulk aqueous phase.¹¹⁸ For the case of whipped cream, the process of whipping the cream introduces air bubbles into the emulsion of part solid, part liquid fat droplet stabilised by the proteins found in milk. Mulder and Walstra (1974) described the process that eventually leads to the formation of a stable emulsion of air encapsulated by fat in aqueous as such;¹¹⁹ Fat droplets penetrate the bubbles' surface and partially spread, displacing any stabilising layer, inhibited from full spreading by their solid fat content. Many of the larger bubbles then immediately coalesce with the surface due to the unstable coating layer. Over time, as the insoluble aqueous, gas, and oil phases become vigorously mixed, the effective viscosity of the solution increases, allowing time for larger bubbles to become fragmented before they can coalesce. These smaller bubbles are then coated and stabilised by a close-packed, semi-spread, particle network layer. The network then adds to the firmness of the overall whipped cream solution. Figure 2.3 shows electron microscopy images of the whipped cream gas domains, presenting how the gas, fat, and protein/aqueous phases are organised. Schmidt and van Hooydonk (1980) used a cryo-scanning electron microscopy technique to show the build-up of fat droplets around the air bubbles (Figure 2.3a).¹²⁰ Using an osmium staining technique followed by transmission electron

microscopy of thin sections of whipped cream Graf and Müller (1965) were able to show that no membrane exists between the stable air and fat phases (Figure 2.3b).¹²¹ Since the emulsion is stable, it is therefore most likely that a stabilising protein layer exists between the fat and aqueous phases. These findings were important to this thesis as they showed that incorporation of oil droplets can hinder bubble formation, by increasing coalescence, and can destabilise an already stable emulsion of bubbles, but that the controlled introduction of droplets during the formation of bubbles can lead to bubbles stabilised by a spread oil film as long as the oil layer is allowed time to spread and stabilise fully before contact with another bubble.

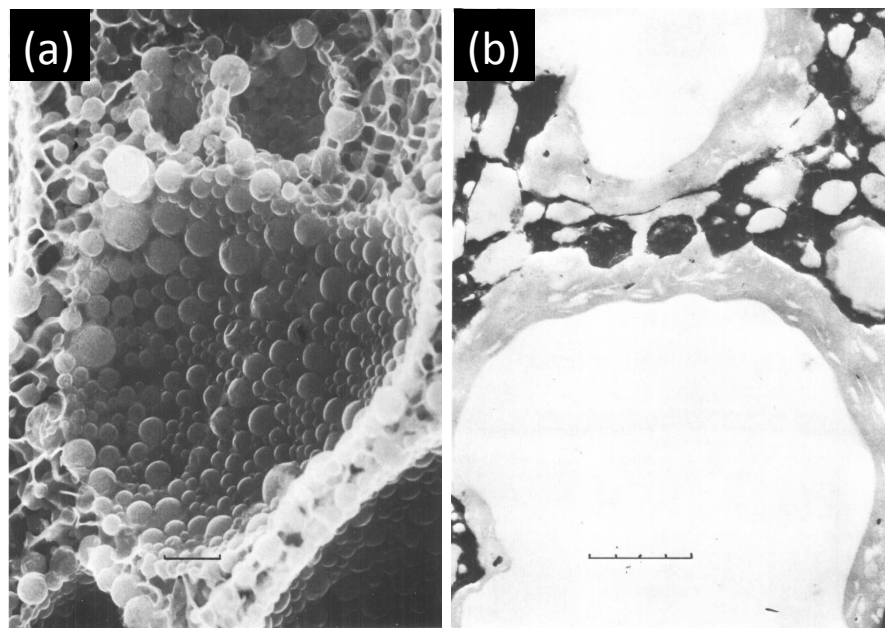


Fig. 2.3. (a) Scanning electron microscopy image of fat droplets adsorbed at the surface of an air bubble in whipped cream. (b) Thin section transmission electron microscopy of a fat encapsulated air cell in whipped cream. (White) Air, (grey) stained fat, and (black) protein/aqueous phase. Bars represent (a) 1 and (b) 5 μm respectively. These Figures have been taken from references [117,121].

2.2. Three phase microfluidic production of microbubbles

The second OLI-MB formation route discussed in this thesis aimed to improve on the work that had been presented by Hettiarachchi *et al.* (2009), Kendall *et al.* (2012), and Shih *et al.* (2013).^{31,82,94,95} Here, they had presented a three-phase microfluidic technique for the formation of oil coated MBs using a single FF nozzle, with the two latter publications improving on the formation rate and MB stability.

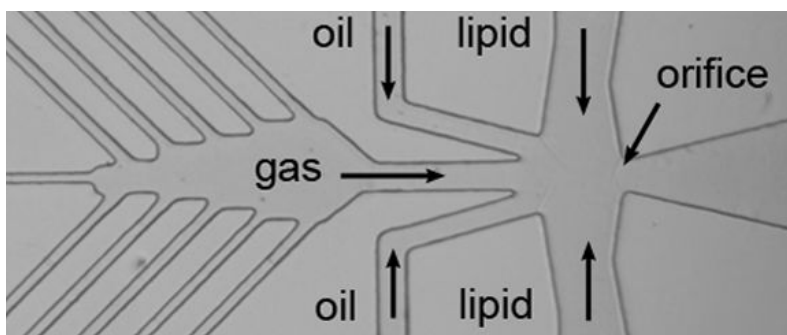


Fig. 2.4. Geometry of Hettiarachchi *et al.* (2009) device for the production of oil coated MBs. All channels had a rectangular cross section and a height of 25 μm . The main functional area is shown with a 25 μm orifice and filtering channels. The arrows indicate direction of flow. This Figure has been taken from reference [31].

Figure 2.4 shows an image of the region of interest of the PDMS device that Hettiarachchi *et al.* (2009) presented for the formation of oil coated MBs (termed multi-layer gas lipospheres).³¹ An inner C_4F_8 gas phase, an outer lipid solution phase, and a triacetin oil phase located in-between the gas and lipid solution, were introduced to each other at close proximity at a microfluidic nozzle. The oil phase was loaded with 0.01 mg/ml Oil Blue N dye or 1 mmol/l Doxorubicin for fluorescence and drug encapsulation respectively. The lipid solution consisted of 0.5 mg/ml lipid (89.1 mol% DSPC + 9.9 mol% DSPE-PEG2000-biotin + 1 mol% DiI-C18 molecular probe) in a 10 w% glycerol/propylene glycol solution. They were able to show the successful formation of MBs on-chip at a maximum of 1×10^3 MB/s, with a degree of control over the MB size. Keeping the oil flow rate constant at 0.016 $\mu\text{l/s}$, varying the lipid solution flow rate and gas pressure was found to give a minimum MB size of $7.5 \pm 0.2 \mu\text{m}$ at a lipid solution flow rate of 0.33 $\mu\text{l/s}$ with a gas pressure of 1 psi. At higher flow conditions, larger MBs were formed due to on-chip coalescence. Coalescence occurred because of the small distances between MBs and the low shell resistance on MB contact due to the MBs only being given time to partially stabilise. Figure 2.5 shows off-chip imaging of larger 15-30 μm MBs. These MBs showed a blue hue and a thin fluorescent exterior, attributed to the fluorophore and Doxorubicin. The major problem for this work was that, while it claimed to show clinically relevant MB formation, the stability of a sample of MBs less than 8 μm , with a confirmed oil layer, was not shown off-chip. On-chip the MBs were claimed to have a polydispersity index under 5%. However, transferring the MBs off-chip may have easily changed this due to coalescence or Ostwald ripening, giving a portion of MBs too large to use clinically. Added to this, those MBs that were shown off-chip showed a very thin layer of fluorescence. Knowing

that triacetin is highly soluble in water (70 g/l),⁹⁶ and with the aqueous phase not being saturated with triacetin before use, this means that there was a high likelihood that the oil layer could have solubilised into the surrounding solution after MB stabilisation, leaving behind the hydrophobic payload but not the oil phase. This could be a route to give a far higher drug shell-loaded MB composition than seen previously (see Figure 1.3 for the composition of shell-loaded MBs), but the work did not confirm the formation of MBs with a stable oil layer.

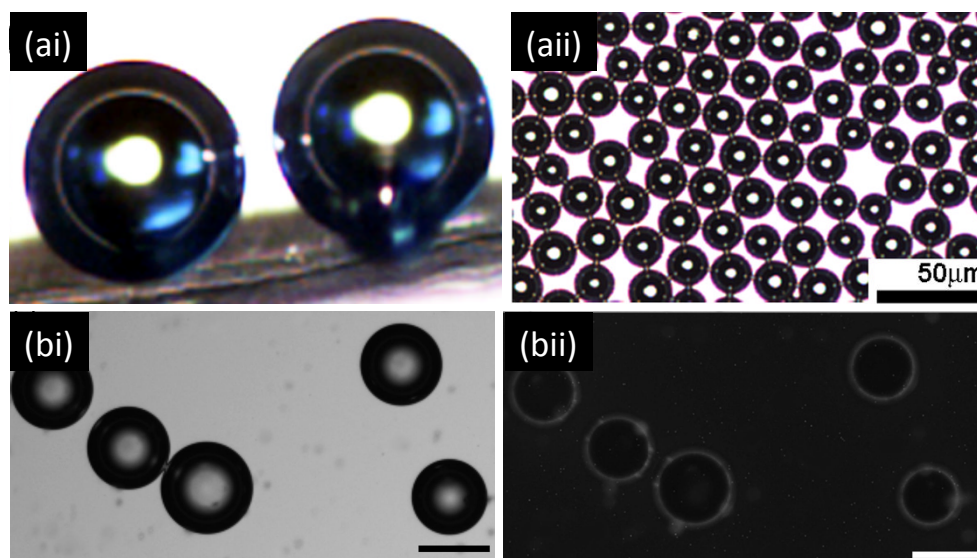


Fig. 2.5. Multi-layer gas lipospheres showing (ai) a close-up, where the inner blue hue can be seen, (aai) and a larger population in bright field. (bi) Bright field and (bii) fluorescence of Doxorubicin loaded lipospheres. Scale bar is 15 μm . This Figure has been taken from reference [31].

A study by Kendall *et al.* (2012) aimed to improve the low formation rate found in Hettiarachchi *et al.* (2009).⁹⁴ Figure 2.6 shows how, using a very similar microfluidic design to Hettiarachchi *et al.* (2009), the working region was multiplexed into a 4- and 8-channel multiarray, where all outlets met in a single MB collection point. Again, triacetin with 0.01 mg/ml Oil Blue N dye was used, however this MB formation used nitrogen gas, and after initial formation of the lipid solution (as in Hettiarachchi *et al.* (2009)) Pluronic F-68 was added at 1 vol%. Pluronic is a non-ionic, triblock copolymer used to control shear forces and reduce foaming and cell attachment to glass, effective down to 0.1 vol%.¹²² Using 280 $\mu\text{l}/\text{min}$ and 12 psi for lipid solution and gas, formation rates were pushed up to 1×10^5 MB/s in the 8-channel multiarray. However, this work found the MBs to be limited to formation at 18.6-22.4 μm with polydispersity index of 9%. While the MB concentration was improved for clinical application, this study actually reduced clinical relevance in terms of the MB size.

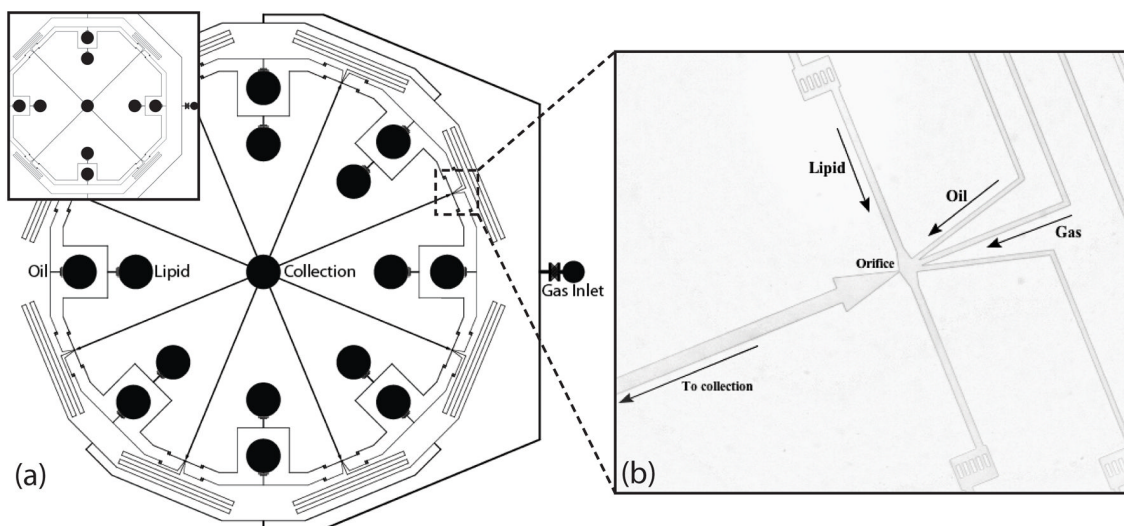


Fig. 2.6. Geometry of Kendall *et al.* (2012) device for high production rate of oil coated MBs. (a) Schematic view and (b) image of the hydrodynamic flow-focusing region. All channels were rectangular with a height of $25\ \mu\text{m}$. Lipid solution, oil, and gas inlet channels measure $50\ \mu\text{m}$, $35\ \mu\text{m}$, and $35\ \mu\text{m}$ in width and directed flow to orifices $9\ \mu\text{m}$ in width. This Figure has been taken from reference [94].

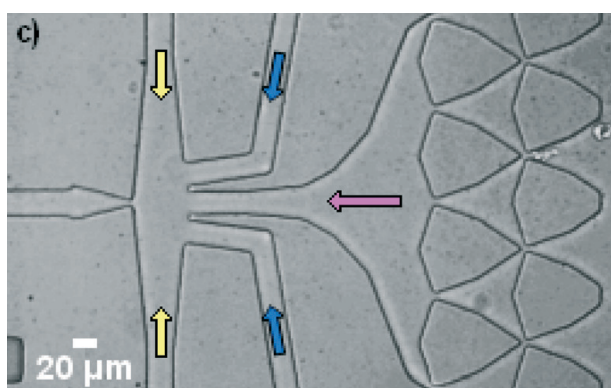


Fig. 2.7. Geometry of Shih *et al.* (2013) device for production of oil coated MBs. Microscope view of empty device, with arrows denoting how gas (pink), oil (blue), and lipid solution (yellow) phases were flowed in. This Figure has been taken from reference [95].

Shih *et al.* (2013) tackled the same problem of low MB formation rate found in Hettiarachchi *et al.* (2009), but instead of multiplexing the microfluidics, they focused on extending the use of Pluronic F-68 in order to reduce coalescence, allowing higher flow velocities to be used.⁹⁵ Figure 2.7 shows the PDMS microfluidic design that was used. In the device outlet, expansion was significantly reduced from the Hettiarachchi *et al.* (2009) design. This was designed to keep the distance between MBs high, reducing the chance for coalescence to occur. The lipid solution consisted of $0.5\ \text{mg/ml}$ $90\ \text{mol}\%$ DSPC + $10\ \text{mol}\%$ DSPE-PEG2000 made up with ultra-pure water. The oil phase was triacetin with $0.01\ \text{mg/ml}$ Oil Blue N dye or Fluorol Yellow 088 for fluorescent imaging. Pluronic F-68 was added to either the lipid or oil phase, or both, at a concentration of 2

vol%. The gas phase was C_4F_8 . Figure 2.8a shows the resultant formation of MBs with and without pluronic in the liquid phases. It was claimed that the addition of pluronic to either phase showed reduced coalescence. This was most likely due to the size distribution of MBs formed. However, addition of pluronic to the oil phase also led to the formation of debris. As such, further study only added pluronic to the lipid solution. Formation of MBs down to 7-8 μm could be achieved on-chip, of which reached 3×10^5 MB/s. However, closer inspection showed that for the MBs formed at this size range the oil phase may not have pinched off successfully, bridging the MBs, which would have led to significant coalescence further down stream of the device. In the concluding remarks it is explained that collection of MB solutions for observation off-chip encountered problems with dissolution and size variation. This was likely due to coalescence and potentially the oil-MB constructs being unstable. Figure 2.8b shows off-chip imaging of a number of MBs above 10 μm that could be collected as a small sample volume. These MBs showed fluorescent exteriors, including a bead of concentrated fluorescence, which was claimed as excess oil. Since again the oil used here was triacetin, the oil layer could have solubilised into the surrounding aqueous phase, as explained with the Hettiarachchi *et al.* (2009) results. However, due to the presence of the fluorescent beads, it is believed by this author that this was an indication of ‘pseudo-partial’ wetting as was seen later for the successful OLI-MB formation results of this thesis (see Chapter 6, Figures 6.23, 6.39). From the Shih *et al.* (2013) publication, this thesis project took information on developing the microfluidic design, such as decreasing the width of the outlet, and using high concentrations of pluronic in the liquid phases.

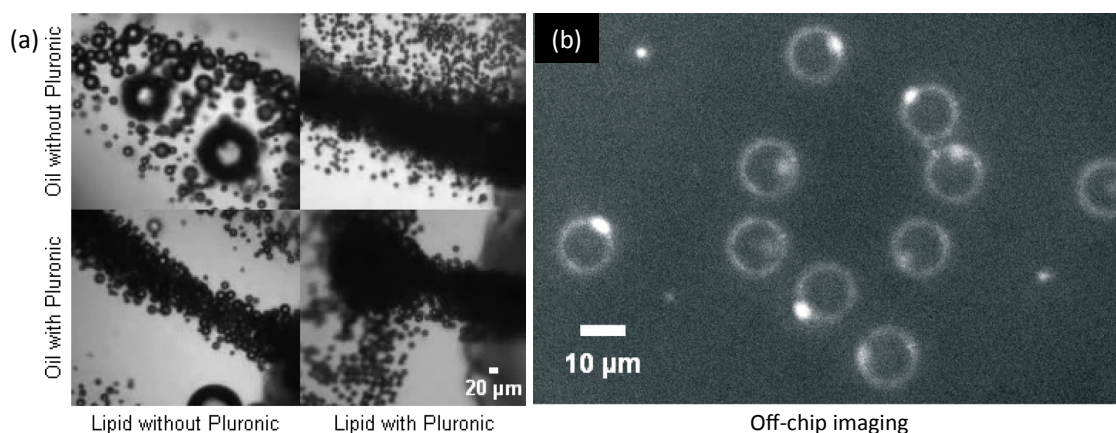


Fig. 2.8. (a) MBs imaged on exiting the microfluidic device where pluronic was in neither phase, the lipid solution, the oil, or both phases. (b) Fluorescence from Fluorol Yellow 088 contained in the MB shell. This Figure has been taken from reference [95].

The main issue with these publications was that they formed OLI-MBs that were too large to be used *in-vivo*, did not confirm the presence of the oil layer, and were not stable when transferred off-chip. The work in this thesis aimed to address these issues, forming OLI-MBs at smaller, more clinically relevant, sizes, with a higher stability off-chip. It also looked into the use of a wider range of less water-soluble oils for less chance of oil layer solubilisation.

2.3. Activation of liquid perfluorocarbon droplets to gas bubbles

The third OLI-MB formation route discussed in this thesis studied the potential for double emulsion, liquid perfluorocarbon (PFC)-in-oil-in-aqueous nanodroplets to be used as precursors for activation into MBs of gas PFC-in-oil-in-aqueous, OLI-MBs. This section therefore gives a brief overview of the large background into the formation and activation of single emulsion PFC-in-aqueous droplets, and then details the limited publications on formation and activation of double emulsion PFC-in-oil-in-aqueous droplets.

The previous chapter explained why MBs offer a promising tool for drug delivery (see Introduction Chapter 1.1-1.2, p 4-13). However, due to the typical size of clinically relevant MBs, 1-5 μm , they are often too large for complete circulation, having varied access across the chaotic vasculature of tumour sites. Compared to healthy tissue, tumour vasculature typically has larger inter-endothelial gaps and poor lymphatic drainage.¹²³⁻¹²⁶ If nanoparticles are introduced to a tumour site, these can pass into the tumour, but due to the poor drainage, they have trouble leaving. This leads to a retention effect, where the number of nanoparticles entering the tumour site outweigh those leaving.¹²⁴ A method known as acoustic droplet vapourisation (ADV) takes advantage of these findings. ADV involves forming a nanoemulsion of liquid PFC droplets that are later phase converted into gas PFC MBs using ultrasound (US). The liquid PFC droplets can enter a tumour site more effectively than pre-formed MBs, be activated into MBs by US exposure, and then deliver drug payload by the same mechanisms of MB enhanced drug delivery as regular MBs, but over a wider target area. During clinical US imaging, PFC droplets show a strong echogenic response due to their high acoustic impedance mismatch with aqueous phases, though the response is not as strong as PFC MBs of the same size (the reason for this is explained in the Theory Chapter 3.2.2, p 39-41).¹²⁷

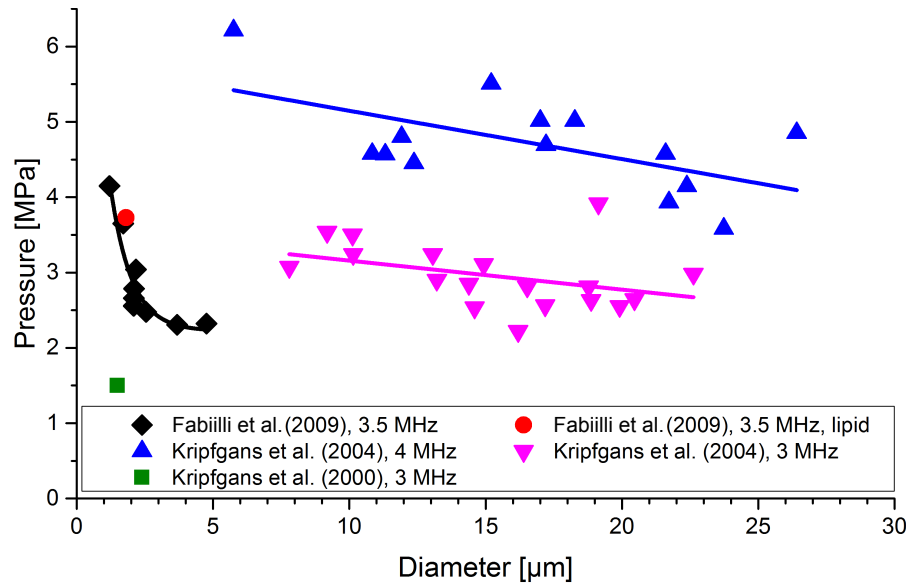


Fig 2.9. Pressure threshold to activate C_5F_{12} droplets of given diameters from a number of publications. All droplets were BSA shelled, with US exposure at duty cycles $<1\%$ and occurring at $37\text{ }^{\circ}\text{C}$ (black diamond, red circle) or $\sim 25\text{ }^{\circ}\text{C}$ (blue and pink triangles, green square). The data in this Figure has been acquired from references [127–129].

Activation of PFC droplets into MBs was first presented by Apfel *et al.* (1998).¹³⁰ Since then ADV of PFC droplets has been proposed for use in tissue occlusion, gene transfer enhancement, phase aberration correction, drug delivery, and as a cavitation nucleation agent for non-thermal US therapy.^{131–134} Bovine serum albumin (BSA) coated C_5F_{12} droplets have seen the most publication.^{127,129,131,132,134–141} Bulk C_5F_{12} has a boiling point of $29\text{ }^{\circ}\text{C}$. This offers a volatile liquid state at room temperature, which is simple to handle when care is taken, yet offers the lowest energy requirement for activation into gas compared to other PFCs that are bulk liquid at room temperature. ADV of C_5F_{12} micro-nanodroplets has been regularly found to require US negative peak pressures of 1 to 3 MPa,¹³⁸ with micrometre sized droplets being capable of activation into 20–80 μm MBs with short tone bursts of US in the diagnostic range (1.5–8 MHz).¹²⁷ The pressure threshold for activation is primarily dependant on the US frequency, exposure time, the introduction of bubbles to the solution (including pre-formed bubbles and ones activated from droplets), and droplet size, with the threshold decreasing on an increase to any of these factors.^{127,129,137,142} Figure 2.9 shows the recorded ADV pressure threshold, based on C_5F_{12} droplet sizes, for a number of publications. However, contrary to the frequency relationship, Rapoport *et al.* (2009) claimed that lower frequencies can allow for more efficient activation due to the longer rarefaction (low pressure) period of the wave, though they also stated that this can increase the chance for coalescence and gas diffusion.¹⁴³ Theory states that on activation the droplets should increase to five

times their initial diameter (see Theory Chapter 3.5.1, p 54).^{127,144,145} However, publications from many groups have seen that the post-activation MB size is often much larger than this.^{127,137,143,146–148} Where 500 nm droplets should give 2.5 μm MBs, MBs of 10s – 100s of micrometres are often observed. It has been proposed that this observation was due to a three-step process of droplet activation, MB coalescence, and diffusion of dissolved air and PFC into the newly formed MBs.¹²³ Fabiilli *et al.* (2009) studied the relationship between the thresholds for C_5F_{12} droplet ADV and inertial cavitation (IC).¹³⁵ Where ADV identifies the point of PFC droplet activation into a gas MB, IC identifies the onset of US driven oscillations that would lead a MB to collapse. Figure 2.10a shows how ADV and IC changed with droplet size. They found that for all cases the threshold for ADV was below IC. Schad and Hynynen (2010) also studied the thresholds of ADV to IC for C_5F_{12} droplets of 1-6 μm , at ~ 25 and 37°C , using US within the therapeutic range (0.6-2.9 MHz).¹⁴² They found that while the ADV threshold decreased with an increase in either droplet size or frequency, IC threshold increased with an increase in frequency and was independent of droplet size. Figure 2.10b shows how the ADV and IC thresholds changed with US frequency for two different publications on similar droplet emulsions. While the US duty cycle (DC - the time an US wave is active within an entire exposure duration) of the two publications differed greatly, these results, with the findings of Schad and Hynynen (2010) based on the size dependence, offer the hypothesis that at a certain limit to droplet size and US frequency, IC could occur at a lower threshold than ADV. Rapoport (2009) presented activation of C_5F_{12} PEG-PLLA and PEG-PCL droplets, where 70% of the population was 590 nm.¹⁴³ They showed that droplet activation occurred at 1.3-1.7 MPa when using DC 100% US of 1-3 MHz, which was dropped to 0.7 MPa when using 90 kHz in the presence of pre-existing MBs. For the latter case, the droplets were held in a gel where the semi-flexible solid would have likely dampened the potential for activation. It was claimed the “explosive” 90 kHz activation was due to presence of pre-existing MBs, which was most probably due to their ability to act as concentration sources for the US. They also explained that activation of PFC droplets by thermal routes is an ineffective way to activate droplets, and that physiological temperatures would not be expected to result in any activation.

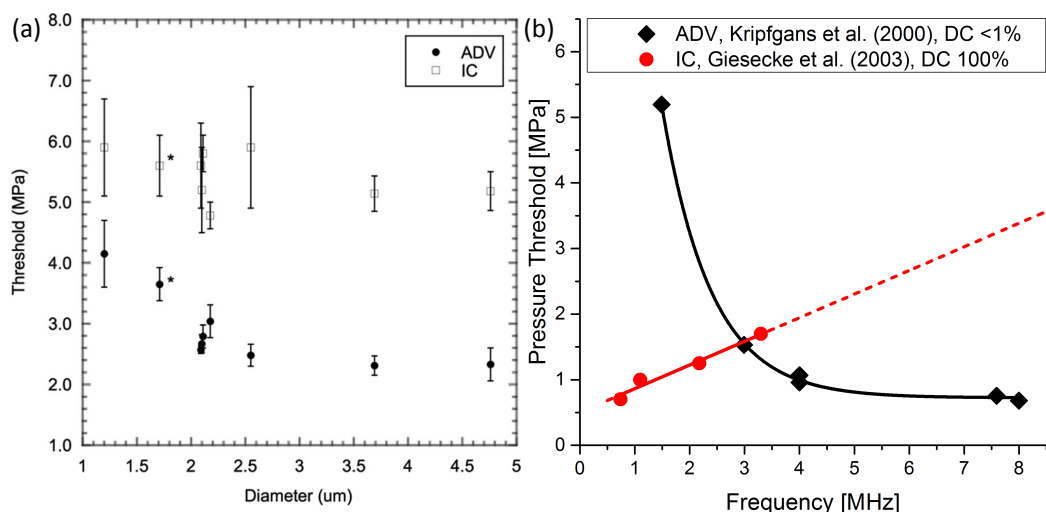


Fig 2.10. ADV and IC thresholds dependant on (a) droplet size and (b) US frequency. C_5F_{12} BSA or DPPC-DPPA (*) droplets. All droplets in degassed water at 37 °C. DC of (a) 0.03% and (b) <1 (diamond) or 100% (red circle). For Figure *a*, the frequency is constant at 3.5 MHz, for *b*, the droplet size is constant at ~1.5 μm. Figure *a* has been taken from reference [135].

The above text described the formation and activation of single emulsion PFC droplets. The following text describes the same but for double emulsion oil-PFC droplets.

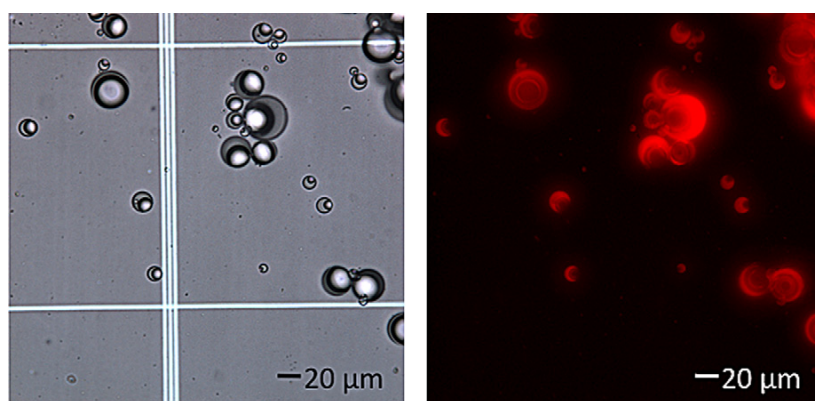


Fig 2.11. C_5F_{12} -in-soybean oil-in-BSA double emulsion droplets, showing fluorescence loaded into the oil phase. Although large droplets appear in this Figure, droplets ≤ 10 μm diameter accounted for only 4.9% (by number) of total droplets. This Figure has been taken from reference [138].

Fabiilli *et al.* (2010) presented a mechanical agitation route for the formation of C_5F_{12} -in-soybean oil-in-BSA double emulsion droplets.¹³⁸ 45 s mechanical agitation of 12 vol% C_5F_{12} and 12 vol% oil in 4 mg/ml BSA PBS solution formed droplets of 3.1 ± 0.2 μm, with $\sim 1.2 \pm 0.4$ μm PFC cores, and a wide size distribution up to ~ 30 μm. 25 mg/ml chlorambucil was loaded into the oil before droplet formation. Figure 2.11 shows imaging of these double emulsion droplets. Figure 2.12 shows how these droplets were then introduced to a 37 °C OptiCell with Chinese hamster ovary cells adhered to the top

surface, before US exposure at 6.3 MHz, 1.57 MPa peak negative pressure, DC 1%. After US the droplets were seen to float to the top of the cell, indicating activation into MBs. Activation required less than 20 s. Growth inhibition studies showed that activated drug loaded droplets showed the same inhibition effect as free drug, indicating effective drug release. However, it was shown that only a small fraction of the droplets were successfully phase converted. 10 μm droplets activated at an efficiency of 90%, dropping to 5% for 2 μm droplets. In terms of the oil released, 6-30 μm droplets released 50%, dropping to 2% for the more clinically relevant 1-6 μm droplets. In this work they showed a significant lack of efficient droplet to MB conversion where the final MB was of clinically relevant size, $< 8 \mu\text{m}$. Dayton *et al.* (2006) presented work using $\text{C}_6\text{F}_{14}:\text{C}_5\text{F}_{12}$ (90:10 or 100:0 vol%) droplets with a triacetin oil shell (≤ 50 vol% of the total droplet volume), stabilised by a DPPC:DPPA:DPPE-PEG(5000) (82:8:10 mol%) shell, purchased from ImaRx Therapeutics.¹⁴⁹ These droplets were $270 \pm 90 \text{ nm}$. US of 10 MHz, 3 MPa, 10 cycles, lead to expansion of the droplets by less than 5% diameter, indicating that the PFC cores did not phase convert into gas. Presumably this was due to the high C_6F_{14} content and small droplet diameter. Fang *et al.* (2009) showed a high-shear homogenization formation route for PFC-in-coconut oil-in-lipid droplets.¹⁵⁰ C_5F_{12} and C_6F_{14} droplets were encapsulated in coconut oil with a lipid shell of 3.5 w/v% HSPC or HSPE, 1.5% cholesterol, 1% Pluronic F-68, and 0.05% camptothecin. Formation with 2 w/v% oil in the solution (PFC at 20 w/v%) led to average 250 nm droplets, which increased to 425 nm when using 20 w/v% oil.

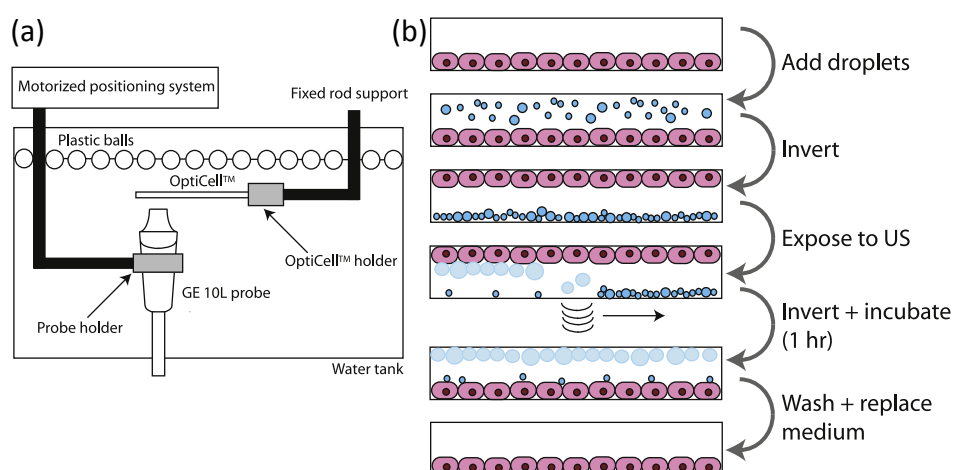


Fig 2.12. Experimental (a) setup and (b) method used to perform double emulsion oil-PFC droplet ADV experiments with adherent CHO cells in an OptiCell. This Figure has been taken from reference [138].

These three publications showed effective means of forming PFC-oil double emulsion droplets from a variety of oils and shells. The latter two could be of more clinical interest due to their smaller formation sizes, which (according to theory) would lead to MBs within clinically relevant size limits, and their lipid shell that could potentially be functionalised with more precision than BSA shells. However, as previously stated, for activation, C_5F_{12} cores would be required. These publications lacked observations of the droplets' changes during activation or an understanding of how the droplets grew and how the oil layer was displaced. The work in this thesis looked to address these issues and to study further the optimisation of droplet size and oil layer thickness.

3. Theory and Background

This chapter contains the underpinning theory relevant to this thesis. The following pages were considered for both design of experiments and analysis of experimental data. This covers; the microfluidic theory of MB formation, the relationships that govern the ultrasound properties and life-time of MBs, the conditions under which a liquid can be activated into a gas through control of temperature and pressure, and Fluorescence, in particular reference to Fluorescence Resonance Energy Transfer (FRET).

3.1. Microfluidics

There are a number of equations that govern microfluidics that have to be considered when developing a microfluidic device. On top of this, microfluidics that concern multiphase flow, specifically with pinch-off of a discontinuous phase in a continuous phase, have relationships that help predict how the phases will interact. When considering two phases where one is encapsulated in another, the phase that is or has been broken up (pinched-off) into discrete objects is referred to as the discontinuous phase, and the phase that pinches-off the discontinuous phase but remains as one complete phase is referred to as the continuous phase. However it should be noted that, throughout this thesis, if the intent was for pinch-off to occur, then these phases are still referred to as the discontinuous and continuous phases before pinch-off and even if pinch-off did not occur (for example, if pinch-off of one phase in another did not occur at a microfluidic nozzle, the central phase which was intended to be pinched-off is still referred to as the discontinuous phase).

3.1.1. Fluid flow in micrometre scale channels

Reynolds Number

One of the key quantities for describing flow of liquids is the dimensionless parameter known as the Reynolds number (Re). Re is used to indicate whether flow will be under laminar or turbulent conditions, where viscous or inertial forces dominate respectively.¹⁵¹ Re is a measure of the ratio of the inertial to viscous forces acting in a fluid and is given by:

$$Re = \frac{\text{inertial forces}}{\text{viscous forces}} = \frac{\rho v D_H}{\mu} \quad (3.1)$$

Where ρ is the density, v is the flow velocity, D_H is the hydraulic diameter ($D_H = \frac{4A}{P}$, for a channel of cross-sectional area A and wetted perimeter P), μ is the fluid viscosity.¹⁵²

$Re < 2300$ predicts laminar flow. $Re > 2300$ predicts turbulent flow. Re in microfluidic devices is typically found to be < 1 , so well within predicting laminar flow.¹⁵³

Microfluidics often deals with volumetric flow rates (Q) [m^3/s] rather v [m/s], as a phase will typically be introduced at one end of a microchip design with a specified Q that remains constant. On the other hand v is dependent on the variable width of the channel, so may change. Therefore, it is important to consider Re with respect to the Q . Since $v = Q/A$:

$$Re = \frac{4\rho Q}{\mu P} \quad (3.2)$$

As a channel's cross sectional area changes in a microfluidic system, the only variable that changes is P . Therefore, a decrease in dimensions at constant Q will increase Re back towards predicting turbulent flow. Most often however, Q is too low to reintroduce turbulence to the system. When one dimension of a channel's cross sectional area becomes significantly smaller than the other (for example in a microfluidic nozzle), the fluid flow will be constrained by the smaller dimension (x) far more than the larger dimension (y). In this case, to make Re represent the flow conditions better, $D_H \sim 2x$.¹⁵² Since $A = x.y$:

$$Re_{x \ll y} \approx \frac{2\rho Q}{\mu y} \quad (3.3)$$

Figure 3.1 shows how Re is approximated in this case, when considering flow down a thin channel. Under these conditions, Re unintuitively becomes independent of x as it is always balanced by an opposing change in v . Only a further change to y would cause a change to Re . This last consideration was crucial to this project as microfluidic nozzles and flow channels were used where one dimension (width) was around an order of magnitude smaller than the other (height) ($\sim 7 \times 25 \mu\text{m}$ for a nozzle and $25 \times 300 \mu\text{m}$ for a flow channel).

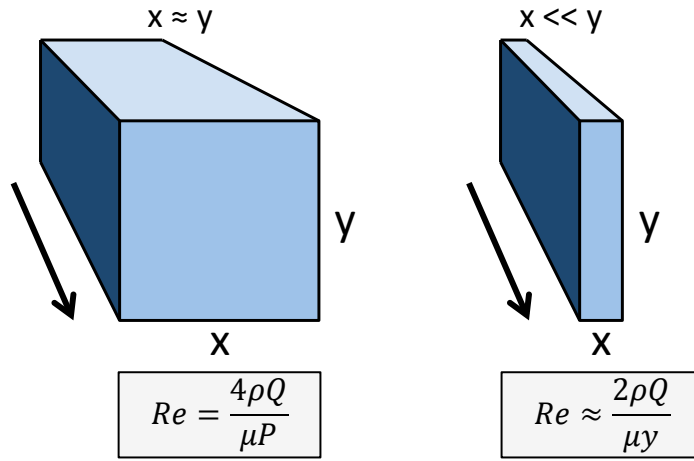


Fig. 3.1. Schematic showing how Re is approximated when considering volumetric flow rate in a thin channel ($x \ll y$).

During this project, typically the highest possible on-chip Re value was ~ 20 , occurring at nozzles. A high Q of ~ 3.5 ml/min (which was experimentally unusable, due to the high pressure that would be required to flow fluid through the small microfluidic dimensions of this project, as explained in the flowing section “*Flow resistance*”) would be required to make $Re = 2300$ and introduce the conditions for prediction of turbulence. This indicated that laminar flow was expected throughout all of the devices used in this project, aiding co-flow of species and preventing turbulent mixing.

Flow resistance

It is important to consider the resistance to flow (R_ϕ) within microfluidic channels in order to determine how multiple fluid components interact throughout a microfluidic network.

$$R_\phi = \frac{2f^{Re}l\mu}{A(D_H)^2} \quad (3.4)$$

$$\Delta P = QR_\phi \quad (3.5)$$

Where f^{Re} is the coefficient of friction ($f^{Re} = 24$ for a filled rectangular channel), l is the channel length, and ΔP is the pressure difference across the channel.¹⁵⁴

It should be noted that R_ϕ is dependent on the viscosity of the fluid in the channel. During this project, microfluidic experiments often dealt with two or three phase flow. This meant that it was often necessary to consider the resistance of a number of fluids relative to each other through the same channel to avoid backflow of one phase due to the force supplied by another. Practically, R_ϕ must be considered as a limiting factor to microfluidic systems. If the resistance increases too high, the pressure required to flow a

fluid down the channel may not be experimentally attainable with the equipment available.

3.1.2. Microfluidic droplet and bubble pinch-off formation

Capillary number

Capillary number (Ca) defines the relative importance of the viscous forces (local shear stress) against the interfacial tension/capillary forces acting across the interface between two immiscible fluids. Ca is used to predict the regime under which a discontinuous phase pinches-off in a continuous phase.

$$Ca = \frac{\text{viscous forces}}{\text{interfacial forces}} = \frac{\mu v}{\gamma} = \frac{\mu Q}{\gamma A} \quad (3.6)$$

Where γ is the interfacial tension.^{155,156}

A Ca value is often obtained for both of the fluid phases. However it has been recognised that the continuous phase plays a greater role in defining the pinch-off regime.¹⁵⁷ Ca studies have typically considered three microfluidic pinch-off geometries; (1) coaxial, where the discontinuous phase inlet ends inside of a wider parallel continuous inlet, such as a tube within a tube, (2) flow focusing (FF), where the continuous phases forces the discontinuous phase through a small nozzle from both sides, and (3) T-junction, where the discontinuous phase inlet joins onto the continuous phase inlet (typically at 90°), giving a ‘T’ shape. As shown in Figure 3.2, a very low Ca predicts a **squeezing regime**, also known as “**geometry controlled**”, where the discontinuous phase repeatedly plugs up the nozzle before the continuous phase builds up enough pressure to push a packet of the discontinuous phase through the pinch-off region. A low to medium Ca predicts a **dripping regime**, where the discontinuous phase is held at the nozzle and packets of the discontinuous phase rapidly shear off the tip. A high Ca predicts a **jetting regime**, where the continuous phase travels through the nozzle and destabilises into packets a small distance downstream of the nozzle.¹⁵⁶ It is suggested that a far greater Ca predicts laminar **co-flow**, or rather a non-pinch-off regime.¹⁵⁸ For a FF geometry a $Ca \ll 10^{-1}$, $<10^{-1}$, $>10^{-1}$, and $\gg 10^{-1}$, would predict a squeezing, dripping, jetting and co-flow regime respectively, with a rough transition zone at $10^{-2} - 10^0$ between the characteristic regimes, where it would be difficult to predict which fluid flow rates would give what regimes.¹⁵⁶

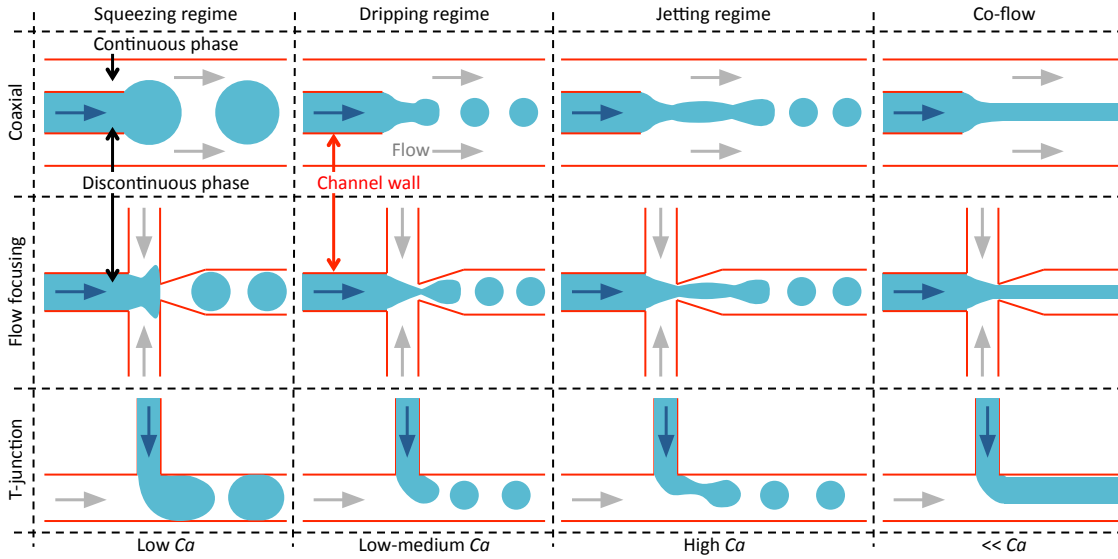


Fig. 3.2. Schematic showing (rows) the three most common pinch-off geometries, coaxial, FF, and T-junction, with (columns) the four pinch off regimes, squeezing, dripping, jetting and co-flow (non-pinching). This project was most concerned with the FF/dripping and T-junction/co-flow regimes.¹⁵⁶

Typical flow rates used in this project for aqueous and oil phases centred around 30 $\mu\text{l}/\text{min}$ and 1 $\mu\text{l}/\text{min}$ respectively. These flow rates gave $Ca \leq 10^{-1}$. Therefore, pinch-off was typically expected in the dripping regime.

Weber number

Weber number (We) defines the relative importance of the inertial forces against the interfacial tension/capillary forces acting across the interface between two immiscible fluids.

$$We = \frac{\rho d_0 v^2}{\gamma} = \frac{\text{inertial}}{\text{interfacial}} = \frac{\rho d_0 Q^2}{\gamma A^2} \quad (3.7)$$

Where d_0 is the diameter of the discontinuous phase bubble/droplet during pinch-off in the continuous phase. We is typically calculated in reference to the discontinuous phase.^{156,159–161}

We becomes an important characteristic of pinch-off and aids predictions for microfluidic geometry design when inertial forces are no longer negligible (when $We \geq 1$). However, typical flow rates used in a planar FF geometry, including the higher end of the flow rates used in this project ($\sim 100 \mu\text{l}/\text{min}$), usually lead to $We \ll 1$, so for most cases We can be neglected in favour of concentrating on Ca which defines the pinch-off characteristics in more detail.^{159,160}

Pinch-off scaling law

During microfluidic pinch-off of one phase in another, it is expected that for every distinct discontinuous phase flow rate, Q_d , there will be a range of continuous phase flow rates, Q_c , that facilitate pinch-off. For example, when using a FF geometry, if the continuous phase flow rate is set too low the discontinuous phase will flow through the nozzle without pinching off, if it is set too high the discontinuous phase will be held at the nozzle or be pushed back up its own inlet. Within this pinch-off region, the lowest Q_c is expected to produce the largest discontinuous phase bubble/droplet and the highest Q_c is expected to produce the smallest bubble/droplet. Between these two points, the bubble/droplet diameter is described by the following scaling law;

$$d/D \propto (Q_d/Q_c)^n \quad (3.8)$$

Where d is the apparent diameter of the bubble/droplet (if the outlet channel is thinner than the bubble/droplet's diameter, so that it is squeezed, this is the diameter observed from the top/bottom interface), D is the characteristic diameter of the nozzle, and n is a value dependant on the geometry of the microfluidic chip.⁴³ The value of n varies between different chip geometries. For example, $n = 0.17, 0.37$ and 0.4 for axisymmetric geometries, FF designs with elongated nozzles, and planer FF short nozzle designs respectively.^{43,159,162–164}

3.2. Microbubbles and ultrasound

The following theory covers how MBs respond to ultrasound and how their size and concentration changes over time.

3.2.1. Echogenicity

When an ultrasound wave is incident to an interface between two substances, a portion of that wave is reflected/scattered and a portion of that wave is refracted. The higher the acoustic impedance mismatch between the two substances, the greater the reflected portion.⁴¹ The scattered portion is what is typically collected during ultrasound imaging. Medical ultrasound images of the body have a relative higher contrast when imaging bone against soft tissue and a lower contrast when imaging organs against soft tissue, where the acoustic impedances are on the orders of 10^{6-7} , 10^6 , and 10^{4-5} $\text{kg.m}^{-2}.\text{s}^{-1}$ for bone, soft tissue, and organs respectively.^{51,165,166} One of the greatest acoustic impedance differences in the human body are between lung tissue and teeth enamel, at

1.80×10^5 and $1.60 \times 10^7 \text{ kg.m}^{-2}.\text{s}^{-1}$ respectively.^{165,166} Air and blood have acoustic impedances of 4×10^2 and $1.66 \times 10^6 \text{ kg.m}^{-2}.\text{s}^{-1}$ respectively.^{51,165,166} This two orders of magnitude greater mismatch allows MBs in the blood stream to be capable of scattering far greater ultrasound intensities per unit area of interface, compared to any human tissue components. However, the compressibility of MBs pushes their echogenetic properties even higher.

$$I_s = \frac{I_i \sigma}{4\pi R^2} \quad (3.9)$$

$$\sigma \propto r^6 f^4 [f(Z)] \quad (3.10)$$

Where I_s is the intensity of scattered ultrasound, I_i is the intensity of incident ultrasound, σ is the scattering-cross section, R is the distance the wave has travelled after scattering, r is the radius of the scattering particle, f is the frequency of incident ultrasound wave, $f(Z)$ is a variable which takes into account acoustic impedance mismatch between the phases inside and outside of the scattering interface.

A large acoustic mismatch leads to an increase of $f(Z)$. This leads to a high σ , resulting in a high I_s . As the MB r increases so does I_s . However, MBs for medical use have an upper diameter limit of $<8 \mu\text{m}$ to allow them to transit the microcirculation, cross the lung capillary bed and to prevent health issues such as atrial embolisms.^{43,167,168}

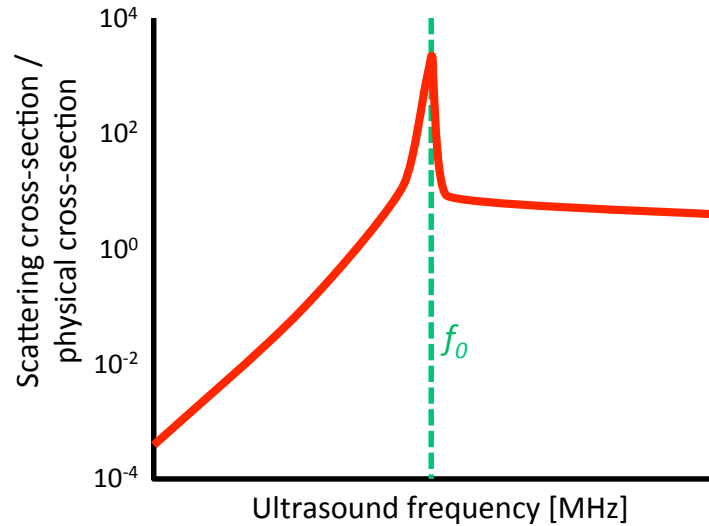


Fig. 3.3. A sketch to show how the scattering cross-section of a MB, proportional to the scattering intensity, changes with the frequency of an incident ultrasound wave. The resonant frequency, f_0 , is indicated. Adapted from reference [41].

Equations 3.9 and 3.10 apply to any particle. However, due to a MB's gas core being compressible, MBs can additionally respond to exposure of ultrasound waves by

oscillating.¹⁶⁷ Here, the MBs contract and expand with the ultrasound wave's frequency as it presents the MBs with an environment that oscillates between a relative high and low pressure. This process is called stable cavitation.⁴⁷ When the f of the ultrasound wave is equal to the MB's fundamental/resonant f, f_0 , the oscillation of the MB become resonant, where the amplitude of the oscillation becomes greater. At these large oscillation amplitudes, the compression against the encapsulated gas is smaller than the expansion. On average, this leads to the MB being larger over time.¹⁶⁷ Since σ increases to the sixth power with r , only a small increase in size leads to a very large increase in σ and I_s , giving a many orders of magnitude higher echogenic particle.^{41,169} Whilst the high acoustic impedance mismatch is enough to give MBs a large I_s , the property of oscillation gives them a vastly superior scattering yield.⁴¹ Additionally, due to the non-symmetrical oscillation, this gives the MB a non-linear response. The non-linear response can be especially useful for distinguishing MBs from surrounding tissue, which will typically oscillate in a strongly linear manner. MBs also oscillate with peak amplitudes in response to US waves at subharmonic and harmonic frequencies of the MB's resonant frequency ($f_{\text{subharmonic}} = f_0/n$ and $f_{\text{harmonic}} = f_0 \cdot n$, where n is a positive integer). In general, the scatter of a MB at f_0 provides the most intense signal, with subharmonic and harmonic signals being progressively less intense. However, the second harmonic can be two or three times more intense than that at f_0 . On the other hand, human tissue gives off a far lower signal at these harmonic frequencies. This means that if the harmonic signals are used for imaging it is possible to achieve a higher signal-to-noise ratio.^{41,167}

If a MB is exposed to a high acoustic pressure ultrasound wave, then the expansion and compression of the MB can become large enough to destabilise it, causing the MB to be destroyed in a catastrophic nature.¹⁶⁷ This type of mechanism is called ***inertial cavitation*** and generally leads to the fragmentation of the original MB, forming smaller MBs.⁴⁷ Figure 3.4 represents the differences between ***stable*** and ***inertial cavitation***, whilst Figure 3.5 shows how the latter technique can be used to release encapsulated drugs.

The increased intensity of the scattered ultrasound due to the MB's oscillations is also dependent on effective energy and momentum transfer to the MB, which in turn is controlled by the mechanical properties of the shell, with a more rigid shell requiring a higher acoustic power to drive the same scale of oscillations and rupture.^{167,170}

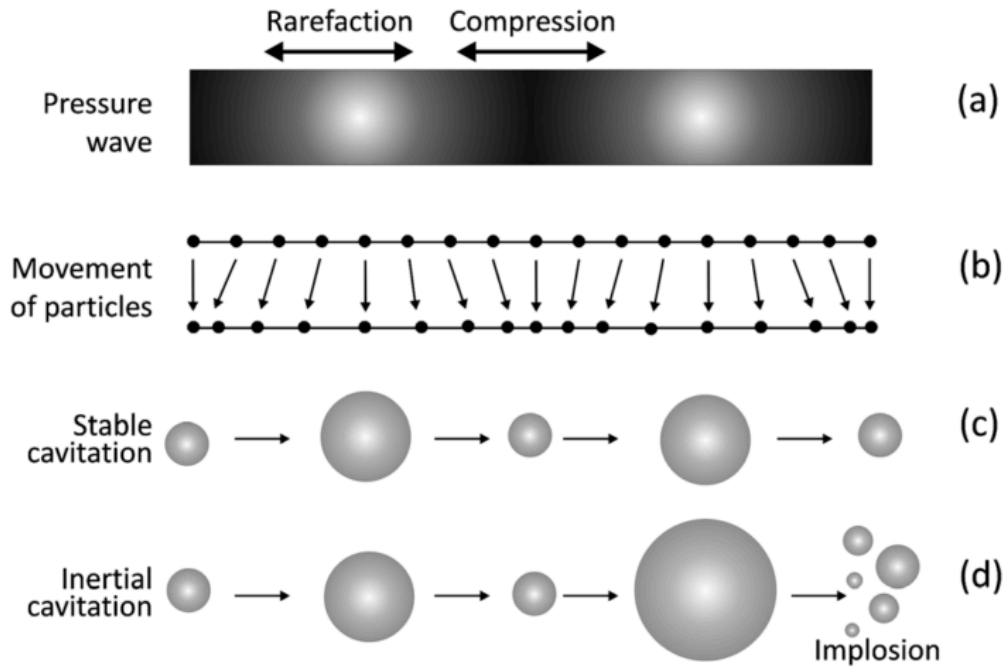


Fig. 3.4. Schematic of the link between (a) the rarefaction (expansion) and compression sections of a pressure wave created from an ultrasound wave, (b) the displacement of particles in the solution the wave is exposed to, and (c) stable and (d) inertial cavitation of a bubble under the applied pressure wave.⁴⁷

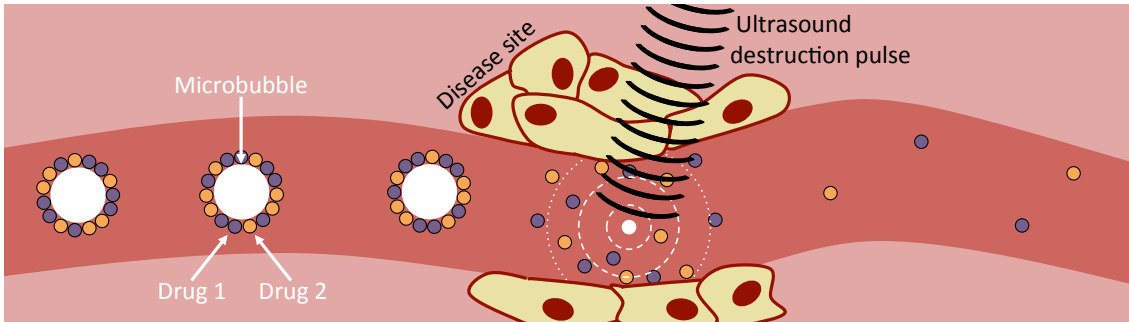


Fig. 3.5. Schematic of a bubble being destroyed by an ultrasound signal and releasing a loaded drugs in a patient's vasculature. Adapted from Bekeredjian *et al.* 2005.¹⁷¹

The oscillations of the gas core can be modelled by the Rayleigh-Plesset equation

$$\frac{P_B - P_{L\infty}}{\rho_L} = r \frac{d^2 r}{dt^2} + \frac{3}{2} \left(\frac{dr}{dt} \right)^2 + \frac{4\nu_k}{r} \left(\frac{dr}{dt} \right) + \frac{2\gamma}{\rho_L r} \quad (3.11)$$

Where P_B is the pressure inside the MB, $P_{L\infty}$ is the pressure of the liquid at infinite distance from the MB (when at rest $P_{L\infty} = P_a$), ρ_L is the density of the liquid, t is the time, ν_k is the kinematic viscosity,

For the case of an external pressure source, like a moving ultrasound wave, P_B is assumed to be uniform across the MB.

3.2.2. Resonant frequency, f_0

The resonant frequency of a MB, considering the shell stiffness, can be given by the following model, which was introduced by Marmottant *et al.* (2005) and later linearised by van der Meer *et al.* (2007).^{172,173} This equation assumes that the acoustic pressure of the US wave being used to oscillate the MB is not high enough to cause buckling of the shell or MB rupture:

$$f_0 = \frac{1}{2\pi} \sqrt{\frac{1}{\rho r_0^2} \left[3\omega P_0 + \frac{2\gamma}{r_0} (3\omega - 1) + \frac{4\chi}{r_0} \right]} \quad (3.12)$$

Where ρ is the density of the surrounding continuous phase, r_0 is the radius of the MB at rest, ω is the polytropic gas index (1.07 for C₄F₁₀), P_0 is the hydrostatic pressure (which for most cases considered in this work is equal to atmospheric pressure, P_a), and χ is the elastic modulus of the shell.

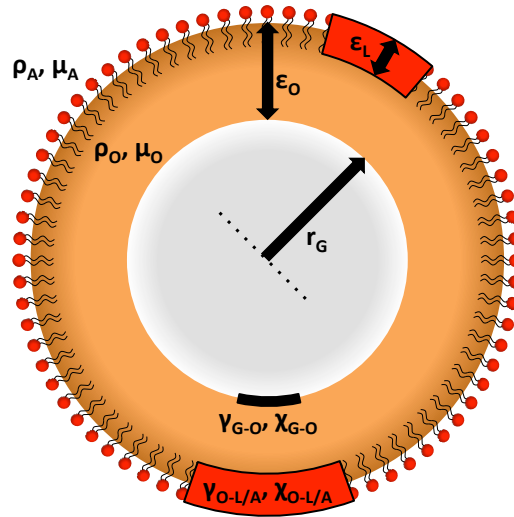


Fig. 3.6. Schematic showing how the parameters of density, viscosity (μ), shell thickness (ϵ), interfacial tension, and elastic modulus apply to an OLI-MB, given the addition of the oil layer.

Figure 3.6 shows how the MB parameters for determining resonant frequency are applied to an OLI-MB due to the addition of the oil layer. For the case of an OLI-MB, the ρ could be equal to the oil layer (ρ_O), the surrounding aqueous phase (ρ_A), or more realistically a coupling of the two. This is due to the gas core oscillations being constrained by displacement of the surrounding solution. Here, it can be assumed that an infinitely thin oil layer would not impart much of a damping force on the oscillations, with damping instead being supplied by the aqueous phase, compared to an OLI-MB with an effectively infinitely thick oil layer, where almost all (if not all) of the damping would be supplied by the oil. For simplification, we assume that the higher ρ fluid

would be dominant here. χ can be assumed to be equivalent to that of a lipid shelled MB as the elastic modulus of the oil layer would be negligible compared to the lipid monolayer. Calculations using equation 3.12 (Figure 3.7) considered MBs and OLI-MBs with POPC shells. For an uncoated MB, $\chi = 0$ N/m. For a DPPC and DSPC lipid shelled MB, $\chi = 0.06$ and 0.26 N/m respectively.¹⁷⁴ Apart from one C=C bond, POPC's two tails are identical to one tail from DPPC and one from DSPC. We can therefore estimate POPC's $\chi \approx 0.16$ N/m. An OLI-MB would have two interfaces, both of which would contribute to the pressure inside the structure. Therefore:

$$\Delta P = 2 \left(\frac{\gamma_{G-O}}{r_G} + \frac{\gamma_{O-L/A}}{r_0} \right) = \alpha \quad (3.13)$$

$$r_0 = r_G + \varepsilon_O \quad (3.14)$$

Where γ_{G-O} and $\gamma_{O-L/A}$ are the surface tensions at the gas-oil and oil-lipid/aqueous interfaces respectively, r_G is the radius of the gas core at rest, and ε_O is the thickness of the oil shell.

Factoring Equation 3.13 into Equation 3.12 gives:

$$f_0 = \frac{1}{2\pi} \sqrt{\frac{1}{\max(\rho_A, \rho_O)} r_0^2 \left[3\omega P_0 + \alpha(3\omega - 1) + \frac{4\chi}{r_0} \right]} \quad (3.15)$$

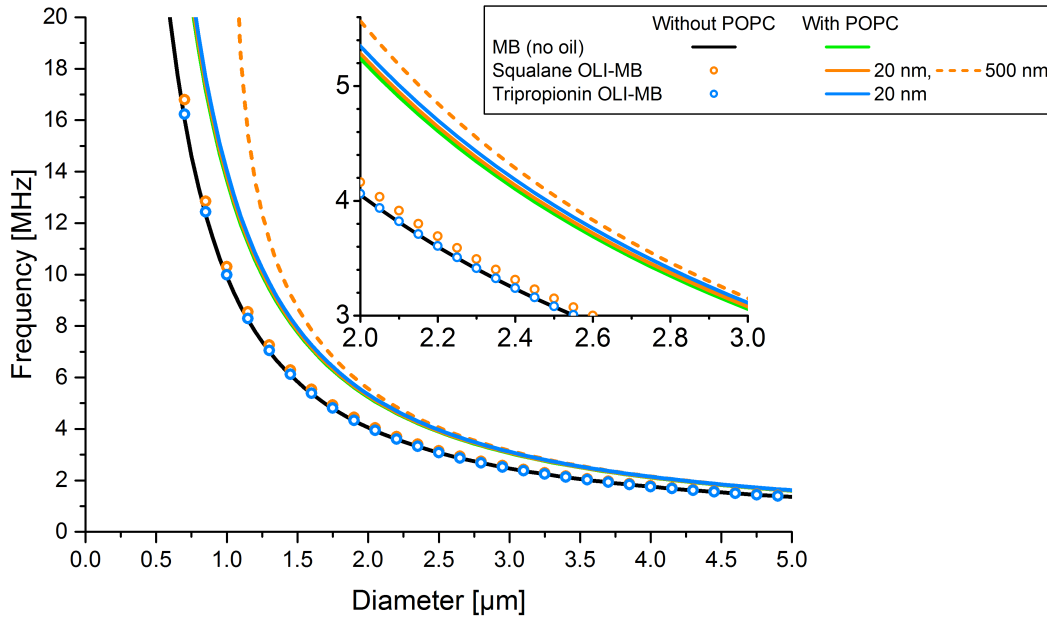


Fig. 3.7. Graph showing the dependence of a MB's resonant frequency on its size, for an uncoated (black) and lipid shelled (green) MB, and OLI-MBs with a 20 nm shell of squalane (orange solid) and tripropionin (blue), and a 500 nm squalane shell (orange dotted). Diameter given is for the whole MB including any oil layer. All lipid shells are POPC, $\rho_A = 998.2$ kg/m³, $P_0 = 101$ kPa, $\mu_A = 1$ mPa.s, $\gamma_{G-L/A} = 26.3$ mN/m. All oil parameters, including surface tensions, are detailed later in the thesis methods and results. Relationships use Equations 3.12 and 3.15.

Parameters that the above resonance theory neglects are the thickness of the surfactant shell (ϵ_L), and the viscosities of the oil and aqueous phases. As equation 3.12 has been used before to adequately model lipid shelled MBs such as DPPC and DSPC, and DPPC MBs with long chained DPPC-PEG-SPDP molecules, it can be assumed that the ϵ_L parameter is negligible for all similarly structured lipid shelled MBs, including POPC.^{70,174} Marmottant *et al.* (2005) discussed that a MB with a higher modulus of compression (the ratio between the force applied per unit area to an object and that object's change in volume per unit volume) will have a higher resonant frequency.¹⁷² On oscillation, the gas core of a MB or OLI-MB must displace the surrounding fluid, which provides resistance against the oscillations, effectively increasing the MB's modulus of compression. For an OLI-MB, the thicker the oil layer, the more the oil's viscosity will contribute to this resistance. Since squalane and tripropionin have viscosities of ~ 31 and ~ 8 times that of water, it can therefore be assumed that Figure 3.7 underestimates the resonant frequency for the OLI-MBs, where a thicker oil layer should give higher resonant frequencies. Unfortunately the degree of underestimation is unknown. It should also be noted that Figure 3.7 is in terms of the full MB size, not the gas core, so for OLI-MBs the gas core will be smaller. This leads to an increase in the resonant frequency, but not as significantly as for a single interface MB due to the total volume, and so the outer interface, remaining the same. This effect is almost negligible for the 20 nm oil layer thickness OLI-MBs. The effect can be seen on the 500 nm OLI-MBs, but it only becomes significant when the oil layer makes up two thirds of the OLI-MB diameter, and asymptotic approaching the loss of all gas to a 1 μm oil droplet. Morgan *et al.* (2000) and McLaughlan *et al.* (2017) have previously presented an alternate model for calculating the resonance frequency of MBs, the Herring equation.^{175,176} This equation does include the above parameters that equation 3.12 lacks. When compared to equation 3.15, the Herring equation gives the same results for uncoated MBs and squalane OLI-MBs without a lipid monolayer (where χ is assumed to be 0 N/m). However, when considering the more realistic case where stabilising lipid monolayers are present, the resonances of both MB types are reduced. This does not agree with experimental findings from non-oil MBs, where a lipid monolayer is found to increase resonance (see Luan *et al.* (2012) and van Rooij *et al.* (2015)).^{70,174} Therefore, the Herring equation was not used to estimate the OLI-MB resonance. The parameter that appears to contribute most to the significant difference between equation

3.15 and the Herring equation is the surface/interfacial tension, which, on addition of a lipid monolayer to a MB, typically reduces by half to approaching zero.

3.2.3. MB life-time

Single MB lifetime

MB lifetime is limited by two mechanisms. An external force can disrupt them or cause them to collapse, or the gas can leak out of the MBs over time, leading to a passive dissolution. The following details how a MB dies passively.

When at rest, P_B , which is equal to the MB's gas pressure (P_G) plus the vapour pressure (P_V), must be equal to the pressure of the liquid directly outside of the MB (P_L) plus the pressure acting inwards on the bubble due to surface tension (P_σ).¹⁷⁷

$$P_B = P_G + P_V = P_L + P_\sigma \quad (3.16)$$

$$P_B - P_L = P_\sigma = \Delta P = 2\gamma/r \quad (3.17)$$

Where ΔP is pressure difference across the MB interface.

This means that for a MB at rest the internal pressure will always be above the pressure outside, with the excess pressure being equal to P_σ , described by the Laplace pressure, ΔP (Equation 3.17). Since the bubble has a higher pressure inside compared to the outside environment, there is a driving force for dissolution of the gas to occur into the surrounding environment in order to lower the pressure difference (there are other driving forces such as the concentration gradient of the gas molecules inside to outside of the MB). Over time the gas dissolves into the surroundings, reducing the MB radius. By giving the MBs a surfactant shell (such as a phospholipid), γ is reduced at the gas-liquid interface. This reduces ΔP , inhibiting gas dissolution and prolonging bubble lifetime.¹⁷⁸ Theory dictates that the bubbles should dissolve completely. However evidence from scattering experiments has suggested that nanobubbles of ~100 nm could last for several days if allowed to sit at a hydrophobic interface.¹⁷⁹ Other groups have found that during dissolution the MB shell can compact, leading to a relative rapid MB shrinkage rate until the shell molecules are fully close-packed, followed by a distinct, far lower shrinkage rate.¹⁸⁰ The rate of decay for a MB with constant γ is described by the Epstein-Plesset equation (advanced by Borden and Longo (2002) to take into account the resistance towards mass transfer across the MB shell, R_{shell}):

$$-\frac{dr}{dt} = \frac{H}{(r/D_w) + R_{shell}} \left(\frac{1 - P_{xy} + (2\gamma/P_a r)}{1 + (4\gamma/3P_a r)} \right) \quad (3.18)$$

Where r is the radius, H is the Ostwald coefficient (the concentration ratio of dissolved gas in the surrounding aqueous phase to that of the gas inside the MB core), D_w is the diffusivity of the gas in the surrounding aqueous phase, P_{xy} is the ratio of the partial pressure of the diffusing gas in the surrounding medium to that at saturation.^{177,181}

To increase the bubbles lifetime, dr/dt needs to be reduced towards 0. This can be achieved by pre-saturating the solution with gas, decreasing H , using a low D_w gas, and using a surfactant shell that provides a high R_{shell} and reduces γ . The MB shell can be defined as being soft (also known as thin or flexible) or hard (also known as stiff). A soft shell, such as a lipid monolayer, will be $\sim 2\text{-}3$ nm thick, allowing large oscillations and acoustic signal, but typically provides a small R_{shell} . A hard shell, such as denatured albumin, will be $\sim 10\text{-}200$ nm thick, proving a large R_{shell} , producing a very stable MB, but reduces the ability to oscillate, giving rise to lower acoustic signals.¹⁸² Extreme temperatures and high pressures aid diffusion of the gas and may make the shell more fluid, reducing its rigidity and resistance, thereby decreasing life-time. However, practically this is only a user controllable concern when storing MBs since the temperature and pressure of blood during medical MB use is fixed to the patient.¹⁶⁷ Many MB designs include a polyethylene glycol (PEG) brush to the MB shell. This further increases R_{shell} . However, as well as giving a MB stability, a PEG brush coat is also important for use of MBs within the body as it provides stealth against the immune system, increasing *in vivo* lifetime.¹⁸³ The PEG layer acts as an antifouling layer, inhibiting the build up of biological material, primarily the adsorption of plasma proteins,¹⁸⁴ on the MB's exterior, preventing immune system antibodies from binding to the MB and the body's immune system from destroying the bubble. PEG is a hydrophilic, flexible, long chain, which sticks out from the MB. Each chain forms hydrogen bonds with surrounding water molecules, occupying the space adjacent to the MB's surface. This blocks access to the large majority of the MB's surface from any blood proteins that would activate the immune system to it.¹⁸⁵

For the lifetime of the proposed OLI-MB structure, there are a number of elements to consider about the above descriptions of lifetime due to the addition of the oil layer with considerable thickness. Similar to the Borden and Longo (2002) approach, the mass transfer resistance of water (R_{water}) can be approximated through the nondimensional Sherwood number (N_{Sh}), $R_{water} = r/(N_{Sh} \cdot D_w)$,¹⁸¹ the resistance due to the oil-gas interface (R_{oil}) could be estimated as, $R_{oil} = d/(N_{Sh} \cdot D_o)$, where D_o is the diffusivity of the gas in the oil. Equation 3.18 can be modified with the assumption that $R_{shell} = R_{lipid} + R_{oil}$,

where R_{lipid} is the resistance due to the lipid monolayer (typically $\sim 1 \cdot 10^3 \text{ s/cm}^{181}$). However R_{oil} has proven difficult to calculate since N_{Sh} cannot be approximated to 1 (as it is for R_{water}) due to the oil layer not being long enough to provide a fully developed concentration profile of dissolved gas. Since gas diffusing out of the core would need to first pass through an oil layer before reaching the outer fluid, the effective D_w could only be decreased. If D_o was low, the gas would take an increased length of time to reach the outer fluid, making the effective D_w dependent on the oil. The thinner the oil layer, the less effect this would have, however as the r_G shrinks due to dissolution, the ε_o would increase as the oil volume would remain constant. Therefore D_o would become more dominant as the MB decreased in diameter. If D_o was high, then the gas would take little time to reach the interface to the outer fluid, but would still take as long to diffuse into the fluid as if the oil was not there, making the effective D_w almost completely dependent on the outer fluid. A primary consideration would be the change to the Laplace pressure as an OLI-MB would have two interfaces, requiring the use of Equation 3.13. As the gas-oil interface is a hydrophobic-hydrophobic interface, the surface tension would be difficult to lower, so would be a limiting factor in reducing the internal pressure. This could result in the OLI-MB having a lower lifetime due to the oil layer.

Factoring the above, including Equation 3.13, into Equation 3.18 gives:

$$-\frac{dr}{dt} = \frac{H}{\frac{r_G + (\varepsilon_o/2)}{\min(D_w, D_o)} + (R_{lipid} + R_{oil})} \left(\frac{1 - P_{xy} + (\alpha/P_a)}{1 + (2\alpha/3P_a)} \right) \quad (3.19)$$

As stated above, there are a number of unknowns for estimating OLI-MB lifetime. However, if N_{Sh} is set to 1, and D_o is made equal to D_w , an estimate can be made which shows that the addition of an oil layer can prolong MB lifetime (Figure 3.8). Due to the second interface increasing the internal pressure, the lifetime is reduced for OLI-MBs with thin oil layers ($< 200 \text{ nm}$), but increases for thick oil layers as R_{oil} becomes dominant.

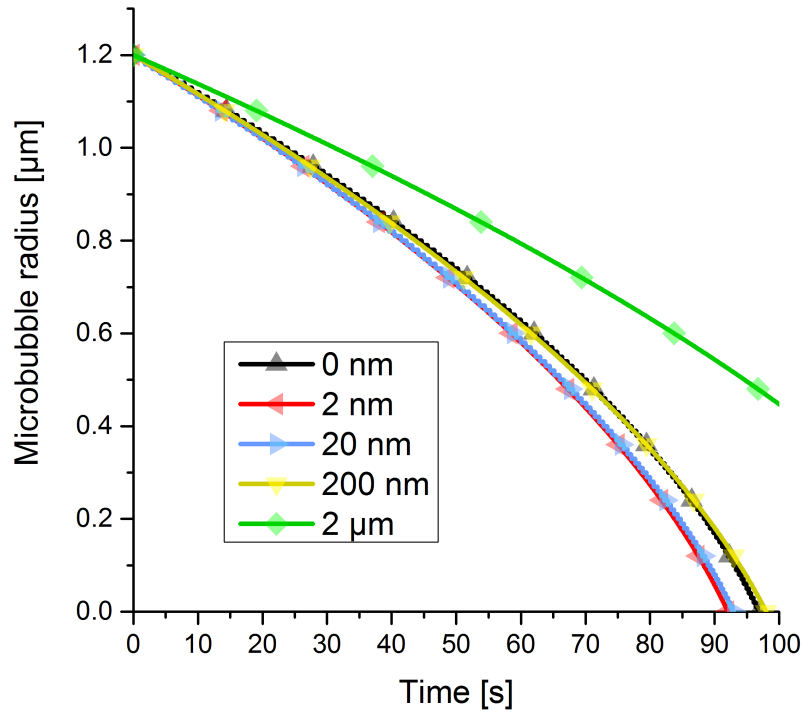


Fig. 3.8. Estimated results for the passive dissolution time of C_4F_{10} OLI-MBs, with given oil layer thickness and a POPC lipid monolayer, in water, at room temperature. Bubble radius refers to the gas core only. Initial bubble diameter = $2.4 \mu\text{m}$, $H = 2.02 \times 10^{-4}$, $P_{xy} = 5/6$, $P_a = 101 \text{ mPa}$, $\gamma_{G-L/A}$, $\gamma_{G-L/A}$, and $\gamma_{G-L/A} = 26.5, 28.0, \text{ and } 1.9 \text{ mN/m}$ respectively, $D_o = D_w = 6.9 \times 10^{-6} \text{ cm}^2/\text{s}$, $R_{lipid} = 100 \text{ s/cm}$. Values acquired and estimated from Borden and Longo¹⁸¹ and Sarkar¹⁸⁶.

Ostwald ripening

In the above section, the lifetime of a MB was described by the Epstein-Plesset equation. However, practically this only describes a single MB in solution. A population of MBs will generally follow this trend statistically, however another phenomenon termed ‘Ostwald ripening’ also takes place at the same time. Ostwald ripening is a thermodynamically driven process whereby smaller particles of gas, liquid or solid in a liquid medium shrink whilst contributing material to larger particles of the same material. More specifically, over time, the particles shed their surface molecules through diffusion into the solution, in order to reduce the concentration gradient from inside to outside of the particles. Meanwhile, there is a redeposition of a portion of the dissolved material onto the surface of the larger particles since surface molecules are less energetically favourable than interior ones (this is what leads to surface tension) and the larger a particle becomes the smaller the ratio between surface molecules to interior molecules becomes. Ostwald ripening is a balance between these two energetically driven mechanisms. If the redeposition mechanism dominates, the end result is fewer particles (eventually one), each of a greater diameter than the particles of

the starting solution. Ostwald ripening is quantified by the Lifshitz– Slesov–Wagner equation:

$$r^3 = \frac{8\gamma S V_m^2 D_C}{9\rho R T} t \quad (3.20)$$

Where r is the average particle radius, S and D_C are the solubility and diffusion coefficient of the particle material in the surrounding solution respectively, V_m the molar volume, ρ is the particle material density, R is the gas constant, and T is the temperature, t is the time.^{187,188}

3.3. Wettability

Wetting is a term used to describe the degree to which one material spreads at the interface between two other materials. The result is that the material might spread fully, ‘wetting’, not spread at all, ‘dewetting’, or form an intermediate lens at the interface, ‘partial wetting’. To understand wetting, the concepts of cohesion, adhesion and spreading must firstly be understood.

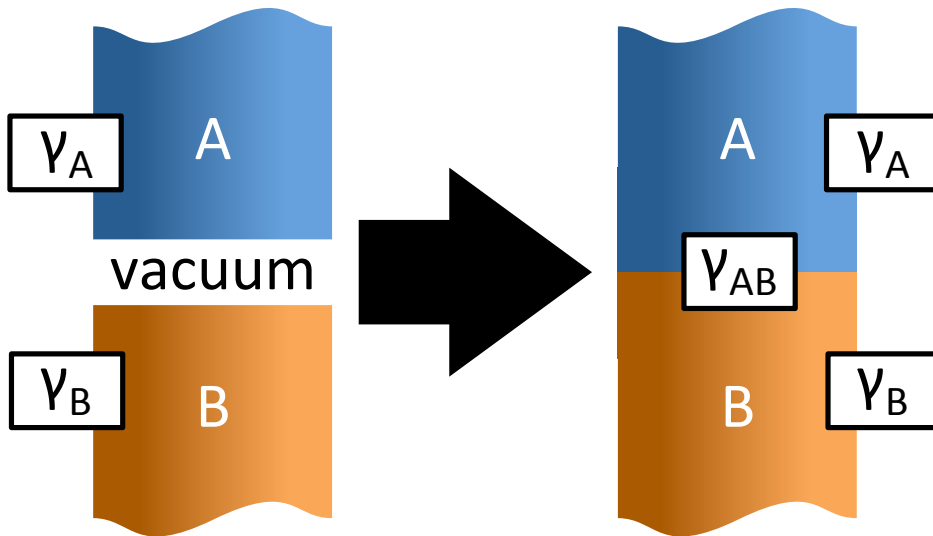


Fig. 3.9. Schematic of the adhesion of two immiscible materials (A and B), showing the interfaces that are formed. Materials are in a vacuum.

The amount of energy, per unit area, it takes for two immiscible materials to go from being separate to touching is known as the work of adhesion, W_{AB} . Figure 3.9 shows a schematic of two materials going through adhesion, noting the interfaces present before and after adhesion. This work can be defined using the Dupré equation:

$$W_{AB} = \gamma_A + \gamma_B - \gamma_{AB} \quad (3.21)$$

Where γ_A , γ_B , and γ_{AB} , are the surface tensions (or energies) of materials A and B in a vacuum, and the interfacial tension between materials A and B respectively.¹⁸⁹

The lower the value of W_{AB} the more energetically favourable it is for materials A and B to contact over a larger surface area, leading to a greater spreading. Alternatively for two volumes of the same material this is known as the work of cohesion, W_{AA} , where Equation 3.21 simplifies to:

$$\frac{1}{2}W_{AA} = \gamma_A \quad (3.22)$$

This allows Equation 3.21 to be written as:

$$\gamma_{AB} = \frac{1}{2}W_{AA} + \frac{1}{2}W_{BB} - W_{AB} = \frac{1}{2}W_{ABA} = \frac{1}{2}W_{BAB} \quad (3.23)$$

Where W_{ABA} and W_{BAB} are the work cleavage of material B between A , and material A between B respectively.

When three phases are considered, where work is given in terms of the cleavage of material C between materials A and B , W_{ACB} , Equation 3.23 is factored into Equation 3.21 (where the vacuum is now considered as material C) to give:

$$W_{ACB} = \gamma_{AC} + \gamma_{CB} - \gamma_{AB} = W_{CC} + W_{AB} - W_{AC} - W_{CB} \quad (3.24)$$

When $W_{ACB} < 0$, $\gamma_{AB} > \gamma_{AC} + \gamma_{CB}$, leading material C to fully displace material B from material A , wetting the interface. Under these circumstances, W is often then referred to as the spreading coefficient, S , where $W_{ACB} = -S_{ACB}$.¹⁸⁹

The Young's equation considers a three-phase system between a flat solid, a liquid droplet and surrounding gas/vapour:

$$\gamma_{S_oG} = \gamma_{S_oL} + \gamma_{LG}\cos\theta_L \quad (3.25)$$

Where S_o , L , and G , denote if the surface tension is between the solid, liquid or gas/vapour interfaces respectively, and θ_L is the angle the liquid droplet makes at the solid-liquid-gas triple point.

If the gas/vapour is considered a vacuum and materials $S_o = B$ and $L = A$, the Young's equation factors into the Dupré equation, to give the Young-Dupré equation:

$$\gamma_A(1 + \cos \theta_A) = W_{AB} \quad (3.26)$$

Figure 3.10 shows how an emulsion of material C in B can result in spreading, a partial spreading lens, or no spreading, dependant on the cleavage of materials A - C with respect to one another. As stated above, when $W_{ACB} < 0$, C will displace B from A . However this does not mean that when $W_{ACB} > 0$, C will not spread at A . (For the case where material C originates from material B) Instead, partial wetting may occur where both materials B and C are in contact with A , here $W_{BAC} < 0$, giving rise to lenses of C , or dewetting of C may occur where C does not spread at the interface. For dewetting of C to occur, $W_{ABC} < 0$.¹⁸⁹

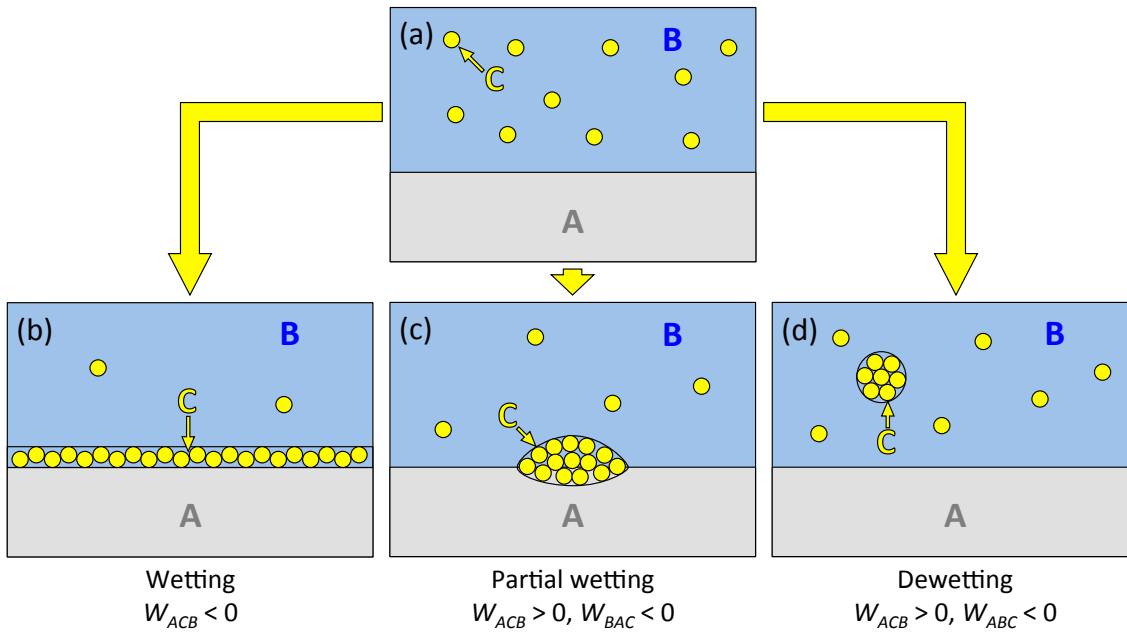


Fig. 3.10. Schematics of interaction between materials A , B and C in respect of the work of adhesion. Starting with (a) material C dispersed in B , where B is in contact with A , C either (b) fully wets the A - B interface, (c) partially wets the interface, or (d) begins to coalesce without wetting the interface, based on the work of adhesion between the materials being positive or negative as indicated below each image. (Adapted from Israelachvili, 2011)¹⁸⁹

3.3.1. Droplets entering a stabilised interface

The above theory describes what is observed for bulk materials, or where material C is solubilised in B and precipitates out. However, when finite particles/droplets of C are in the system, the 'entering' or 'rupture' coefficient, E_R , must be considered.^{115,190} For a system where droplets of liquid C , dispersed in immiscible liquid B , are introduced to an interface between B and fluid A (A can be a third immiscible liquid, but for most cases, including what we consider from this point on, A is a gas) there is almost always

some surfactant dispersed in B which keeps C stabilised in B , preventing coalescence of C , and that surfactant can also stabilise the B - A interface. In this case, even though energetically it may be preferable for the phases to have a conformational interface of A - C -surfactant- B , the surfactants at C - B and B - A can produce a thin water film which separates C from A with a kinetic energy barrier. The primary factor that inhibits the droplets of C from entering the B - A interface is if the surfactants sufficiently decrease the interfacial tension of B - A without C . Sirks (1938), Schokker *et al* (2002), and King (1955) have all reported on this phenomenon experimentally, with the latter finding that fat globules resting below a milk-air surface would not enter the surface until it was disturbed by contact with a platinum loop.^{191–193} Here it was theorised that the contact disturbed the milk proteins at the surface that were acting as the surfactants to give the energy barrier.¹¹⁵

$$E_R = \gamma_{AB} + \gamma_{CB} - \gamma_{CA} = W_{ACB} + 2(\gamma_{AB} - \gamma_{AC}) \quad (3.27)$$

If $E_R < 0$, then the droplet of C remains submerged in B . However if $E_R > 0$ then the droplet of C enters B - A , resulting in a lens of C if $S < 0$, or a thin film of C if $S > 0$.

An important thing to note is that the surfactants will usually pack at the B - A interface at their equilibrium spreading pressure (ESP), before the droplets of C come into contact. If C is calculated to become a thin film; as it enters B - A and then begins to spread from a lens into a thin film, the surfactants at B - A can become compressed at a greater rate than they move to the increasing C - B interfacial area. If this happens then the γ of B - A will decrease. This will continue until $S = 0$, at which point the rate of spreading will be limited by the surfactant diffusion, or an equilibrium will have been reached (the ESP and collapse pressure concentrations at A - B will likely be different than that at C - B) and spreading will stop entirely.

3.4. Fluorescence and Förster/Fluorescence Resonance Energy Transfer (FRET)

Figure 3.11 shows a Jablonski diagram that illustrates the excitation and emission mechanisms that occur during standard fluorescence and Förster/Fluorescence Resonance Energy Transfer (FRET). During typical fluorescence, an excitation source (most commonly a photon) comes into contact with a fluorescent molecule. In Figure 3.11 this molecule is the ‘donor’ (though for typical fluorescence this name can be ignored). An electron in this molecule takes in part or all of the energy of the excitation source, and is excited into a higher energy band, relating exactly to the amount of

energy it acquired. After this, the electron may lose energy, whilst remaining within the same energy band, by moving down vibrational energy states, but eventually the electron will relax down to the initial energy band by releasing a photon with the same amount of energy as the difference between the two energy bands. Since the energy of a photon is inversely proportional to its wavelength, the energy difference between the molecule's energy bands, which the excited electron was excited up and down, directly defines the wavelength of the emitted photon. On the other hand, FRET is an interaction that occurs between two molecules (at least one fluorescent) whereby one molecule, the donor, is excited and then passes its energy over to a second molecule, the acceptor, allowing the second molecule to release that energy (typically) as fluorescence. This is different from the first molecule being excited and fluorescing radially and then a second molecule being excited by that fluorescence and fluorescing radially. Instead, a long-range, non-radiative, dipole-dipole coupling transfer takes place between the donor and acceptor molecules. Here, the donor electrons relax back to the ground state without releasing fluorescence.¹⁹⁴ A different way to think about this would be to consider the excited donor as having an oscillating dipole, where the energy of the oscillation is passed to the acceptor dipole, which has a similar resonant frequency.¹⁹⁵ Figure 3.12 shows an example schematic of the excitation and emission spectra for FRET fluorophores, where the important aspect is that FRET will only occur if there is a significant spectral overlap of the donor emission with the acceptor excitation (their wavelength bands must overlap). Typically, FRET only occurs when donor and acceptor molecules are within 1-10 nm as the efficiency of transfer, E_T , decreases rapidly with the sixth power of inverse distance, d :

$$E_T = \frac{1}{1+(d/d_E)^6} \quad (3.28)$$

Where d_E is the distance when E_T is at 50% of its maximum.¹⁹⁶

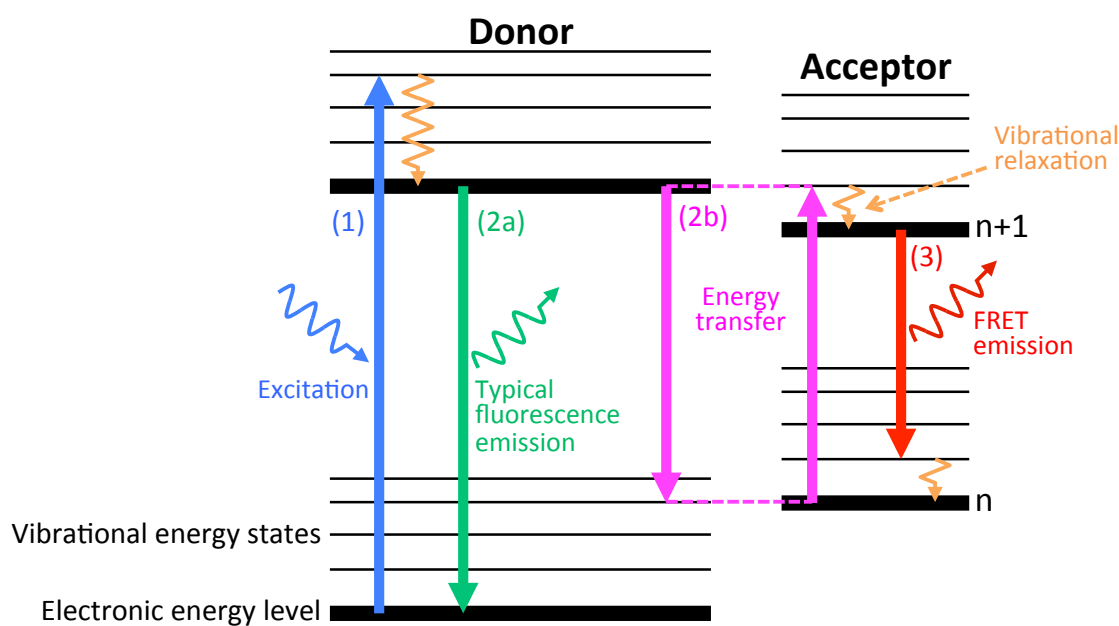


Fig. 3.11. Jablonski diagram showing the interactions that lead to (1 and 2a) typical fluorescence emission, and (1, 2b, and 3) FRET emission between a donor and acceptor.

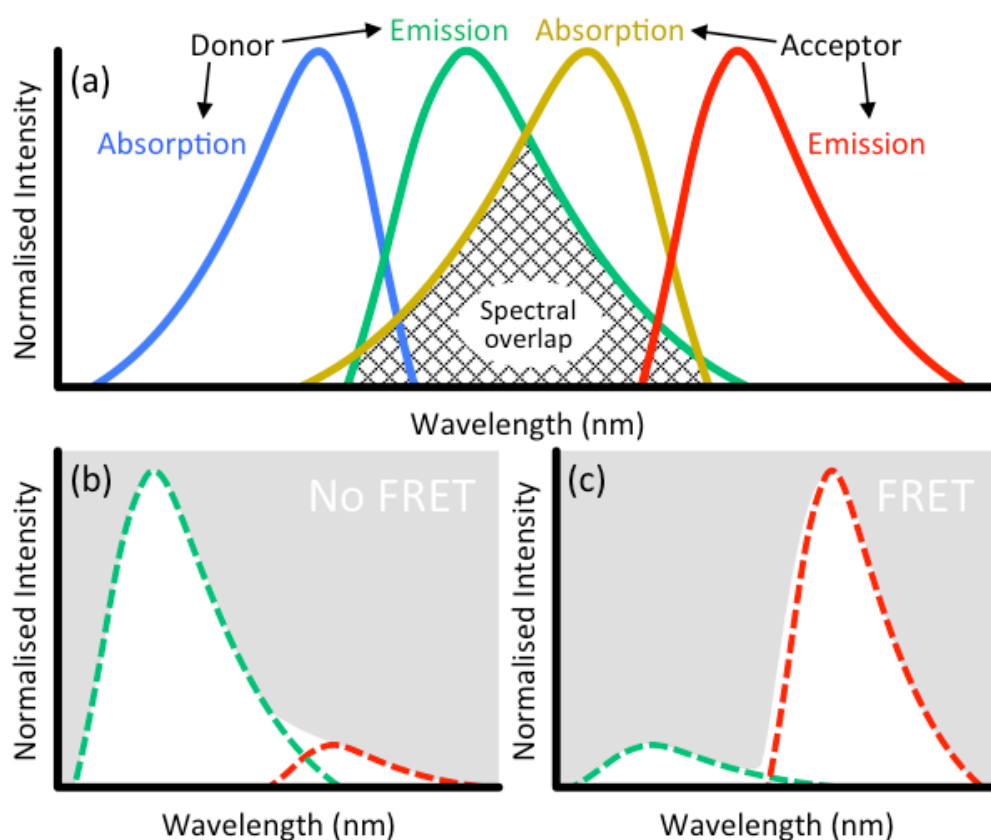


Fig. 3.12. Sketches to show (a) how donor emission and acceptor absorption spectra must overlap for FRET to occur and the expected emission observed from a sample where (b) donor and acceptor molecules are too distant and (c) close enough for FRET to occur.

3.5. Activation of perfluorocarbon liquid droplets to gas bubbles

One route to forming MBs, which has been extensively studied in recent years, is the vapourisation of liquid (typically PFC) nanodroplets into gas MBs. The following details the equations to determine the ratio of liquid to gas expansion and the conditions under which droplets would be expected to phase convert.

As a droplet of liquid decreases in size the thermal energy/temperature required to boil it into a gas, the vaporisation temperature, increases above the bulk boiling point. This increase is due to the Laplace pressure increasing the internal pressure of the droplet as its radius is reduced. If the droplets are brought above the bulk boiling point in literature they are often termed as being superheated, without regarding the vaporisation temperature change.^{34,35} If the droplets are heated enough (past the point of being superheated) or the pressure of the surrounding solution dropped enough (which can be supplied by an ultrasound wave), or through a combination of both, the droplets will phase convert into bubbles.^{36,37} After activation, the MBs are larger than the droplets they were formed from, and the interfacial tension is expected to be different between liquid PFC- and gas PFC-water. Hence, the Laplace pressure differs, resulting in the boiling/condensation points not being the same for a single PFC particle in liquid or gas phase.

3.5.1. Droplet to MB size expansion

The droplet radius that will result in any given MB radius, due to a phase change of the material, can be gained by combining the ideal gas law (Equation 3.29) and the Laplace equation:

$$P_B V_B = n_B R T \quad (3.29)$$

$$r_D = \sqrt[3]{\frac{(2\gamma + P_a r_B) r_B^2 M_W}{R T \rho_D}} \quad (3.30)$$

Where subscripts refer to the type of cavity, for the post-activation MB, B , or the pre-activation droplet, D . n is the number of moles of material in the cavity, M_W is the molecular weight.

Evans *et al.* (2006) described how Equation 3.30 gives an overestimate of the expansion found practically, as it works on the assumption that the number of droplet molecules, n_D , is equal to the number of post-activation MB molecules, n_B .¹⁹⁷ Equation 3.30

neglects that the solubility of the material, when confined in a droplet or a MB, is different. Taking solubility into account:

$$n_B = n_D + V_s(S_D - S_B) \quad (3.31)$$

$$S_t = S_0 \exp\left(\frac{2\gamma M_W}{\rho_t r_t RT}\right), \text{ where } t = D \text{ or } B$$

Where subscript t refers to the type of cavity the calculation is made on, either the post-activation MB ($t = B$) or the pre-activation droplet ($t = D$), V_s is the volume of fluid around the MB which has the volatile material solubilised into it as a shell, $S_{(D \text{ or } B)}$ is the enhanced solubility of the material in the surrounding fluid due to confinement, and S_0 is the bulk solubility of the material in the surrounding fluid.¹⁹⁷

Factoring this into Equation 3.30 gives:

$$r_D = \sqrt[3]{\frac{(2\gamma + P_a r_B) r_B^2 M_W}{RT \rho_D} - \frac{3 M_W V_s (S_D - S_B)}{4\pi \rho_D}} \quad (3.32)$$

For use inside the body, MBs have an upper practical limit to their size. Meanwhile, droplets require more energy to activate the smaller they are. Therefore, it is important to form droplets as large as possible whilst keeping their maximum activated MB size under the upper limit. The maximum activated MB size occurs at the moment of activation, when $V_s = 0$, when no additional solubilisation has yet occurred due to phase change. Equation 3.32 collapses back to Equation 3.30, and so this is the equation that we use for estimating droplet to MB expansion, keeping in mind that experimentally this would be an overestimate.

Conversely to this, it was found by Kripfgans *et al.* (2000) that experimentally PFC droplet activation forms MBs far larger than expected from Equation 3.30. This is because even though Evans *et al.* (2006) took into account the solubility of the droplet/MB material in the surrounding solution, they neglected diffusion of the dissolved gasses from the surrounding solution into the MB.¹²⁷

Figure 3.13 shows the resulting bubble size after single droplet activation, as a function of initial droplet size, considering cases for; **interfacial tension**, 0 mN/m (fully stabilised by surfactant) to 72 mN/m (bare air-water interface), **temperature**, below the water freezing point to the water boiling point, **PFC cores**, where all PFC molecules follow a $C_n F_{2n+2}$ formula, for $n = 3-6$, and the **pressure** of the system after activation into a MB. The first three variables indicate that to produce a 3 μm PFC MB, a PFC

droplet of ~600-700 nm would be required. Due to the Laplace pressure, an exponential growth in the diameter expansion ratio is seen for droplets up to ~200 nm in diameter, after this the relationship becomes linear, with a diameter expansion ratio of ~4-5 times. Pressure was indicated to cause a far larger size variation due to the compressible nature of the MB gas core. However, just considering atmospheric and body pressure (1.00 and 1.13 atm respectively), which are the primary ways that the droplets would be stored and delivered, leads to a negligible size change.

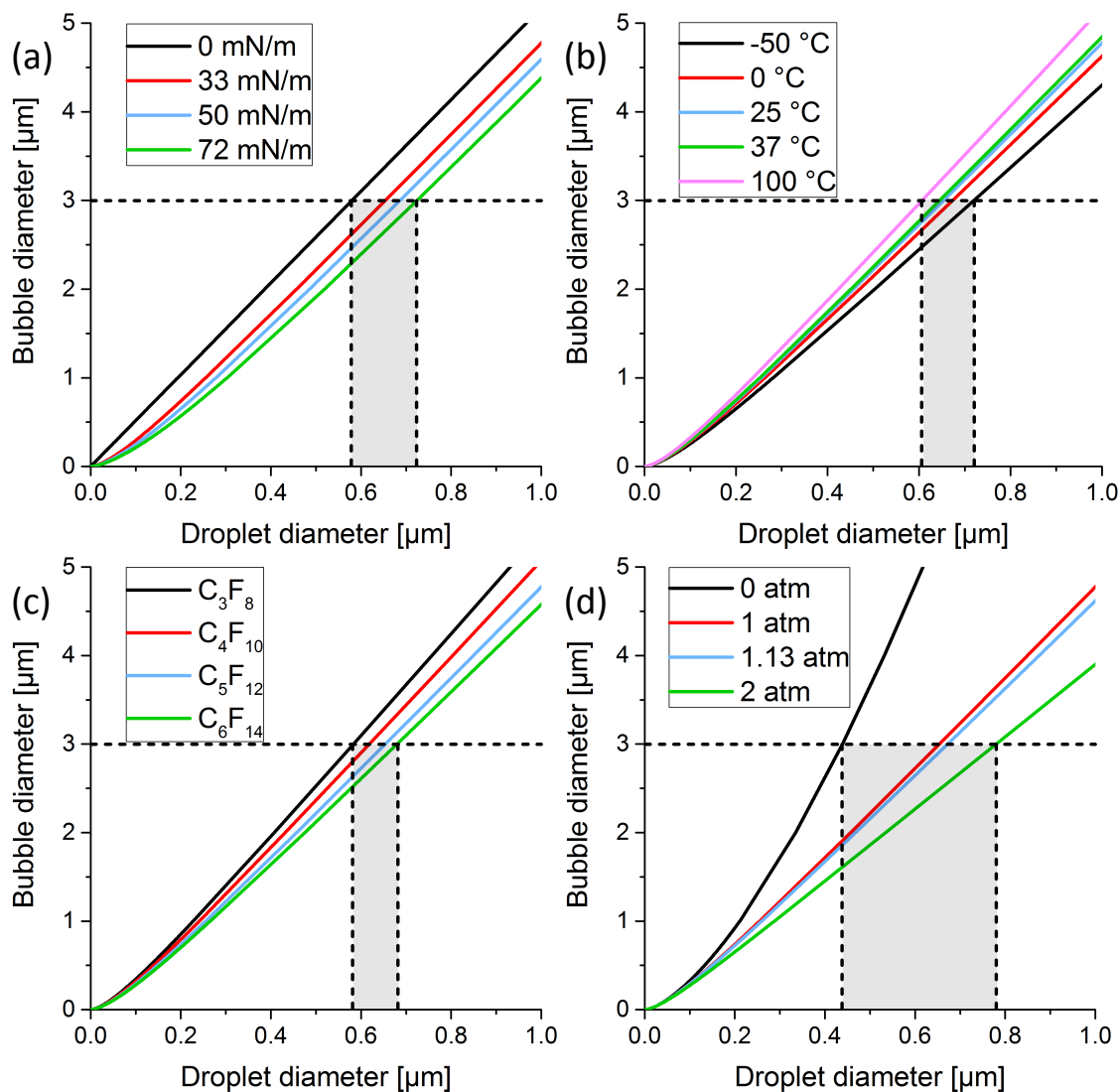


Fig. 3.13. Diameter expansion of PFC droplets to bubbles, outlining how different variables affect the expansion, and indicating what size droplets would be needed to produce a 3 μm bubble (dotted black line and grey box), as desired. Variables are; (a) surface tension, (b) temperature, (c) PFC type, and (d) constant pressure after activation. Unless varied as indicated, droplets were calculated to have a surface tension of 33 mN/m, at 25 °C, to have a PFC5 (C_5F_{14}) core, and were at 1 atm.

3.5.2. Vapourisation temperature as a function of droplet size

How the vapourisation temperature increases due to a decrease in droplet size can be gained by combining the Antoine equation (Equation 3.33), a correlation which describes the relationship between a bulk material's vapour pressure (P_{V0}) and the temperature, the Kelvin equation (Equation 3.34), which describes how the vapour pressure (P_V) increases for a curved interface, and the Laplace pressure equation, with the assumption that droplet to MB expansion occurs when the resultant droplet pressure (P_D) = P_V .

$$\log_{10} P_{V0} = A - \frac{B}{C+T} \quad (3.33)$$

$$P_V = P_{V0} + \exp\left(\frac{2\gamma V_m}{r_D RT}\right) \quad (3.34)$$

$$\frac{2\gamma}{r_D} + P_a = 10^{A - \frac{B}{C+T}} + \exp\left(\frac{2\gamma V_m}{r_D RT}\right) \quad (3.35)$$

Where A, B and C are model parameters specific to a material (acquired from the National Institute of Standards and Technology (NIST) Chemistry WebBook (Linstrom and Mallard 2010) for temperatures between -50.98 and 149.75 °C).¹⁹⁸

Due to how Equation 3.35 has variables T and r_D arranged, it is laborious to rearrange it in terms of either variable. However, we can simplify Equation 3.35 knowing that the Kelvin equation is negligible below a certain droplet diameter; for C_5F_{12} , the primary PFC liquid used in these studies that dealt with this section of theory, P_V is only affected significantly (defined as when $P_V = 1.1 \times P_{V0}$) below droplet diameters of 85 nm, which would result in a 240 nm MB after activation (calculated in the previous section). This allows us to approximate $P_V \approx P_{V0}$ when $r_D > 85$ nm. This leads to the simplified equation of:

$$\begin{aligned} \frac{2\gamma}{r_D} + P_a &= P_{V0} = 10^{A - \frac{B}{C+T}} \\ r_D &= \frac{2\gamma}{10^{A - \frac{B}{C+T}} - P_a}, \text{ when } r_D > 85 \text{ nm} \end{aligned} \quad (3.36)$$

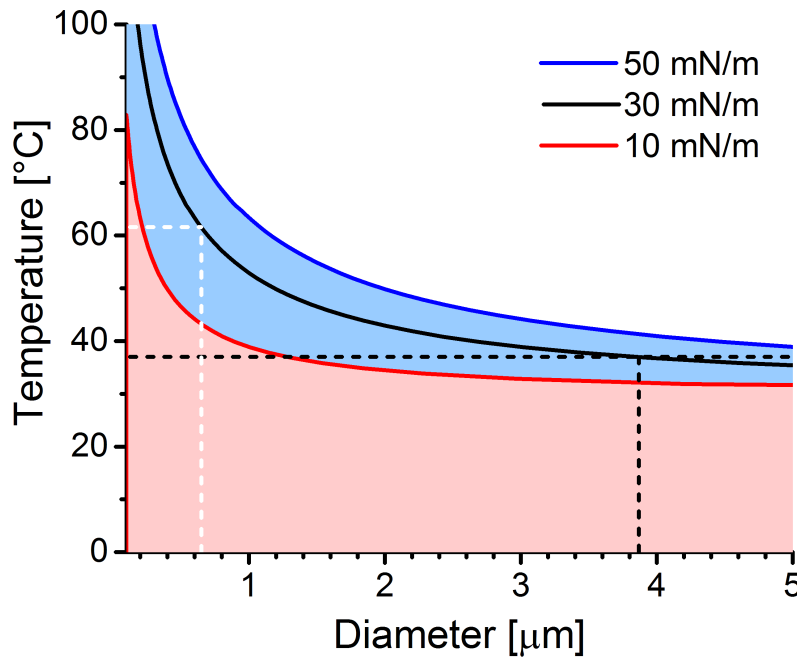


Fig. 3.14. C_5F_{12} droplet vapourisation temperature, given three values for the droplet shell interfacial tension, as a function of initial droplet diameter. Dotted lines give the 30 mN/m shell droplet activation point at body temperature, 37 °C (black), and for droplets of 650 nm (white).

As shown in Figure 3.14, as a C_5F_{12} liquid droplet decreases in size the temperature required to vapourise the liquid into a gas increases from the bulk vapourisation temperature of 29 °C. A 650 nm droplet, defined as the desirable in the previous section, with an interfacial tension of 30 mN/m, would vapourise at ~62 °C, whilst any droplet of 4.5 μm or larger would activate at *in vivo* temperatures of ~37 °C.

3.5.3. Vapourisation pressure as a function of droplet size

In the previous section an assumption was made that a liquid droplet will activate into a MB when $P_D = P_V$. It follows that as well as increasing the temperature of the droplet, the pressure of the system/surrounding solution, P_0 , can be reduced until the resultant P_D would be equal to P_V at a given temperature. Rearranging Equation 3.35 in terms of P_0 gives:

$$P_0 = 10^{A - \frac{B}{C+T}} + \exp\left(\frac{2\gamma V_m}{r_D RT}\right) - \frac{2\gamma}{r_D} \quad (3.37)$$

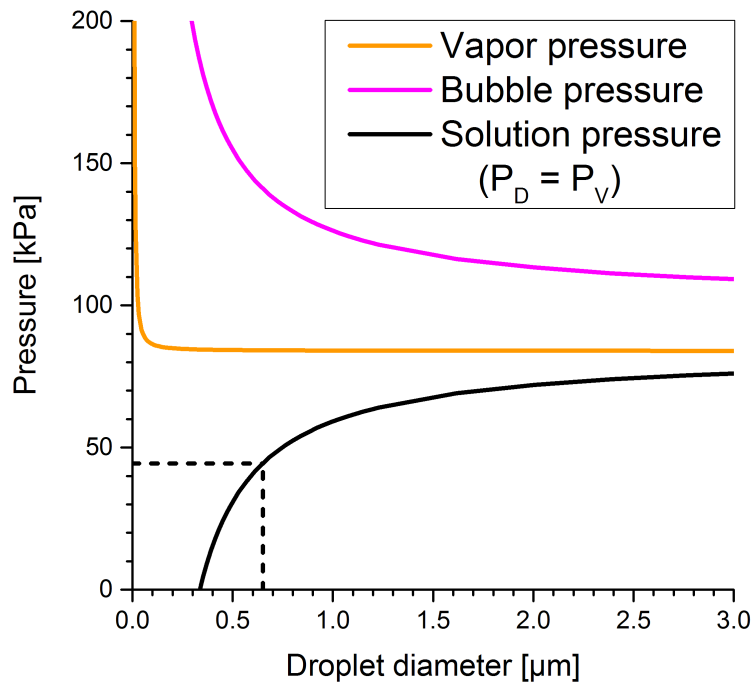


Fig. 3.15. Pressure properties of a C_5F_{12} MB, with a shell interfacial tension of 50 mN/m, as a function of the C_5F_{12} droplet diameter before activation into a MB. Vapour pressure (orange), MB internal pressure at atmospheric conditions (pink), and the maximum surrounding solution pressure required to cause $P_D = P_V$, at which point phase conversion from a C_5F_{12} droplet to MB would occur (black). Temperature at 25 °C.

Figure 3.15 shows the degree to which the pressure of a C_5F_{12} emulsion needs to be reduced in order to cause phase change to occur, and how the required pressure drop increases due to a decrease in the initial droplet diameter. The required pressure drop increases because as the droplet decreases in size its internal pressure increases (due to Laplace pressure) at a faster rate than the vapour pressure. For droplets of 650 nm, a pressure drop of 57 kPa (from atmospheric conditions) would be required for phase conversion at 25 °C.

4. Experimental

In this chapter the chemicals, instrumentation, and procedures used throughout the work presented in this thesis are described.

During this thesis, results are presented in the following format; $a \pm b$ (SD or FWHM c). Where a is the calculated mean or the peak of a typically Gaussian distribution, b is the standard error, and c is the population spread given either in terms of a standard deviation (SD) or the full width half maximum (FWHM) of a Gaussian distribution.

4.1. Chemicals, solutions, and microscopy

Table 4.1 lists the chemicals commonly used in this study (other than the oils) and their suppliers. Table 4.2 lists the oils used in this study, their suppliers and their physical properties that impacted this work.

Tab. 4.1. List of chemicals (apart from oils) used throughout this project, with suppliers.

Abbreviation in this thesis / Chemical formula	Long name	Supplier
Atto488	1,2-Dioleoyl- <i>sn</i> -glycero-3-phosphoethanolamine labeled with Atto 488	Avanti Polar Lipids, USA
Atto590	1,2-Dioleoyl- <i>sn</i> -glycero-3-phosphoethanolamine labeled with Atto 590	Avanti Polar Lipids, USA
BSA	Bovine serum albumin	Sigma-Aldrich, UK
C ₄ F ₁₀	Perfluorobutane	F2 Chemicals, UK
C ₅ F ₁₂	Perfluoropentane	F2 Chemicals, UK
C ₆ F ₁₄	Perfluorohexane	Sigma-Aldrich, UK
Dil	1,1'-Diocadecyl-3,3',3'-tetramethylindocarbocyanine perchlorate	Sigma-Aldrich, UK
DiO	3,3'-Diocadecyloxycarbocyanine perchlorate	Sigma-Aldrich, UK
Dotap	1,2-dioleoyl-3-trimethylammonium-propane (chloride salt)	Avanti Polar Lipids, USA
DPPA	1,2-dihexadecanoyl- <i>sn</i> -glycero-3-phosphate (sodium salt)	Avanti Polar Lipids, USA
DPPC	1,2-dipalmitoyl- <i>sn</i> -glycero-3-phosphocholine	Avanti Polar Lipids, USA
Nile red	9-diethylamino-5-benzo[α]phenoxazinone	Sigma-Aldrich, UK
ODT	Octadecanethiol	Sigma-Aldrich, UK
Oregon green	1,2-Dihexadecanoyl- <i>sn</i> -Glycero-3-Phosphoethanolamine labeled with Oregon Green 488	Life technologies, USA
PBS	Phosphate Buffered Saline	Life technologies, USA
PDMS	Polydimethylsiloxane	Dowcorning, USA
DSPE-PEG	1,2-distearoyl- <i>sn</i> -glycero-3-phosphoethanolamine-N-[amino(polyethylene glycol)-2000] (ammonium salt)	Avanti Polar Lipids, USA
Pluronic	Pluronic F-68 / Poloxamer 188	Life technologies, USA
POPC	1-palmitoyl-2-oleoyl- <i>sn</i> -glycero-3-phosphocholine	Avanti Polar Lipids, USA
Span 80	Sorbitan monooleate	Sigma-Aldrich, UK
Stearic acid	Octadecanoic acid	Sigma-Aldrich, UK
SU-8	SU-8 photoresist	Microchem, USA
Triton	Triton X-100	Fisher Scientific, USA
CHCl ₃	Chloroform	Sigma-Aldrich, UK
C ₅ H ₁₀ O ₃	Ethyl lactate solvent	Microposit EC solvent, Microchem, USA

Tab. 4.2. List of oils used throughout this project, and their physical properties that were critical to the work. All oils were purchased from Sigma-Aldrich (UK).^{96,199–206}

Oil	Other names	Molecular formular	Density [g/cm ³]	Viscosity @ 20 °C [mPa.s]	Solubility in water @ 20 °C [g/L]	Excitation [nm]	Emission [nm]	Suface tension [mN/m]
Water		H ₂ O	0.9982	1				72.8
Isoamyl Acetate	Banana	C ₇ H ₁₄ O ₂	0.88	0.88	2			25.6
Squalane		C ₃₀ H ₆₂	0.81	~31	Immiscible	300	334	28 ± 3
Squalene		C ₃₀ H ₅₀	0.858	12	Immiscible	350	463	29 ± 3
Triacetin		C ₉ H ₁₄ O ₆	1.1562	23	70	275	330	36.5
Tripropionin		C ₁₂ H ₂₀ O ₆	1.1 ± 0.1	7.63	3.07 @ 37 °C			35.9 ± 3.0
Dodecane		CH ₃ (CH ₂) ₁₀ CH ₃	0.7808	1.34	1			25.3
Soybean	12% w/w α-Linolenic acid	C ₁₈ H ₃₀ O ₂	0.917	40.5 @ 30 °C	Immiscible			31.3
	48% w/w Linolenic acid	C ₁₈ H ₃₂ O ₂						
	16% w/w Oleic acid	C ₁₈ H ₃₄ O ₂						
	5% w/w Steric acid	C ₁₈ H ₃₆ O ₂						
	17% w/w Palmitic acid	C ₁₆ H ₃₂ O ₂						

Phosphate Buffered Saline solution

PBS was prepared by dissolving one 5 g tablet of PBS powder in 500 ml of MilliQ water (pH 7.45, 140 mM NaCl, 10 mM PO₄, 2.68 mM KCl). PBS was filtered through a 200 nm cellulose membrane syringe filter (Minisart RC4, Sartorius Stedim, UK) prior to use.

Bovine Serum Albumin solution

BSA protein is commonly used in biochemical procedures as a blocking reagent. Blocking agents are introduced to surfaces and biological molecules before studies begin to reduce non-specific binding of biological entities of interest, such as proteins and antibodies, which are introduced afterwards. The entities of interest are then forced to compete for binding/adherence with the blocking agent, which they will not achieve at non-specific binding sites.¹⁵³ BSA solutions were prepared by dissolving 250 mg of lyophilised BSA crystals in 50 ml of MilliQ or PBS solution. These solutions were stored for up to two weeks at 4 °C and diluted further if required. For most work involving glass surfaces, the surface was incubated at ~25 °C in BSA at a concentration of 1-5 mg/ml for 10-30 min, followed by a MilliQ rinse and N₂ dry if required.

Bubble buffer solution

A 100 ml solution, termed bubble buffer (BB), was made from 4 mg/ml NaCl dissolved in MilliQ and 1 vol% glycerol (unless stated as otherwise). BB was used for preparing

standard lipid solutions used throughout the work presented in this thesis, such as in typical on-chip microbubble (MB) production. BB was stored for up to two months at 4 °C and filtered through a 200 nm cellulose membrane syringe filter prior to use.

Standard lipid solution

Dried lipid stocks of DPPC, DSPE-PEG, and POPC were dissolved in chloroform:methanol (1:1). The lipid solutions were pipetted into a glass vial at 100 mol% DPPC or 100 mol% POPC, or at 5 mol% DSPE-PEG with 95 mol% DPPC or POPC (to give a DPPC-PEG or POPC-PEG lipid solution respectively) and dried under nitrogen gas for 30 minutes. BB was then added to the lipid to give a final concentration of 1 mg/ml lipid. When stated, Pluronic was added, from a stock of 10 vol% in deionized, distilled water, to the dried lipids, to give a final concentration of 0.1 or 2 vol% pluronic. The final volume was 1 ml. The solution was vortexed for 1 min and further sonicated in an ultrasonic bath for at least 1 hour to facilitate lipid re-suspension, then filtered through a 200 nm PTFE membrane syringe filter (Minisart SRP4, Sartorius Stedim, UK) to remove non-suspended lipid.

Fluorescence, including hydrophobic fluorescence resonance energy transfer (FRET)

For labelling lipid shells of MBs or droplets, Atto590, or Atto488 was added to the lipid solution at 0.1 mol% during the lipid-drying step.

For labelling the oil phase, the fluorescent label Nile red was dissolved into oil at 3.20 µg/ml, 2.29 µg/ml and 24.0 µg/ml (unless otherwise stated) for triacetin, isoamyl acetate and squalane/squalene oils respectively. Nile red was also added to soybean oil at a non-optimised concentration as a few flakes in 10 ml of oil. For fluorescence resonance energy transfer (FRET), powdered DiO or DiI was solubilised into the oils at 1 mg/ml (unless otherwise stated). For solubilisation, the oil with fluorophore was vortexed for 30 s, followed by bath sonication for 30 min. Excitation and emission recordings for DiO and DiI in bulk oil and oil nanodroplets are described in section 4.9.7 (p 94-95).

Excitation/absorbance and emission was recorded from Nile red in triacetin, isoamyl acetate and squalane oil. Nile red was dissolved at ~1 mg/ml, then dilutions were made down to 0.76 µg/ml. Quartz cuvettes were used to hold samples during these studies, which were cleaned with chloroform:methanol (1:1) before, during and after use.

Absorbance measurements were performed on a Lambda 35 Ultraviolet-Visible spectrometer (UV-Vis) (Perkin Elmer, USA). Here, a 300-800 nm sweeping excitation laser light source was emitted through a fluorophore + oil sample contained in a 1 ml

cuvette. Transmission of the light source was recorded at 480 nm/min across excitation light wavelengths with a 1 nm slit width window, in reference to a control sample in an identical cuvette, which contained only oil. As in Equation 4.1, the recorded transmission was converted into an absorbance measurement.

$$Absorbance = \log (1/Transmittance) \quad (4.1)$$

Emission measurements were performed on a LS 55 Fluorescence Spectrometer (Perkin Elmer, USA). Here, a constant wavelength excitation laser source was used to excite the fluorophore (in oil) in a 1 ml cuvette. Excitation light of 530, 520, or 505 nm was used for triacetin, isoamyl acetate and squalane oil respectively, based on the peak absorbance measurements. Emission intensity was recorded with a detector positioned at 90° to the excitation laser source. The detector performed a 500–900 nm sweep with a 4 nm window at 5 nm steps.

Microscopy

The most commonly used microscope during these studies was an inverted fluorescence microscope (Eclipse Ti-U, Nikon, Japan) with FITC and TexRed filters, 10x and 40x magnification lenses, and an optional 1.5x internal magnification. Unless otherwise stated, videos were collected at 100 fps, or at 50 kfps with the use of a high frame rate camera (FASTCAM SA-X, Photron, USA). Within this report this microscope will be referred to as the ***inverted microscope***. An upright fluorescence microscope (Eclipse E600, Nikon, Japan) with FITC and TexRed filters, and a 60x magnification lens was also used. Within this report this microscope will be referred to as the ***upright microscope***. A second inverted microscope (Eclipse Ti-S, Nikon, Japan) was used, though with an attached dark field condenser, and 100x oil immersion lens. Within this report this microscope will be referred to as the ***dark field microscope***. Lastly, a dual function Confocal-Raman system (Confocal Laser Scanning Platform, Leica TCS SP8 on a DMI8 microscope, Leica Microsystems, UK) (inVia Raman, Renishaw, UK) was used, primarily for the Confocal functionality, with 10x, 40x, and 100x oil immersion lenses. Within this report this microscope will be referred to as the ***confocal microscope***.

4.2. Microfluidic microchips

This section describes how microfluidic devices were fabricated, the designs that they were formed into, and how fluid phases were flown into them.

4.2.1. Microchip fabrication

PMMA-SU8-PMMA microchips were fabricated by Epigem Ltd (Redcar, UK) utilising photolithography to a depth of 25 μm . These chips were used for on-chip MB production and imaging during ultrasound (US) exposure. All other fluidic devices, for use as described in the design section below, were formed from PDMS on glass.

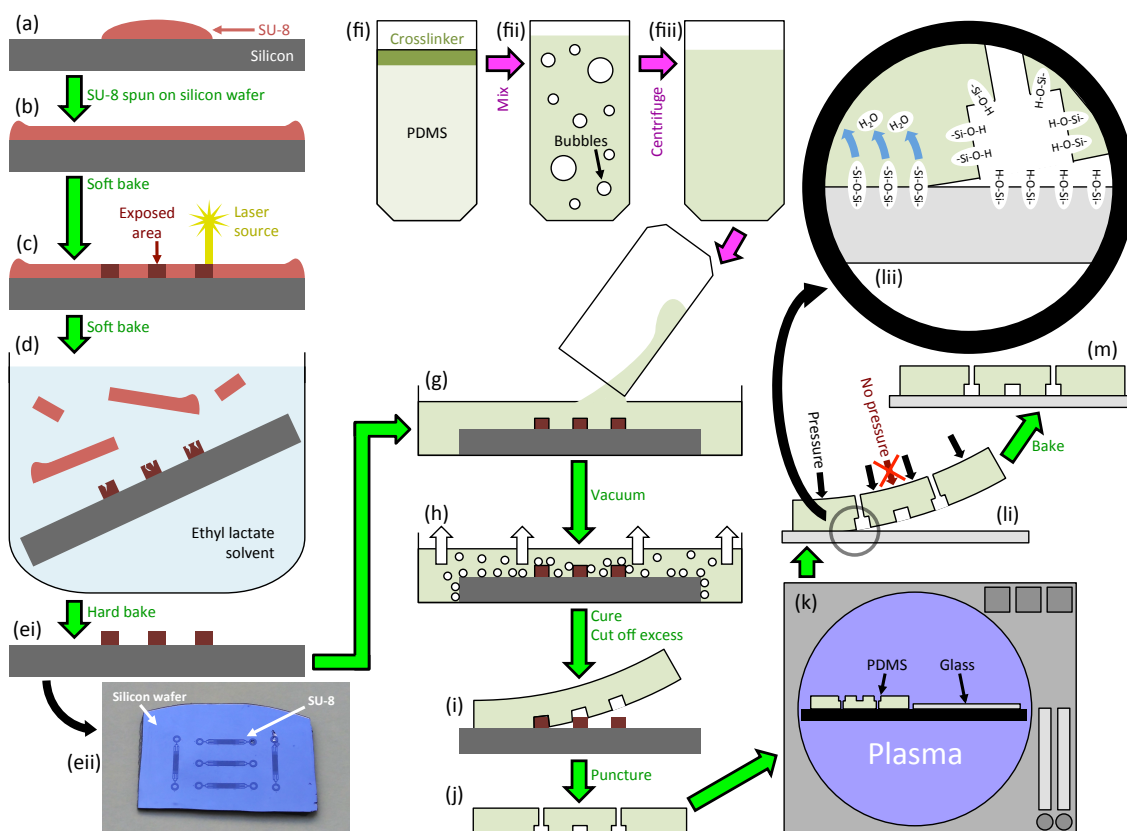


Fig. 4.1. Schematic of fabrication of (a-e) a SU-8-silicon master and its use in the fabrication of (g-m) a PDMS device on glass. (Green and pink arrows) Direction of production steps indicated, with associated text describing actions not shown. (fi-iii, pink arrows) Preparation of PMDS before introduction to master shown as a separate group of steps. (eii) A real complete SU-8-silicon master is shown besides its (ei) schematic version. (h) PDMS under vacuum is shown mid-process. (k) A cleaned glass slide (preparation not shown) is introduced in the plasma treatment step. (li) Contact of the plasma treated PDMS and glass is shown with (lii) a zoomed in section, to indicate the covalent bonding that occurs.

Two types of PDMS design were formed on glass; ones with large open chambers (on the order of millimetres in scale (see section 4.2.2, '*Microfluidic flow cells*', p71), and one with microfluidic channels (with micrometre scale design). The initial step to form either designs was to form the master.

For the large open chambers: Either a thin silicon wafer (0.55 mm thick) or glass slide (~1.0 – 1.2 mm thick) (Smith Scientific, UK) was cut into the shape of a master.

For microfluidic designs: A microfluidic master (Figure 4.1eii) was formed from negative photolithography of SU-8 photoresist onto a silicon wafer that had been cleaned by submersion in acetone, IPA, rinsing with water and baking. To form the SU-8-silicon master; (Figure 4.1a-b) the SU-8 was spun on the wafer accelerating at 100 rpm/s up to 500 rpm, where it was kept for 10 s, then accelerated at 300 rpm/s up to 2800 rpm, where it was kept for 60 s. This gave a 25 μm thick layer. The SU-8-wafer was then soft baked with a slow ramp up to 55 °C, kept at 55 °C for 30 min, then a slow ramp down to room temperature. (Figure 4.1c) The SU-8-wafer was then exposed to a raster scanning 375 nm laser, at 400 mJ/cm^2 , following the microfluidic design specified, in order to harden the exposed areas against development. The SU-8-wafer was baked again as before, (Figure 4.1d) then developed, whereby unexposed SU-8 was removed by placing it in ethyl lactate solvent for 4 min with a following IPA rise and dry. A final hard bake was performed, at 210 °C for 30 min, annealing any surface cracks that had formed, (Figure 4.1e) completing the microfluidic master.

At this stage, either a millimetre scale or micrometre scale master had been formed. From this point on, both masters were used with PDMS in an identical manner.

(Figure 4.1f) PDMS (9 w% crosslinker) was centrifuged (Megafuge 16R, Thermo Scientific, USA) at 1 krpm for 1 min to remove bubbles, after which it was (Figure 4.1g) poured over the master in a small petri dish and (Figure 4.1h) put under vacuum for 1 h to remove any remaining gasses that were solubilised in the PDMS. The PDMS was allowed to cure at 75 °C until set. Curing could take 30 min – 2 h, based on the thickness and total volume of the PDMS layer. Excess PDMS was cut from the cured disk and the remaining PDMS (Figure 4.1i) was carefully peeled away from the master. Circular inlets and outlets were punctured through the PDMS with a 1 mm diameter biopsy punch. A glass coverslip, or slide, was cleaned through a four-step sonication with Decon, acetone, isopropanol, MilliQ and N_2 dried. Meanwhile the PDMS was cleaned of any dust that had settled using Scotch tape. (Figure 4.1k) Both the PDMS and glass were placed inside a plasma-cleaning chamber (Zepto, Diener electronics, Germany) face up, and were plasma treated for 2 min, at 0.8-1 mbar of O_2 . The surfaces of both PDMS and glass are made of $-\text{Si}-\text{CH}_3$. After reaction with the reactive gas, these were both replaced by a $-\text{Si}-\text{O}-\text{H}$ surface. (Figure 4.1li) The PDMS and glass surfaces were then brought into contact for bonding by pressing down on the contact areas while making sure not to collapse the engraved chip design. (Figure 4.1lii) This

formed a -Si-O-Si- covalent bond between the PDMS and glass.²⁰⁷ (Figure 4.1m) Finally the completed chip was baked at 75 °C for 30 min. The strength of the -Si-O-Si- bonds can withstand pressures of 75 psi.²⁰⁸

4.2.2. Microchip designs

The different microfluidic designs that were used throughout this project are outlined below.

Two-phase flow focus / monodisperse MB microchip

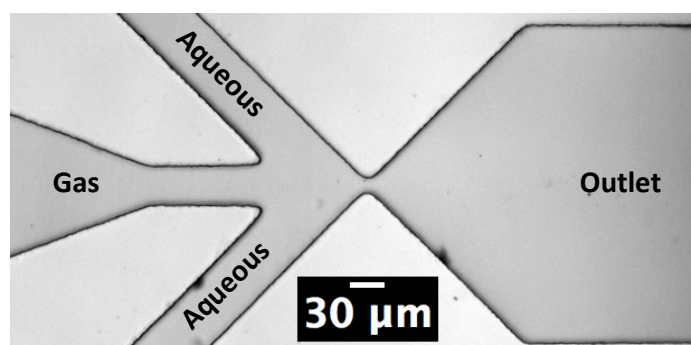


Fig. 4.2. Two-phase FF microchip design used primarily for the production of monodisperse MBs.

Flow focus (FF) microchips are commonly used in the production of monodisperse droplets and MBs.⁴³ (Figure 4.2) A simple two-phase FF system was used in this project, primarily for the production of monodisperse MBs and droplets. This design was fabricated from PMMA-SU8-PMMA to a constant depth of 25 μm , and included one gas inlet feeding to a 30 μm channel and one aqueous inlet branching to two 50 μm channels, one either side of the gas channel. Up stream, on chip filters prevented larger agglomerates from reaching the nozzle. The three channels converged, 46.34° aqueous to gas, at a 7 μm nozzle and further progressed as only one outlet channel. Here, two outlet designs were used. Figure 4.2 shows the first outlet design when the outlet was expanded to 270 μm , which remained constant until off-chip. The second outlet design expanded to 260 μm over 320 μm , before shrinking back down to 100 μm over 200 μm , finally continuing as a 100 μm outlet. The shrinkage and following expansion of the channel at the nozzle gave a pressure drop across this area, which draws the gas phase through the nozzle. The pressure drop, inertia, surface tension, and high shear around the nozzle area, then facilitated pinch-off of the central gas phase in the surrounding aqueous phase.^{88,90,159}

Micro-spray MB microchip

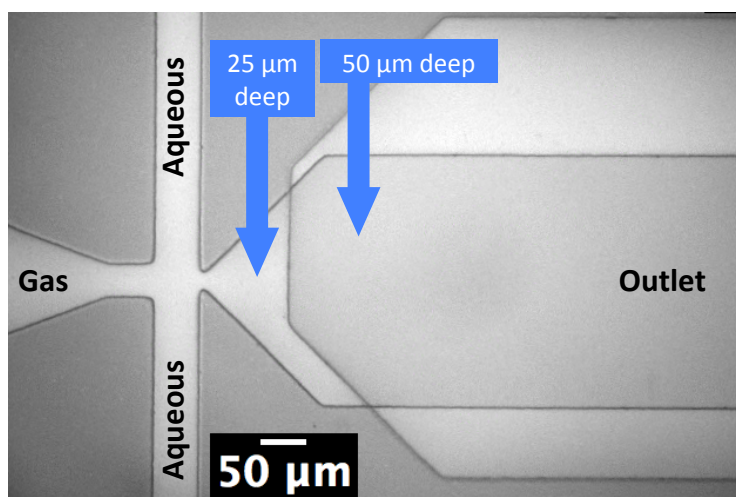


Fig. 4.3. Two-phase microchip design used primarily for the production of microspray MBs. Depth change from 25 μm to 50 μm is indicated.

(Figure 4.3) The microspray microchip was a development from the two-phase FF chip, which aims to increase MB production rate and concentration. In this project, this design was fabricated from PMMA-SU8-PMMA. Here, aqueous and gas inlets were brought together at 90° with a constant depth of 25 μm , the exit channel expanded to 270 μm over 140 μm , then an additional 25 μm depth was added as a step increase, after which the design then continued as a 270 μm wide, 50 μm deep exit channel. This extra depth produced a greater pressure drop across the nozzle, causing an atomisation process on the gas phase.^{43,209} The micro-spray production regime has been shown to bring MB solutions up to clinically relevant concentrations 10⁸-10⁹ MBs/ml.⁴³

Single-module and multiplexed four-module chips were used during this project. For multiplexing, single aqueous and gas inlets were used, both which branched off into four channels, one for each module. The outlets for all four modules were brought to one outlet for collection.

Three-phase flow focus microchip

Three-phase FF microchips were modifications to the two-phase flow focus microchips, designed to add an extra immiscible oil phase inlet in between the gas phase inlet and the aqueous phase inlet. Four three-phase microfluidic microchip designs were used in this project. These design were all fabricated from PMMA-SU8-PMMA. Two separate designs were originally used (Figure 4.4a-b, 5C1 and 3C1) with a further two generations of one of these designs being formed (Figure 4.4c-d, 3C2 and 3C3).

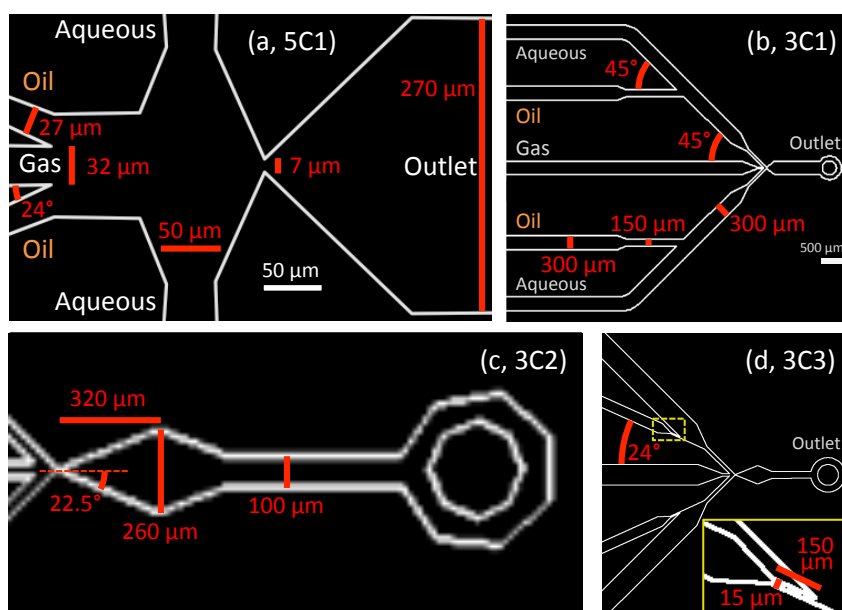


Fig. 4.4. Schematics of three-phase microchip designs used for OLI-MB production. Evolution of design is shown from 5C1 to 3C3, zoomed to show the progressive changes in microfluidic design. Channel wall and measurements are shown in white and red respectively.

One of the original designs focused all three phases at the nozzle (Figure 4.4a), leading to a five-channel FF chip (5C1). Other groups have studied this and similar geometries before for multilayer MB and droplet formation.^{31,82,94,95} The aqueous, oil and gas phases were introduced at the nozzle through inlets of 50 μm , 27 μm and 32 μm wide respectively. The oil and aqueous inlets were angled at 24° and 90° to the gas inlet respectively. The three phases were then focused through a 7 μm wide nozzle, after which the outlet then expanded to 270 μm over 140 μm , at which point it continued on unchanged.

The second original design (Figure 4.4b) introduced the oil and aqueous phases upstream of the gas phase, and then focused the resulting liquid channels and gas phase at the nozzle, giving a final three-channel FF chip (3C1). Here, on either side of the gas inlet channel, a 300 μm wide oil inlet channel shrank to 150 μm over 160 μm , and then after 1150 μm contacted the 300 μm wide aqueous channel at 45°. After this, the combined oil-aqueous channel reduced to 50 μm wide and continued straight, towards the gas inlet, at 45°, and the nozzle. The three channels were then focused through the 7 μm wide nozzle and continued as in the 5C1 design.

The first 5C1 and 3C1 chips to be used had hydrophilic surfaces (only when specified), after which these and all following designs were treated to have a hydrophobic coat (treatment performed by Epigem).

(Figure 4.4c) The second generation of the 3C1 microchip design (3C2) changed the outlet. Here, the outlet expanded from the nozzle at 22.5° for 320 μm until it was 260 μm wide. The outlet then retracted at 22° for 200 μm until it was only 100 μm wide, at which point it continued on unchanged.

(Figure 4.4d) The third generation of the 3C1 microchip design (3C3) changed the oil inlet. When thinning to 150 μm , the oil inlet was angled to the aqueous phase at 24°. The last section of the oil inlet was further thinned to 15 μm for 150 μm prior to introduction to the aqueous inlet to increase flow resistance in that channel.

Microfluidic particle trap device

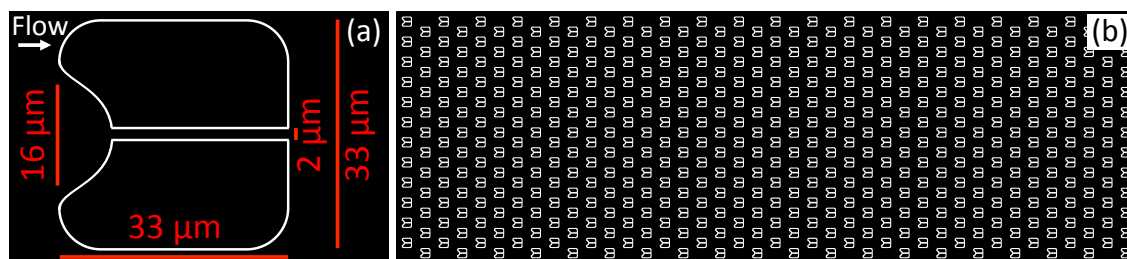


Fig. 4.5. Schematics of (a) the main microfluidic particle trap design used in the project, and (b) the total trap array that was used. Channel wall and measurements are shown in white and red respectively.

Microfluidic particle traps were formed from PDMS on glass aiming to catch 5-30 μm MBs. A few updates were made to the design, where the main device used is shown in Figure 4.5. The trapping channel had a constant depth of 25 μm . Each individual trap was essentially a rounded solid square, width and length of 33 μm , with a semi-circular opening at the trap's forward edge with a radius of 8 μm . From this semicircle a thin channel, 2 μm wide, led to the trap's rear edge. There were 40 columns of traps with the next column being staggered up the channel width by half of the trap-to-trap distance from the previous. Figure 4.6 shows an optimised trap design, which was developed with a geometry that aimed to trap 2-5 μm particles (this device was introduced near the end of the project, so is specified when used). This geometry balanced the flow resistance throughout the device to make it more preferable for particles to fall into empty traps, and zigzag around full traps, whilst keeping traps distant enough to prevent clogging. An algorithm to calculate this optimal geometry was developed by J. Gala De Pablo, based on the work by Xu (2013).²¹⁰

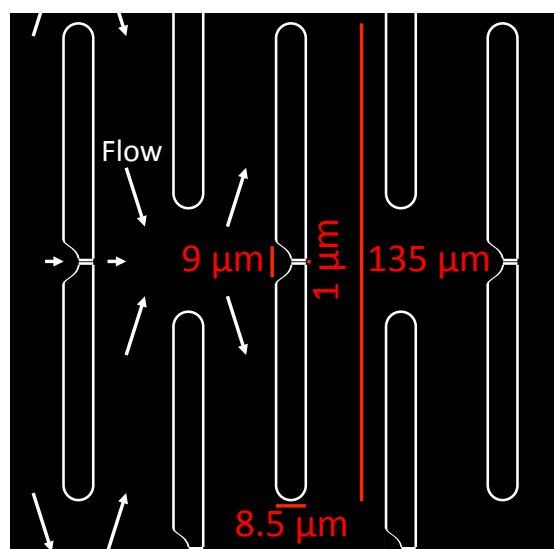


Fig. 4.6. Schematics of the optimized trap design and array that was made with the aim to capture 2-5 μm particles. Channel wall and measurements are shown in white and red respectively.

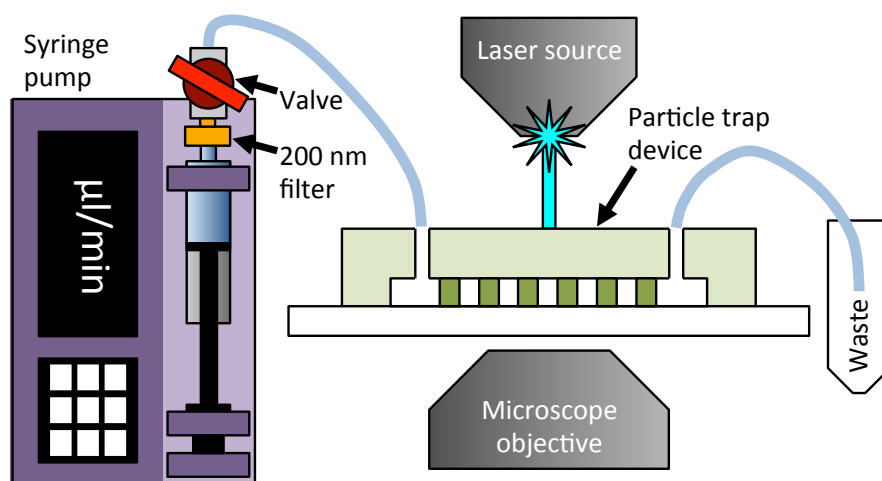


Fig. 4.7. Schematic of apparatus for PDMS particle trapping devices using the confocal microscope.

Figure 4.7 shows how trap devices were set-up for use with the confocal microscope. All traps devices were flowed through with 1 ml 70% isopropanol or ethanol at 50–100 $\mu\text{l}/\text{min}$ prior to use. This was followed by 500 μl MilliQ at 50–100 $\mu\text{l}/\text{min}$, then 1 ml of 1 mg/ml BSA or 1 mg/ml POPC at 50–100 $\mu\text{l}/\text{min}$ to coat the chip walls to reduce non-specific binding of the following sample. MBs were flown into the trap device at 10 $\mu\text{l}/\text{min}$ for at least 30 min or until traps stopped being filled (up to 80 min), and washed by further flowing PBS into the chamber at 10 $\mu\text{l}/\text{min}$ for 30 min. All flow into the chamber was delivered via a syringe pump connected to a switch valve. When changing the fluid type, the valve was closed to prevent all flow between the valve and the trap device outlet, allowing the syringe to be removed from the system and replaced without disturbing the trapped sample. For the flow of all fluids apart from the sample to be trapped, a 200 nm PTFE filter was placed between the syringe and the valve. After the

initial isopropanol/ethanol wash, it was imperative that no air be re-introduced to the system. This was prevented by allowing all relevant components to be filled with the next fluid before connections were made.

Polystyrene, 15 μm diameter, red fluorescent (580 nm excitation, 605 nm emission) coated beads (FluoSphere, Life Technologies, USA) were flown into these traps at 50 $\mu\text{l}/\text{min}$. This was done to assess their trapping capabilities, and so that it could be identified how known spheres would be observed by confocal imaging (552 nm excitation laser, at 1 % power, with a 570 – 781 nm emission window, 364 V gain), with priority on z-stack imaging from top to bottom of the spheres.

During confocal fluorescent imaging with microfluidic trap devices, the walls of the PDMS regularly gave off a fluorescent signal. This occurred as long as the trap device was filled with a liquid, including MilliQ, even if the device was fresh and fluorophore was not present and had not come into contact with the device. This was thought to be due to reflections off of the PDMS walls. Non-fluorescent MBs did not give off a fluorescent signal when used with these devices, including whilst trapped, meaning that reflection off of MBs from the PDMS walls did not need to be considered.

Microfluidic flow cells

Three microfluidic flow cell designs were used for imaging static MB and droplets. One design was fabricated from PMMA-SU8-PMMA. Here four 0.5 mm wide inlets spanned one short edge of a 4 mm wide, 19 mm long rectangular chamber, followed by four 0.5 mm wide outlets spanning the chamber's other short edge. Inlets and outlets were spaced out equally along their edge. Two alternative designs were also fabricated from PDMS. For the first, a one ~ 3 mm wide, ~ 0.5 mm tall inlet led to a ~ 1 cm x ~ 2 cm wide viewing chamber, ~ 5 mm tall, with a following outlet mirroring the inlet. The ceiling of this flow cell was a glass coverslip, which allowed it to be used for US studies (PDMS has a high US attenuation and was difficult to produce with a defined ceiling thickness). The second design, as shown in Figure 4.8, had a ~ 1 cm x ~ 2 cm wide viewing chamber, was ~ 1 mm tall, and had a ceiling of PDMS.

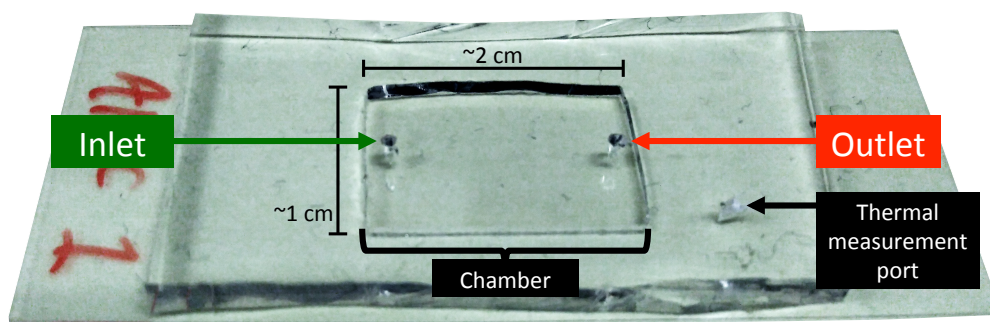


Fig. 4.8. Photograph of a ~1 mm tall PDMS flow cells, indicating a 'slice' into the PDMS that was used for measuring temperature during studies where the flow cell was heated.

4.2.3. Interfacing fluid phases to the microfluidic chips

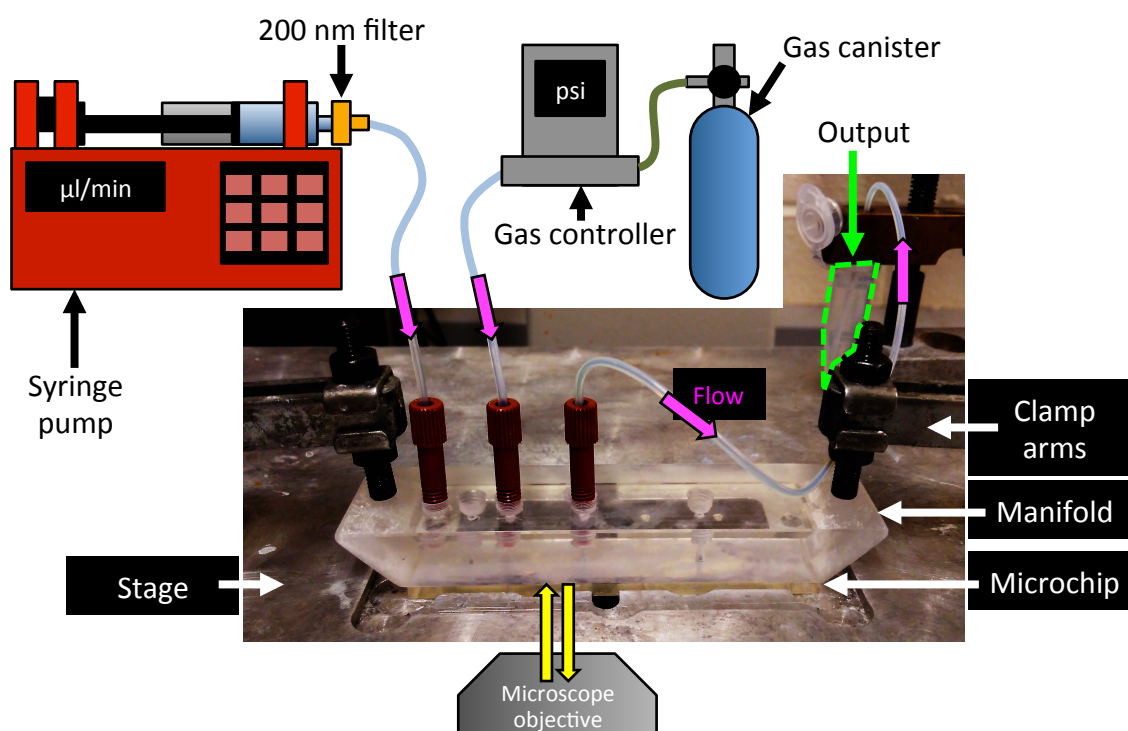


Fig. 4.9. Photo-schematic of the microfluidic apparatus for PMMA-SU8-PMMA microchips. Specifically, the image shows the set-up for two-phase FF. For three phase experiments an extra syringe pump system was added between the two inlets seen here, and for some experiments the syringe pump seen here was changed to the P-Pump system.

PMMA-SU8-PMMA microchip interfacing

As shown in Figure 4.9, PMMA-SU8-PMMA microfluidic chips were mounted into the recess of a custom-built holder on the moveable stage of an inverted microscope. PTFE tubing ferrules (Supelco Analytical, USA) were used to connect the microchip inlets and outlet to an in-house made PTFE manifold, which was brought into firm contact with the microchip by level clamping arms, forming a gas tight seal at least up to 40 psi.

Further PTFE tubing, 0.3 mm I.D. 1.58 mm O.D., was used for inlet and outlet lines protruding out from the manifold.

PDMS microchip interfacing

PTFE tubing (Smith Medical, UK) lines, 0.36 mm I.D. 1.09 mm O.D., were placed directly into punctured PDMS inlets and outlets, which gave a water/air tight seal.

Gas and liquid controllers

Flow of liquids into microchips was controlled by a 1 ml glass lure lock Hamilton syringe mounted into a syringe pump (Aladdin, World Precision Instruments, USA). If the liquid was standard lipid solution, it was controlled by a Mitos P-Pump (Dolomite) using Mitos Flow Control software. The P-Pump could only deliver at flow rates down to 6 $\mu\text{l}/\text{min}$, below which a syringe pump was used, even for aqueous samples. Gas flow of C_4F_{10} into microchips was delivered from a compressed gas cylinder using a digital gas flow controller (Alicat Scientific, USA). When using the PDMS flow cell to image static samples, the sample was injected directly by hand using a 1 ml glass Hamilton syringe and a square cut 0.84 mm I.D., 1.27 mm O.D. needle at ~ 2 ml/min. When using the PMMA-SU8-PMMA flow cell to image static samples, the chip was placed in a tight fitting plastic collar with PTFE tubing 0.3 mm I.D. inlet lines located to match up with the microchip inlets and outlets. One of these PTFE inlets was used to inject liquid sample by hand into the flow cell via a glass Hamilton syringe at ~ 2 ml/min.

4.3. Non-microfluidic imaging chambers

Two imaging chambers were used through the work described in this thesis; a 50 μm deep glass chamber and a non-microfluidic flow cell. When using these chambers to image MBs, the MBs were allowed to float to the top surface, and concentration was taken as a measurement in regards to the chamber depth. The 50 μm deep chamber was the standard cell used for imaging MBs. The flow cell had a greater chamber depth allowing for concentration measurements from samples of low concentration. A third method of sample observation (used on low concentration samples) was to place a droplet of solution directly onto a glass slide.

50 μm deep chamber and a droplet of solution on glass

This chamber was made from a glass slide, a glass coverslip, and 50 μm thick plastic (polyethylene terephthalate film) spacers (Goodfellow, UK) (Figure 4.10a). Both glass

surfaces were cleaned with an acetone, isopropanol, MilliQ wash and N₂ dry before use. Capillary action was used to insert sample into the chamber. If this chamber had to be turned upside down for following imaging or was imaged over time, the chamber was sealed on all four sides with wax (1:1:1, Vaseline:Paraffin wax:Lanolin, made in-house, recipe from Institut Curie, Paris) to prevent the chamber from displacing and to avoid sample evaporation.

If the sample to be imaged was of too lower concentration for the 50 μm chamber to give accurate particle size and concentration measurements, a droplet of the sample solution could be placed directly onto a glass slide, uncovered (Figure 4.10b). The meniscus would then lead any buoyant particles to concentrate at the highest point. The problems with this sample preparation method were that the sample concentration was not possible to measure reliably, and the particles were not static (due to solution convection and air currents) leading to inconsistencies between subsequent images, for example brightfield followed by fluorescence.

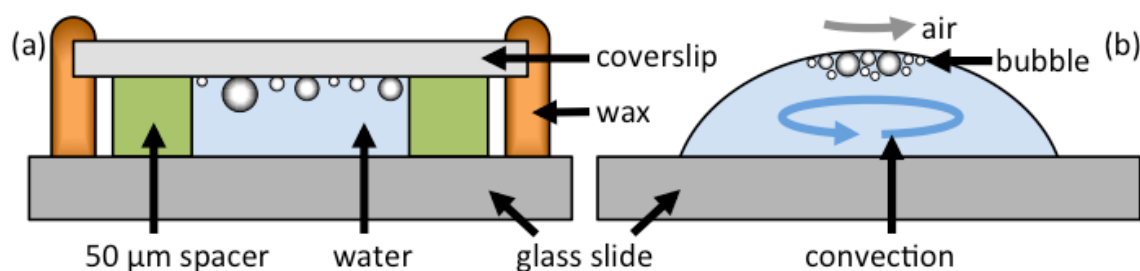


Fig. 4.10. Sample preparation methods for microscope imaging. (a) 50 μm deep chamber, where the number of particles imaged per sample solution volume can be known, and (b) a droplet of sample solution on a glass slide, where the meniscus leads buoyant particles to concentrate. The former and latter methods allowed for a measurement of particle concentration and imaging of a low concentration sample respectively

Non-microfluidic flow cell for imaging of low concentration samples

(Figure 4.11) This flow cell was made from a plastic base, a circular O-ring wall and a cleaned glass coverslip ceiling. This flow cell had a circular diameter of 12.5 mm, and a height of ~ 500 μm . Inlets and outlets were located on the plastic base, close to the wall edge. Sample was flowed into the flow cell through a needle in the side of the flow cell wall. The inlet had an I.D. of 1 mm at smallest.

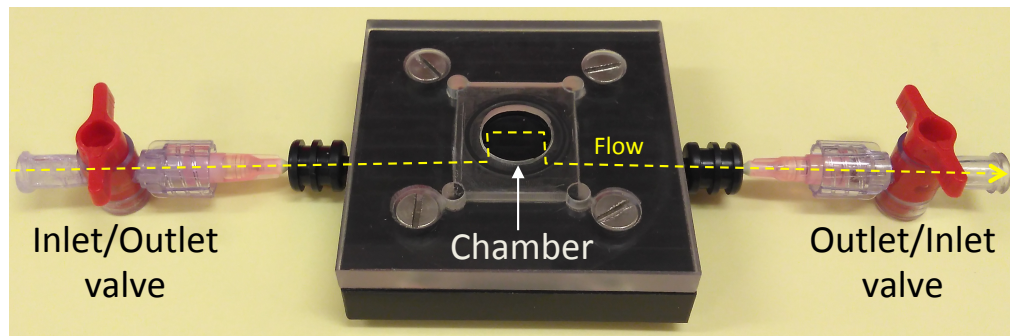


Fig. 4.11. Non-microfluidic flow cell, showing (yellow dotted line) the flow pattern of sample through the device.

4.4. Non-oil MB production

Non-oil MBs were produced via three methods, namely by mechanical agitation, monodisperse microfluidic, or spray microfluidic production.

Mechanical agitation

The most common method used for the preparation of MB samples is mechanical agitation.^{211–216} This is because it is a robust approach, which gives a clinically relevant concentration of MBs, orders of magnitude higher than most microfluidic methods can achieve, with minimal effort or time. Generally, the method includes the rapid shaking of a vial semi-filled with free lipid solution, topped up the desired MB core gas.⁹⁴ The forces provided by the rapid agitation are sufficient enough to introduce gas from the headspace into the aqueous environment. Agitation protocols for leading medical MB solutions commonly use ~4500 oscillations per minute.⁸⁸ However, since the stresses used to break up the gas into MBs are non-uniform, monodisperse MB populations can be difficult to form.^{160,212} This reduces their bulk sensitivity to US, since their resonant frequency is different, and MBs are often found $> 8 \mu\text{m}$, which could pose health risks.^{89,95} During this project, a 1.75 ml vial filled with 1 ml standard lipid solution, had C_4F_{10} gas bubbled through it, filling the vial head space. This vial was then tightly sealed with parafilm before undergoing mechanical agitation (3M ESPE CapMix, 3M UK PLC, Bracknell, UK) for 45 s. Due to the high concentration produced, these MBs were often diluted 1:1000 in PBS buffer before counting and sizing or further use.

Monodisperse MBs

To produce MBs under a monodisperse microfluidic production, the two-phase FF microchip was used. Gas pressure was set to 3-4 psi and standard lipid solution was flown into the microchip at 20-30 $\mu\text{l}/\text{min}$.

Spray MBs

The spray MB microchip was used to produce MBs under a spray regime at a high concentration and fast rate. Gas pressure was set to 20 psi, for the single-module and four-module designs standard lipid solution was flown into the microchip at 20 $\mu\text{l}/\text{min}$ and 80 $\mu\text{l}/\text{min}$ respectively.

For both monodisperse and spray production, samples were allowed to pass from the PTFE tubing outlet into a 1.75 ml glass vial or a 2 ml eppendorf, in which 10 μl of liquid C_6F_{14} had been pre-injected. The liquid C_6F_{14} was there to saturate the MB solution bolus with perfluorocarbon (PFC) molecules, reducing/removing the positive concentration gradient of PFC from the MB interior to exterior. It has also been shown that adding C_6F_{14} to a lipid MB solution bolus causes C_6F_{14} molecules to intercalate into the lipid shell, reducing the surface tension, decreasing Laplace pressure inside the MBs, and increasing shell resistance. These effects act to slow the leakage of the PFC gas into the surrounding solution, increasing MB lifetime.²¹⁷

4.5. Surface pressure measurement of air-aqueous interfaces by a Langmuir-Blodgett trough

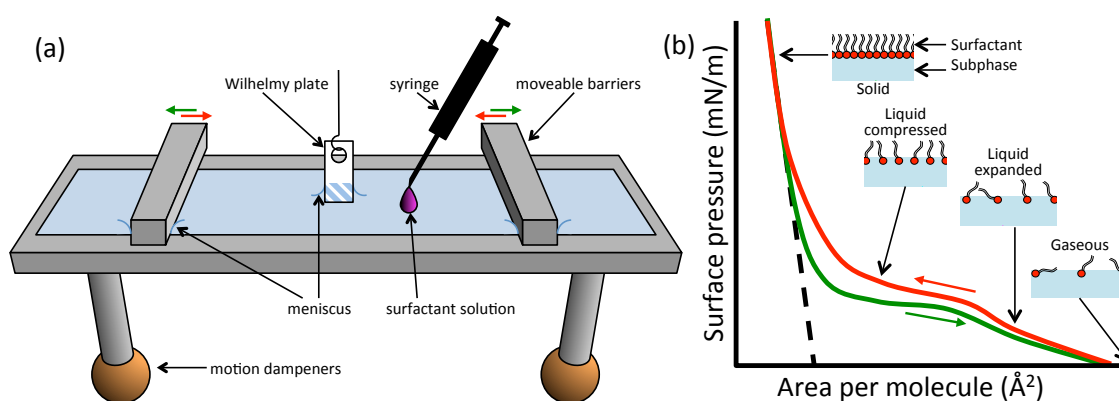


Fig. 4.12. Set-up and basic output for a LB trough, showing (a) how droplets of surfactant solution were deposited on to the surface, and then the barriers moved to change the active surface area, whilst a Wilhelmy plate (b) recorded the change in surface pressure. The pressure-area isotherm relationship shown is typical of DPPC lipid.

Much of the work described in this thesis is underpinned by the self-assembly of surfactant molecules (primarily lipids) at hydrophilic-hydrophobic interfaces, lowering the interfacial tension to give a more energetically favourable state, often leading to the stabilising of one phase in another as an emulsion. More specifically, MBs are stabilised by these surfactants self-assembling at their gas-liquid interface, which reduces the surface tension (see Theory Chapter, Equation 2.17). A Langmuir-Blodgett trough, as shown in Figure 4.12, was used to model a MB surface for measures of how the surface tension of air-aqueous surfaces changed due to the concentration of surfactant molecules.

A KSV NIMA Langmuir-Blodgett (LB) trough (Biolin Scientific, Sweden), placed inside an air-flow inhibiting, transparent box, was used to measure surface pressure change of an air-MilliQ interface during a change of lipid concentration at the interface. Surface pressure, π , relates to surface tension by the following equation:

$$\pi = \gamma_0 - \gamma \quad (4.2)$$

Where γ_0 = native surface tension of subphase liquid, and γ = surface tension of subphase with surfactant.

The LB trough was prepared for use by a typical cleaning method. The Teflon trough was filled with MilliQ from a sterile, thoroughly cleaned, glass container to form a meniscus in-between and either side of two movable Teflon barriers. The MilliQ was fully aspirated, always removing from the surface, and the trough was refilled afterwards. This process was repeated at least twice. After this just the top few millimetres of surface was aspirated to remove surface contaminants by eye, refilling the trough as needed. Compressions of the barriers were performed on the semi-clean central meniscus with further cleaning and filling, making sure to keep the menisci from falling below the barriers, until the π (measured via a Wilhelmy plate) did not rise above 0.3 mN/m at full compression. The central meniscus was now considered free of contaminants. A 1 mg/ml steric acid, POPC, DPPC, or DPPC-PEG lipid in chloroform, hexane, or hexadecane solution was prepared fresh in a glass vial, sealed with parafilm and stored at 4 °C until use.

4.5.1. Pressure-area isotherms

With the trough area set to maximum (324 mm x 75 mm), a ~ 30 µl droplet of the lipid solution was deposited directly onto the central meniscus from a cleaned glass syringe, allowing the droplets to spread directly from the needle tip. The solution was allowed 10 min for the volatile solvent to evaporate, leaving a gaseous phase (low concentration) lipid monolayer. The barriers were then compressed up to a set π (~30 mN/m) and expanded back to 0 mN/m at 5 mm/min three times each. This transitioned the lipid through gaseous to liquid to solid phases. Changes in π were measured against changes in area per lipid molecule, A_s , at the subphase surface.

$$A_s = \frac{A_T \cdot M_w}{V \cdot C \cdot A_v} \quad (4.3)$$

Where A_T is the current trough area, M_w is the molecular weight, V is the volume, C is the lipid solution concentration, and A_v is Avogadro's constant.

As shown in Figure 4.12b, by tracing the linear solid phase relationship back to the area per molecule where $\pi = 0$, it was possible to measure the native molecular area of the lipid. When surfactant molecules in a monolayer are fully close-packed and under their maximum compression possible, any more compression will require some of the surfactant to leave the monolayer. If single molecules leave the monolayer a significant decrease in the gradient of the π over area per molecule will be observed. Often however this occurs as a small section ‘flake’ of the monolayer delaminating from the rest, which can lead to the formation of a small section of bilayer or the surfactant flake can enter the subphase. Either way, at this point the π will significantly decrease, due to the bare section of surface. If surfactant molecules are forced out of the monolayer under any of these mechanisms the monolayer is being said to collapse, with the π at this point being termed the collapse pressure. To measure the collapse pressure, the LB trough barriers were allowed to compress slowly at 5 mm/min after a typical isotherm, only being stopped after the lipid was observed to collapse.

4.5.2. Equilibrium spreading pressure: Spreading of lipid from a volatile solvent

When a structure is formed by the self-assembly of surfactant molecules between two phases, without an external stimulus, they will accumulate up to an equilibrium interfacial tension/pressure, termed the equilibrium spreading pressure (ESP).

The trough surface area was set to be static (at 138 cm²). Known volume (~5 µl) droplets of the lipid solution were deposited directly onto the central meniscus from a cleaned glass syringe, allowing the droplet to spread directly from the needle tip. Equation 4.3 was used to calculate A_S against changes to π . It was expected that the lipid solution would spread at the subphase surface until ESP was reached. At this point, additional lipid solution would remain as a droplet/lens on the surface, becoming a concentrated crystal/flake as the volatile solvent evaporated. Here, an equilibrium would be reached between lipid molecule spreading to the surface from the crystal lattice structure and reversibly re-joining the lipid crystal lattice from the surface. However, as is detailed later (see Results Chapter 5.1, p121), all results using this method followed each lipid's pressure-area isotherm. This method of lipid solution addition did not identify the ESP.

4.5.3. Equilibrium spreading pressure: Spreading of lipid from a deposit on glass

This section describes an alternative method for determining the ESP, adapted from the method introduced by Bois (1989),²¹⁸ who found that measuring the ESP of DPPC from deposits on the surface was insufficient.

The trough surface area was set static at 138 cm². ~ 10 µl of the lipid in chloroform solution was pipetted onto the end of a cleaned glass plate and allowed to dry. Further 10 µl lipid solution volumes were added on top, up to ~ 50 µl, allowing the solution to dry each time. The plate was then slowly drawn through the gas-subphase interface and pulled back out. This allowed the top surface of lipids on the lipid coated plate to migrate to the gas-subphase interface in order to stabilise it, observed as an increase of π . The above process was repeated with new lipid coated plates until the surface pressure was found to remain constant. This indicated that the lipid was in equilibrium between spreading at the gas-subphase surface and adhering to the remaining lipid at the glass plate. This was assumed to be the ESP.

Subsequently, a pressure-area isotherm was performed on the monolayer in order to compare the total trough surface area when the lipids were in a solid phase to the area when ESP. As the native molecular area of the lipids was known from previous typical pressure area isotherms, the number of lipids present could be calculated, allowing the lipid concentration at ESP to be calculated.

This method was used to measure the ESP for monolayers of steric acid, DPPC, and DPPC-PEG. Due to the order that experiments were carried out, later contamination of

the equipment, and time constraints of this thesis project, it was not possible to reliably measure the ESP for a lipid monolayer of POPC using this technique.

4.6. Contact angle measurements and total surface energy calculations

During the work outlined in this thesis a number of solid surfaces needed to be measured for water contact angle in order to measure their hydrophobicity/hydrophilicity.

A FTA4000 contact angle system (First Ten Angstroms, USA) was enclosed in a box to restrict airflow and reduce dust settling on any surfaces to be measured. (Figure 4.13a) A 30 psi vacuum water pump system (The Lee Company, USA) ending in a 30 gauge needle, I.D. 0.159 mm, pointing vertically down was used to delivery and contact a MilliQ droplet to the solid surface underneath to be measured. A 12x magnification lens camera (Navitar, USA), with internal 0.58-7x modifier, observing horizontally across the solid surface was used to acquire images of the MilliQ droplet and ImageJ was used to measure both the left and right contact angles, which were averaged. Contact angles were measured for the water droplet both advancing, θ_A , and then receding, θ_R , at least six times, each time in different places across the surface, aiming to be as spaced out as possible.

The following equations were used to acquire the equilibrium Young contact angle, θ_0 :

219

$$\theta_0 = \arccos \left(\frac{\Gamma_A \cos \theta_A + \Gamma_R \cos \theta_R}{\Gamma_A + \Gamma_R} \right) \quad (4.4)$$

where

$$\Gamma_A = \left(\frac{\sin^3 \theta_A}{2 - 3 \cos \theta_A + \cos^3 \theta_A} \right)^{\frac{1}{3}} \quad (4.5)$$

and

$$\Gamma_R = \left(\frac{\sin^3 \theta_R}{2 - 3 \cos \theta_R + \cos^3 \theta_R} \right)^{\frac{1}{3}} \quad (4.6)$$

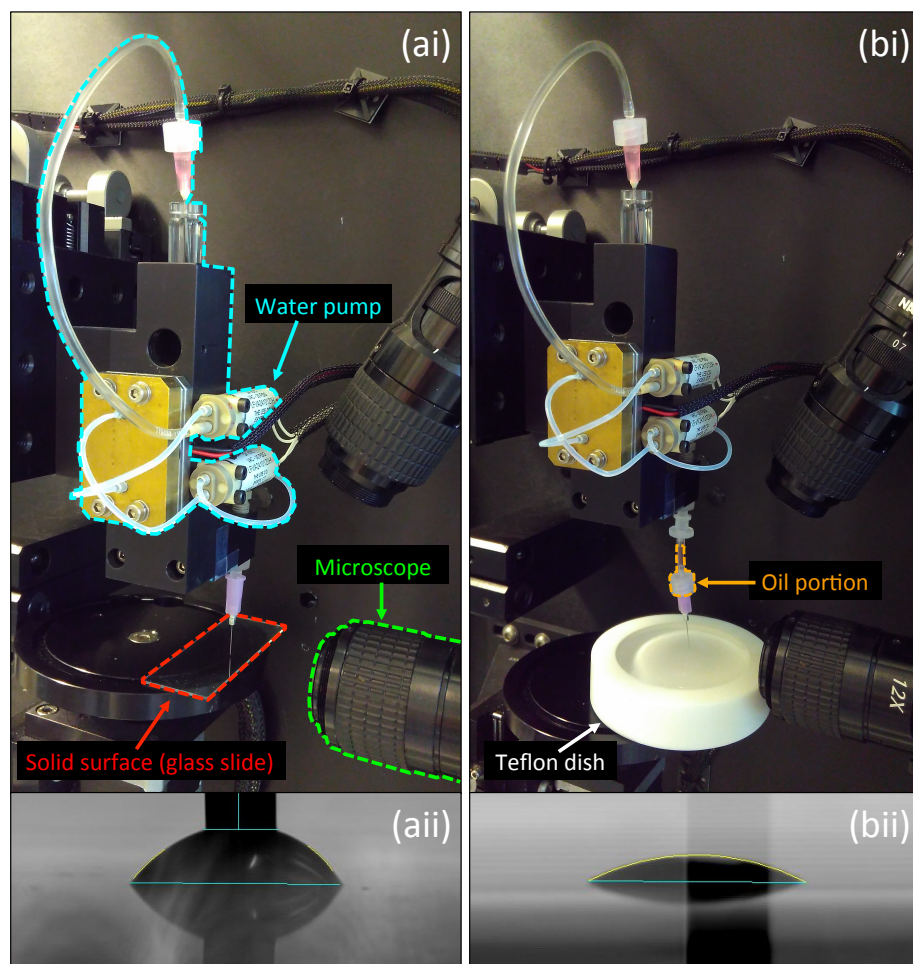


Fig. 4.13. Apparatus used for the contact angle measurement of (a) water on a solid flat surface (here glass), and (b) oil on a water surface.

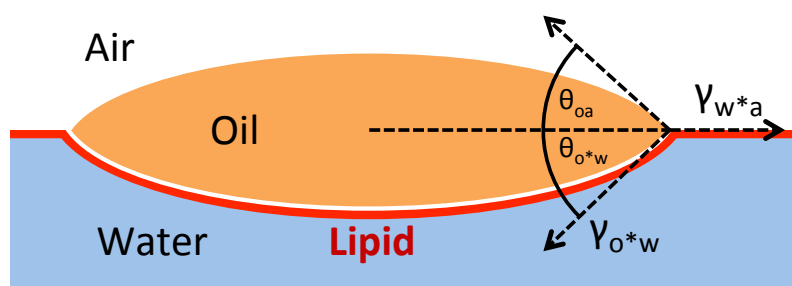


Fig. 4.14. A schematic showing the arrangement of air, oil, and water phases, and the position of the lipid monolayer from the Figure 4.13bii images. The surface tensions, γ , and contact angles, θ , of the three-phase geometry are indicated.

As shown in Figure 4.13b, contact angle measurements were also taken of droplets of squalane and tripropionin oil against a water-lipid-air interface to determine the interfacial tension of water-lipid-oil interfaces.

A 6 cm diameter, circular Teflon dish was filled with MilliQ to allow a meniscus to form above the top of the dish walls. This meniscus was aspirated before the dish was refilled. This was repeated at least five times to remove surface contaminants. POPC,

DPPC, or DPPC-PEG lipid, solvated in chloroform at 1 mg/ml, was added directly to the water surface as droplets to give concentrations of; (1) no lipid, (2) the equilibrium spreading pressure (ESP) (see section 1.8.1 for LB trough experiment to acquire ESP for DPPC), or (3) enough lipid until additional lipid-chloroform solution no longer spread, at which point the monolayer was assumed to be at the collapse pressure. The sessile drop technique was used for contact angle measurement, where a droplet of oil was added directly to the air-lipid interface via an oil filled syringe needle. The contact angle was measured on both the left and right sides of 6-9 droplets for each lipid monolayer type.

Figure 4.14 shows how the air, oil, and water phases, and the lipid monolayer were thought to have arranged from observation of the Figure 4.13bii images. Using Young's relation altered for a two liquid with one gas phase system (Equation 4.7), the oil-lipid-water interfacial tension was calculated. It was assumed that no lipid migrated to the oil-air interface, keeping the surface tension at constant 28 mN/m for squalane and 36.5 mN/m for tripropionin oil. Due to a limitation in the experiment (that only the oil-air surface could be observed, and therefore measured for its contact angle), it had to be assumed that the oil-air and oil-lipid/water contact angles were equivalent. This means that any calculations made using the results from these experiment should be considered as estimates. The surface tension of the water-lipid-air interface was known from LB trough experiments (see sections 4.5 and 4.5.1, p76-78). Using the calculated interfacial tension, the total surface energy was calculated for one 2 μm OLI-MB with a range of oil layer thicknesses (Equation 4.8). Using the same oil and gas volumes, the equivalent total surface energies were calculated for a separate MB and oil droplet, and an oil-in-air-in-water structure.

$$\gamma_{olw} = \frac{\gamma_{wla} - \cos\theta_{oa}\gamma_{oa}}{\cos\theta_{olw}} \quad (4.7)$$

$$E = \gamma_{oa}A_{oa} + \gamma_{olw}A_{olw} \quad (4.8)$$

Where γ is the surface/interfacial tension, θ is the contact angle (θ_{olw} was assumed equal to θ_{oa}), E is the total surface energy, and A is the surface area.

4.7. Particle sizing and concentration measurements

Nanoparticle size measurement

Particle sizing and concentration measurements were made using Zetasizer Nano ZSP system (Dynamic Light Scattering, DLS) and by a NanoSight NS300 system (Malvern Instruments, Malvern, UK).

To calculate particle size, DLS uses an autocorrelation function (ACF) (Equation 4.9), and both DLS and NanoSight use the Stokes-Einstein relationship (Equation 4.12).

$$ACF = e^{-2\Gamma\tau} \quad (4.9)$$

$$q = \left(\frac{4\pi n}{\lambda}\right) \sin\left(\frac{\theta}{2}\right) \quad (4.10)$$

$$D_t = \frac{\Gamma}{q^2} \quad (4.11)$$

$$D_h = \frac{k_B T}{3\pi\eta D_t} \quad (4.12)$$

Where Γ is the decay constant, τ is the delay time, q is the scattering vector, n is the refractive index of the continuous liquid, λ is the laser wavelength, θ is the scattering angle, D_t is the diffusion coefficient, D_h is the hydrodynamic diameter, k_B is the Boltzmann's constant, T is the temperature, and η is the dynamic viscosity.

For DLS, the process of particle sizing is limited in that it cannot measure samples of polydisperse size, particles are assumed to be spherical, and it cannot determine concentration. DLS is also more sensitive to larger particles, so a near monodisperse sample, or a sample with a few larger contaminants, relative to the sample particles, will be measured as larger than reality.

For a DLS experiment, 1 ml of sample, diluted to $\sim 10^8$ - 10^{10} particles/ml, was placed in a plastic cuvette and measured immediately, to prevent particles from precipitating before/during measurement. Three measurements were taken of the same sample, one after the other, for averaging and error calculation.

The NanoSight used a ~ 50 μm wide laser to illuminate particles in solution. These particles scatter the light, which is collected by a long working distance x20 lens. Particles appear as bright point sources moving under Brownian motion, which is recorded as a video. Nanoparticle tracking analysis software then analyses the random walk pattern of the particles to give a D_t value, and thus, using the Stokes-Einstein relationship (Equation 4.12), give a D_h value for each particle. This process of particle sizing excels at giving high resolution sizing analysis of 10 – 2000 nm particles, due to

direct observation and measurement of diffusion events from single particles. This allows for polydisperse samples to be analysed for size and allows for concentration calculation due to knowing how many particles are measured per given imaging volume.²²⁰

For a NanoSight experiment, the sample was diluted with an aim at $\sim 10^8$ particles/ml (concentrations were estimated from similarly formed, previous samples, or multiple trial and error dilutions were run for samples of entirely unknown concentration). The sample was then injected from a sterile 1 ml syringe into the NanoSight's $\sim 100\ \mu\text{l}$ viewing flow cell. Measurements were taken, and then fresh sample was then flown into the flow cell and the process repeated for a total of five times. The flow cell system was thoroughly cleaned between samples, and before and after use, using MilliQ, 70 vol% ethanol and polyester cellulose wipes (Integrity cleanroom, UK).

At early stages in the project a qNano (Izon Science, UK) device was used for both sizing and concentration measurements. The qNano works on the basis of measuring changes in current flowing through nanopores of defined diameter causing blockade events where the current is momentarily decreased. During a qNano experiment, a voltage is applied across the pore, with the ionic current being recorded in real time. As a particle crosses this pore it leads to an increase in electrical resistance, seen as a resistive pulse, where the magnitude of the pulse is proportional to the particle's volume. The rate of these resistive pulses, defined by the pressure applied, is proportional to the particle concentration.²²¹

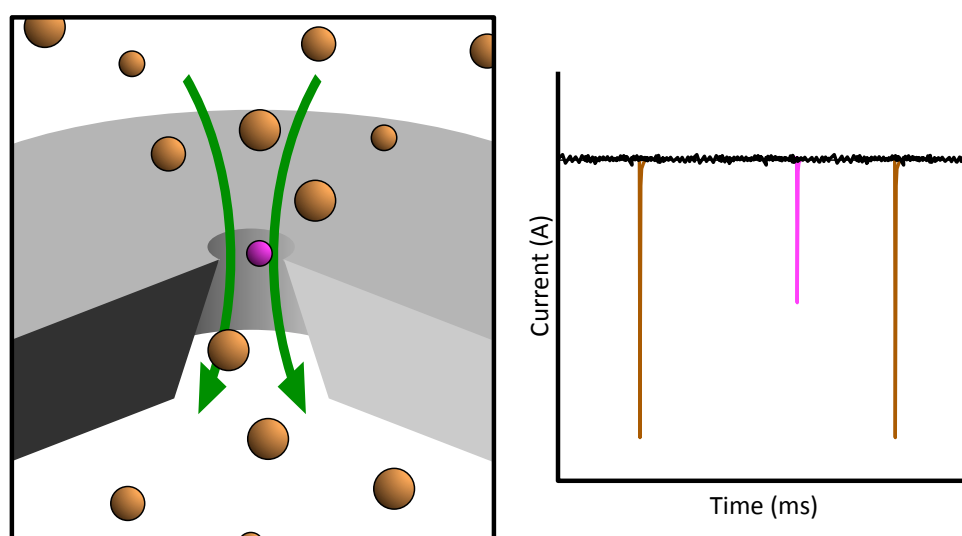


Fig. 4.15. Schematic of (a) nanoparticles passing through a qNano pore, with (b) the observed resistive pulses shown over time. Orange and purple particles shown to represent difference in size seen as a difference in resistive pulse magnitude.

Nanoparticles to be measured, and calibration particles, were diluted to 10^8 particles/ml in PBS, vortexing the calibration particles for 30 s before dilution. The apparatus was set up so that the horizontal pore connected two PBS filled chambers, with the pore stretched to a known value, which was factored into the software. The PBS in the upper chamber was then replaced with either the calibration or sample solution. A given pressure was applied to the top chamber, forcing particles in the solution to cross the pore. This allowed for measurement of the sample particle's size distribution and concentration in reference to the calibration particles.

Microscale particle sizing

Many experiments detailed in this thesis either used or formed droplets and/or MBs which required information to be collected on both their size and concentration. To do this, a sample was taken directly from the droplet or MB stock after gentle agitation to prevent pre-concentration. This sample was then either injected into a 50 or 120 μm deep viewing chamber, or flown into the non-microfluidic flow-cell. The chambers or flow-cell were then imaged either at the top or bottom of the internal volume based on the oil/gas buoyancy with an assumption that all particles had risen or fallen to one of the faces. For the chambers, an inverted fluorescence microscope, upright fluorescence microscope, or inverted darkfield microscope were used for imaging, whereas the flow-cell only used the upright fluorescence microscope. At least 10 images were taken to ensure wide sampling. (Figure 4.16) Measurements on all imaged particles were undertaken using ImageJ (National Institutes of Health, USA) with a graticule for pixel to real length calibration. These were averaged with a standard deviation and error. For concentration measurements, all particles counted in each image were compared to the known area of the image and the internal volume's depth. This gave each image a concentration, all of which were averaged with a standard deviation and error.

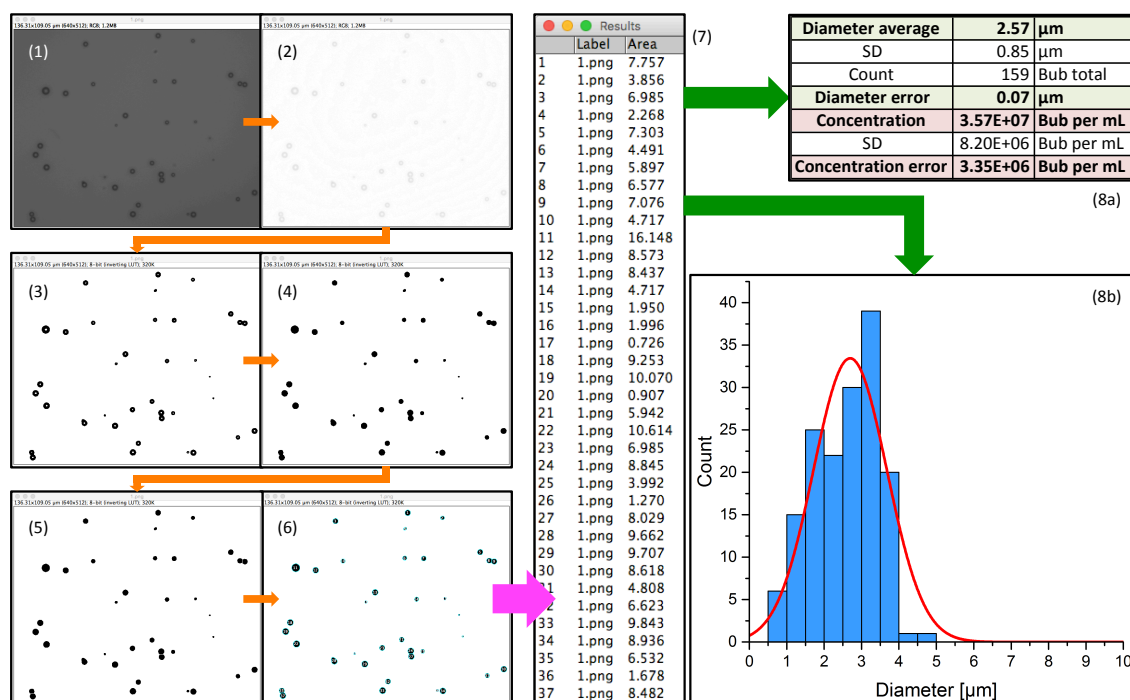


Fig. 4.16. Method used to measure microscale particles (here MBs) for diameter and concentration information.

Figure 4.16 shows the step-by-step method for measuring mean average microscale particle size and concentration, as well as plotting of a sizing histogram with a Gaussian (often LogNormal) fit.

Steps taken were; (1) Image loaded into ImageJ and calibrated for size against graticule measurement (graticule image not shown). (2) Image background corrected to remove illumination gradient. (3) Image made binary, where grey scale values above 50% of the maximum grey scale value across the image (ignoring single pixel noise) were set to white, 'empty', and values below 50% were set to black, 'full'. (4) Black shapes filled. (5) Black shapes watershed, where shapes determined as two merged circles are cut to two shapes. (6,7) Black shapes identified and measured for area, noting the image that the particles are measured from. The next image was loaded and steps 1-7 were repeated until all images were measured. (8a) Areas converted into diameters, mean averaged with SD and error calculated. Number of particles observed calculated into a concentration, knowing imaged area and chamber depth, per image, then averaged with SD and error calculated between the images. (8b) All diameters measured were plotted as a histogram, with a Gaussian or log-normal fitting, for determining singular or multimodal distribution. If a multimodal distribution was found, then mean averaging was not accepted as indicative of the distribution and peak analysis would be used for size distribution.

4.8. US equipment calibration – transducer drive voltage to pressure at the target

Three US transducers were used in this project, a high intensity focused US 1.1 MHz transducer (H102, Sonic Concepts, USA), a focused 3.5 MHz transducer (V380, Olympus Industrial, UK), and an unfocused broadband transducer, centred on 3.5 MHz (V384, Olympus Industrial, UK). The first two transducers were used for activating liquid PFC droplets (section 4.11.3.3, p 109), whilst the third transducer was used for MB scatter measurements (section 4.12, p 111-112). All transducers were tested for their pressure output at the focal point in the same manner, as described below for the first 3.5 MHz transducer. The pressures delivered by the remaining two transducers had previously been calibrated by Dr J. McLaughlan (Electronic and Electrical Engineering, University of Leeds).

A waveform generator (33250A, Agilent Technologies, UK) was connected to an amplifier (Broadband Power Amplifier A150, Electronics & Innovation, USA), which was then connected to the transducer to be calibrated. This transducer was directed at a 0.2 mm needle hydrophone (Precision Acoustics, UK), with both being submerged in a degassed distilled water tank, roughly separated by the manufacturer's quoted focal length of the transducer. The hydrophone was then connected up to an oscilloscope (WaveSurfer 104Xs, Teledyne LeCroy, UK). Additionally, separated from the main apparatus above, the waveform generator and amplifier were both connected to the oscilloscope. The entire system had a resistance of 50 Ω . When a mVpp (peak-to-peak) voltage was output from the waveform generator this signal was amplified by the amplifier $\times 123 \pm 2$ (SD 7), causing the transducer to output a pressure wave. Attenuation occurred on this wave until it reached the hydrophone, where the remaining pressure would be recorded as a voltage, with a sensitivity of 338 mV/MPa for a 3.5 MHz wave. The voltage profiles as a function of time at the waveform generator, amplifier, and hydrophone were observed on the oscilloscope. Before any measurements were taken, the hydrophone was positioned into the transducer's focal spot using xyz roller translation stages.

Measurements of peak negative hydrophone voltages, which were converted into negative peak wave pressures, were then taken at waveform generator voltages from 0 – 450 mVpp, with 50 mVpp steps.

The waveform generator to transducer set up (without the oscilloscope) were used in this way during experiments to supply US waves with calibrated peak negative pressures to samples.

4.9. Monitoring the mechanics of Lipid Oil Nanodroplet (LOND) rupture into an oil layer and the production of OLI-MBs from LOND precursors

Emulsions of oil in lipid solution, termed lipid oil nanodroplets (LONDs) were examined, through the methods described in this section, as a precursor tool for the production of an oil layer at the gas-aqueous interface of MBs.

4.9.1. LOND formation

LONDs were formed via two methods, as shown in Figure 4.17, either by tip sonication or homogenisation. Fluorophores were used both as drug mimics and for analytical purposes.

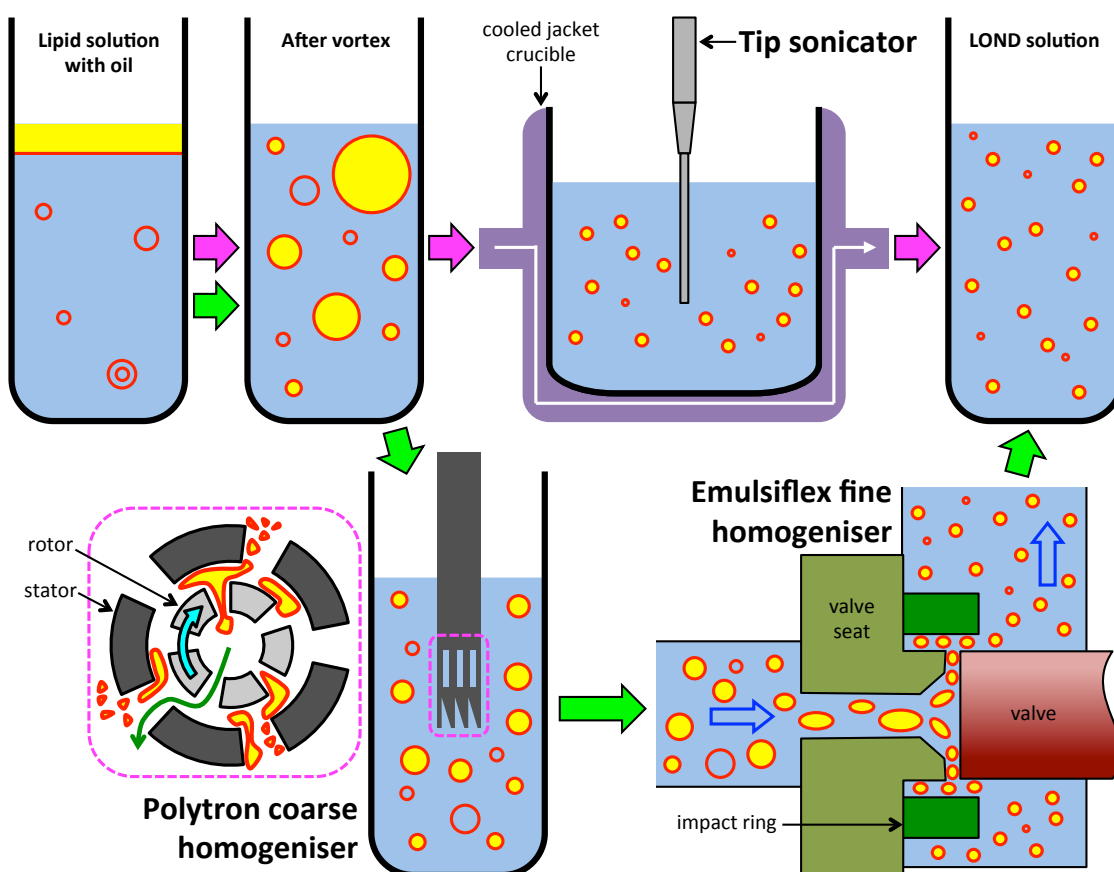


Fig. 4.17. Schematics of LOND production via (pink arrows) tip sonication and (green arrows) polytron and emulsiflex. (Yellow) Oil with (red) lipid is shown to homogenise into nanodroplets through a step-by-step process. (Dotted purple) An inset of the polytron head is shown, with the (green arrow) motion of the oil by centrifuge shown.

Tip sonication

10 mg POPC lipid, with or without 5 mol% DSPE-PEG, suspended in 1:1 chloroform-methanol, was dried under nitrogen in a glass vial for 30 min, then redispersed in 930 μ l of PBS. 70 μ l of squalane, squalene or tripropionin oil was added. To form an emulsion, the solution was vortexed for 30 s, then tip sonicated (Sonifier S-250A, Branson Ultrasonics, UK) at 200 W, 20% power, 100% duty cycle, for 15 min in a 4 °C cooled jacketed glass vessel. The emulsion was dialysed utilising a 100 kDa pore size membrane for over 12 hr in PBS to remove non-encapsulated oil and fluorophore, and to remove any excess lipid in solution down to equilibrium with the LONDS.

To confirm that tip sonication was suitably emulsifying the oil into monodisperse LONDS, a post-vortex sample was sized by DLS during 30 min of tip sonication. 50 μ l was removed from the centre of the sample every 5 min during emulsification for investigation.

Homogenisation

100 mg dried lipid was redispersed in 3.3 ml of PBS. 700 μ l of the oil was added. To form an emulsion, the solution was vortexed, coarsely homogenised with a Polytron PT1300 D (Kinematica AG, Luzern, Switzerland) at 12.5 krpm, 40 °C and atmospheric pressure for 10 min. The emulsion was made up to 10 ml with PBS buffer and, to form a LOND emulsion, finely homogenised under high-pressure in an Avestin EmulsiFlex-C5 (Avestin Europe GmbH, Germany) at ~175 MPa, 4 °C for 20 min. The emulsion was then filtered using a KrosFlow Research Ili Tangential Flow Filtration System (Spectrumlabs Europe, The Netherlands) at 100 kDa, 45 ml/min for at least 2 hours for the same reason as dialysis above.

Sizing and concentration of LONDS was performed by DLS and NanoSight. LONDS were diluted 1:100000 before measurement in both systems. Typically, LONDS were produced at 10^{13} LONDS/ml with 170 nm diameter for both preparation techniques.

4.9.2. Hydrophilic/hydrophobic treatment of surfaces

To observe and monitor how LONDS interacted with both hydrophobic and hydrophilic interfaces, from their aqueous continuous phase, glass slides and quartz crystal microbalance with dissipation monitoring (QCM-D) crystals were treated to have either a hydrophobic or hydrophilic surface. These solid surfaces then acted as a model for

LOND interaction with the surface of an unstabilised MB's hydrophobic gas core in aqueous solution.

Glass slides were treated through a range of methods, giving a range of hydrophobicities/hydrophilicities. (1) Glass slides were cleaned through a decon, acetone, isopropanol, MilliQ sonication bath process for 15 min each step, dried with N₂, then stored in N₂ (unless otherwise stated, this was the typical cleaning procedure for all glass slides and coverslips used in this entire work) or (2) 1 mg/ml BSA solution. (3) Fresh glass slides were etched with sand paper to produce a 'rough' surface, then cleaned as above. (4) Cleaned glass slides were further cleaned with piranha solution and stored in MilliQ. (5) Glass slides coated with 200 nm of evaporated Au (cleaved from a silicon wafer), were exposed to UV ozone for 20 min, washed with the above sonication process, dried with N₂, re-exposed to UV ozone for 20 min, then submerged in 1 mg/ml ODT in ethanol for ≥ 12 hrs. This allowed the thiol to covalently bond to the Au surface, forming a self-assembled monolayer. The slides were rinsed in ethanol, then MilliQ, and dried and stored under N₂. All glass surfaces prepared as above were used within three days and as soon as possible.

QCM-D crystals (Q-Sense AB, Sweden) (explained further in section 4.9.4, p 87-89) were purchased either with a quartz or Au surface for treatment as a hydrophilic or hydrophobic surface respectively. To give a hydrophilic surface, the quartz surface QCM-D crystals were thoroughly cleaned by UV-ozone cleaning for 20 min, followed by immersion in Decon 90 and then MilliQ whilst in a sonication bath, and finally vigorous agitation in isopropanol. The crystals were kept in each solution for about 10 min. The crystals were dried in N₂, then re-exposed to UV ozone for 20 min and stored under N₂. To give a hydrophobic surface, the Au surface QCM-D crystals were prepared in the same way as the quartz surface QCM-D crystals, and then hydrophobic self-assembled monolayers were formed on the Au coated crystals by immersion in ODT in ethanol (1 mg/ml) for ≥ 12 h, after which they were rinsed with ethanol, to remove excess ODT, and MilliQ. These were then dried and stored under N₂. All QCM-D surfaces prepared as above were used immediately.

When surfaces were treated in any of the above processes, the θ_0 of one reference treated surface was measured (as explain in section 4.6, p 76-78) to assess hydrophobicity/hydrophilicity.

4.9.3. LOND interaction with hydrophobic/hydrophilic treated glass surfaces

LOND solution was added to slides treated to be hydrophilic, hydrophobic, and roughened. Whilst the LONDS were nanoscale, macro and microscale observations were made here.

Glass slides were treated as above in section 4.9.2 and dried under N_2 if stored in solution. 30 μ l of Nile red squalane POPC LOND solution was pipetted directly onto each glass slide. Camera phone (D626, HTC, UK) videos were recorded from a ‘birds-eye’ view to record any millimetre-scale solution displacement. If displacement of solution occurred, the top surface of the glass, where displacement had occurred, was observed on an inverted microscope under both bright field and TexRed fluorescence. After the introduction of Nile red squalane POPC LOND solution to 50 μ m deep chambers, where all glass surfaces had been treated as in section 4.9.2, the glass-solution interfaces were observed under confocal microscopy, using a 552 nm excitation laser, 5 % power, and 570 – 781 nm emission window, 750 V gain.

4.9.4. Quartz crystal microbalance with dissipation monitoring

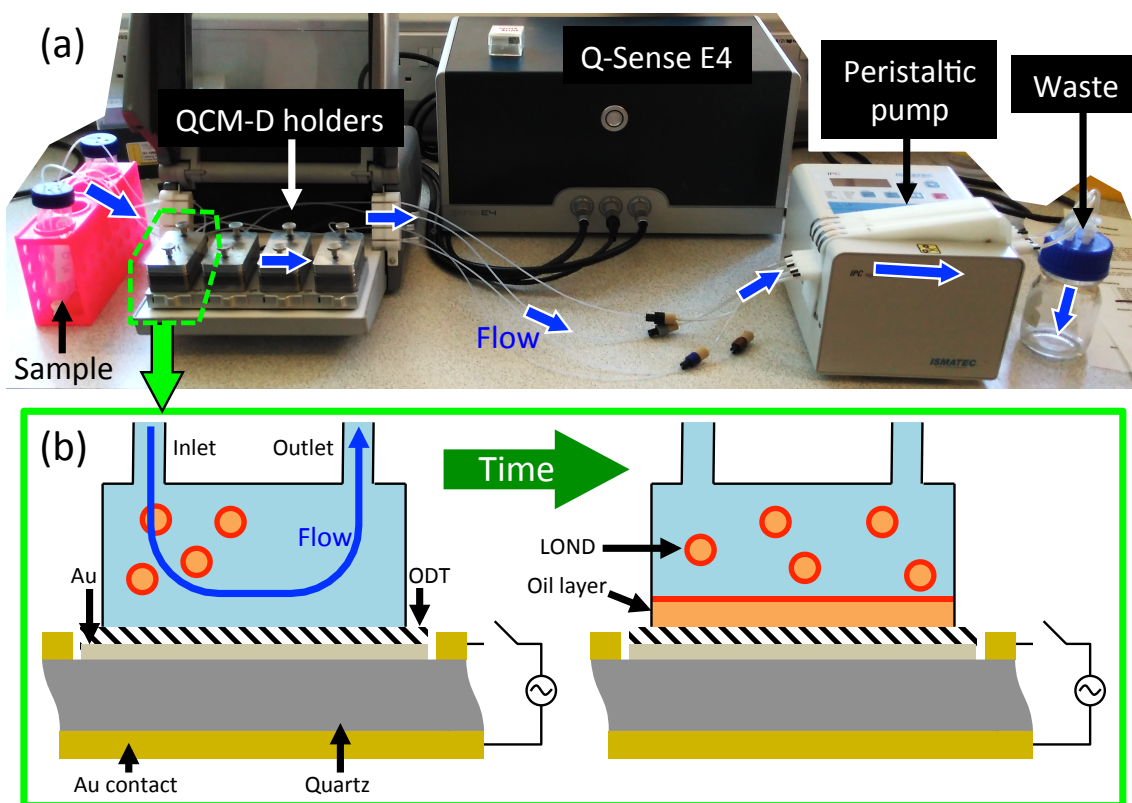


Fig. 4.18. (a) Apparatus used for QCM-D experiments with a (b) schematic of the internal workings around the QCM-D crystal.

Quartz crystal microbalance with dissipation monitoring (QCM-D) was used to study LOND interactions with hydrophilic and hydrophobic solid surfaces in an aqueous environment, with the latter being used as a mimic to the gas-aqueous MB interface. QCM-D utilises the piezoelectric properties of quartz to measure the damping in resonant frequency of the oscillations as a response to mass addition to the surface of the crystal. The technique (without dissipation monitoring) was originally introduced by Sauerbrey (1959), with an added mass resolution of 4 ng/cm^{-2} .²²²

As shown in Figure 4.18, a Q-Sense E4 (Q-Sense AB, Sweden) was used to monitor the interaction between LONDS and QCM-D crystals treated to be hydrophilic or hydrophobic. Crystals were allowed to equilibrate for at least 1 h in degassed PBS, flowing at $14 \text{ } \mu\text{l/min}$. The 5th, 7th, 9th and 11th overtones were recorded and used in the analysis. The LONDS were introduced in to the flow chambers at a dilution of 10^{12} LONDS/ml in PBS, at $140 \text{ } \mu\text{l/min}$. The flow was then stopped for $\sim 2 \text{ h}$ until no further frequency or dissipation changes were observed. PBS was used to rinse the system, in order to remove any unattached material ($140 \text{ } \mu\text{l/min}$), followed by a MilliQ rinse, and another rinse in PBS to monitor any change in attached material due to buffer change. The Sauerbrey and the viscous models were fitted to the above harmonics to calculate the mass adhered to the crystal during the experiment and estimate the thickness of any oil-lipid layer formed.

The Sauerbrey equation presents a proportional relationship between the change in frequency (Δf) of a resonating flat quartz crystal and the change of mass (Δm) to the crystal's surface.

$$\Delta f = - \left[\frac{2nf_0^2}{A\sqrt{\rho_q G_q}} \right] \Delta m \quad (4.13)$$

Where n is the overtone being measured, f_0 is the native resonant frequency of the crystal, A is the active area of the crystal, and ρ_q and G_q are the density and shear modulus of the crystal.^{223–225}

As more mass is added to the crystal it acts to slow down the vibrations of the crystal, lowering the resonant frequency. Strictly, the Sauerbrey equation is only true for the crystal and added mass resonating in a vacuum. This is because interactions occur between the crystal/mass's top surface and the fluid the mass is being deposited from. However, the Sauerbrey equation only needs to be corrected for this when the deposited mass is from a soft viscoelastic material. When the material is an elastic film, and for many practical cases, the correction would be negligible, and so the Sauerbrey equation

remains valid.²²⁶ This model assumes that the mass being deposited onto the crystal acts as an extension of that crystal, notably that it moves with the same elastic properties (is rigid) and is flat. If the material is too viscoelastic, then it causes energy dissipation during oscillation, further changing the frequency measured. For a film of thickness below 40 nm, the Sauerbrey equation is sufficient to model the change in mass as any viscoelasticity is negligible.²²³

The Kelvin-Voigt viscoelastic model addresses the limitations of the Sauerbrey equation, allowing measurement of a viscoelastic film by modelling it as a spring and dashpot in parallel, measuring the Δf and change in dissipation (ΔD).²²⁷ The equation takes into account the shear modulus and viscosity of the added mass and properties of the fluid the mass has come from. It assumes that the added mass is applied as a discrete number (i) of flat material layers.

$$\Delta f \approx -\frac{1}{2\pi\rho_q h_q} \left(\frac{\eta_w}{\delta_w} + \sum_i \left(h_i \rho_i \omega - 2h_i \left(\frac{\eta_w}{\delta_w} \right)^2 \frac{\eta_i \omega^2}{\mu_i^2 + \omega^2 \eta_i^2} \right) \right) \quad (4.14)$$

$$\Delta D \approx -\frac{1}{2\pi f \rho_q h_q} \left(\frac{\eta_w}{\delta_w} + \sum_i \left(2h_i \left(\frac{\eta_w}{\delta_w} \right)^2 \frac{\mu_i \omega}{\mu_i^2 + \omega^2 \eta_i^2} \right) \right) \quad (4.15)$$

Where h_q is the thickness of the quartz, η_w and δ_w are the viscosity of the surrounding fluid and the penetration depth of the shear wave into the fluid respectively, h_i , ρ_i , η_i , and μ_i are the height, density, viscosity and shear modulus of the material layer i , and ω is the angular frequency of oscillation.^{224,227,228}

In the analysis throughout this project, i was set to 1, being a single layer of mixed oil and lipid, where the oil was assumed to be the dominant material. The model was used to calculate μ_i and h_i from ranges given in the relevant results sections. The fluid was set to water, $\eta_w = 1000 \text{ kg/m}^3$ and $\delta_w = 1 \text{ mPa.s.}$

4.9.5. Changes to surface pressure due to interactions between LONDS and an air-lipid/aqueous surface

Using the LB trough previously described in section 4.5 (p 72), changes to the π of an air-lipid/aqueous surface were monitored during the introduction of LONDS into the aqueous subphase and their floating and further interaction with the surface. This worked as a model to the surface of a MB, with LOND interaction occurring from the surrounding solution. In this work, the LB trough was washed and subphase prepared as in section 4.5 (p 73), but with a PBS subphase in order to more closely represent the LOND solution aqueous phase.

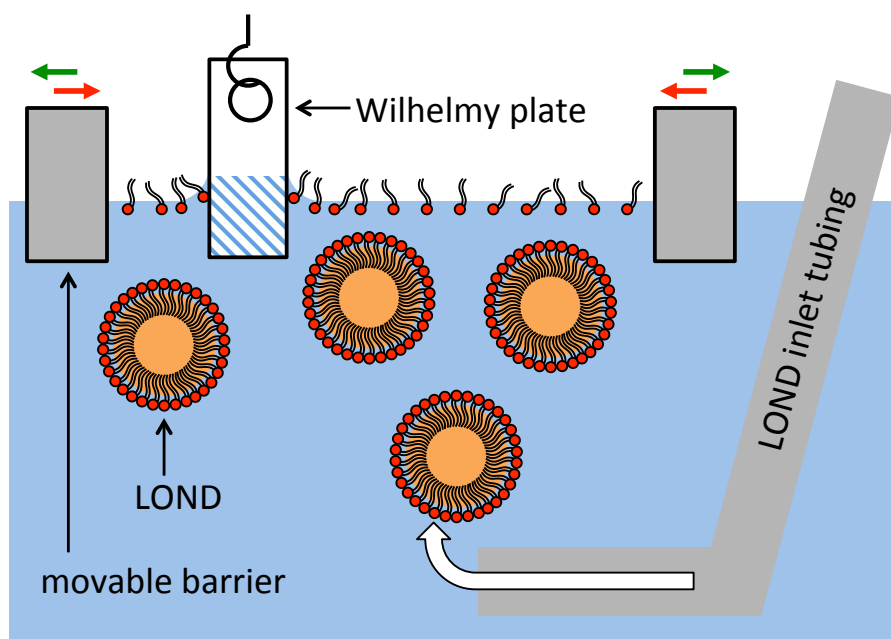


Fig. 4.19. Schematic of experimental set-up used for measuring surface pressure changes due to the introduction of LONDs to a monolayer pre-set to a defined surface pressure. Here, whilst the moveable barriers are shown with green and red moving arrows to mirror Figure 4.12, they were static.

LOND addition to static monolayers set to defined surface pressures

DPPC lipid, representing a typical MB shell, was spread onto the subphase surface so that after barrier compression to a target π of 15, 8, 4, or 0 mN/m (just prior to any increases in surface pressure) the LB trough area would be between 50 and 200 cm². The subphase was also prepared without a lipid monolayer and compressed to 60 cm². The surface was monitored for 30 min to confirm π stability. As shown in Figure 4.19, squalane POPC or POPC-PEG LONDs were injected into the sub-phase via a syringe and tubing that travelled from one of the two subphase volumes outside of the barriers, under one barrier, into the main subphase volume. The outlet of the tubing was gently moved around the bottom of the main subphase to avoid surface fluctuations whilst promoting uniform LOND distribution across this subphase. The tubing was then slowly and fully removed from the system. Enough LONDs were added so that, after floating to the surface, they would close-pack. From the Hadamard-Rybczynski equation, each LOND would individually take 14 days to rise the trough depth (0.5 cm).²²⁹ However, by eye, the bulk of the LOND emulsion was observed to rise to the surface seconds after injection. Therefore, the change to π was recorded over an hour following an initial rise in π , where it was assumed that the majority of the LONDs

were either at or approaching the monolayer. These experiments were conducted at 21.3 ± 0.2 °C.

LOND addition to fully compressed monolayers with following expansion

POPC lipid was spread onto the subphase surface with a following pressure-area isotherm being performed to confirm the monolayer's validity. The monolayer was compressed to a π of 35-40 mN/m, close to POPC's collapse pressure, aiming for a trough area of 10 – 20 cm², and allowed 30 min to relax to a constant π . POPC squalane LONDS were introduced to the subphase as in the previous section and 30 min was allowed for the LONDS to rise, equilibrate under the surface monolayer, and for any change in π to plateau. The trough area was rapidly expanded by moving the barriers outwards at 27 mm/min, either (1) constantly until the π decreased to 0 mN/m or (2) sequentially decreasing by ≤ 10 mN/m steps, allowing the π 10 min to relax and plateau before the next decrease. After this step, and potentially a recording of how the π relaxed from a stretch to 0 mN/m, a new pressure-area isotherm was taken and the surface was compressed to the same area as the initial compression to be compared with the recordings before LOND addition. It was proposed that on decreasing the π of the initially compressed monolayer, the LONDS would enter and spread at the surface, increasing the number of lipids and adding a volume of oil at the surface. This would allow observations to be made of the critical surface pressure under which LOND entering and spreading would occur, and then how the addition of the oil component would alter the surface pressure of a monolayer at different compressions in respect to the number of lipid molecules in the system at each time.

4.9.6. Production of OLI-MBs from LOND solution

Two-phase FF devices (section 4.2.2, p 63) were used for on-chip production of OLI-MBs from LOND solution. POPC squalane, squalene or tripropionin LOND solution was diluted to 10^{12} LONDS/ml in 10 vol% glycerol, 4 mg/ml NaCl. If the LONDS were tripropionin, then the solution the LONDS were diluted into was firstly saturated with tripropionin by heating to ~ 50 °C and stirring for ~ 30 min. LOND solution flow rates of 15-50 μ l/min were delivered via a syringe pump, passing first through a 200 nm PTFE filter to remove any oil that was not successfully homogenised or from LONDS that had destabilised over time. C₄F₁₀ gas pressures of 20-34.5 kPa were regulated by a digital gas flow controller. At the nozzle the gas was pinched off and stabilised as a MB by the LOND solution. The MB solution contained 10 μ l of liquid C₆F₁₄ per 1 ml of

precursor MB solution to extend MB lifetime by intercalation of the C_6F_{14} into the MB shell.²¹⁷ High frame rate imaging (FASTCAM SA-X, Photron, USA) between 10 – 50 kfps, performed on an inverted light microscope (Eclipse Ti-U, Nikon, Japan), was used to observe single MB pinch off and flow immediately after the nozzle during production. For size and concentration measurements squalane and squalene OLI-MBs were imaged in 120 or 50 μm deep chambers by darkfield (Eclipse Ti-U, Nikon, Japan), whereas tripropionin OLI-MBs were imaged in a flow-cell (as detailed in section 4.7, p 70-71). Squalane and tripropionin OLI-MBs were also imaged over 4 h for lifetime measurements. Here, three wax sealed 50 μm MB loaded glass chambers, or a single MB loaded flow cell were observed over time at ambient conditions.

OLI-MBs were also produced via a mechanical agitation method. This gave a high proportion of $>8\ \mu\text{m}$ diameter MBs, allowing for higher resolution imaging of the MB surface fluorescence from 10-30 μm MBs, in comparison to $\sim 2\text{-}3\ \mu\text{m}$ MBs produced microfluidically. The LOND stock solution was first diluted to 10^{12} LONDS/ml in PBS. The mechanical agitation method was then continued as in section 4.4 (p 71), with the dilute LOND solution replacing the standard lipid solution. Size and concentration measurements were taken using 50 μm deep chambers and the inverted microscope detailed previously. These measurements were performed over 4 h, at ambient conditions, using three wax sealed chambers for lifetime measurements.

OLI-MBs made from LONDS loaded DiO/DiI were washed in microfluidic particle traps, whilst imaged by confocal microscopy to confirm the fluorescence and stability of the oil component (excitation 488 nm at 10 % power, and emission windows 500-520 nm and 561-582 nm, 600 V gain). OLI-MB samples were flown into a microfluidic particle trap device (prepared as in Chapter 4.2.2) at 10 $\mu\text{l}/\text{min}$ for 30 – 60 min. A following PBS wash was performed at 10 $\mu\text{l}/\text{min}$ for ~ 60 min. Single slice and z-stack images were taken of the trapped MBs both before and after washing occurred. The resulting images' grey scale values located at and off the MBs' shells were compared to assess the MB fluorescence retention, indicating the stability of the oil portion, and confirm fluorescence removal from the surrounding solution, indicating the successful washing/removal of the LOND solution.

To further understand the production of OLI-MBs, mechanically agitated non-oil-MBs stabilized by a POPC or DPPC-PEG shell were trapped and washed as with the OLI-

MBs in particle traps. 500 μ l of DiI squalane POPC LONDS were washed past the MBs at 10 μ l/min, and then the chamber was washed with 500 μ l of PBS at 10 μ l/min. During this experiment the fluorescence was recorded as before on the confocal microscope (excitation 488 nm at 10 % power, and emission windows 500-520 nm and 561-582 nm, 600 V gain) to assess if the MBs gained and then retained a fluorescent shell. This would indicate if the LONDS were capable of entering and spreading at a MB shell after the MB was already stable or if spreading only occurred in order to stabilise a MB.

4.9.7. Förster/Fluorescence resonance energy transfer (FRET) enabled LONDS

Fluorescence/Förster resonance energy transfer (FRET) was used to follow LOND destabilisation and LOND-LOND mixing at gas-aqueous interfaces, eventually leading to the positive conformation of oil layer formation at the MB surface.

As shown in Figure 4.20, the general experimental concept used in these experiments was the following. Two LOND samples would be made, one encapsulating a FRET donor, and another encapsulating a FRET acceptor. After mixing of these two stable samples, if the LONDS remained stable then the FRET pair would not come into proximity to allow FRET to occur, on the other hand, if the LONDS destabilised and mixed their oil and loaded fluorophore then FRET proximity would be achieved. This method would firstly allow identification of the self-assembly/attachment of LONDS around a MB shell given by a fluorescent outside, with the further identification of if the LONDS had spread into an oil layer or remained stable by the presence or lack of FRET signal.

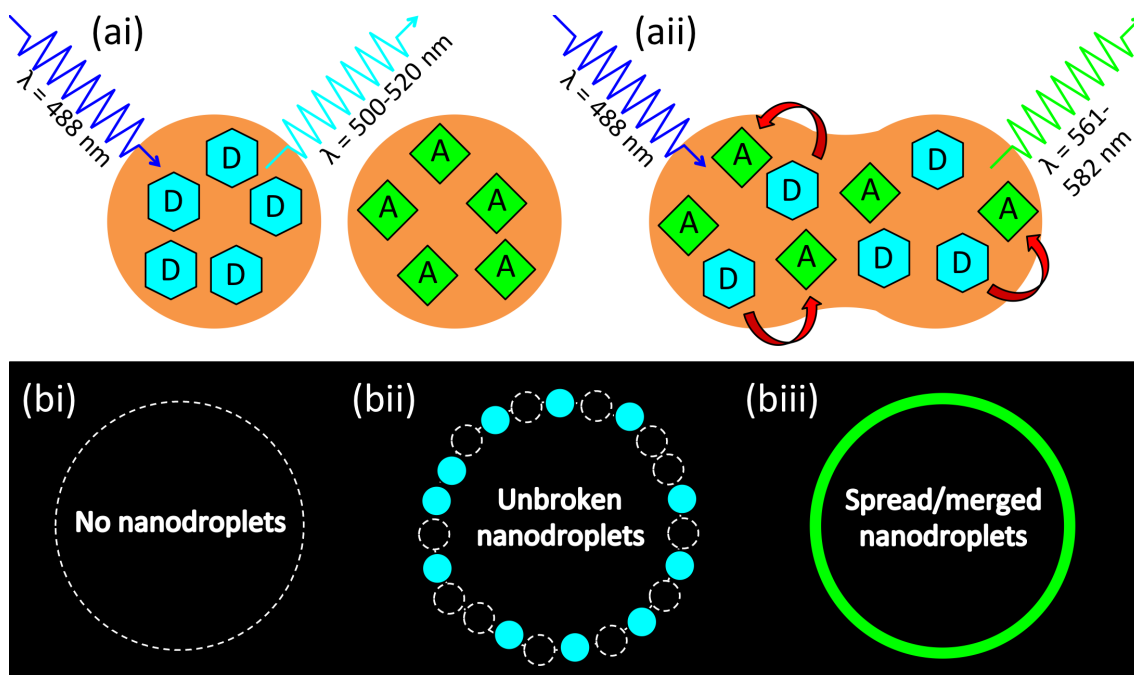


Fig. 4.20. Schematic of the concept of FRET loaded LONDS for OLI-MB formation. Showing donor (D) excitation leading to (ai and bii) D emission if the nanodroplets remain stable, and (aii and bii) acceptor (A) emission if the nanodroplets merge/spread. Wavelength given are for DiO and DiI in squalane oil.

DiO and DiI as hydrophobic FRET agents

DiO and DiI have previously been used in literature as hydrophobic FRET agents both in oil phases and as the core of micelles.^{230–233} In both cases, it is well known that after excitation of DiO (donor) or DiI (acceptor) separately by a source within the donor excitation window, both fluorophores have emission signal in the donor and acceptor emission window without FRET occurring. However, when DiO and DiI are within proximity for FRET to occur, the DiO + DiI emission within the donor window is reduced and the DiO + DiI emission within the acceptor window is enhanced beyond that of the addition of the two separate DiO and DiI emissions. As shown in Equation 4.16, in order to identify any enhanced FRET fluorescence, it was therefore necessary to compare all samples containing donor + acceptor to the maximum intensity from control samples containing just donor and just acceptor.^{231,234} The concentrations of donor and acceptor had to be kept constant throughout all samples.

$$FRET_f = FRET_i - (I_{\max_{Donor}} + I_{\max_{Acceptor}}) \quad (4.16)$$

Where $FRET_f$ is the final FRET image, $FRET_i$ is the initial FRET (donor + acceptor) image, and I is the intensity.

For all following experiments, without exception, stocks and samples were kept in light blocking containers or wrapped in foil when not in use, and handled in low-light environments when moving between the two. During imaging experiments, alignment and focusing were performed primarily in bright field, swapping to fluorescence imaging only when absolutely necessary for final adjustments and before imaging. This was done in order to minimise bleaching effects and keep all samples comparative for use in Equation 4.16.

Calibration of DiO/DiI FRET in oil

Excitation/absorbance and emission measurements were taken of DiO and DiI in squalane and triacetin oil, as in Chapter 2.1. Each fluorophore was solubilised at 30 $\mu\text{g/ml}$, then diluted down to 0.015 or 2.1 $\mu\text{g/ml}$ for samples containing one or both fluorophores. Absorbance measurements were performed with a 200-700 nm sweeping excitation laser light source, 480 nm/min, with a 1 nm slit width window, in reference to a control oil only sample. Emission measurements were performed with a 488, 549 or 560 nm excitation laser for DiO in either oil, DiI in triacetin, and DiI in squalane respectively, based on peak absorbance measurements. The receiver performed a 500-700 nm sweep, at 100 nm/min, with a 4 nm window. Control oil only samples were also measured as a reference for background correction of intrinsic oil fluorescence.

Calibration and conformational measurements of DiO and DiI as a FRET pair were performed on the same inverted confocal microscope that would later be used for LOND FRET experiments. Here, three 50 μm deep chambers were filled with squalane oil loaded with 30 mg/ml DiO, DiI, or DiO + DiI, sealed, and turned over so that the glass coverslip was pointing toward to microscope lens. Each sample was excited by a 488 nm source at 10 % power and observed through a x40 lens, with filters of 500-520 and 561-582 nm, at a constant gain of 720 V, constant image dimension, without line averaging, and a pixel dwell time of 1.20 μs . Histograms of the white number of each image were then recorded, defining the image intensity that allowed for their use in Equation 4.16.

Preparation of FRET LONDS

Separate preparations of POPC squalane LONDS were made containing either DiO (donor) or DiI (acceptor) dye at 30 $\mu\text{g/ml}$ or 1 mg/ml.

Emission measurements were performed on the LOND solutions to examine if the fluorophore concentration was high enough to overcome scatter from the presence of

small particles (the LONDS) making the solution turbid. This was done using the fluorometer as explained above with a 488 nm excitation laser, over a range of LOND concentrations, $10^7 - 10^{12}$ LONDS/ml, diluted in PBS. As a control PBS alone was also tested.

When considering the use of these FRET enabled LONDS in further experiments it was important to realise that by mixing the DiO and DiI LONDS at a 1:1 ratio, if their rupture and mixing occurred, then on average both the DiO and DiI would be diluted to half of their original concentration in the newly merged oil. Therefore, when performing all further comparative experiments of DiO only or DiI only LONDS, they were always mixed at a 1:1 ratio with a third batch of prepared POPC squalane LONDS which were non-fluorescent/empty. This meant that to reveal enhanced FRET fluorescence donor LOND + acceptor LOND samples were compared to control donor LOND + non-fluorescent/empty LOND and empty LOND + acceptor LOND samples, changing Equation 4.16 to:

$$FRET_f = FRET_i - (Imax_{Donor+Empty} + Imax_{Empty+Acceptor}) \quad (4.17)$$

FRET at large bubble surfaces

Separate donor, acceptor and non-fluorescent/empty LOND solution stocks were diluted 1:10 in PBS to 10^{12} LONDS/ml then mixed 1:1 to make the sample and two control solutions as explained above of donor + acceptor, donor + empty, and empty + acceptor LOND solutions. Three 50 μ m deep chambers were prepared where the spacers were arranged to prevent the solution from fully filling the chamber, leading to the active capturing of millimetre scale air pockets with near vertical water-air interfaces which fully filled the chamber from the top glass coverslip to the bottom glass slide. The air-water interfaces of the gas pockets were then observed on the confocal microscope, as above in the bulk oil DiO/DiI calibration experiment, with the 488 nm laser at 10 % power, observing through both a x10 and x40 lens, at a constant gain of 800 V. The experimental images were compared as in Equation 4.17 to reveal any FRET signal, which would indicate LOND merging at millimetre-scale air-water interfaces that would appear flat relative to the nanoscale LONDS.

FRET at OLI-MB surfaces

In the following experiment, both squalane POPC and POPC + 5 mol% DSPE-PEG LONDS were tested. OLI-MBs were produced by both the microfluidic (just POPC lipid

shell) and mechanical agitation (both lipid shell types) method. OLI-MB samples were then loaded into BSA coated 50 μm deep glass-viewing chambers. Fluorescence was observed as before on the confocal system with a 40x objective, using the 488 nm excitation laser at 10 % power with a gain of 600 V. The experimental images were compared as in Equation 4.17 to reveal any FRET signal, which would indicate LOND merging at MB air-water interfaces.

Washing OLI-MBs

In order to confirm that the fluorescent regions of interest in the FRET experiments originated from the structure of the above OLI-MBs, rather than being due to something such as reflection, washing of mechanical agitation FRET OLI-MBs was repeated as in section 4.9.6 (p 92).

4.10. Microfluidic FF formation of OLI-MBs from bulk phases

The work in this section revolved around the concept of introducing bulk phases of aqueous lipid solution, oil and gas on-chip in FF regimes, with the intention of forming a gas-oil-lipid/aqueous interface around a gas bulb held at the microfluidic nozzle. This oil layer, with controllable oil layer thickness, would then pinch off with the gas through the nozzle to form OLI-MBs.

All of the experimental work in this section used the inverted microscope described earlier (section 4.1, p 60).

4.10.1. Evaluating oils for the control of the oil layer thickness during on-chip co-flow

The large majority of the work described in this section of the project centred on using the ‘three-phase flow focus microchip’ geometry, described in Chapter 4.2.2 (p 65), where it was necessary for the oil and lipid solution phases to come into contact and co-flow upstream from meeting the gas phase. As such, a number of the available oils that were used in the whole project were tested for their oil layer thickness and the thickness’s uniformity during this co-flow, over a range of flow rate and flow rate ratios between the oil and lipid solution. The aim here was to optimise the system for greater control over the oil layer thickness using a greater range of flow rates.

Using a 3C1 microchip, C_4F_{10} gas was held at a constant pressure of 3 psi (20.7 kPa). Squalane, isoamyl acetate, triacetin or dodecane oil was set to a specified flow rate at 0.5, 0.1, 0.05, or 0.02 $\mu\text{l}/\text{min}$. The lipid solution flow rate was then varied from 6 to 40

$\mu\text{l}/\text{min}$ (up to $100 \mu\text{l}/\text{min}$ for triacetin) with videos being recorded of the co-flow immediately after lipid solution and oil phase introduction. As shown in Figure 4.21, the oil layer thickness was measured over $390 \mu\text{m}$ for every other pixel column down the co-flow channel and at least three videos were taken for each flow rate ratio.

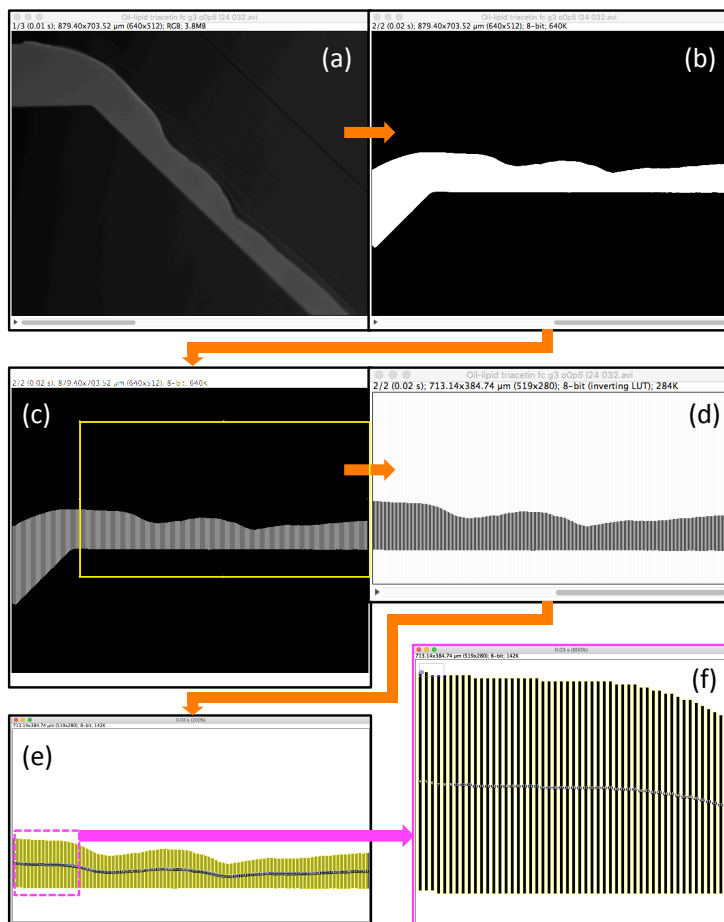


Fig. 4.21. Method used to measure the thickness of oil during the co-flow channel. (a) The fluorescence video is scaled into micrometers against a reference graticule measurement. (b) The stack is rotated to have the co-flow channel horizontal, and is made binary (black and white). (c) Every other pixel column, for each image, is made black. The stack is cropped to the co-flow channel only, (d) and colour inverted. (e-f) Each black shape is measured for the area and the minimum Feret diameter (the shortest edge, one pixel). During further analysis, each measured area is divided by the minimum Feret diameter to give the vertical height, equal to the oil layer thickness.

4.10.2. Evaluating on-chip pinch off mechanics of gas-in-oil and oil-in-aqueous

The methods in this section of the project revolved around the idea of progressing to a system where pinch off of gas was achieved in oil with that oil being simultaneously pinched off in lipid solution, all at one FF nozzle. Therefore, it was necessary to understand the mechanisms under which pinch off occurred in two-phase FF systems

with an equivalent nozzle (to that of the three-phase FF design). Further mapping out the liquid flow rate and gas pressure ranges that achieved pinch off in a two-phase FF system would aid in estimating the velocity ranges for the three-phase FF system.

Using the two-phase FF microfluidic design (described in section 4.2.2, p 63), the continuous phase, of lipid solution or oil, and the discontinuous phase, of oil or C₄F₁₀ gas, were introduced on-chip. Aqueous flow rates tested ranged between 1 and 200 μ l/min. When the oil was being used as the discontinuous phase (with lipid solution) flow rates tested ranged between 0.01 and 30 μ l/min. When the oil was being used as the continuous phase (with the gas) flow rates tested ranged between 2 and 160 μ l/min. Gas pressures tested ranged between 1 and 15 psi. 1 vol% Triton solution and standard lipid solution was tested for use with an aqueous phase. For the oil and gas experiments, no surfactant and 1 vol% Span 80 in the oil phase were tested. Squalane, dodecane, isoamyl acetate, and triacetin oil were all tested.

For both two-phase setups, the lipid solution flow rate or the gas pressure was set to a given value and then the oil phase was varied through a set of flow rates from the point that the discontinuous phase was held as a bulb at the nozzle to where the discontinuous phase flew through the nozzle without pinch off, remaining as a bulk phase. Pinch off was observed using the same apparatus as the three-phase experiments in the previous section.

4.10.3. Three-phase FF trials

This section of the work includes the experimental trials that were performed with the aim to produce OLI-MBs using three-phase FF microfluidics.

The microfluidic designs that were used here were 5C1, 3C1, 3C2 and 3C3 as described in section 4.2.2 (p 65). Microchips in early experiments began with PMMA-SU8-PMMA channel walls that were natively hydrophobic, however this was quickly changed to microchips that were treated to make the channel walls hydrophilic. Hydrophilic treatment was performed by Epigem before delivery and use.

Primarily, 1 mg/ml standard lipid solution was flown through the aqueous inlet, which was changed to 1 vol% Triton in MilliQ, or 4 mg/ml BSA solution for a small number of experiments where specified. C₄F₁₀ gas was flown through the gas inlet. Triacetin, squalane, isoamyl acetate, dodecane or soybean oil was flown through the oil inlet. When specified, 1 mg/ml DPPC + 5 mol% DSPE-PEG lipid was added to the oil phase. Lipid was added to the oil as in the standard lipid solution, where it was dried in a glass

vial from a chloroform/methanol solution, then the oil was added and the vial was bath sonicated to redisperse the lipid.

Pluronic F-68, with a stock of 10 vol% in deionised water, was added to both the lipid solution and oil phases at a variety of final concentrations; 0 and 0 vol%, 10 and 0 vol%, 10 and 2 vol%, and 2 and 2 vol% respectively. For addition to aqueous phases, the required volume of pluronic simply replaced that volume of MilliQ, BB or PBS when it was added. For addition to oil phases, the pluronic was gently evaporated under nitrogen to remove all of the water, before it was redispersed in the oil. Pluronic polymers are triblock copolymers of [polyethylene oxide]_a-[polypropylene oxide]_b-[polyethylene oxide]_a, where *a* and *b* are commonly 2-130 and 15-67 units respectively. The naming describes the structure. For the pluronic naming, the initial letter defines the substance as liquid (L), paste (P) or solid/flake (F) at room temperature (not dissolved in water). The first number x300 gives the approximate molecular weight of the polypropylene oxide core block. The final number x10 gives the approximate percentage of the entire polymer that is polyethylene oxide. Pluronics have seen regular use in pharmaceuticals as emulsion stabilisers and for the solubilisation of hydrophobic drugs,²³⁵ and were used by Shih and Lee (2013) when they formed oil layer inclusive MBs through a FF system.⁹⁵

The full flow rate and pressure ranges recorded were 6 - 190 µl/min, 0.02 - 4 µl/min, and 0.8 - 25 psi for the lipid solution, oil and gas phases respectively. The lipid solution flow rates had three distinctive flow ranges, with the oil phase flow rate and gas pressure matching to allow the phases to be at a balance between not moving through the nozzle and flowing too greatly through it. Lower lipid solution flow rates around 6 µl/min were tested to reduce flow velocities, which has previously been shown to inhibit coalescence of MBs during on-chip production.³¹

Most of the experiments carried out in this section used fluorescence to distinguish the oil phase and lipid in the lipid solution. Nile red was added to the oil phase and imaged through either the FITC or TexRed filters dependent on the oil used. Oregon green was added to the lipid solution at 1 mol% of the entire lipid concentration and imaged through the FITC filter.

Most data in this section of the work was collected using videos of the three phases flowing through the nozzle. Videos were captured under fluorescence and bright field, primarily using a x10 lens with an internal x1.5 modifier, and using high frame rate imaging in bright field only at 50 kfps, with the same magnification but without the internal modifier.

4.11. Activation of double emulsion liquid perfluorocarbon (PFC)-in-oil-in-aqueous droplets into OLI-MBs

In this section of the work, the potential to form highly stable, long-lived liquid PFC droplets, both with and without oil shells, and further phase change them into gas PFC MBs was evaluated. If a PFC droplet with a surrounding oil shell was successfully activated into a stable MB, this would potentially produce the desired OLI-MB structure.

4.11.1. Single emulsion PFC droplet production

Single emulsion PFC droplet were stabilised in an aqueous continuous phase via the three methods described below. Surfactants tested were 0.5 mg/ml DPPC and 1 vol% Triton (or 10 vol% only when stated), both in PBS. Only when stated, isoamyl acetate, squalane, triacetin, or dodecane oil was used as the continuous phase with no surfactant, 1 vol% Span 80, or 1 vol% Triton. All droplet solutions were measured for size or concentration as in section 4.7 (p 78-82).

Two-phase microfluidics

Microfluidic PFC droplet formation was used to give a microdroplet sample, with high monodispersity and repeatability. Here, two-phase FF microchips (described in section 4.2.2, p 63) were used. Triton solution was pumped through the microchip at 1 – 40 $\mu\text{l}/\text{min}$, with optimal production at 3 $\mu\text{l}/\text{min}$. C_5F_{12} , C_6F_{14} , or a 60:40 volume mix of both, was pumped through the microchip at 0.5 – 10 $\mu\text{l}/\text{min}$, with optimal production at 1 $\mu\text{l}/\text{min}$. The droplet solution was collected in a 1.75 μl glass vial or eppendorf, and stored at 4 °C for up to one week. Concentration and size measurements were performed over a one-month period to assess stability.

Tip sonication

PFC droplet formation by tip sonication was used to give a nanodroplet sample, with high concentration and repeatability. In a falcon tube, a 4 ml solution was made up of 2.5, 5 or 25 $\mu\text{l}/\text{ml}$ C_5F_{12} or C_6F_{14} in Triton or DPPC solution. 5 $\mu\text{l}/\text{ml}$ was the routine concentration. The solution was vortexed for 30 s, then transferred to a 4 °C cooled jacketed crucible, for tip sonication, making sure to retain all of the dense PFC with the solution. Tip sonication (Sonifier S-250A, Branson Ultrasonics, UK) then proceeded at 200 W, 20% power, 100% duty cycle, for 5 min. The sample was collected and stored at 4 °C for use during up to one month. If stated, this solution was further extruded

through a 400 nm filter. Concentration and size measurements were performed over 5 h and the following day to assess stability.

Mechanical agitation

PFC droplets were made by mechanical agitation to give a high concentration, high polydispersity, fast production sample. A 1.75 µl glass vial was filled with 99 vol% aqueous or oil and 1 vol% C₅F₁₂ or C₆F₁₄. If lipid were to be used, it was dried on to the glass vial before it was filled with solution. This method then followed that for mechanical agitation MB formation, as detailed in section 4.4 (p 71). After agitation, the vial was allowed to cool (often the vial, prepared at or below room temperature, was warm to the touch immediately after agitation) and then the lid was slowly removed for access to the droplets. This last step was done to inhibit droplets from prematurely activating into MBs due to the undesired apparent increase in temperature in combination with the pressure drop during the opening of the vial. The sample was used immediately.

4.11.2. Double emulsion PFC droplet production

Microfluidic, homogenisation, and mechanical agitation methods for the formation of PFC droplets, with surrounding oil layers, stabilised in aqueous (a.k.a. double emulsion PFC droplets) were trialled as detailed below. However, it was found that only the mechanical agitation method produced a double emulsion sample, and so for any further studies that was the method used. Nile red was added to the oil phase in all of the below experiments for fluorescent distinction from the outside aqueous and inside PFC phases. Droplet solutions were measured for size and concentration as in section 4.7 (p 78-82). Figure 4.22 shows how the ratio of PFC core to oil layer was measured for a double emulsion sample. For each droplet, the radius of the central PFC core and the radius of the total double emulsion droplet were measured and compared, resulting in a PFC core divided by total droplet radius ratio. For a sample with multiple droplets, an average was calculated from the ratios (rather than averaging the radiuses of the PFC cores and total droplets first).

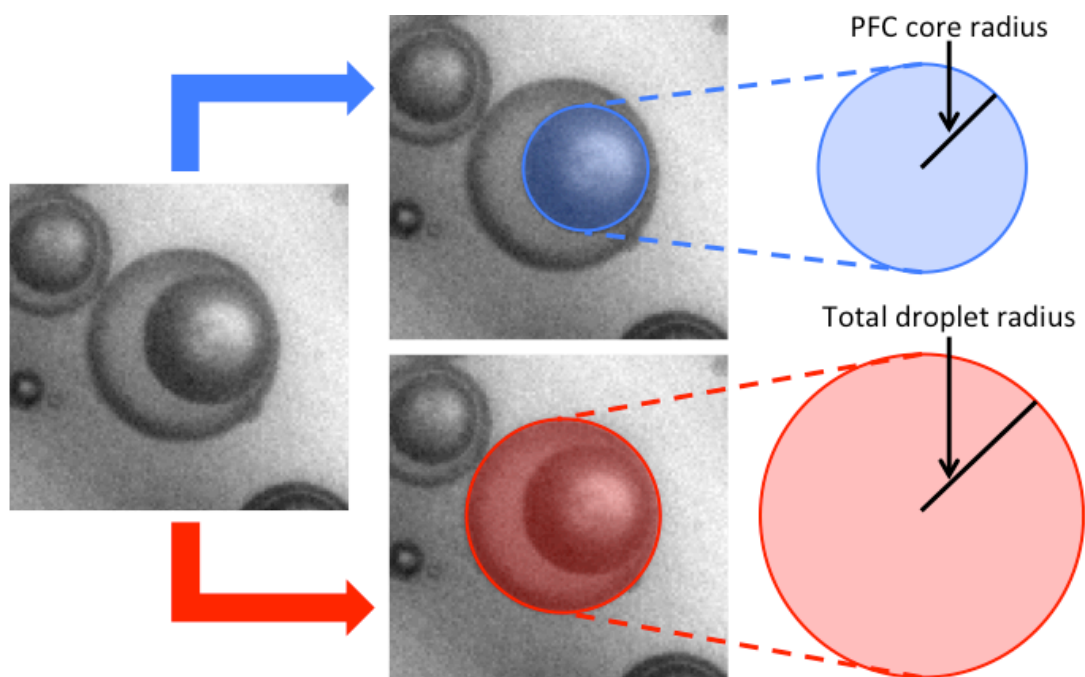


Fig. 4.22. Method used to compare the PFC and oil contributions of a PFC-oil double emulsion droplet. The area of the PFC core (blue) and total droplet (red) were measured. These measurements were then calculated into radii and compared to obtain a core to total droplet radius ratio

Microfluidic method

Two solutions were prepared for use in two-phase FF microfluidics (described in Chapter 4.2.2.). The continuous phase was 1 vol% Triton in PBS, and was pumped in at 0.05 - 0.5 $\mu\text{l}/\text{min}$. The discontinuous phase consisted of PFC droplets stabilised in oil, made using the mechanical agitation single emulsion PFC droplet method described in the previous section. Here, the oil used was dodecane and the surfactants tested were 1 vol% Triton and 1 vol% Span 80 in the oil phase. The discontinuous phase was pumped in at 0.7 – 10 $\mu\text{l}/\text{min}$. Nile red in the oil phase allowed for imaging of on-chip pinch off as well as analysis of PFC core pinch-off efficiency.

Homogenisation

Tip sonication was performed on a three phase PFC, oil, aqueous solution under the same method as that for tip sonication of single emulsion PFC droplets as described in the previous section. The solution was 0.5 vol% C_5F_{12} and 0.5 vol% soybean oil in 6 mg/ml BSA in PBS solution. Control samples without the oil and without the BSA solution, increasing the oil to 99.5 vol%, were also tested.

Coarse homogenisation of 0.5 vol% C₅F₁₂ and 0.5 vol% triacetin in 6 mg/ml BSA in PBS solution was performed on the Polytron system used for LOND production (section 4.9.1, p 84-85), for 30 s – 5 min.

Mechanical agitation

A 1.75 µl glass vial was filled with 1 ml of 0.5 vol% C₅F₁₂, 0.5 vol% oil, in 6 mg/ml BSA in PBS. Soybean, isoamyl acetate, triacetin, dodecane, and squalane oil were all tested, with the oil being soybean if not specified in the remainder of this thesis. This method then followed that for mechanical agitation MB formation, as detailed in section 4.4 (p 71). After agitation, the vial was allowed to cool (often the vial, prepared at or below room temperature, was warm to the touch immediately after agitation) and then the lid was slowly removed for access to the droplets. This last step was done to inhibit droplets from prematurely activating into MBs due to the undesired apparent increase in temperature in combination with the pressure drop during the opening of the vial. The sample was used immediately.

In order to assess control over the diameter, concentration and oil layer thickness of the double emulsion droplets, the volume of oil and concentration of BSA were tested at 0, 0.5, 1 and 2 vol% and 0, 2, 4 and 8 mg/ml respectively, whilst keeping the PFC volume constant at 1 vol%. This was also compared to initial experiments that used 10 vol% PFC, 10 vol% soybean oil, and 6 mg/ml BSA.

4.11.3. Activation of single and double emulsion liquid PFC droplets

4.11.3.1. Thermal activation methods

Thermal activation of both single and double emulsion liquid PFC droplets was tested both on macroscale, observing the entire solution by eye for volume change or an increase in turbidity, indicative of larger particles (MBs) appearing in the solution, and on microscale, observing single or a small number (≤ 30) of droplets for direct activation into gas. The general method here aimed to raise the PFC solution temperature to the point that the droplets' were in a hotter environment than their boiling point.

Heating plate

1 ml of PFC microdroplet solution in a 1.75 ml glass vial was placed on a heater plate. The temperature at the centre of the solution was monitored. The temperature was increased from 25 °C to 68 °C, and then allowed to cool back down. The solution was observed by eye, with camera photographs being taken, for a change in turbidity or a clear sign of boiling of the PFC droplets, which had quickly sank to the bottom of the vial before the thermal ramp began.

This method was only used on 60 vol% C₅F₁₂ + 40 vol% C₆F₁₄ Triton PFC microdroplets that had been produced microfluidically. As such, bulk C₆F₁₄ and Triton were separately tested for their boiling points in 5 ml volumetric flasks using the above method with a stirring flea. Bulk C₅F₁₂ could not be tested in this manner since, even though the boiling point is 29 °C, the liquid begins to vapourise at room temperature, and due to material use.

Peltier heating in a chamber

As shown in Figure 4.23, observations were made of single PFC droplets under thermal ramping by injection of either a nano- or microdroplet PFC solution into a 50 µm deep viewing chamber, a PMMA-SU8-PMMA microfluidic chip or a PDMS flow cell, and the use of a Peltier heater. The chamber or chip was mounted onto the inverted microscope described in previous sections, but with the microscope stage changed to an in-house built plastic stage, for thermal insulation from the microscope, with a thin top copper plate, for thermal conduction, with a lens viewing port. The Peltier and the chamber or chip were then placed in close proximity on the copper plate, using thermal coupling gel (340, Dow Corning, USA), with the latter being placed over the viewing port. The temperature of the top surface of the chamber or chip was monitored with a thermocouple, using more thermal coupling gel, which led back to the Peltier controller. The static droplet solution temperature was ramped from 25 °C to 80 °C whilst droplet observations were made.

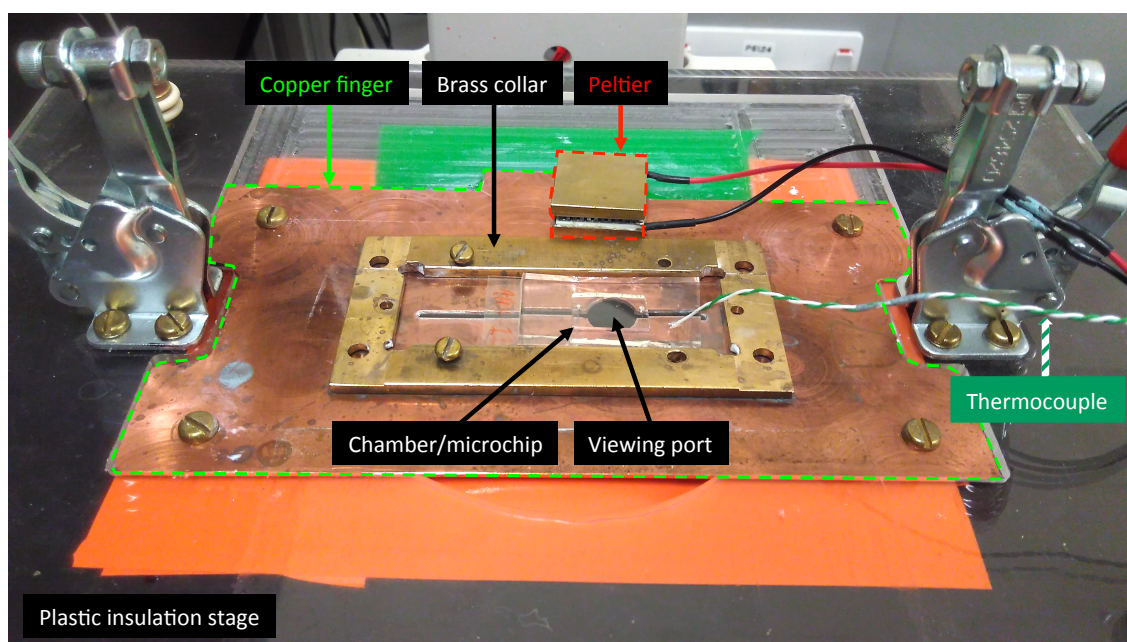


Fig. 4.23. Set-up for thermal control of microchip/chamber during imaging by the upright microscope. Chamber is the device from Figure 4.8.

DLS temperature ramp

PFC nanodroplets were measured for diameter change by DLS during heating of the solution. Here, if droplets activated into MBs, any nanoscale particle measurements were expected to become less significant due to a rising microscale particle measurement or the sample gaining turbidity. The method used for DLS measurement was as described in section 4.7 (p 78-79), however instead of measuring at a constant 25 °C, the temperature was ramped from 20 – 70 °C, with three measurements occurring every 10 °C. In order to prevent sample evaporation, a lid, provided with the DLS specifically for heating use, was loosely fitted onto the cuvette.

4.11.3.2. Hypobaric activation and on-chip pressure drop

Pressure drop activation of both single and double emulsion liquid PFC droplets was tested with a hypobaric activation method and an on-chip pressure drop. Generally observations were made before and after activation for the first method and during the second method.

Hypobaric activation

A hypobaric activation method for transitioning PFC droplets into MBs was first discussed by Forsberg et al. (1998).²³⁶ A syringe was filled to ~10 % of its full volume with PFC solution. The plunger was then fully retracted, creating a pressure drop inside

the syringe, held for a few seconds, then released. It was understood that the pressure drop activates the PFC droplets into MBs, then a shock wave, produced from the release of the plunger, propagates through the liquid breaking apart any larger MBs, leaving only MBs of diagnostic relevance ($< 10\ \mu\text{m}$). The shock wave is heard as an audible ‘pop’.

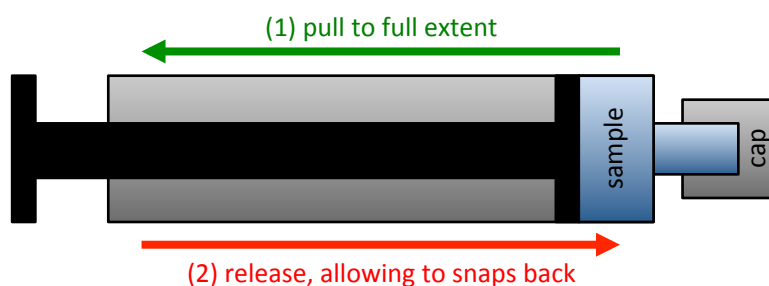


Fig. 4.24. Schematic of hypobaric activation apparatus. Capped syringe containing solution to be activated at $\sim 10\%$ of the full syringe volume.

As shown in Figure 4.24, a 5 ml syringe was filled with $500\ \mu\text{l}$ of PFC solution. The end of the syringe was then capped whilst preventing any gas pockets. The plunger was drawn back to its full extent with one smooth, rapid motion, held for $\sim 1\ \text{s}$, then immediately released. The audible ‘pop’ was heard during every experiment otherwise the method was repeated with new PFC solution. The activated solution was then transferred to a vial for samples to be taken for imaging. Immediately after gentle agitation, samples were taken from the bottom and middle of the vial and placed in $50\ \mu\text{m}$ chambers, imaging for remaining PFC droplets and MBs respectively (as described in section 4.7, p 82). For direct comparison, samples were taken from the solution and imaged in the same manner before activation. Experiments were performed at ambient temperature.

Single emulsion $1\ \text{vol}\%$ Triton droplets were activated using this technique. Triton solution has the ability to stabilise gasses previously solubilised in the aqueous continuous phase until being put under the stress of low pressure, in a similar way to cavitation. Control hypobaric activation experiments were performed on MilliQ and dilutions of $1\ \text{vol}\%$ Triton. It was found no MBs were stabilised in either MilliQ or Triton solution at $0.001\ \text{vol}\%$. Therefore, before activation of any Triton PFC droplets, the droplets were evenly disperse in a falcon tube and then allowed to settle ($\leq 1\ \text{min}$), the supernatant was removed, then the tube was refilled with MilliQ. This was repeated until the continuous phase was diluted 1000x.

Hypobaric activation on C₅F₁₂ nanodroplets was also tested at elevated temperature to examine if having the PFC fluid above its bulk boiling point (29 °C) would increase activation efficiency. Here, 1 ml of C₅F₁₂ Triton nanodroplets, diluted of excess Triton, were heated to 32 °C in a heating block and allowed to remain there for 10 min. Meanwhile, the syringe for hypobaric activation was filled with 32 °C MilliQ in order to prevent cooling of the PFC solution on contact. The PFC solution was then transferred to the syringe and the method continued as described above.

In order to observe single droplets during hypobaric activation, a PMMA-SU8-PMMA microfluidic chip was mounted onto the inverted microscope with the manifold in place, as described in section 4.2.3, p 69-70. The chip was filled with PFC solution before all of the channels were sealed, with a 5 ml syringe connected to one entrance. Hypobaric activation then occurred as above with the droplets being observed by high frame rate microscopy, at 5 – 50 kfps.

On-chip pressure drop under flow

Correas et al. (1997) discussed a technique for activation of C₅F₁₂ nanodroplets (~300 nm diameter), by passing them through a 1.2 µm filter, inducing a pressure drop.^{236,237} In an attempt to observe this mechanism and assess it under a more controlled regime, C₅F₁₂ Triton nanodroplet and microdroplet solutions were passed through the discontinuous phase inlet of a two-phase FF microchip and a spray MB microchip, both with nozzles of ~7 µm. Further 1 vol% Triton solution was passed through the continuous phase inlet. The droplet solution was observed before, at and immediately after the nozzle. Flow rates tested were 5 – 200 µl/min for the PFC solution, and 0 – 200 µl/min for the Triton solution. These experiments were performed at ambient temperature. C₅F₁₂ Triton nanodroplet solution was also tested at 29 °C, using the Peltier set up in the previous section. In a more direct comparison to Correas's work, C₅F₁₂ Triton nanodroplet solution was flown through a 0.4 µm filter by hand via a 1 ml syringe. All of the C₅F₁₂ Triton nanodroplet solution work presented in this section was compared by measuring the diameter and concentration of nanodroplets in solution prior to the experiment, and directly after flow stopped, using the qNano described in section 4.7 (p 80).

4.11.3.3. US activation methods

US activation of both single and double emulsion liquid PFC droplets was tested in the kHz and MHz regions for non-localised and localised activation respectively. Observations were made before and after activation for the first method and during the second method. The general method here aimed to lower the PFC solution pressure to the point that the droplets' were in a lower pressure environment than their vapour pressure. During ultrasonification of a fluid the forward half of a wave compresses the fluid, causing an increase in pressure, which would pass through any incompressible PFC droplets, however the tail half of a wave expands the fluid, leading to the desired pressure drop, causing the droplets to activate into MBs.

45 kHz US

Following the work by Rapoport *et al.* (2009), where low frequency (90 kHz) US was used for PFC droplet activation,¹⁴³ 45 kHz US was supplied to a PFC solution by an ultrasonication bath (USC200T, VWR, USA). Here, 1 ml of PFC solution was diluted to 10 ml, with its continuous phase, in a ~1.5 cm diameter falcon tube. After gentle agitation, a sample was taken from the middle of the solution and imaged in a 50 μ m chamber for size and concentration (section 4.7, p 82). If PFC microdroplets were being used, they were imaged at the bottom of the chamber and allowed to settle in the tube (\leq 5 min) before continuing. The lower ~2 cm of the tube was then submerged into an US bath, emitting a 45 kHz, continuous wave, for 10 s. Again after gentle agitation, a sample was taken and imaged as before, looking at the top of the chamber for MBs. Samples were measured at ambient temperature and at 37 °C by placing the falcon tube in a heating block before use. PFC Triton nanodroplets were additionally observed over 60 s of US exposure, removing samples at 5 s exposure and then, starting from 10 s, at 10 s intervals. As a control for both single emulsion PFC Triton droplets and double emulsion PFC-oil-BSA droplets, a 1 vol% triton, 6 mg/ml BSA mixed solution was sonified and imaged with the same method. Only one MB was observed, suggesting that cavitation of the continuous phases alone did not lead to MB stabilisation from the gases solubilised in the solution.

1.1 and 3.5 MHz US

US in the MHz region was supplied locally to a region of PFC droplets.

For 1.1 MHz US; a high intensity focused US transducer with a centre frequency of 1.1 MHz was submerged in a degassed distilled water bath, at 34 °C, and directed vertically

down. Attached to the base of the water bath, and at the transducer's focal length, was a flow cell with a 0.17 mm plastic lid and base (Ibidi) where inlet and outlet lines travelled up and out of the water bath. Below the flow cell was a 60x lens, focused at the flow cell. PFC solution was then injected into the flow cell, after which flow stopped. Images were taken of the PFC droplets prior to US exposure. The droplets were then exposed to ≤ 1 s of US at 1.1 MHz, 12 ms peak repetition frequency (prf), at 1%, 20%, and 100% duty cycle (DC), where the peak negative pressure at the focal point was set to 0.5 or 3.5 MPa. Images were again taken after US exposure. Triton solution without PFC droplets was tested up to 20% DC, with no MBs observed.

(Figure 4.25) For 3.5 MHz US; a transducer (V380 NDT, Olympus Panametrics, Japan) with a centre frequency of 3.5 MHz was attached to a fitted plastic collar, which was 2 mm short of the acoustic focal depth (6.35 cm), and filled with degassed distilled water. The collar base was covered with acoustically transparent material (12.5 μ m thick cling film), and the transducer directed downwards. A 50 μ m chamber, spray microchip, PMMA-SU8-PMMA flow cell, or glass-PDMS-glass flow cell were filled with PFC solution, then placed on the inverted microscope detailed in previous sections. The collar base was brought into contact with the PFC filled device, using acoustic gel (Polaris II, GE medical systems, UK) for transparency. Acoustic gel was spun down in a centrifuge (Megafuge 16R, Thermo Scientific, USA) before use to remove any MBs. The droplets were then exposed to ~ 1 s of US at 3.5 MHz, 12 ms prf at 0.02% DC, 1 ms prf at 1 or 10% DC, or continuous wave. Drive voltages were 400-550 mVpp, which related to a focal point negative pressure of 0.92-1.04 MPa. High frame rate imaging was used at 5 – 50 kfps to capture videos of droplets during US exposure. The Peltier set up was used, as described in section 4.11.3.1 (p 104-105), to keep the PFC droplet chamber at ~ 40 °C.

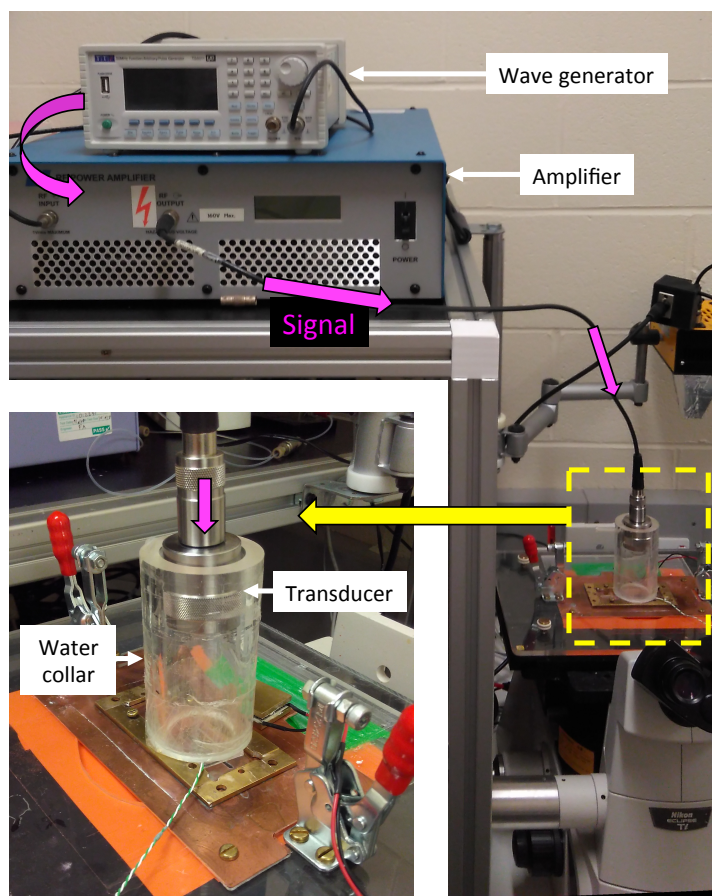


Fig. 4.25. Set-up used for US exposure to a MB/droplet sample using the heating stage from Figure 4.23.

Acoustic cluster therapy (ACT), first presented by Sontum et al. (2015), where a MB and a PFC droplet of opposite charge are allowed to form a two part cluster, has previously been shown to dramatically lower the negative US pressure required to activate the PFC droplets into MBs.²³⁸ As such, a similar method was used with the 3.5 MHz US as described above. Here, mechanical agitation DPPC + 10 mol% DPPA MBs, and mechanical agitation DPPC + 10 mol% DOTAP C₅F₁₂ microdroplets were made, both in a MilliQ-lipid suspension. The MBs were diluted 100 times, then the two solutions were mixed 1:1. The mixed solution was gently agitated before being injected into the desired chamber for US exposure. Zeta potentials were taken of both solutions on the DLS described in section 4.7 (p 78-79).

4.12. MB echogenicity

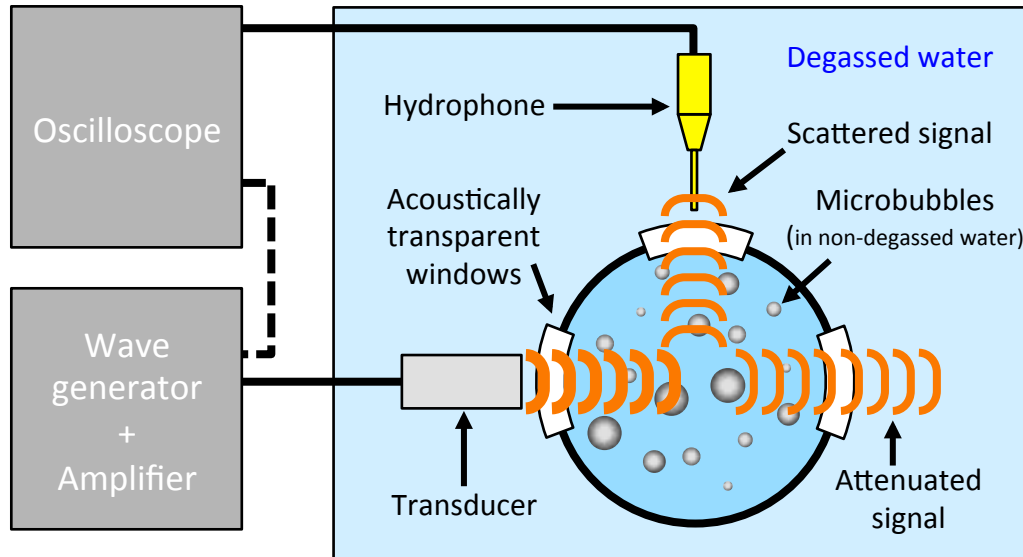


Fig. 4.26. Schematic of setup for measuring US scatter signal from a MB population. The attenuated signal (parallel to the transmitted signal) is also shown, but is not recorded in this setup.

US scatter measurements were used to determine the resonant frequency of MB samples. Figure 4.26 shows a schematic of the setup that was used for this. An in-house water tank was prepared with an open topped 30 mm diameter, cylindrical acrylic chamber placed in the middle (~100 or 10 ml). The tank was filled with degassed, 20 °C de-ionised water, while the chamber was filled with non-degassed de-ionised water and a magnetic stirrer. The chamber included three 20 mm diameter, circular, acoustically transparent (12.5 μm thick cling film) windows, each 90° apart, half way up the chamber wall. An unfocused, 3.5 MHz central frequency US transducer was placed millimetres from the chamber wall, facing through one of the windows. A 1.0 mm needle hydrophone (Precision Acoustics, UK) was placed 90° to this, again facing through one of the windows.

The MB sample was added to the chamber from the top, to give a concentration of 10^5 MBs/ml in the chamber. 20 seconds passed to allow the bubbles to disperse themselves. A custom-built US array research platform was then used with US excitation waveforms designed in MatLab (Mathwork, USA), and the setup as described in section 4.8 (p 83), to drive the transducer. The transducer was driven across a range of 0.5 – 5 MHz frequencies, at a peak negative pressure of ~ 0.5 MPa. The signal scattered by the MB sample was then measured by the hydrophone. These results were processed and averaged using MatLab, outputting US scatter intensity across transducer frequency. Typically during these experiment, a MB sample with a stock concentration of at least 10^8 MBs/ml was desired. This would allow small volumes of the stock MB solution to

be added to the 100 ml chamber, and a single measurement to be acquired at one defined frequency. The chamber would then be emptied, refilled, and MBs added again for measurement at the next frequency. This allowed for at least 10 separate measurements, including repeats. During this thesis project, OLI-MB samples were only ever collected at low concentrations and volumes (10^6 OLI-MBs/ml, 1 ml total). Therefore during OLI-MB measurements, the 10 ml chamber was used, and immediately the entire stock OLI-MB solution was added and then measured over a frequency sweep with a larger number of frequency steps.

5. Results: Surface Energy of an OLI-MB

The three results chapters that follow this one cover three separate approaches that were explored with the primary aim of producing OLI-MBs to a medically relevant size and concentration, with a high degree of control and repeatability. However, the possibility for each route to even begin to produce OLI-MBs that were stable enough to be useful hinged on one very crucial question; *'Is an OLI-MB structure energetically favourable?'* This chapter addresses that question first by presenting surface pressure data collected at the air-water interface of the lipids used for the formation of OLI-MB shells. This included using the Langmuir method to determine the surface collapse pressure, and techniques to obtain the surface pressure and surface concentration at the characteristic "Equilibrium Spreading Pressure" (ESP). Contact angle experiments were also performed of several oils at air-lipid/MilliQ surfaces, with the lipid concentration informed by the experiments described above. Results from both of these experiments made it possible to calculate the total surface energy of an OLI-MB structure, and compare it to other possible conformations of the gas, oil, lipid and aqueous phases. This permitted for an estimation of whether the OLI-MB structure was theoretically thermodynamically stable or whether it should phase separate over time to result in other structures.

5.1. Pressure-area Isotherms and the Equilibrium Spreading

Pressure of lipids at the air-water interface

The studies in this section were concerned with characterising the lipid monolayers that were used during this thesis, towards the formation of OLI-MBs, for the surface pressures they provided at an air-water surface when fully compressed and when allowed to spread to equilibrium, ESP.

Pressure-area isotherms of DPPC, DPPC-PEG, and POPC lipid were performed on a Langmuir trough system (as discussed in the Experimental Chapter 4.5.1, p 74). Lipid was spread from a 1 mg/ml chloroform solution and three compression/expansion cycles were performed at 5-10 mm/min. The first cycle was ignored (due to the lipid interactions needing to equilibrate before a reliable measurement can be obtained), with the second and third being used for analysis providing their surface pressure relationships were equivalent. Figure 5.1 presents compression cycles for a DPPC monolayer over a range of speeds. ≤ 20 mm/min the differences in results were

negligible. Figure 5.2a presents the pressure-area isotherms for monolayers of stearic acid, DPPC, DPPC-PEG, and POPC. The compression cycle of stearic acid is well known with well defined characteristics, so was used as a reference to confirm that the protocols for set-up, cleaning, and use were being sufficiently carried out. The area per molecule was measured by tracking a straight line down to 0 mN/m from the ‘solid’ phase expansion of the lipid, and was found to be 21, 53, 67 and 66 Å²/molecule for stearic acid, DPPC, DPPC-PEG, and POPC respectively. Literature values for stearic acid, DPPC and POPC were found to be 22 ± 2 (SD 3),^{239–241} 52 ± 2 (SD 3),^{242–245} and 87 ± 8 (SD 17)^{242,246–250} Å²/molecule respectively. Apart from POPC, which was experimentally found to repeatedly have the same area per molecule, and in literature was found to have a wide spread of values, as given by the standard deviation of the values recorded, the experimental results were in good agreement with literature.

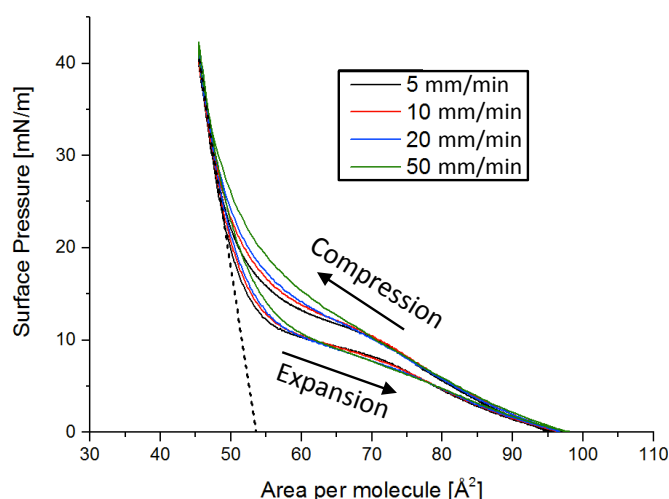


Fig. 5.1. Pressure-area isotherms of DPPC measured over a variety of barrier compression and expansion speeds, showing the average result between the second and third compression-expansion cycle.

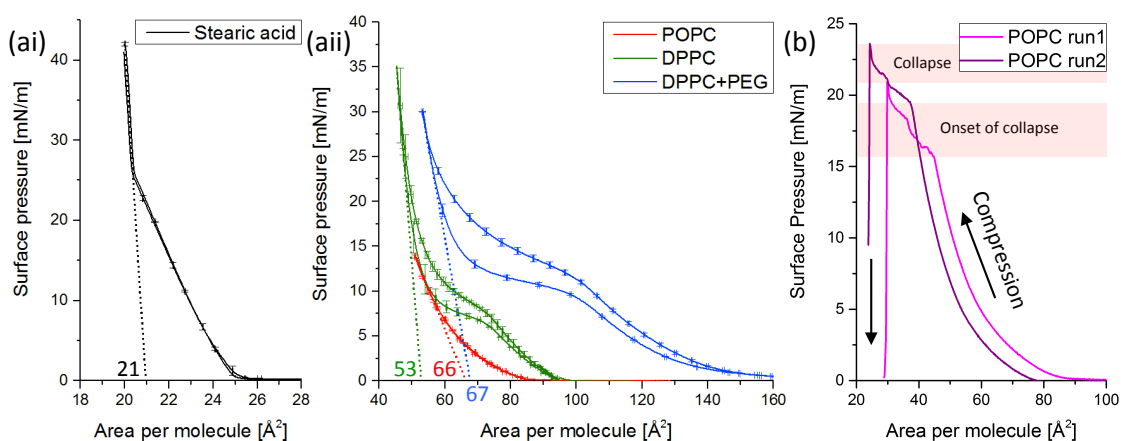


Fig. 5.2. Pressure-area isotherms for (ai) stearic acid and phospholipids (aii) DPPC, DPPC-PEG, and POPC, with measured area per molecule (dotted lines). (b) Pressure-area isotherm of POPC where the lipid monolayer was compressed until the barrier reached collapse, barrier speed 5 mm/min.

Figure 5.2b shows the pressure-area relationship of a POPC monolayer where barrier compression continued past the point of the monolayer collapse. It was observed that the sharp decrease in surface pressure, which indicated monolayer collapse, was accompanied by a collapse of the air-MilliQ meniscus, in the Langmuir trough's Teflon dish, over the Teflon walls. Performing this type of compression allowed the determination of the maximum surface pressure that the lipid monolayer could withstand. This was important in the wider context of this thesis when MBs shrink due to gas diffusion, leading to a loss of surface area and subsequently concentrating their lipid monolayer shell. Early experimental work (as shown in Figure 5.2b) found the onset of collapse to occur at 18 ± 2 (SD 3) mN/m, with the highest achievable surface pressure before collapse to be 22 ± 1 (SD 2) mN/m. However, later work (at higher compression rates of 10 mN/m) found that surface pressures of 38 mN/m could be achieved before the onset of collapse. Literature values for the collapse pressure of POPC lipid have been recorded on average as 46.5 ± 0.5 mN/m.^{246,249–251} The lower collapse pressures seen in these results, compared to literature, could have been due to differences in the compression speed and any additives to the subphase. Since the values recorded experimentally for the POPC monolayer collapse were so varied, the literature value was used going forward with this project. The maximum surface pressure attained before collapse for both DPPC and DPPC-PEG was repeatedly recorded around 40 mN/m, with a spread of ~ 5 mN/m. Literature values for the collapse pressure of DPPC have been recorded as 55 ± 1 mN/m.^{242,245} However, since the experimental value was repeatable, it was used in further calculations.

After the pressure-area traces and the collapse pressures had been acquired, the next step was to measure the ESP of the same lipid monolayers. Whereas the collapse pressure defines the maximum surface pressure that a lipid monolayer can withstand before collapse, the ESP defines the surface pressure attained when lipid monolayer molecules have equilibrated at a surface, only being driven by the surface tension, which will drive the further accumulation of lipid molecules, and their interaction with each other, which will inhibit further accumulation after a certain concentration.

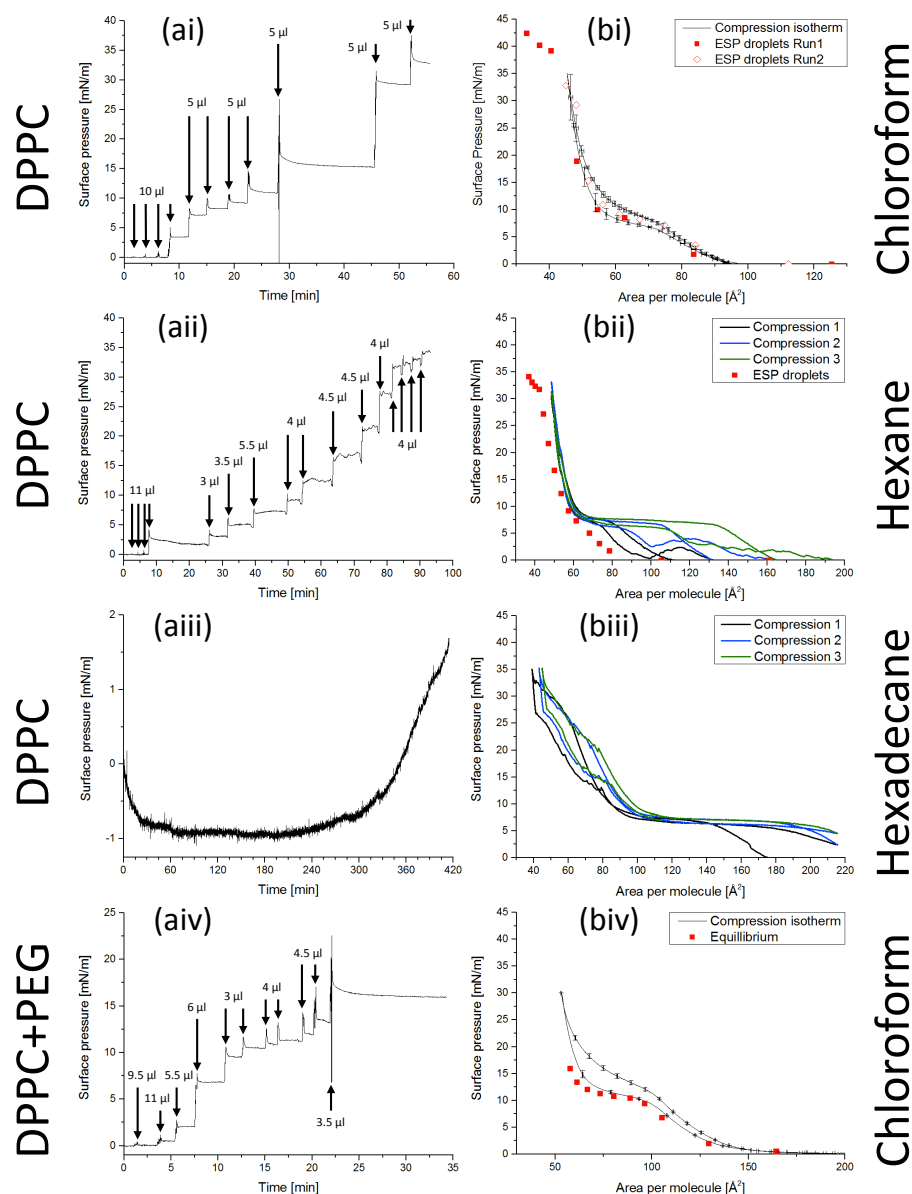


Fig. 5.3. Equilibrium spreading pressure experiments where lipid was added drop-wise to the air-MilliQ surface. Surface pressure over time as droplets of (ai-iii) DPPC or (aiv) DPPC-PEG in (i and iv) chloroform, (ii) hexane or (iii) hexadecane were added to a air-MilliQ surface, allowing time for the surface pressure to plateau. Defined volumes of lipid solution were added at time points as shown. Solution concentration was 1 mg/ml lipid. (bi-iv) The calculated (red dots) area per lipid molecule at each plateau regions is shown on the surface pressure-area isotherms performed on the same lipid.

ESP experiments were undertaken by setting the Langmuir trough area to be constant, then adding lipid to the surface drop-wise from a chloroform, hexane, or hexadecane solution, and recording the surface pressure as the number of lipid molecules on the surface increased (Experimental Chapter 4.5.2, p 74-75). After each droplet was deposited, the solvent was allowed to evaporate. As the lipid approached the ESP it should have reached equilibrium between spreading on the air-MilliQ interface and

remaining solubilised in the droplet solution, leaving a solid lipid crystal after solvent evaporation. Solvents with different spreading behaviours were tested. Hexane has a low spreading coefficient and higher boiling point (longer evaporation time) relative to chloroform. Whilst Hexadecane has a negative spreading coefficient, meaning that any spreading would be purely from the lipid escaping the droplet (lens) formed at the air-water interface. Figure 5.3a shows how the surface pressure changed with additions of lipid solution droplets and Figure 5.3b shows the relationship between the average area per lipid molecule and the surface pressure during these experiments compared to typical pressure-area isotherms of the same lipid formed during compression-expansion cycles. The results indicated that the relationship between the surface pressure and the molecular area of the lipid monolayers followed the general shape of pressure-area isotherms all the way to collapse. This showed that the lipids spread beyond the ESP and instead of forming a lipid deposit, they simply continued spreading up to the collapse pressure as the solvent evaporated. These observations did confirm that the previous measurements of molecular area were carried out correctly.

A further ESP technique was introduced by Bois and Albon (1985) (Experimental Chapter 4.5.3, p 75).²¹⁸ Here, they suggested that it is not possible to measure the ESP of DPPC from lipid crystals placed on the air-MilliQ surface below its lipid phase transition. They also found that the surface pressure recorded would be different dependant on whether the lipid monolayer had been taken through its ordered to fluid phase-transition temperature prior to the measurement.²¹⁸ However, they introduced a new technique of depositing a highly concentrated lipid-chloroform solution onto a clean platinum plate, waiting for solvent to evaporate, and then passing this plate with lipid deposit through a clean air-water surface. As the plate was slowly passed through the interface the surface pressure was found to steadily increase over time, followed by a decrease in this rate until, after ~50 min, a plateau of ~9 mN/m was reached.²¹⁸ At this point an equilibrium had been reached between lipid molecules transferring onto the air-water interface and back onto the plate, with excess lipid passing into the water subphase or staying as a deposit on the plate. In these experiments, a similar technique was used, where a cleaned glass plate with lipid deposits was introduced to the aqueous phase (term as being 'dipped') and was retracted. This was repeated for multiple plates as shown in Figure 5.4 which shows how the surface pressure changed during dipping of the lipid deposits, with each dip being shown as a spike and following stabilisation in surface pressure. It was concluded that ESP had been reached when the surface pressure before and after multiple dips centred

around a single surface pressure value. After the surface pressure at ESP had been found, a typical pressure-area isotherm was performed on the ESP monolayer in respect to the total trough area. This was done to acquire the lipid per surface area concentration at ESP by comparing the trough area when the monolayer was in its ‘solid’ phase, to the known area per molecule from previous pressure-area isotherms. The surface pressure and lipid concentration at ESP were expected to intersect with previous pressure-area isotherms of the same lipid. This would aid in understanding the morphology of the monolayer at ESP. Intersections like this were found to occur for stearic acid and one of the two repeats for both DPPC and DPPC-PEG monolayers. Table 5.1 presents the results found including the surface pressure, lipid concentration, and monolayer morphology at ESP. For DPPC the surface pressure at ESP was found to be negligibly different over two separate runs, however the concentration at ESP was significantly different (57.2 and 71.1 Å), whereas for DPPC-PEG the lipid concentration at ESP was found to be negligibly different over two separate runs with the surface pressure being recorded as significantly different (7.0 and 10.1 mN/m). The more reliable value, recorded in Table 5.1, was determined by noting the alignment of the ESP surface pressure and concentration intersection with the pressure-area isotherms for the same lipid. A combination of the data from the DPPC and DPPC-PEG monolayers (which only differed by 5 mol% of lipid) suggests that the ESP for DPPC and DPPC-PEG occurred at the transition from the liquid expanded to liquid condensed phases, but that, due to the inconsistencies between recordings, the technique used might not always lead to a uniform monolayer.

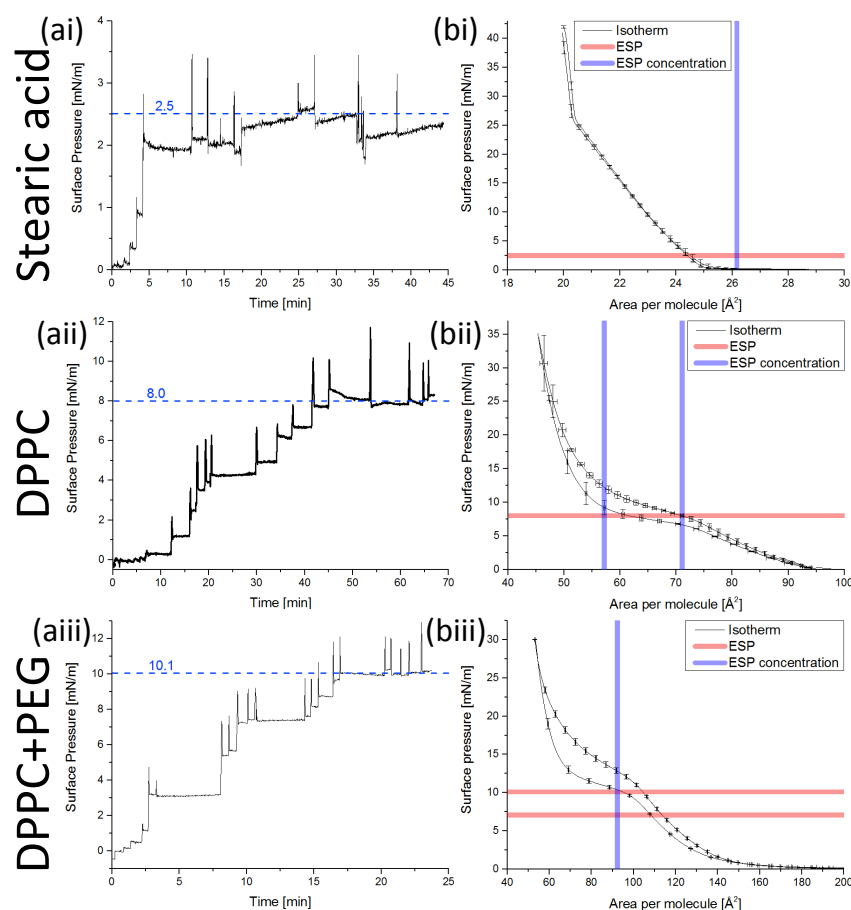


Fig. 5.4. EPS experiments where lipid was added to air-MilliQ surfaces from concentrated deposits on glass. (a) Surface pressure over time as glass plates coated with (i) stearic acid, (ii) DPPC, or (iii) DPPC-PEG were ‘dipped’ through air-MilliQ interfaces and then removed, observed as spikes in the surface pressure. (Blue dotted line) The ESP found is shown. (bi-iii) The (red line) surface pressure at ESP and (blue line) lipid concentration at ESP overlaid onto pressure-area isotherms of each lipid.

Tab. 5.1. Results from the EPS experiments where lipid was added to the air-MilliQ surface from concentrated deposits on glass.

Lipid	ESP [mN/m]	ESP concentration [mg/m ²]	ESP area per molecule [Å ²]	Monolayer morphology
Stearic acid	2.5	1.8	26.2	Gaseous-Liquid transition
DPPC	8.0 ± 0.1	1.7	71.1	Liquid expanded-compressed transition
DPPC+PEG	10.1	1.5 ± 0.02	92.3 ± 1	Liquid expanded-compressed transition

A mg/m² concentration is noted at ESP in Table 5.1. This determines the lipid content that would be expected on a gas-water MB surface on formation – before concentration due to shrinkage.

5.2. Surface Energy of oil, air, MilliQ/lipid structures

This section outlines studies of the contact angle of oil droplets to air-lipid/water surfaces, at the collapse and ESP pressures as determined by the results of the previous

section, in order to measure the oil-lipid/water surface tension and further calculate and compare the surface energies of gas, oil, and lipid/water constructs (Experimental Chapter 4.6, p 76-78). A lipid monolayer was formed on an air-MilliQ meniscus, in a Teflon dish, at either the ESP or close to the collapse pressure. The former could be achieved by the ESP concentrations as determined in the previous section, and the latter by adding enough lipid until just before the meniscus collapsed onto the Teflon dish walls. Using a contact angle system, oil (of the types that in Chapter 6.1 were used for LOND formation) was delivered on to the monolayer, from the air side, to simulate an air-oil-lipid/MilliQ interface without the need to consider the oil's entering coefficient, E_R (see Theory 3.3.1, p 50-51). Contact angle measurements were performed on the oil, thereby allowing calculations of the oil-lipid/MilliQ interfacial tension.

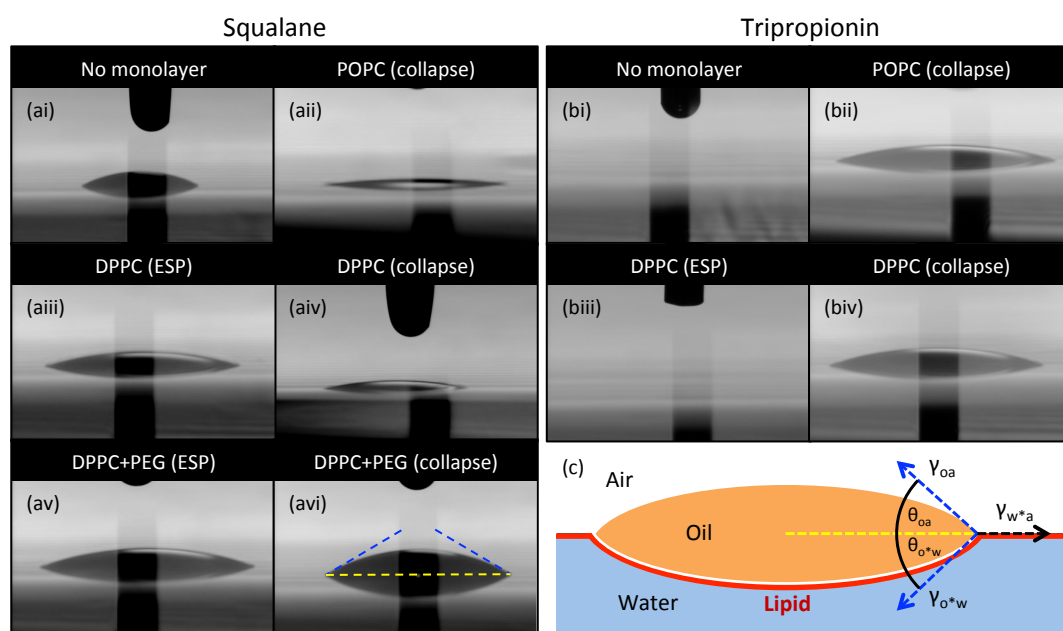


Fig. 5.5. Contact angle images of (ai-vi) squalane and (bi-iv) tripropionin oil on air-lipid/MilliQ interfaces, introduced from the air side. The lipid monolayer type and surface pressure conformations (collapse or ESP) are given. (c) A schematic is given (this is a repeat of Figure 4.14), which should be compared to image *avi*, to show how contact angles were measured.

Tab. 5.2. Average contact angles recorded from the experiments depicted in Figure 4.13 of squalane and tripropionin oils on air-lipid/MilliQ interfaces, introduced from the air side.

Monolayer type (surface pressure)	Contact angle [°]	
	Squalane	Tripropionin
No monolayer	25.0 ± 0.4	0.0
POPC (collapse)	5.9 ± 0.3	14.5 ± 0.3
DPPC (ESP)	16.9 ± 0.9	0.0
DPPC (collapse)	13.8 ± 0.7	20.6 ± 0.4
DPPC+PEG (ESP)	20.8 ± 1.4	
DPPC+PEG (collapse)	28.4 ± 0.6	

Figure 4.13 shows example images for squalane and tripropionin oils at the air-lipid/MilliQ interfaces, and Table 5.2 shows the resulting average contact angles. For all oil/lipid conditions, the average difference between contact angle measurement of the left and right side of the droplets was 1.1° , which was considered negligible. Assuming that all of the lipids remained in contact with the MilliQ interface (the only hydrophilic phase for the hydrophilic side of the lipid amphiphiles to contact to), it was expected that as the concentration of lipid in the monolayer was increased, more hydrophobic tails would be presented to the air and oil phases, causing the oil to spread further, decreasing the contact angle. While this was true for squalane oil on DPPC and POPC monolayers, DPPC-PEG monolayers gave a lower contact angle at ESP, but followed it with an even greater contact angle at collapse. The hydrophilic PEG chain will have protruded directly into the MilliQ phase, so not contact the oil. Therefore this result was surprising since the only difference between the DPPC and DPPC-PEG monolayers in the monolayer portion itself was 5 mol% of DSPE. DPPC and DSPE lipid tail only differ by the addition of two C-C bonds to each of the two tails. Tripropionin on the other hand appeared to form a lens when the monolayers were highly concentrated at collapse and spread when the monolayers were at ESP or on the clean MilliQ surface. Tripropionin is a polar oil and is soluble in water at 3.07 mg/ml, at 37°C .⁹⁶ What might have been observed here is that the E_R for tripropionin across the monolayer and into the MilliQ being achieved. A more accurate way to have performed this experiment would have been to pre-saturate the MilliQ with tripropionin oil.

Table 5.3 gives the acquired surface tensions for the air-lipid/MilliQ and air-oil interfaces as well as the calculated interfacial tension for the oil-lipid/MilliQ interfaces for both squalane and tripropionin oils. It also gives the calculated spreading coefficients, S , of the oil between the air and lipid/MilliQ phases. The surface and interfacial tensions are also presented in Figure 5.6.

Tab. 5.3. Surface and interfacial tensions for air, squalane and tripropionin oils, and lipid/MilliQ phases in different combination, calculated using the contact angles shown in Table 5.2, and the spreading coefficient for the oils between the air and lipid/MilliQ phases (S_{woA}). Surface tensions of air-lipid/water surfaces calculated from surface pressure values given in section 5.1, Table 5.1 and references (246,249-251).

Monolayer type (surface pressure)	Surface tension (air- lipid/water) [mN/m]	Squalane			Tripropionin		
		Surface tension (air-oil) [mN/m]	Interfacial tension (oil- lipid/water) [mN/m]	Spreading coefficient [mN/m]	Surface tension (air-oil) [mN/m]	Interfacial tension (oil- lipid/water) [mN/m]	Spreading coefficient [mN/m]
No monolayer	72.8	28.0 ± 3.0	52.3 ± 5.7	-7.5	35.9 ± 3.0	36.9 ± 3.0	≥ 0.0
POPC (collapse)	26.3 ± 0.5	28.0 ± 3.0	-1.6 ± 3.1	-0.1	35.9 ± 3.0	-8.7 ± 2.9	-0.9
DPPC (ESP)	64.8 ± 0.2	28.0 ± 3.0	39.7 ± 8.2	-2.9	35.9 ± 3.0	28.9 ± 3.0	≥ 0.0
DPPC (collapse)	32.8	28.0 ± 3.0	5.8 ± 5.4	-1.0	35.9 ± 3.0	-0.85 ± 2.8	-2.2
DPPC+PEG (ESP)	64.2 ± 2.1	28.0 ± 3.0	40.7 ± 14.5	-4.5			
DPPC+PEG (collapse)	32.8	28.0 ± 3.0	9.3 ± 8.2	-4.5			

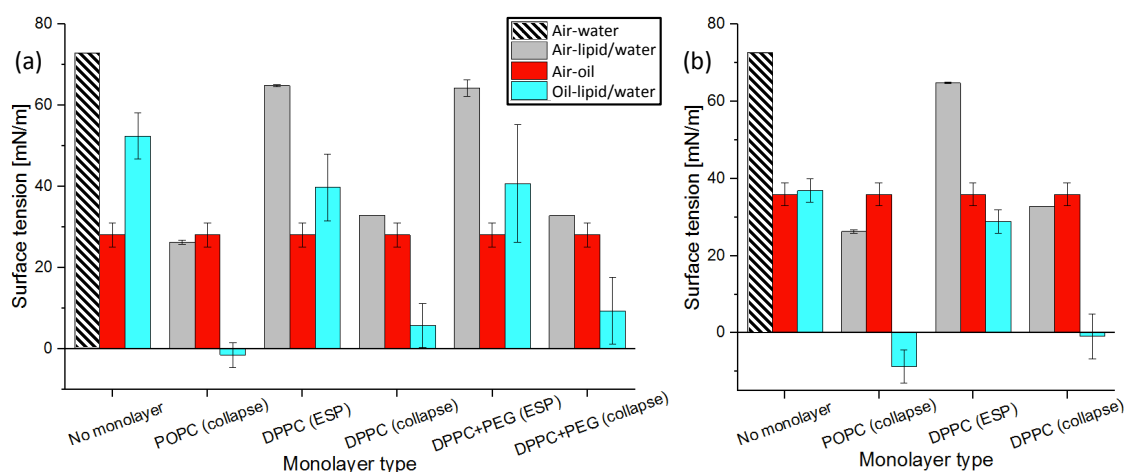


Fig. 5.6. Surface and interfacial tensions for the different interfaces, and (a) squalane or (b) tripropionin oil, using defined lipid monolayers.

The spreading coefficient for squalane oil between the air and water phases (S_{AOW}) was less than zero for all air, oil, water systems. This indicated that squalane oil (O) was expected to either partially spread or not spread at all between the air (A) and MilliQ (W) phases. However, S_{AWO} and S_{WAO} (not shown) were calculated to be even more negative. This indicated that it would be even less energetically favourable for MilliQ to spread between oil and air and for air to spread between oil and MilliQ. This all suggests that whilst it would be unlikely for an OLI-MB to form spontaneously, after formation a squalane OLI-MB would be expected to remain stable. However, it should be noted that this also means that any other surface stabilised between two of the three phases would also be expected to remain stable, for example separate non-oil-MBs and oil droplets.

Tripropionin oil on the other hand showed that $S_{WOA} \geq 0$ at low monolayer concentration and that $S_{OWA} > 0$ at high monolayer concentration. The other S possibilities were found to be negative. This suggested that the oil was expected to spread between the air and MilliQ, allowing for the formation of an OLI-MB.

For both squalane and tripropionin, negative interfacial tensions were calculated at high monolayer concentrations. This may suggest that a portion of both oils were solubilising into the MilliQ phase. As expected, for both oils, the more concentrated the lipid the lower the surface tension of all interfaces except for the oil-air interface which was assumed to be free of lipids and therefore constant.

Using the interfacial tensions presented in Table 5.3, it was possible to calculate the total surface energy for an OLI-MB, over a range of oil layer thicknesses, based on the surface area present from each interface. The OLI-MB total surface energy was compared to that of other possible configurations of the oil, lipid, air, and water, at equal volumes of each fluid phase between the different conformations. This was done in order to calculate the most energetically favourable structure for given volumes of each phase and with a given lipid monolayer type. Figure 5.7 shows how the total surface energies compared for a 2 μm OLI-MB, over a range of oil layer thicknesses (presented as an oil volume% of the constant total OLI-MB volume), a separate oil droplet and non-oil-MB, and an inverted OLI-MB of oil-in-air-in-water, with schematics of each configuration. The configurations are compared for squalane and tripropionin oils, over all of the monolayer types tested, and at equal oil and gas volumes between the configurations. Figure 5.8 shows how these values compared for each conformation equivalent to an OLI-MB with a 50 nm thick oil layer. Formation of OLI-MBs with this range of diameter and oil layer thickness was one of the goals of this thesis project.

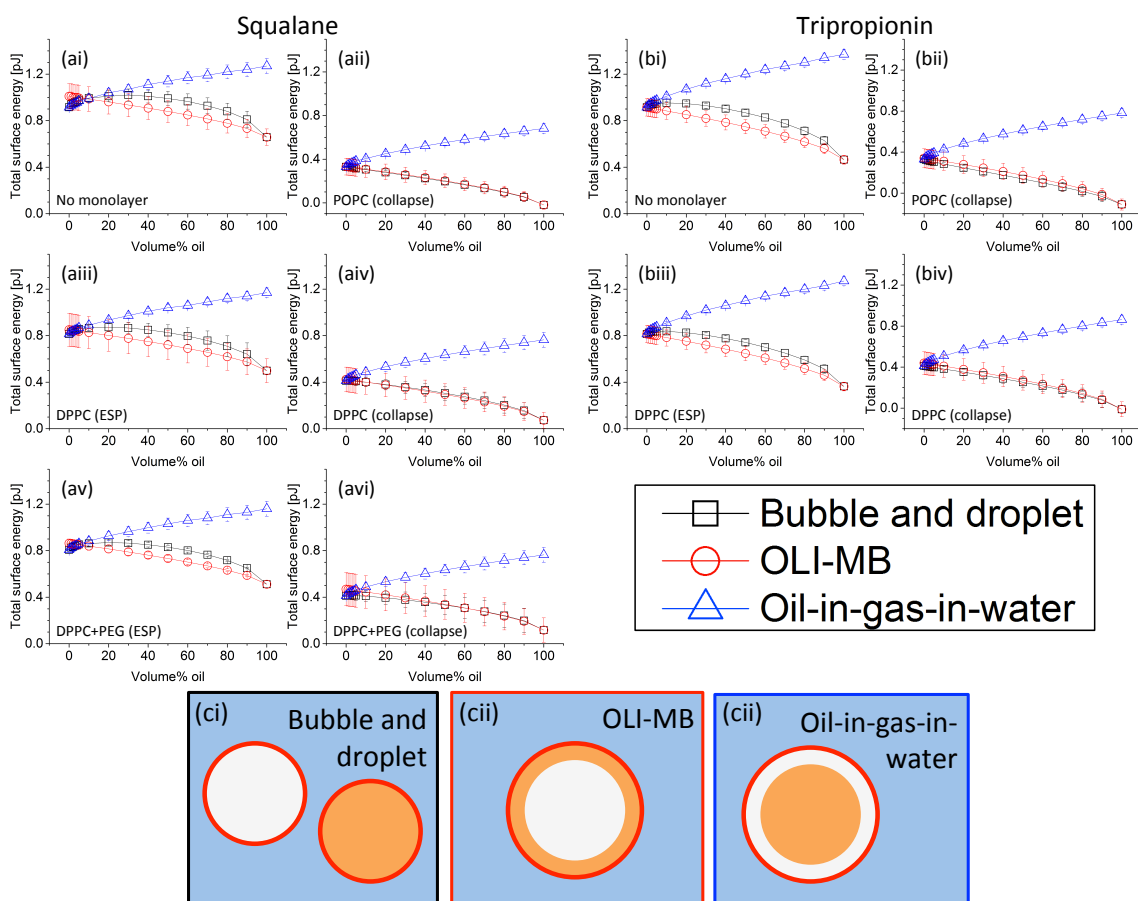


Fig. 5.7. Total surface energy (red) of a 2 μm OLI-MB over a range of oil layer thickness (defined as oil vol% of the total OLI-MB volume), using (ai-vi) squalane or (bi-iv) tripropionin oil, (i) without a shell or with a lipid monolayer of (ii) POPC, (iii and iv) DPPC, or (v and vi) DPPC-PEG, at (ii, iv, and vi) the collapse pressure or (iii and v) ESP. Comparative total surface energies of other possible configurations of air, oil, lipid, and water are given as (black) a separate non-oil-MB and oil droplet, and (blue) an oil-in-air-in-water structure, for equal volumes of the oil and gas phases. Schematics are given of the (ci) non-oil-MB and oil droplet, (cii) OLI-MB, and (ciii) oil-in-air-in-water configurations.

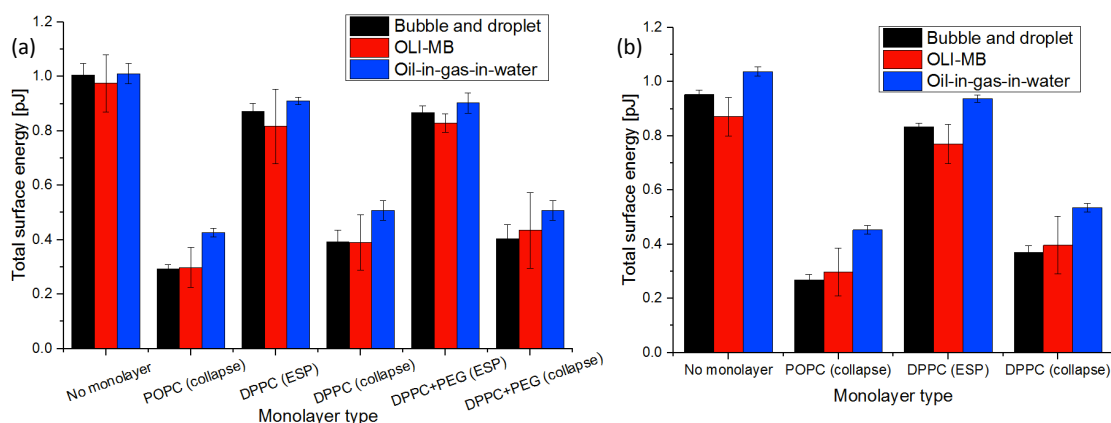


Fig. 5.8. Total surface energy of (red) a 2 μm OLI-MB with a (a) squalane or (b) tripropionin oil layer thickness of 50 nm, for a range of lipid monolayer types. Comparative total surface energies of other possible conformation of air, oil, lipid, and water are given as (black) a separate non-oil-MB and droplet, and (blue) an oil-in-air-in-water structure.

In general, Figure 5.7 shows that an oil-in-air-in-water structure (Figures 5.7ciii) is not energetically favourable for any of the monolayer types considered, with the energy difference compared to the other conformations being greater at higher oil content. Figure 5.8 shows that this energy difference becomes far smaller when considering the small oil content that would be present in an OLI-MB with a 50 nm thick oil layer. Whilst even at this low oil content, the oil-in-air-in-water conformation was still the least energetically favourable state, this could suggest that structures resembling MBs with small core oil droplets could be formed and remain stable, potentially even changing over time to MBs with a small oil lense. Meanwhile, the OLI-MB (Figures 5.7cii) and separate non-oil-MB and oil droplet (Figures 5.7ci) conformations have very similar energies, with the OLI-MB being more favourable without lipid or when the monolayer is at ESP, and the separate non-oil-MB and droplet being more favourable at when the lipid monolayer is compressed up to the collapse pressure. At low oil content (<15 vol%) the energy of all three conformations converge, and at very low oil content (<5 vol%) Figure 5.7 would suggest that the OLI-MB can become the least energetically favourable structure. However the equations used here (see Experimental 4.6, Equation 4.11) defines two interfaces for both the OLI-MB and air-in-oil-in-water structures even at the extremes of 0 or 100 vol% oil, where the oil or gas component respectively should be considered infinitely small. In the oil vol% extremes, this gives these two structures an equivalent surface area twice, and since $\gamma_{A-L/W} \neq \gamma_{A-O} + \gamma_{O-L/W}$ and $\neq \gamma_{O-A} + \gamma_{A-L/W}$ the total surface energies calculated will be incorrect at these vol% extremes. In reality, if the oil content was 0 vol%, all three configurations would result in a single non-oil-MB, so would have identical total surface energy. The same can be said at 100 vol% oil, with all configurations resulting in a single oil droplet.

During introduction of the gas, oil, and water/lipid phases, the gas-oil and gas-water interfaces would be expected to either be bare of lipids, due to the lipids requiring time to self-assemble at the interfaces from the water phase, or contain a monolayer of lipids up to the ESP concentration. Over this monolayer range, the OLI-MB configuration was seen to be the most energetically favourable structure. As such, on introduction of the phases, the OLI-MB configuration would be the most likely and stable structure to be formed. However, as the recorded energies for the three configurations were all within the same range, and in most cases within error of one another, the results also suggests that the other two configurations could be formed along with OLI-MBs if production was not controlled.

Over time, lipid monolayer non-oil-MBs are observed to shrink, due to gas diffusion, until a point at which the rate of shrinking suddenly slows. It is thought that this is due to the lipid shell compressing up to the collapse pressure.¹⁸⁰ Any OLI-MBs successfully formed were expected to go through a similar process. Figure 5.9 shows a schematic of an OLI-MB immediately after formation, followed by this shrinkage and monolayer concentration. It also shows a potential scenario under which the gas core and oil portion could phase separate. As an OLI-MB shrinks and the monolayer is compressed, the above results suggest that the structure could either remain stable or phase separate into a separate oil droplet and non-oil-MB.

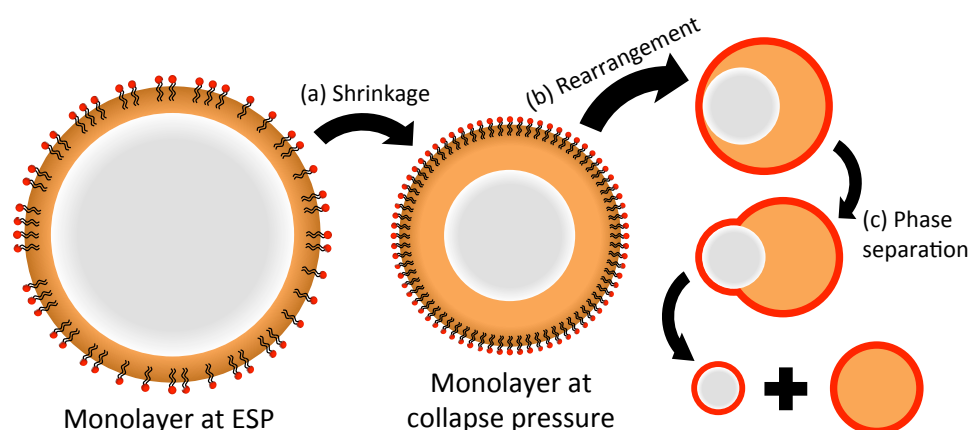


Fig. 5.9. Schematic of an OLI-MB immediately after formation with an oil-lipid/water monolayer at ESP, followed by (a) gas core shrinkage and concentration of the monolayer to the collapse pressure. This is then followed by a potential scenario for separation of the (grey) gas core and (orange) oil portion, whereby (b) the gas core rearranges to the OLI-MB wall, then (c) ejects itself from the oil droplet, acquiring part of the (red) lipid monolayer. The gas would be required to shrink further to accommodate for the increase in total surface area per lipid molecule.

5.3. Mechanical agitation of gas, oil and lipid solution

In respect to the findings in this chapter, it was expected that if gas, oil, and lipid solution phases were mixed chaotically, without control over how the phases were introduced to one another, separate non-oil-MBs, oil droplets, and OLI-MBs would all be formed. This hypothesis was tested using mechanical agitation in a similar technique to that used to typically form mechanically agitated non-oil-MBs (see Experimental Chapter 4.4, p 75). These are typically 1-5 μm , with a small portion $>8 \mu\text{m}$.^{43,211–216} 1 ml of 1 mg/ml DPPC-PEG lipid solution was prepared in a 1.75 ml glass vial, either 5 or 50 μl of squalane oil, loaded with Nile red for fluorescent identification, was added to this. C_4F_{10} gas was bubbled through the solution and allowed to fill the vial headspace. The vial was then mechanically agitated for 45 s. A $\sim 50 \mu\text{l}$ sample of the resulting solution was pipetted, from the middle of the solution, onto a clean glass

slide. Since water was the densest phase in the solution, the sample's curved meniscus allowed for concentration of any structures that had been formed into the centre and top of the sample. Figure 5.10 shows examples of the resulting structures seen in the sample.

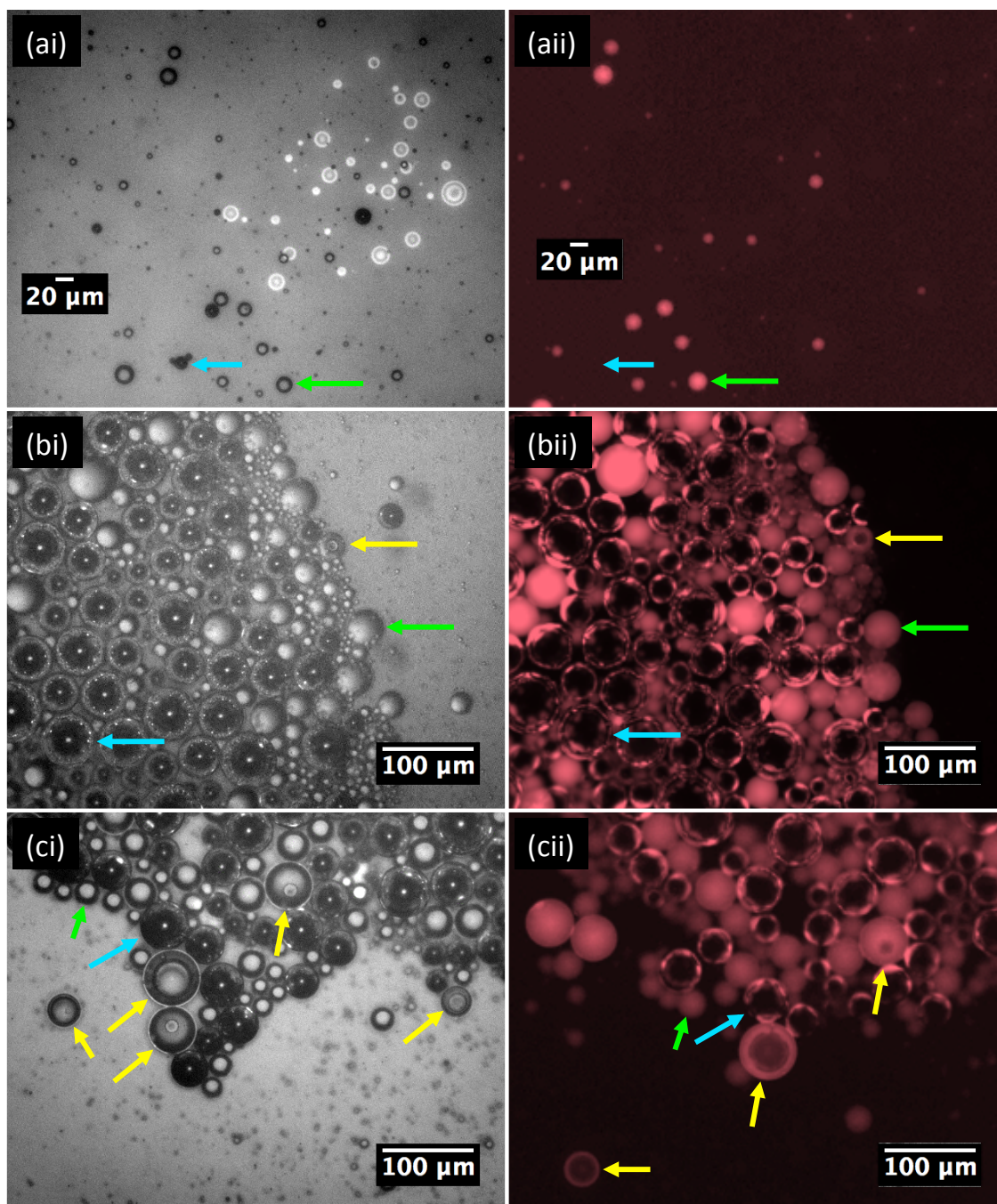


Fig. 5.10. Observations of the structures formed from the mechanical agitation of C_4F_{10} gas and (a) 5 μ l or (b and c - different samples) 50 μ l squalane oil, in 1 ml of 1 mg/ml DPPC-PEG lipid solution. Sample pipetted onto glass to concentrate buoyant particle via sample meniscus. (i) Brightfield and (ii) fluorescence of Nile red solubilised in the squalane is shown, imaged from the same focal area. Example significant structures are labeled; (yellow arrow) non-fluorescent gas cores surrounded by fluorescent oil rings, believed to be larger ($> 8 \mu$ m) versions of the OLI-MB structure, (green arrow) fully fluorescent oil droplets, and (blue arrow) non-fluorescent non-oil-MBs, often showing reflection of fluorescence from neighbouring structures.

The images in Figure 5.10 were taken of selective areas where OLI-MB like structures were found, after concentrating the sample by use of the sample's meniscus. As such any OLI-MBs would be at a higher concentration than representative of the bulk sample. Even so, from a qualitative perspective, for the 50 μl squalane samples (Figures 5.10b-c), OLI-MBs were very sparse, and were vastly outnumbered by non-oil-MBs and oil droplets. The OLI-MBs that were formed were all larger than medically useful ($> 8 \mu\text{m}$), at 30-70 μm , with high polydispersity and no uniformity in oil layer thickness between OLI-MBs. Dropping the oil content to the 5 μl squalane samples (Figure 5.10a) showed no OLI-MB structures, leaving only non-oil-MBs and oil droplets of 10-20 μm . All samples included a high concentration of 1-5 μm structures, however observation with a x60 lens showed that these were either fully fluorescent or held no fluorescence, indicating pure oil droplets or pure non-oil-MBs respectively.

These results agreed with the calculated total surface energy results, which suggested that any self-assembly of the phases from an uncontrolled mixing, like with mechanical agitation, would result in a very mixed sample of OLI-MBs, non-oil-MBs and oil droplets. Though OLI-MBs were observed at even lower concentration than was expected.

5.4. Conclusion

This chapter dealt with the issue of whether the formation of the OLI-MB structure would be energetically favourable. It addressed OLI-MB formation and stability.

Spreading coefficient calculations suggested that the probability for the spontaneous formation of squalane OLI-MBs would be low, but emphasised further that no matter the lipid monolayer concentration, after formation, OLI-MBs would be very stable. On the other hand spreading coefficient calculations for tripropionin oil suggested that OLI-MBs would spontaneously form when the lipid monolayer was at a low coverage. However, upon lipid concentration increasing, for example from the MB core shrinking due to diffusion, the oil and gas components could spontaneously separate. Surface energy calculations for both oils showed that the energetic favourability of OLI-MBs was similar to that of separate oil droplets and non-oil-MBs, meaning that both configurations would be expected to form spontaneously. At low lipid coverage, the OLI-MB structure showed more energetic favourability, whilst at high lipid coverage, the separate oil droplet and non-oil-MBs showed more energetic favourability. This led to the expectation for the formation of OLI-MBs, but with the potential for phase

separation after surface stabilisation. Due to being less energetically favourable than the other configurations, oil-in-gas-in-MilliQ structures were not expected to be produced spontaneously or be stable.

Chaotic mechanical agitation of the gas, oil, and lipid/water phases confirmed what the energetic calculations had suggested. Many oil droplets and non-oil-MBs were observed, whilst few OLI-MBs had been stabilised. Further, little control was shown over size or oil layer thickness between OLI-MBs.

Together, the spreading coefficient and surface energy calculations, and mechanical agitation results all appear to direct to one particular conclusion. That the formation of OLI-MBs would be possible, and that they could be stable after formation, but that only with direct control over how the phases were allowed to meet could a sample be produced at a high concentration, with control over the average OLI-MB size, uniformity of the oil layer thickness between OLI-MBs, and a lack of pure oil droplets and non-oil-MBs.

The three results chapters that follow all looked at this issue of gaining control over OLI-MB formation in different ways: (Chapter 6, p 130-179) Compartmentalising the oil phase into lipid stabilised oil nanodroplets in order to control the amount of oil meeting the gas surface and the position of the lipids. (Chapters 6 and 7, p 130-204) Microfluidics to reduce chaotic turbulence and push the system into controlled laminar flow between each phase as they were introduced to one another. (Chapter 8, p 205-244) Forming defined double emulsion OLI-MB precursors that could be activated from liquid PFC-in-oil structures, in to gas PFC-in-oil structures.

6. Results: Lipid Oil Nanodroplet (LOND) adsorption and spreading to form a thin oil film

In chapter 5 it was established that, due to energetic favourability, the ability to form the OLI-MB structure would be expected, but that its production would require high levels of control over how the phases were introduced (see Chapter 5.4). This chapter addresses that finding first by compartmentalising the oil phase into nanodroplets stabilised with a lipid monolayer shell, giving lipid oil nanodroplets (LONDS). Assembly of LONDS brought defined volumes of oil to the gas surfaces thereby limiting the oil layer thickness of OLI-MBs. For the formation of the thin oil film, the LONDS were required to rupture and spread from the stable nanodroplet emulsion. Due to the LOND's stability against self-coalescence without the presence of a gas surface, this prevented the eventual OLI-MB samples from the inclusion of large oil droplets.

Results in this chapter relate to LOND characterisation (size, concentration, and lifetime), their interaction with functionalised glass surfaces. Using a Langmuir-Blodgett trough (LB) system and Quartz Crystal Microbalance with Dissipation monitoring (QCM-D), interactions between model MB surfaces and LONDS were monitored through changes to the surface pressure and changes to the crystal's oscillations respectively. The thickness of the oil layer that would be provided by LONDS rupturing at the water-gas interface was then estimated from the QCM-D results. MBs were then formed from LOND solutions, both off- and on-chip, and fluorescence and Fluorescence Resonance Energy Transfer (FRET) assessments were made on the presence of oil portions at the MB surface, if the LONDS had remained stable at the surface or formed an oil shell, and the stability of the formed OLI-MBs. OLI-MB formation via microfluidics provided further control over how the phases were introduced to each other, allowing the formation of OLI-MBs to occur within clinically relevant sizes and size distributions. Finally, the OLI-MBs were put through initial tests of their ultrasound (US) properties.

6.1. Size, concentration and lifetime of LONDS

The protocol used for LOND formation by high-pressure homogenisation had previously been optimised by Mico *et al.* (2017).⁶ LOND solution formation by tip

sonication was used more readily during this project due to the 10x lower material volume and ability for parallel production of multiple formations allowing for more rapid testing of fluorescence loading, and use of the entire LOND solution with less concern of fluorescent or oil molecule degradation. This was especially true for the later FRET work and any work with squalene oil, which is prone to oxidation. LOND preparation time by tip sonication was optimised by measuring sample size and concentration after different sonication times using DLS and qNano.

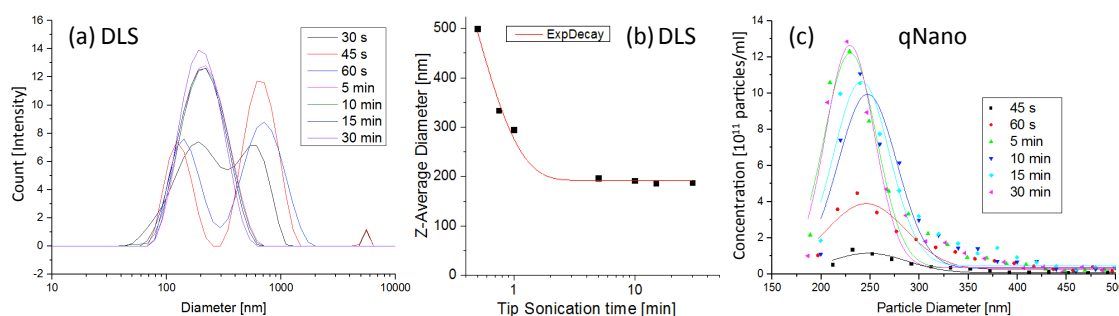


Fig. 6.1. Recordings of LOND diameter and concentration for a single batch of tip sonicated squalane, POPC-PEG+Atto488 LONDS, where samples were taken after different tip sonication times as noted. DLS recordings of (a) intensity counts over particle diameter and (b) Z-average over tip sonication time. (c) qNano recordings of particles/ml concentration over particle diameter using a 200 nm pore.

Figure 6.1 shows how the diameter and concentration of POPC-PEG+Atto488 squalane LONDS evolved during tip sonication. As the total tip sonication time increased, the monodispersity and concentration both increased up to a time point of ~3 min, after which further tip sonication lead to negligible changes in the LOND population. Sizing data obtained by qNano (Figure 6.1c) was recorded using the 200nm pore, meaning that only particles in this size range would be detected. As expected, the peak concentration of 200-300 nm LONDS was relatively low at early time points, and reached a maximum at 5 min after which it remained unchanged up to the 30 min tested. 15 min was decided on as a total tip sonication time valid for all LOND species (shells, oils, and encapsulated fluorophore), as at least for the LOND type tested in Figure 6.1 this was significantly into excess time to give the final LOND population size and concentration.

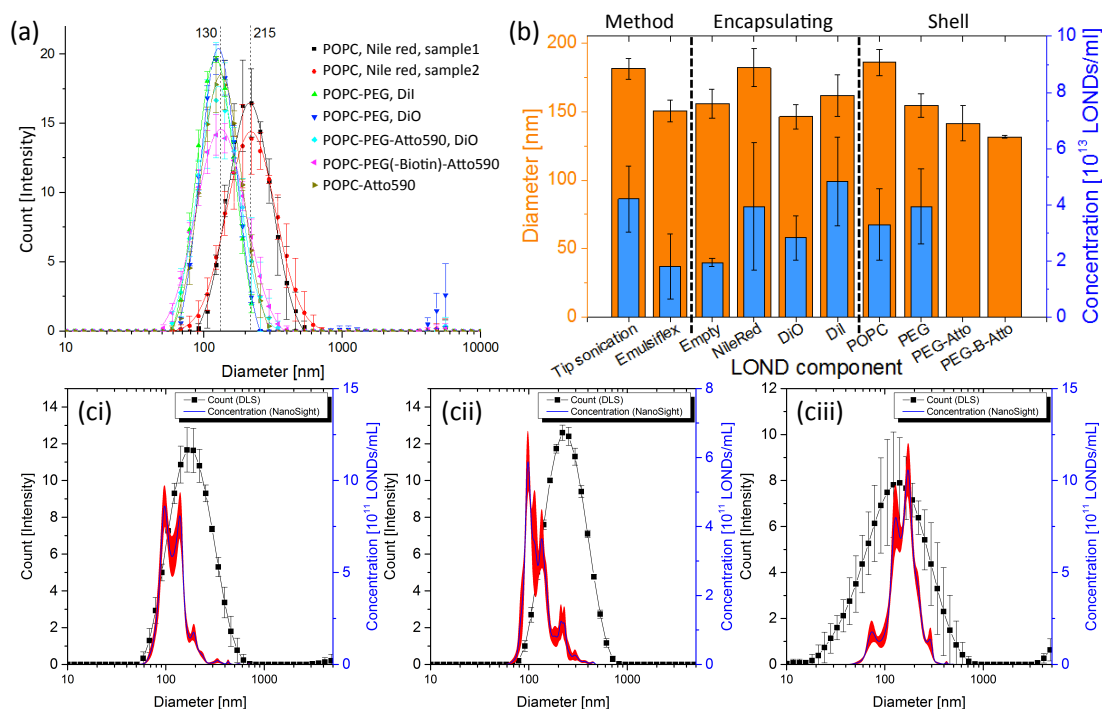


Fig. 6.2. Examples of size and concentration data from multiple LOND types prepared during this project. (a) DLS data collected from multiple squalane LOND solution stocks, indicating shell type and encapsulated species (if any). (b) Comparative (orange) DLS peak size and (blue) NanoSight total concentration from 15 squalane LOND samples. Here, all measurements collected from any LOND samples that included the defined LOND component were averaged to identify which components were significant to the formation process. Typical results from (c) DLS intensity count and NanoSight concentration (red indicates the error), both as a function of LOND diameter, for (ci) squalane, (cii) squalene, and (ciii) tripropionin LONDs with POPC shells, loaded with DiI. Errors calculated from multiple measurements over multiple batches.

Figure 6.2 shows comparative recordings of LOND size and concentration for a range of different LOND components including, (a and b) lipid shell and encapsulated species for squalane LONDS, and (c) oil types for POPC LONDS encapsulating DiI. For the squalane LONDS, the degree of random spread from the encapsulated species component suggested that any correlations observed for the other components were not significant enough to be reliable as a defining factor of final LOND size. All squalane samples gave peak diameters spanning 140-190 nm and $1-6 \times 10^{13}$ LONDS/ml. The size ranges recorded in the three different LOND oil core examples given were typical of all LONDS with those specified oil cores (Figure 6.2c), though the peak concentration often varied between $1-10 \times 10^{11}$ LONDS/ml for the same LOND type. Squalane (Figure 6.2ci) and squalene (Figure 6.2cii) POPC LONDS showed equivalent size results, with peak LOND diameters of ~ 100 nm and ~ 170 nm for NanoSight and DLS respectively. Tripropionin (Figure 6.2ciii) POPC LONDS gave peak diameters of ~ 170

nm for both measurement methods. DLS results for tripropionin LONDS showed a broader size distribution with a greater variation between measurements compared to the other LOND oils, whilst NanoSight results showed a comparable size distribution with similar error. This could suggest that along with the primarily tripropionin LOND population, a high proportion of large non-emulsified oil droplets were present, which could easily be overlooked by the NanoSight.

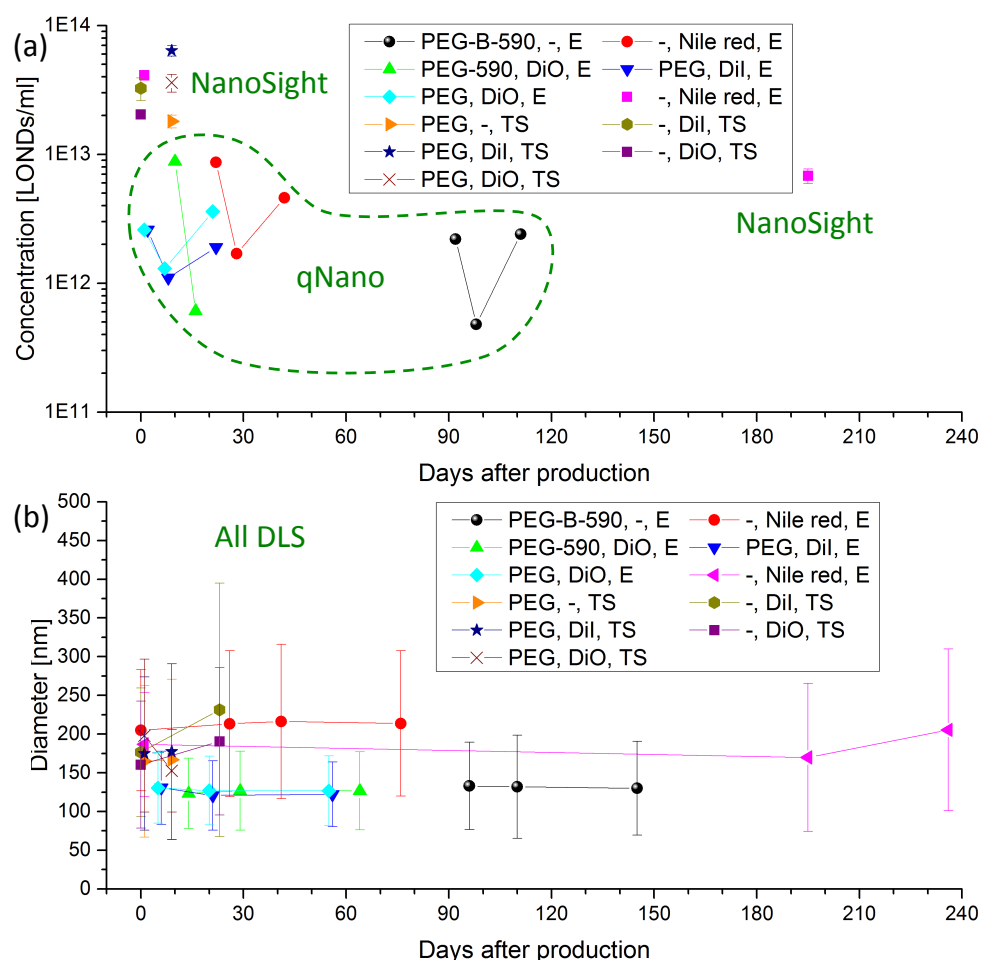


Fig. 6.3. Lifetime of different LOND samples. Changes to (a) concentration and (b) size are shown, measured by qNano, NanoSight, or DLS as indicated (green text and dashed line). All stock LOND solutions were squalane oil. The key label defines the shell type (all shells included POPC, if they were 100 mol% POPC this is defined by “-”, B is short for Biotin, 590 is short for ATTO 590), any species loaded into the oil core (oil cores without a loaded species are defined by “-”), and the method of formation, either Emulsiflex (E) or tip sonication (TS). Errors shown for diameter are the FWHM from the DLS peak diameter distributions (for an example of peak diameter distributions see Figure 6.2).

Figure 6.3 shows lifetime measurements performed on multiple LOND types, in terms of their size and concentration over time. The concentration remained on the order of 10^{12} and 10^{13} LONDS/ml, for at least 4 months as measured by qNano and NanoSight.

Most samples were measured for LOND diameter over 1 or 2 months, within which the size remained stable. The LOND type measured over the longest period of time for size had a 100 mol% POPC shell, which remained stable for at least 7 months. LONDS with added PEG were expected to be even more stable due to added steric stabilisation. Tip sonicated LONDS, which were used for most of the following work, were generally used and replaced within one month, so were expected to be well within stable lifetime.

6.2. LOND interactions with functionalised glass surfaces

Since the goal of this chapter was to introduce LONDS to hydrophobic-hydrophilic MB surfaces with the intent of forming a thin oil layer, it was important to understand LONDS interaction with surfaces of varying hydrophobicity-hydrophilicity from their hydrophilic aqueous phase. Six glass surfaces were prepared and tested for contact angle to assess their hydrophobicity-hydrophilicity (see Experimental Chapter; for glass preparation 4.9.2, p 89, for assessment 4.6, p 80). LOND solution was then added to them as a free droplet or to fill a 50 μm chamber, for observation by eye and microscope respectively.

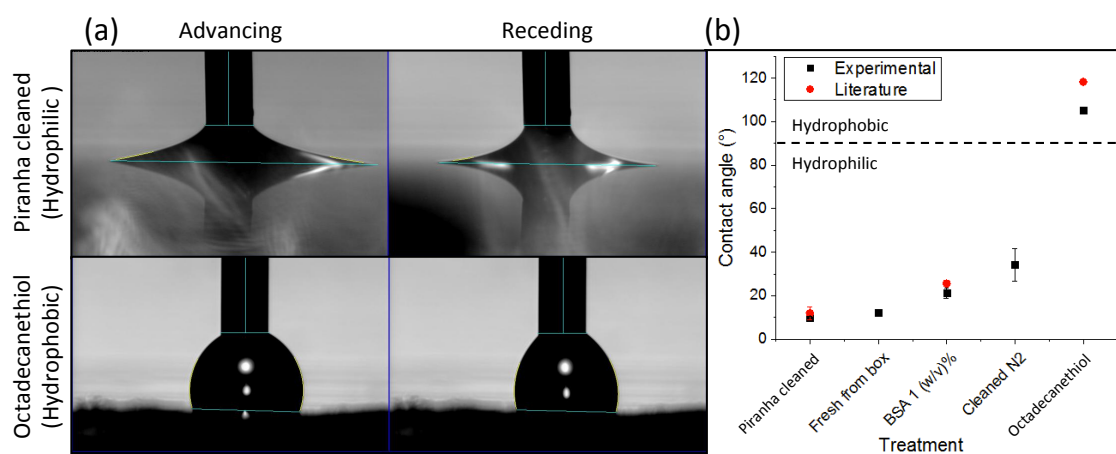


Fig. 6.4. Contact angle measurement of treated glass surfaces. (a) Example contact angles of MilliQ on the most hydrophilic (piranha cleaned) and hydrophobic (octadecanethiol (ODT) SAM) treated glass surfaces that were prepared for this work. Example images shown for advancing and receding contact angles from which, using Equation 4.7, the (b) surfaces' contact angles were calculated. An array of areas were tested for each glass surface of $n \geq 3$.²⁵²⁻²⁵⁴

Figure 6.4 shows examples of the contact angles for the most hydrophilic and hydrophobic surfaces that were assessed, and gives the contact angles determined for each surface. Importantly the glass-Au-ODT treated surface was confirmed to be hydrophobic. Additional to the results shown in Figure 6.4b, a roughened glass surface

was prepared by coarse sanding, resulting in 2-4 μm wide groves, and cleaned to the same standard as the ‘cleaned N_2 ’ surface. Following the results of Figure 6.4 the ‘cleaned N_2 ’, BSA coated, and roughened glass surfaces all showed identical results to the ‘Piranha cleaned’ surface, so for clarity are not shown.

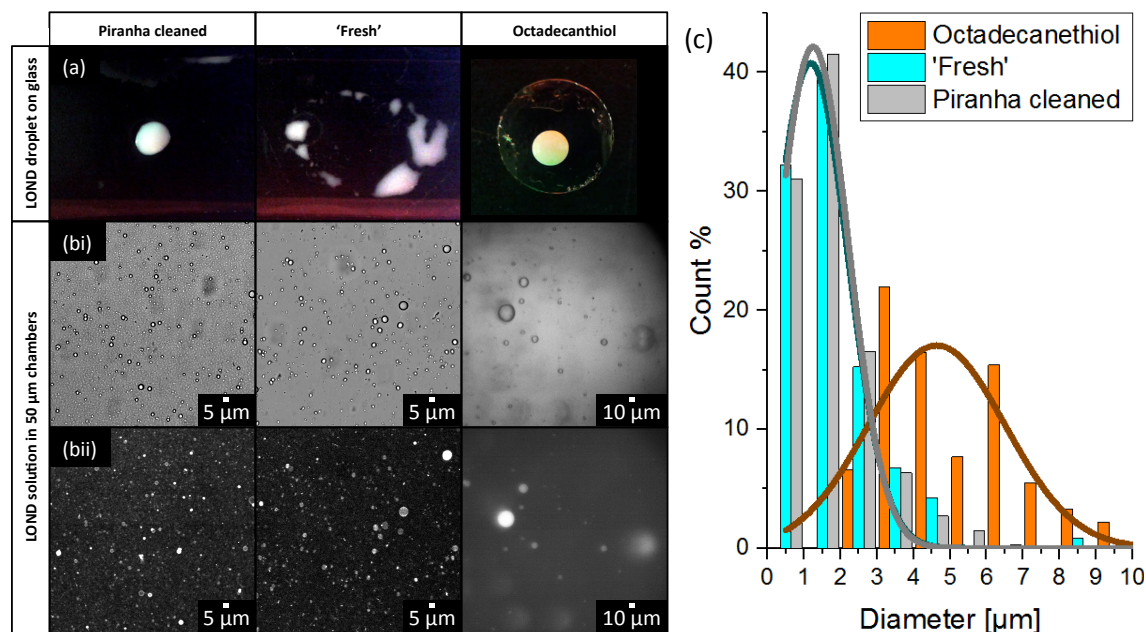


Fig. 6.5. POPC squalane LOND solution on functionalised glass surfaces (oil loaded with Nile red). (a) Birdseye camera phone images of LOND solution ~ 1 min after addition directly to treated glass surfaces. (bi) Brightfield and (bii) fluorescent imaging of LOND solution filling 50 μm deep chambers. (c) Histograms of the droplet sizes observed from in the 50 μm chambers. The LOND solution used here was not filtered immediately before use.

Figure 6.5 shows free droplets of POPC squalane LOND solution placed onto the functionalised glass surfaces (Figure 6.5a). It also shows the LOND solution-glass interface in similarly functionalised 50 μm deep glass chambers (Figure 6.5b), and gives diameter distributions of the droplets observed (Figure 6.5c). The LOND solution droplets remained stationary when placed on all of the surfaces apart from the glass surface that was used untreated, ‘fresh’, from the manufacturers. Here, after ~ 5 s, the solution moved across the glass surface. This glass surface was recorded as being strongly and uniformly hydrophilic. For this displacement of the primarily aqueous solution to occur, the surface must have become hydrophobic. One possible explanation is that of auto-wetting (self spreading), however, it seems more likely that the LOND solution’s displacement was due to a surfactant placed on the glass surface during manufacturing. Figure 6.6 shows a schematic explaining how the LONDS were thought to form a hydrophobic surface, which caused the solution displacement, and

fluorescence imaging of the area that the LOND solution had been displaced from. For the case of the latter, a highly concentrated array of $\sim 1\ \mu\text{m}$ fluorescent circle. These interactions could be explained by the LONDS' oil portion rupturing on the glass surface without sufficient time for the LOND lipids to re-organise and stabilise at the new bare oil-aqueous interfaces. No other glass surface showed the same mechanics, indicating that this hydrophilic to hydrophobic surface transition was not due to the hydrophobicity-hydrophilicity of the initial glass surface, but rather some substance applied by the manufacturers, which was removed on any of the following applied surface treatments. When the same methods were performed with POPC-PEG LONDS no mobility was seen for any of the glass surfaces.

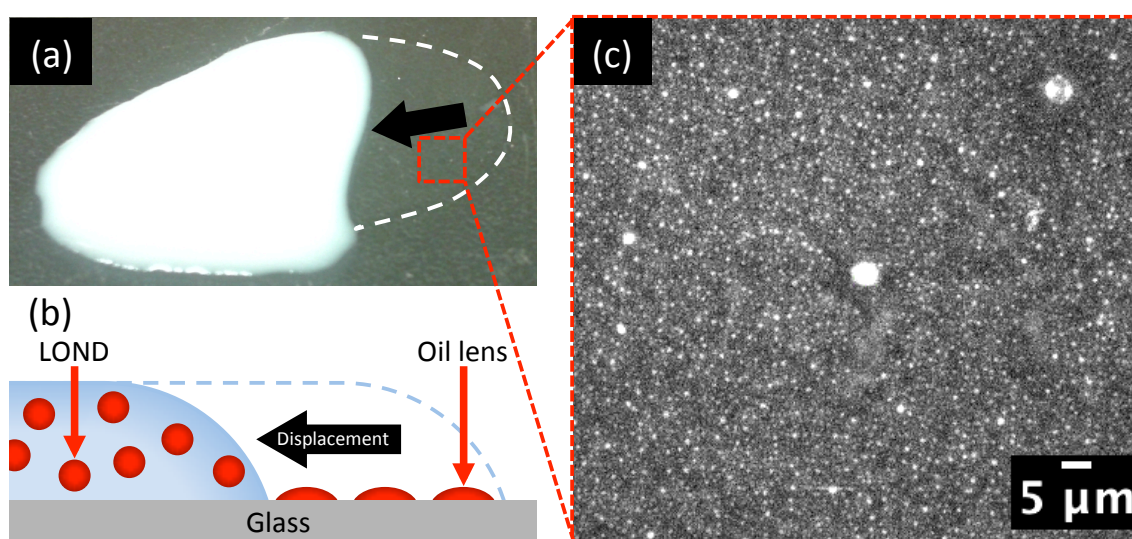


Fig. 6.6. POPC squalane LOND solution on a 'fresh' glass surface (oil loaded with Nile red). (a) An image is shown of the LOND solution after displacement over the glass surface, with a (b) schematic explaining the hypothesis that the LONDS ruptured at the glass surface, forming a hydrophobic surface. (c) Fluorescence imaging of the area where the LOND solution had been displaced from.

Observations of the POPC LOND solution in $50\ \mu\text{m}$ chambers (Figure 6.5b-c) showed a high concentration of 1.2 ± 0.1 (FWHM 2.3) μm droplets for both of the Piranha cleaned and 'fresh' glass surfaces, and 4.6 ± 0.2 (FWHM 4.4) μm droplets for the ODT functionalised glass surface. Since the former two surfaces were measured in the contact angle studies as hydrophilic and the latter as hydrophobic, this suggests that there was a driving force for coalescence on the hydrophobic surface. This was an important result as the same effect would be expected to occur at a freshly formed MB surface, due to its strong hydrophobicity, for example during MB formation, indicating the potential for LOND spreading and merging at the MB surface.

After the above experiments, the LOND solution was passed through a 200 nm filter and re-examined for droplet size both in the solution and at the Piranha cleaned glass surface. DLS measurements of the filtered nanoemulsion were shifted from a peak at 190 nm (FWHM 165 nm) down to 178 nm (FWHM 117 nm) and Darkfield imaging of the filtered LOND solution in a cleaned 50 μm chamber clearly showed that all droplets above 0.5 μm in diameter were no longer present. The tighter LOND size distribution in solution and absence of coalesced droplet at the glass surface indicates that the coalesced droplets seen at the glass surfaces in Figure 6.5b originated from a low concentration of larger droplets within the LOND nanoemulsion. However, the fact that the hydrophobic surface induced more significant coalescence would still be expected to hold true with the nanoscale oil droplets. Importantly, this result also meant that any particle later observed above 0.5 μm , when LOND solution was used for MB formation, could be confirmed as not being from LOND self-coalescence. After this observation, all LOND solutions were filtered from this point forward.

Whilst this work showed that there was a potential positive relationship between the hydrophobicity of a hydrophobic-hydrophilic interface and the amount of POPC squalane oil droplet coalescence at this interface, this could only be applied to the small proportion of larger oil droplets present in LOND solution after formation. However, this work showed that filtered POPC squalane LONDS would not rupture on a cleaned glass surface. This was important as it meant that on the future successful formation of OLI-MBs from LOND solution, these samples could be injected into cleaned chambers with less concern for the oil portion being displaced or reacting with the glass surface on contact.

6.3. QCM-D studies of LOND interactions with hydrophobic/hydrophilic surfaces

In this section the interaction of LONDS with solid hydrophobic/hydrophilic surfaces was studied using Quartz crystal microbalance with Dissipation monitoring (QCM-D) (see Experimental Chapter 4.9.4, p 91-93).

QCM-D sensors were treated either to have a hydrophobic (the quartz-Au surface was treated with an ODT SAM) or hydrophilic surface (the cleaned quartz surface was exposed to UV ozone) (see Experimental Chapter 4.9.2, p 89), and their contact angle was determined to establish their hydrophilicity-hydrophobicity (see Experimental Chapter 4.6, p 80). Squalane POPC or POPC-PEG LOND solution was injected and

then flow stopped, allowing the LONDS time to interact and for any monitored changes to equilibrate. Following this, PBS and MilliQ washes were used to remove excess LONDS and to observe changes in the frequency signal, which would indicate whether the adhered mass remained unchanged or was removed, the latter of which would indicate that the LOND attachment was non-specific.

Figure 6.7 shows contact angle results for the hydrophobic QCM-D crystal. Contact angle results gave an average of $101.2 \pm 0.8^\circ$ (SD 2.8°) for the hydrophobic (n=11) surfaces, and were consistently below 90° (at $\sim 10^\circ$) for the hydrophilic QCM-D.

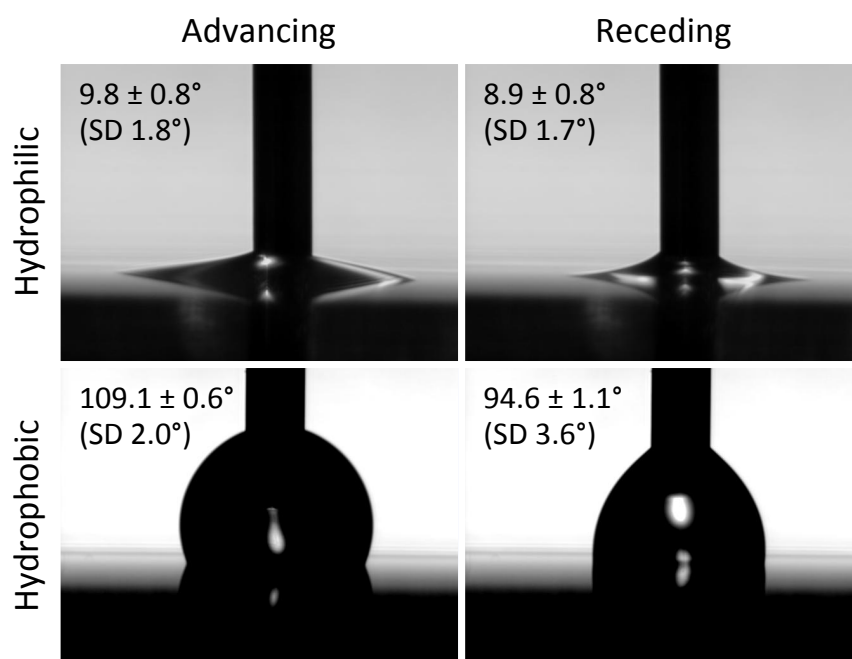


Fig. 6.7. Contact angle images of a QCM-D sensor treated to have a hydrophobic surface (quartz-Au treated with ODT).

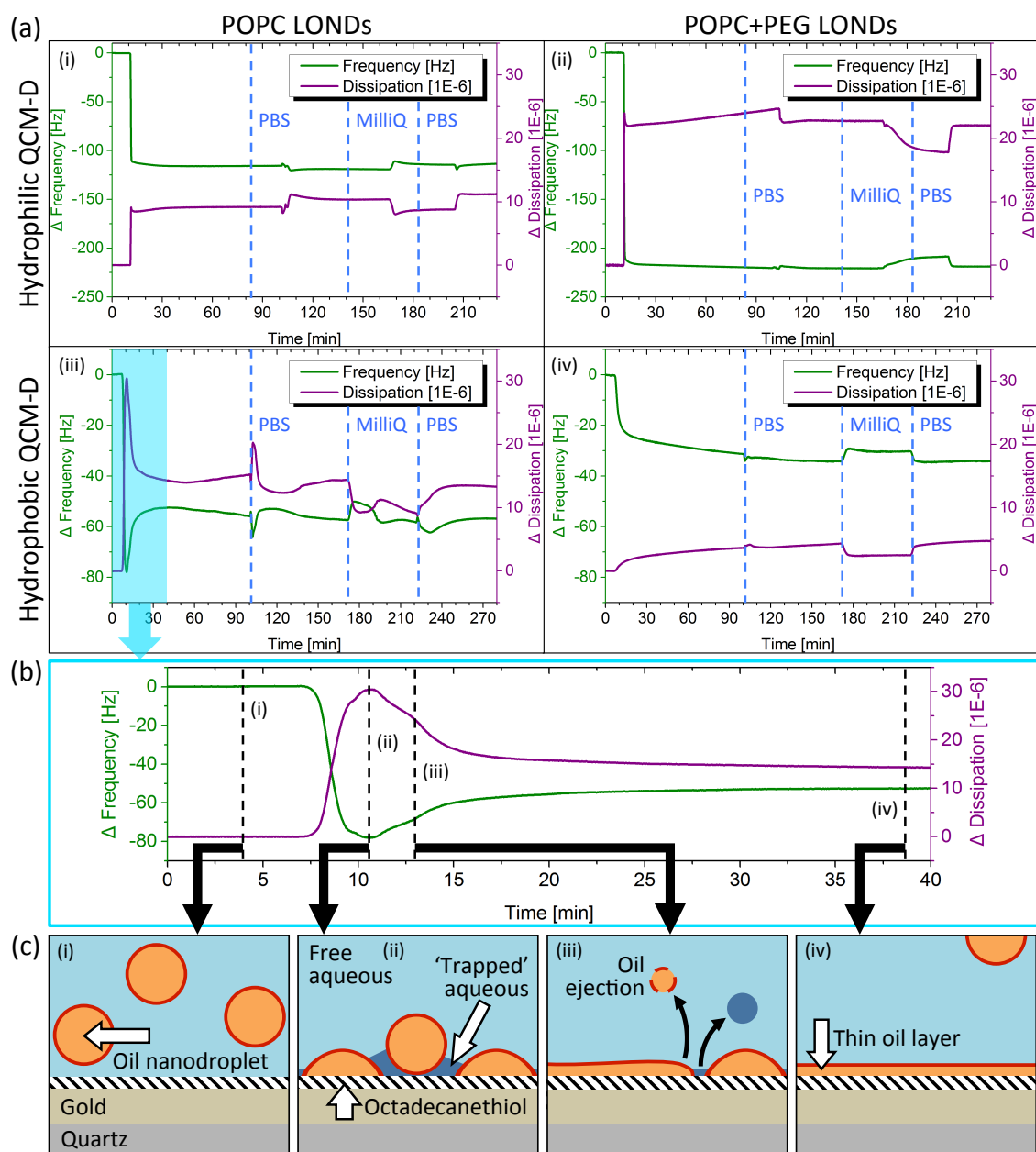


Fig. 6.8. Changes in frequency (green) and dissipation (purple) of a resonating quartz crystal upon the addition of (ai, aiii) Squalane POPC or (ai, aiv) POPC-PEG LONDs. Two different cases were studied, comprising QCM-D sensors where the surfaces were treated to be (ai-ii) hydrophilic (quartz treated with UV ozone) or (aiii-iv) hydrophobic (quartz-Au treated with ODT). The graphs show changes in frequency and dissipation as measured by the 7th overtone. Time points for the start of washes with PBS and MilliQ are indicated (blue dotted lines). For the POPC LONDs on the hydrophobic QCM-D, a (b) zoomed in section is shown of the first 40 min where characteristic time points are indicated (black dotted lines) with (c) schematics of what is thought to be occurring at each time point. The experimental data for this Figure was collected in collaboration with Dr. Victoria Mico.

Figure 6.8 shows the change in frequency (Δf) and dissipation (ΔD) of resonating QCM-D crystals, treated to have a hydrophobic or hydrophilic surface, on the introduction of squalane POPC and POPC-PEG LONDs, and further wash steps. The

Figure also shows schematics to explain what is thought to be occurring at characteristic time points on the POPC LOND, hydrophobic QCM-D crystal sample. For both LOND types interacting with the hydrophilically treated crystals, there was an initial rapid increase in $-\Delta f$, accompanied by a rapid increase in ΔD , indicative of the absorption of LONDS and the formation of a heterogeneous, non-uniform surface layer, which coupled strongly to the aqueous phase. After this, no further changes were observed, with washing showing little change to $-\Delta f$ or ΔD , indicating that the adhered mass remained stable at the sensor, interpreted as the stable attachment of LONDS. A small decrease in $-\Delta f$ and ΔD was observed when swapping from a wash of PBS to MilliQ (and visa versa). This phenomenon has been observed previously, and it is known to occur from the presence and then absence of free ions in the aqueous phase.²⁵⁵ Both $-\Delta f$ and ΔD for the POPC-PEG LONDS was roughly double that of the POPC LONDS. This indicated that roughly double the POPC-PEG LOND mass had adhered. The additional mass could also have been due to entanglement between PEG chains, causing multiple layers of PEG shelled LONDS to adhere. However, in that case, $-\Delta f$ would be expected to continue increasing over time with the entanglement of further LONDS and addition of their mass. POPC-PEG LONDS interacting with the hydrophobic surface showed a similar mechanism. Here, $-\Delta f$ and ΔD were roughly 1/6 that of the POPC-PEG LONDS on the hydrophilic surface, with the two measurements approaching this value over 4 h, again indicating intact adherence. In contrast, introduction of the POPC LONDS to the hydrophobic surface showed a significant and important difference to the other surface-LOND combinations. The initial rapid increase in $-\Delta f$ and ΔD was observed again, here with 3 times the $-\Delta f$ of the POPC-PEG LONDS on the hydrophobic surface. But over the following ~ 10 min Δf decreased and reached a plateau. Simultaneously, the ΔD decreased to a stable value of $\sim 15 \times 10^{-6}$. This behaviour is similar to that of bilayer formation via vesicle adsorption and rupture on hydrophilic surfaces.^{256–258} A similar two-stage mechanism is proposed to explain these observations. The attachment of LONDS (possibly partial wetting of the surface) (Figure 6.8ci-ii) followed by the slower spreading of droplets on the surface (Figure 6.8ciii-iv), leading to the detachment of entrapped water and possibly some oil. At the onset of washing the chambers, LONDS remaining in the dead space were introduced to the surface, leading to a smaller increase of $-\Delta f$ and ΔD , followed by the PBS wash, which resulted in the signal recovering to the “before wash” level and further remaining stable. Further washes showed small changes due to ionic differences between solutions.

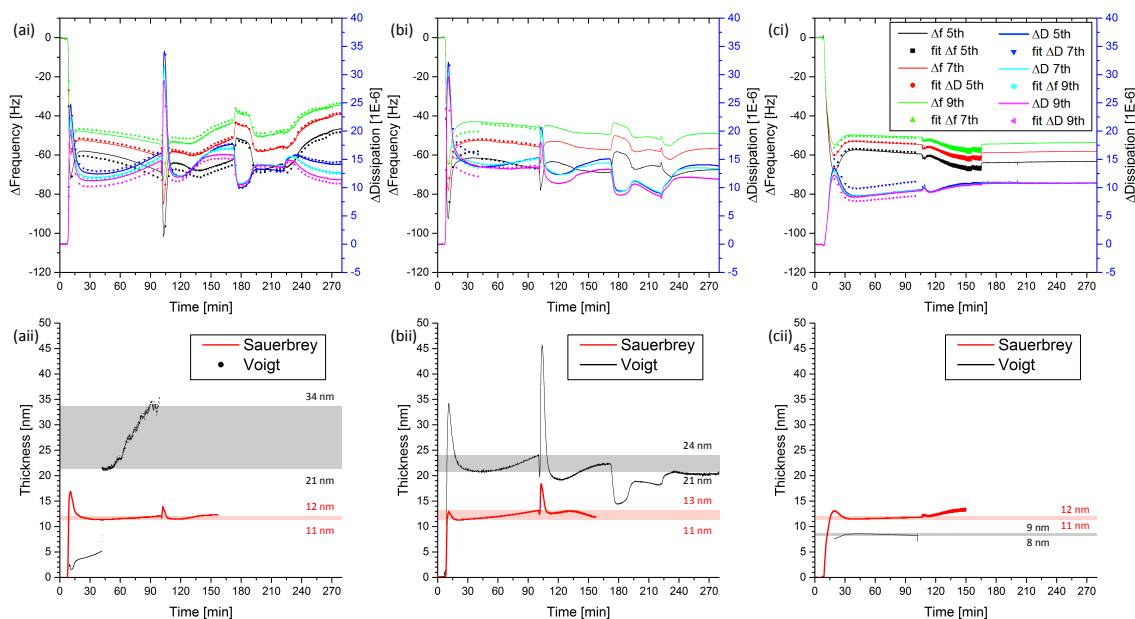


Fig. 6.9. (ai-ci) Effect on Δf and ΔD from three POPC squalane LOND samples being added to hydrophobic QCM-D crystals. The graphs show the 5th, 7th, and 9th overtones with overlaid Voigt viscoelastic modelling curves. Modelling parameters were set to; fluid density = 850 - 1100 kg/m³, viscosity = 0.9 - 1.5 kg/ms, oil-lipid layer density = 700 - 900 kg/m³, viscosity = 21 - 41 kg/ms, shear = 100 - 10¹² Pa, thickness = 10⁻¹⁰ - 10⁻⁵ m. (aii-cii) Oil-lipid layer thickness calculated by the Voigt modelling (black), from the corresponding graph directly above, and the Sauerbrey equation (red), showing semi-transparent boxes to indicate the thickness.

Figure 6.9 shows QCM-D data fitting to both the Voigt viscoelastic modelling and the Sauerbrey equation to estimate the thickness of the resulting oil layer upon POPC LONDS interaction with ODT-coated sensors. Results using the Sauerbrey equation were consistent between all samples recorded, giving an oil-lipid layer thickness of 11.7 ± 0.2 nm (SD 0.3 nm). On the other hand the Voigt viscoelastic modelling gave far more varied results between samples, which often did not appear sensible in relation to the Δf they were calculated from (see Figures 6.9ai-ii). Here, the oil-lipid layer thickness was given as 20 ± 6 nm (SD 10 nm). Taking all measurements into consideration, the oil-lipid layer was estimated as 16 ± 3 nm (SD 8 nm).

It is important to remember that the aim of these experiments was to infer what might occur between LONDS and the surface of a newly formed, uncoated MB, where a hydrophobic gas surface would be presented in place of the solid surface. Therefore, all of the results shown in this section served to show that lipid stabilised oil droplets would adsorb and rupture, and also provide an estimation of the oil layer thickness, which was of the order of 10 s of nm.

6.4. Surface pressure changes to model MB surfaces on the addition of LONDS

This section investigated surface pressure changes to a model MB's aqueous-gas interface upon interaction with LONDS. This was to help understand what conditions would allow LONDS to enter the aqueous-gas interface to aid the formation of a thin oil layer. The following work was performed on a LB system where LONDS were introduced from a PBS subphase.

Initially LONDS were introduced to a fully compressed lipid monolayer surface. Then the surface pressure was monitored as the monolayer was expanded and re-compressed. The aim here was to observe at what surface pressure (and thereby what surfactant concentration) the LONDS would enter the air-lipid/water interface. The second section of the work introduced LONDS to static semi-compressed lipid monolayer surfaces. The aim here was to observe the time dependence of LOND adsorption.

6.4.1. LOND interactions at a water/lipid-air interface

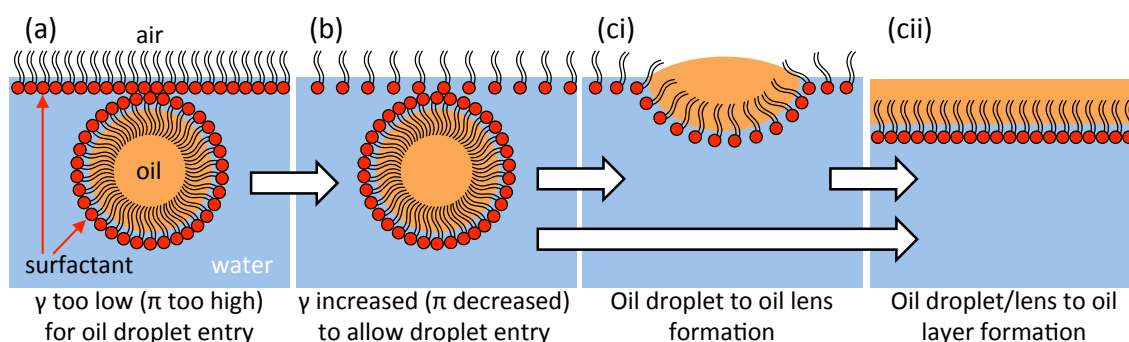


Fig. 6.10. Schematic of how an oil droplet can enter a fully compressed monolayer due an expansion of that monolayer, showing (a) an oil droplet directly underneath a compressed monolayer, (b) the monolayer being expanded, and (c) the oil droplet entering, resulting in either (ci) an oil lens or (cii) oil layer.

Hotrum *et al.* (2002 and 2003) discussed how when fat or oil emulsion droplets come to an aqueous-gas interface, both stabilised by some surfactant, where their inclusion into the interface would be energetically favourable, they can be blocked from entering the interface by a kinetic energy barrier known as the entering coefficient, E_R .^{115,259} As depicted in Figure 6.10, using a custom prepared LB system (with an indefinitely expandable surface), they were able to inject sunflower oil droplets stabilised by either whey protein isolate or sodium caseinate into their subphase, allowing the droplets time to rise, to obtain a system where the droplets were directly below an air-aqueous surface stabilised by the same protein. They then observed changes to the surface pressure on

constant expansion of the surface, defining the point of droplet entry as a ‘kink’ in the otherwise smooth surface pressure over time relationship. The point of droplet entry thereby identifying the surface pressure required from the droplet-free surface.²⁵⁹

The Hotrum *et al.* method was followed during the follow work. In brief, on a LB system (see Experimental Chapter 4.9.5, p 93-95), a POPC monolayer was fully compressed, squalane POPC LONDS were then added to the subphase, and time was allowed for the LONDS to rise to the surface. The majority of the LONDS were observed to float to the surface in < 5 s. Therefore, it was assumed that for the LB trough that allowing 30 min was sufficient time for the LONDS to have reached the surface. The monolayer-LOND surface was then expanded until the surface pressure reduced to 0 mN/m, where any surface molecules were contributing a negligible surface tension decrease on the primarily bare air-aqueous interface.

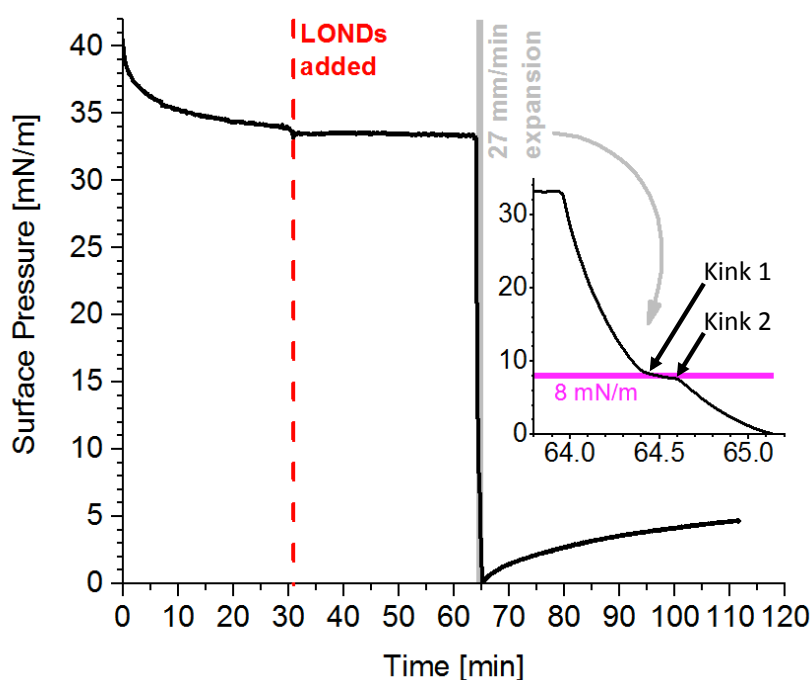


Fig. 6.11. LB trough results showing a fully compressed POPC monolayer, with (red dotted line) POPC squalane LONDS added underneath (enough to 33% close pack under the surface), where time was allowed for their buoyancy, (grey) expanded at a constant rate of 27 mm/min, then allowed to rest. Inset image is a zoom across 64-65 min, where two kinks (pink) were observed in the otherwise smooth surface pressure over time relationship.

Figure 6.11 shows how the surface pressure of the POPC monolayer – POPC squalane LOND surface changed over time during the LONDS’ addition, the surface’s expansion, and allowing the resultant surface to rest. The compressed monolayer was initially allowed to relax, reducing in surface pressure by ~7 mN/m over 30 min. No changes

were observed upon the addition of LOND solution or over the following 30 min, indicating that they remained below the surface monolayer and did not incorporate within it. On constant expansion of the surface, two kinks in the surface pressure over time relationship were observed. The first kink decreased the gradient whilst the second increased it back to before the first kink. These occurred at ~ 8 mN/m, covering ~ 1 mN/m, with the first kink at 8.5 mN/m. It is thought that on the first kink the LONDS began to enter the surface, increasing the surface pressure at a rate slower than the decrease caused by the surface expansion, then on the second kink either there were no more LONDS left to enter the surface or something else was preventing them from further entry. These studies informed that for POPC squalane LONDS to enter the model MB's POPC monolayer, the surface pressure had to be reduced enough to give a surface tension ≥ 64.3 mN/m. This differs from the current literature on the E_R . Using Equation 3.27 (p 48), even if the LONDS were assume stable as possible, with their lipids at the oil-aqueous collapse pressure, they would still be expected to enter a POPC monolayer with a surface tension ≥ 29.6 mN/m (surface pressure ≤ 43.2 mN/m, 3.3 mN/m less than the collapse pressure), with this upper limit decreasing if the LONDS were stabilised less by their lipid monolayer.

From the results shown in Figure 6.11, a new method was used to more accurately assess the entry point of LONDS into the monolayer. The method entailed periodic expansions of the monolayer after LOND introduction, with the intention that once LONDS had entered the monolayer (dotted line), the monolayer could be compressed to the same area as before the expansions, allowing for the change in surface pressure by the oil and LOND lipids to be identified.

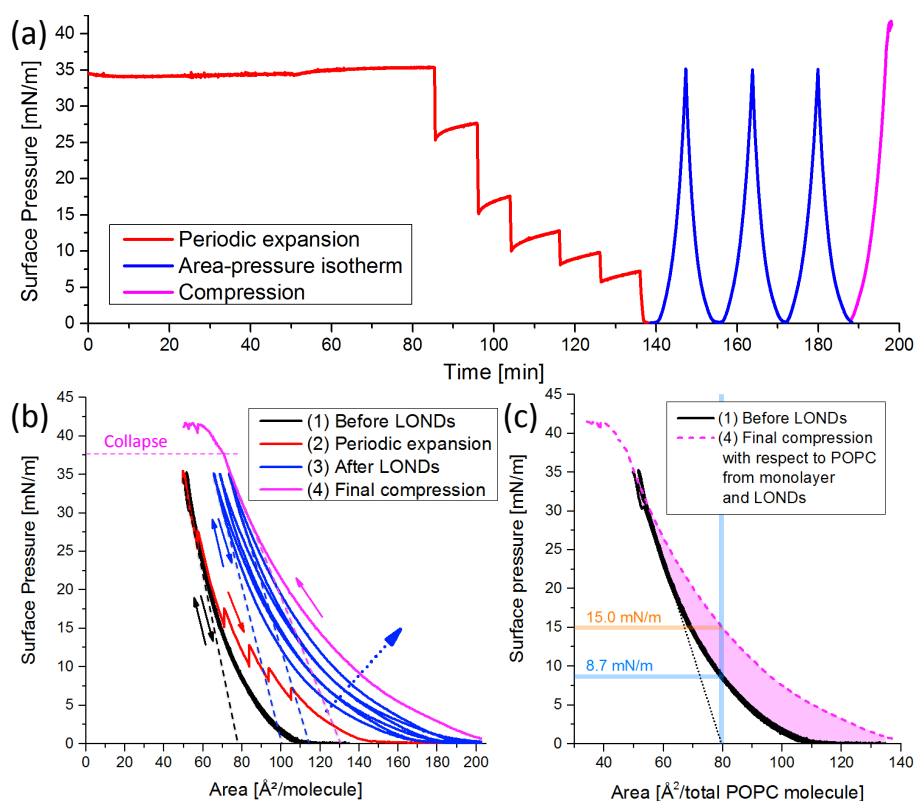


Fig. 6.12. Changes to the surface pressure of a PBS-air surface with a POPC monolayer; (1, black) during a typical pressure-area isotherm, ending in a compression close to collapse of the monolayer, (2, red) on the introduction of POPC squalane LONDS directly underneath the monolayer (enough to close pack at the surface) and subsequent periodic expansions of the surface at 27 mm/min beyond 0 mN/m, (3, blue) compression-expansion cycles on the new surface, and (4, pink) a final compression down to the same surface area as prior to LOND addition. The surface pressure is shown in respect to (a) time, (b) area per molecule of the original POPC monolayer, with arrows to show if the area was being compressed or expanded, and (c, dotted pink) area per molecule re-calculated to account for additional POPC molecules from the LONDS, assuming that all LOND lipids have migrated to the surface.

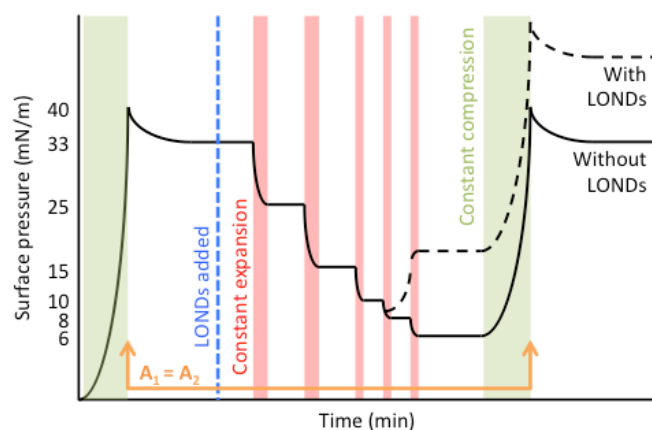


Fig. 6.13. Sketch of the expected result for an experiment in which a POPC lipid monolayer is compressed (first green box), then squalane LONDS are added beneath the monolayer (blue dashed line). The surface pressure is then monitored as a function of the monolayer's periodic expansion (red boxes) and final compression. This was the expected result from the Figure 6.12 experiment, due to the results observed in Figure 6.11.

Figure 6.12 shows how the surface pressure of a POPC monolayer – POPC squalane LOND surface changed during a pressure-area isotherm experiment prior to LOND addition, during the addition of LONDS, for periodic expansions of the surface, following compression-expansion cycles of the new surface, and a final compression down to the same total surface area as before LOND addition. Figure 6.13 shows a sketch of the results that were expected from the experiment of Figure 6.12, based off of the results observed in Figure 6.11. During this experiment, a kink was not observed as in Figure 6.11. Rather, expanding the surface resulted in a greater surface pressure for the same area per molecule, compared to the POPC monolayer alone, starting at ~ 15 mN/m (surface tension of 57.8 mN/m). (Figure 6.12b, blue dotted lines) On following compression-expansion cycles further increases to the surface pressure were observed for the same area per molecule. This suggested that during each expansion of the surface more LOND material was entering the surface monolayer. (Figure 6.12c) Comparing the final compression and the initial monolayer isotherm, both with respect to the total possible POPC molecules at the monolayer, showed the contribution of the oil to the surface pressure. It can be seen that at full compression, just before monolayer collapse ($\sim 55 \text{ \AA}^2/\text{molecule}$), there was negligible contribution from the oil. However, at higher areas (per POPC molecule) the surface pressure had an increased value, meaning that the surface tension, and therefore surface energy, was reduced. Figure 6.12c indicates that at the native area per POPC molecule ($\sim 80 \text{ \AA}^2/\text{molecule}$), the monolayer had a surface pressure of 8.7 mN/m, which was increased by 7.3 mN/m when the monolayer included the oil portion. This means that in cases where the air-water interface would have a low lipid coverage, for instance during the initial stages of MB formation, the Laplace pressure would be reduced, improving stability. If the oil portion was a full oil layer, it was expected that at a large surface expansion the surface would effectively be a non-lipid water-oil-air interface. This would lead to a non-zero plateau of the surface pressure over increasing expansion. However, the surface pressure continued towards 0 mN/m instead. This result suggested the presence of oil lenses, where at larger surface expansion the ratio of water-air interface to water-oil-air interface was increased.

All of these results, including those from Figure 6.11 and Equation 2.27, strongly suggested that the transition of squalane POPC LONDS from below a POPC monolayer to entering it can occur at any surface pressure possible (apart from when the POPC

monolayer is fully close packed at the collapse pressure), but that the transition is a slow LOND by LOND process, rather than many to all of the LONDS entering on mass.

6.4.2. Time dependence of LOND model MB interactions

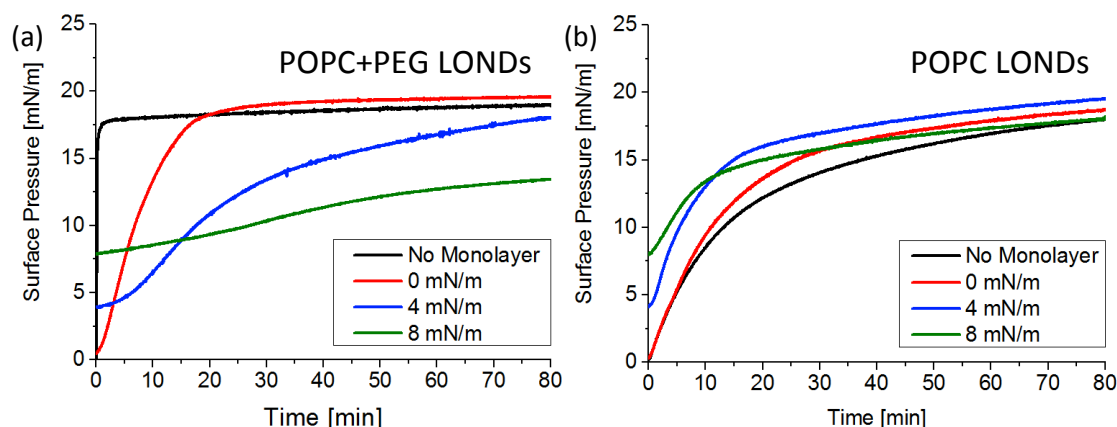


Fig. 6.14. Changes to the surface pressure of static DPPC monolayers, compressed to defined surface pressures, after the addition of squalane (a) POPC-PEG or (b) POPC LONDS underneath the monolayer surface, as measured by a LB trough. Time = 0 min was the moment when an increase in surface pressure was observed (in order to neglect LOND rise time and inconsistent LOND addition between samples).

The previous section suggested that the entering and potential spreading of LONDS into a POPC lipid monolayer was a stochastic process rather than all of the LONDS entering on mass. This section presents the results of experiments aimed at understanding the timescale of LOND adsorption, since this would be important for the stabilisation of MBs from LOND solution. Just after MB formation, the lipid monolayer would be expected to be at the equilibrium spreading pressure (ESP). The air-water interface was either left bare, or had a DPPC monolayer compressed to give a surface pressure of 0 mN/m (at the highest compression possible to give 0 mN/m), 4 mN/m, or 8 mN/m (~ESP, see Results Chapter 5.1, p 119). These surfaces were considered representative of a MB surface during stabilisation. These surface pressures could also be related to an expansion of the monolayer to ∞ , 1.3, 1.1 and 1 times the area per molecule at ESP respectively. This equates to lipid stabilised 2.0 μm MB expanding to ∞ μm , 2.3 μm , and 2.1 μm or not expanded respectively. Figure 6.14 shows how the surface pressure of these surfaces changed upon the introduction of POPC-PEG (Figure 6.14a) or POPC (Figure 6.14b) squalane LONDS from underneath the surface monolayer. Figure 6.15 presents a schematic of a possible explanation for what was observed.

For POPC-PEG LOND addition, without a starting monolayer, the LONDS were seen to rapidly enter the surface within 5 min, increase the surface pressure, and then remain

unchanged. With higher initial DPPC monolayer compressions the timescale for LOND entry and surface pressure increase was significantly increased. After 80 min the initially bare air-water surface, and the DPPC monolayers at compressions of 0 and 4 mN/m had all reached surface pressures of 18-19.5 mN/m. However, the 8 mN/m surface had only been increased by 5.5 mN/m and appeared to have a gradient that would never approach the 18-19.5 mN/m range even on much greater time scales. Since the monolayer at 8 mN/m was already highly compressed, this results could suggest that for the 8 mN/m surface, only a small fraction of LONDS were able to enter the monolayer until it was 'full' (Figure 6.15ai), contributing little surface pressure increase. Meanwhile, the less initially compressed monolayers could be filled by more LONDS (Figure 6.15aii), contributing greater surface pressure increases, which would occur more rapidly for LONDS that were not impeded from reaching the air phase by the presence of a semi-compressed monolayer.

For POPC LOND addition, all of the DPPC monolayers showed an exponential increase to the surface pressure. After 80 min, all of the DPPC monolayers had surface pressures at 18-19.5 mN/m with no apparent dependence on the original monolayer compression. The only factor that the starting monolayer compression affected was the exponential rate in which the surface pressures increased to its final value. For an air-water interface with no monolayer, and starting DPPC monolayer compressions of 0, 4, and 8 mN/m, it took 26, 21, 14, and 10 min for each monolayer to reach 75% of its final surface pressure respectively. These results suggested that at a higher initial monolayer compression, the maximum change to that monolayer (caused by the progressive addition of LONDS) occurred over a shorter time frame, but that after 80 min the surfaces were effectively the same, regardless of the starting monolayer. One possible explanation for these observations was the result of the LONDS spreading (Figure 6.15i-iii). In that way, regardless of the number of LONDS that had entered to the surface, an equivalent surface pressure would be found due to the two interfaces of water/lipid-oil and oil-air. The oil layer in-between these interfaces would then either have a small thickness (Figure 6.15ii), from the entry of a small number of LONDS due to a high initial monolayer compression (hence the more rapid increase to the final surface pressure value seen in Figure 6.14b) or a large thickness (Figure 6.15iii), from the entry of a high number of LONDS due to a low initial monolayer compression (hence the longer time to increase to the final surface pressure value as seen in Figure 6.14b).

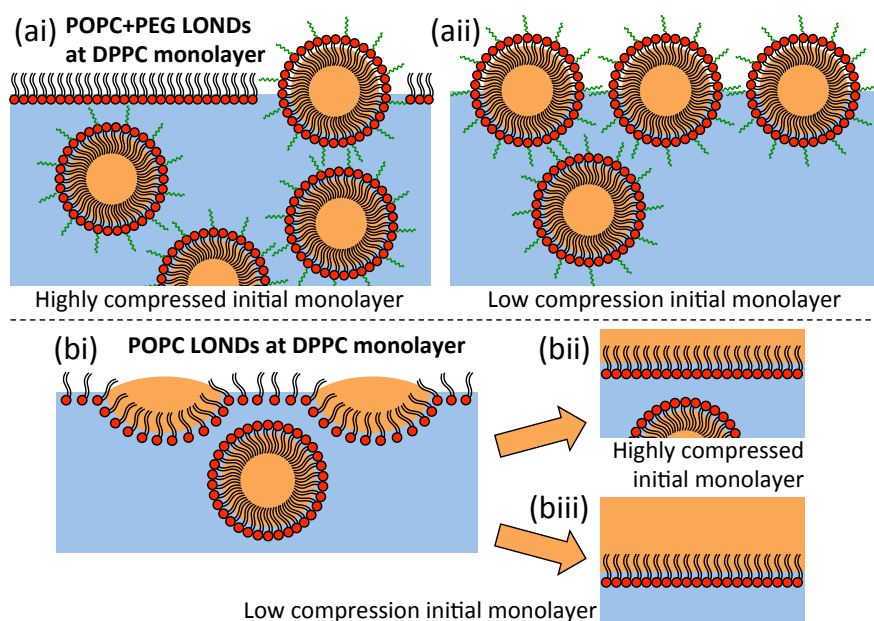


Fig. 6.15. Schematic of the suggested differences between the entering of (a) POPC-PEG LONDS and (b) POPC LONDS on a DPPC monolayer, where the monolayer is defined as being highly compressed (high surface pressure) or of low compression (low surface pressure) before LOND introduction. As shown, for POPC LONDS, the air-oil and oil-lipid/water interfaces remain the same (resulting in the same surface pressure) since the spreading of more LONDS, until the monolayer is 'full', only results in a larger volume of oil. Meanwhile, the intact POPC-PEG LONDS fill the surface less when the initial monolayer is highly compressed due to the surface becoming 'full'.

In conclusion: These results suggested that squalane POPC LONDS were able to enter and spread at a gas-aqueous surface, forming either oil lenses or an oil layer, whilst being relatively unaffected by the possible stabilisation of that surface by non-oil lipid structures. However, this spreading was a long process that occurred over 10-40 min. Meanwhile the results suggested that POPC-PEG LONDS entered but did not spread, forming a LOND covered surface, with the efficiency of entering being strongly dependant on the stabilisation rate of the surface by any non-LOND lipids.

6.5. Formation of OLI-MBs from LOND solution

During this chapter OLI-MBs were typically formed from LOND solution either through a variation on the lipid solution mechanical agitation method or monodisperse MB production method and using a LOND solution in place of the standard lipid solution (see Experimental Chapter, 4.4 and 4.9.6, p 75 and p 95). When reference is made on the use of OLI-MBs later in this thesis they are referring to OLI-MBs formed from by one of these two methods. This section addresses the methods that were undertaken to form OLI-MBs from LOND solution, and analysis of those MBs. All of

the preliminary work in developing and then confirm the success of the formation technique was completed with the use of squalane POPC and POPC-PEG LONDS. Once the formation technique was confirmed, the work moved on to the use of squalene and tripropionin POPC LONDS.

Due to the results of POPC and POPC-PEG LONDS on model MB surfaces (see sections, 6.3 and 6.4) it was predicted that POPC LONDS would form oil lenses/an oil layer at the MB shell (the desired OLI-MB structure) and that POPC-PEG LONDS would form MBs that were shell stabilised by intact LONDS respectively. This prediction was later confirmed by the use of FRET enabled LONDS in section 6.7.3 (Figure 6.39, p 171). As such, from here these two structures will be referred to in this section as OLI-MBs and LOND shelled MBs respectively.

6.5.1. Mechanical agitation formation and MB lifetime

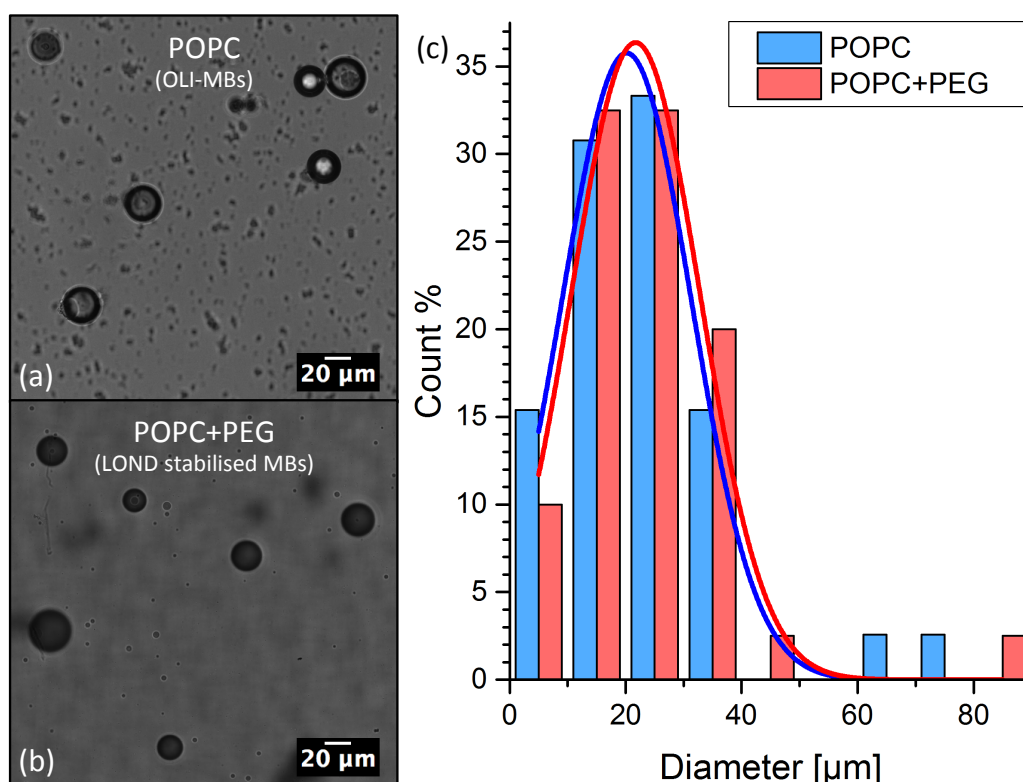


Fig. 6.16. Example MBs formed from squalane (a) POPC and (b) POPC-PEG shelled LONDS through the mechanical agitation method. (c) Size histograms of the POPC LOND MBs (blue) and POPC-PEG LOND MBs (red).

Figure 6.16 shows the size distribution of MBs formed by mechanical agitation of POPC squalane LONDS (giving OLI-MBs) or POPC-PEG squalane LONDS (giving LOND shelled MBs). Mechanically agitated MBs, formed from squalane POPC and POPC-PEG LONDS, had peak diameters of $21.2 \pm 0.7 \mu\text{m}$ (SD $26.2 \mu\text{m}$) and 21.7 ± 0.7

μm (SD $26.0 \mu\text{m}$) respectively, and concentrations of $1.7 \pm 0.5 \times 10^6$ OLI-MBs/ml and $2.4 \pm 1.0 \times 10^6$ MBs/ml respectively. Figure 6.17 shows changes in size and concentration over time of the mechanically agitated OLI-MBs formed from POPC squalane LOND (Figure 6.17ai-ii). By extrapolating the concentration profile to $t = 0$ min - the time that the production stopped, it was found that the OLI-MBs averaging $\sim 15 \mu\text{m}$ took ~ 35 min to halve in concentration. After ~ 100 minutes, the OLI-MB concentration remained constant, whilst the size was observed to slowly increase. This could be due to Ostwald ripening from sub-micron MBs in the solution that were not observed.⁹⁰

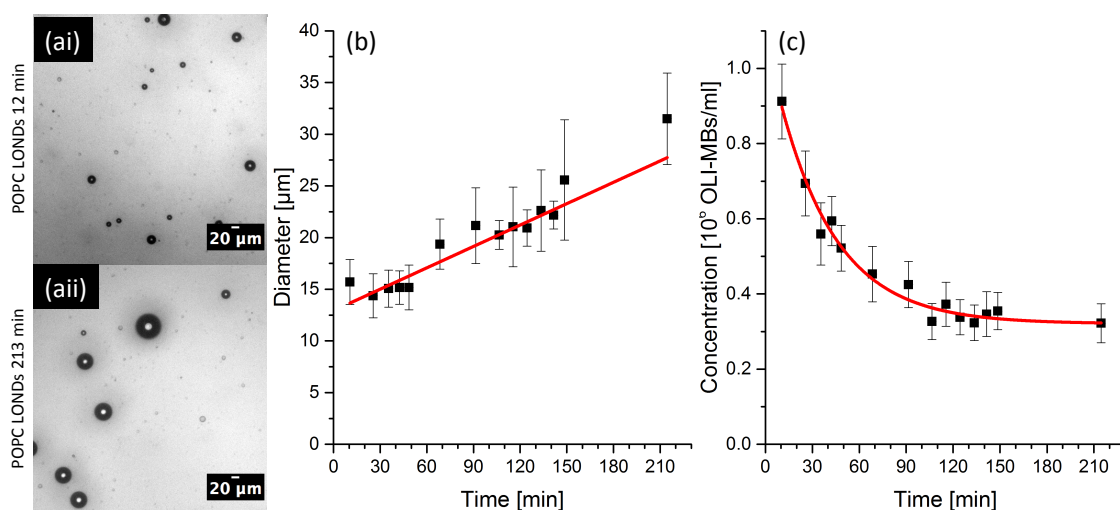


Fig. 6.17. Lifetime results from mechanically agitated OLI-MBs formed from POPC squalane LONDS. (a) Two example Figures are shown from 12 and 213 min time points. (b) Diameter and (c) concentration changes are shown over time. Each time point is measured from three samples, with each sample being measured at ten locations ($n = 30$ images per time point).

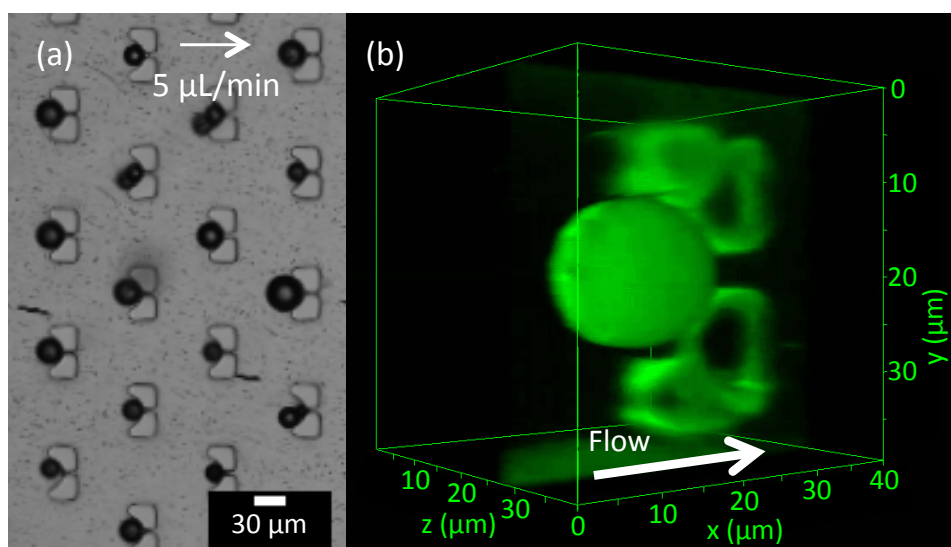


Fig. 6.18. Mechanically agitated OLI-MBs, formed from squalane POPC LONDS, loaded with DiI, microfluidically trapped. Showing (a) trapping of OLI-MBs in excess LOND solution, and (b) a z-stack of the fluorescence of the remaining DiI in oil after washing away excess material.

Figure 6.18 shows a population of mechanically agitated POPC squalane OLI-MBs microfluidically trapped, and a z-stack of the DiI fluorescence from a single OLI-MB after washing of excess LONDS (for trapping details see Experimental Chapter 4.2, p 66-68). As seen, the OLI-MB retained its fluorescence, indicating that the oil portion was still present. The angle of the z-stack image shows that the MB's fluorescence was a-symmetrical (the right side of the MB is more curved than the left). This was due to an imaging artefact whereby fluorescence from the side of the MB facing away from the confocal lens could not be imaged. This artefact was confirmed by comparatively imaging known spherical, fluorescent, polystyrene beads, which also appeared a-symmetrical in an identical manner (result not shown). Figure 6.19 compares the fluorescence intensity from the MB shell and the surrounding solution before and after washing. As seen by the white light image, the excess LONDS in solution were observable as 'noise' before washing, which was not present after the flow of PBS. Whilst the solution fluorescence dropped to $\sim 0.7\times$ that before washing, the OLI-MB shell fluorescence change was negligible. This indicated that the oil portion, which contained the fluorescence molecules, was stable against the increased concentration gradient given by removal of the excess oil and lipid from the surroundings, as well as the shear forces produced by the flow during washing.

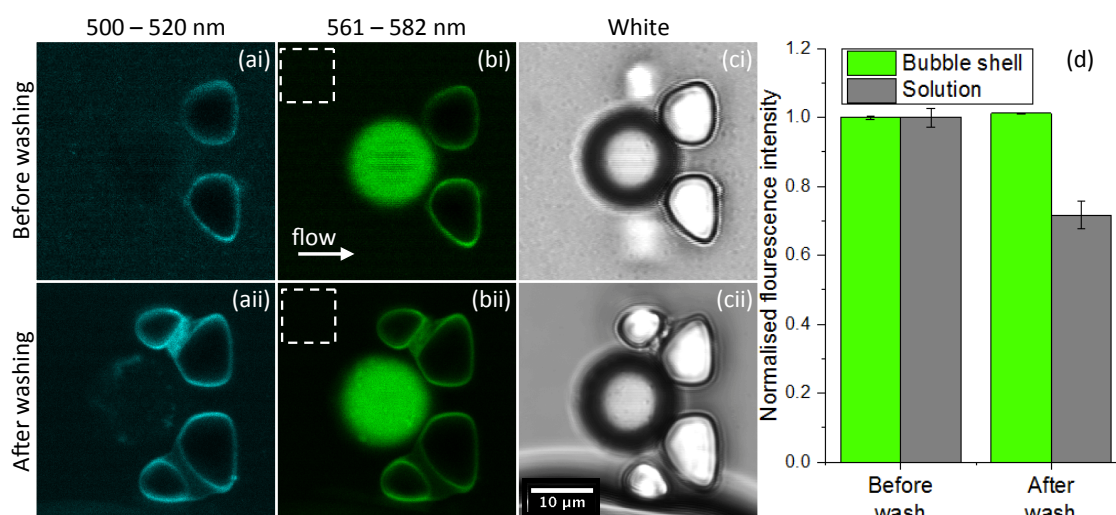


Fig. 6.19. Washing of mechanical agitation OLI-MBs formed from a mix of two squalane POPC LOND solutions, loaded with either DiO or DiI. The fluorescence signals are shown from the (a) DiO and (b) DiI emission windows, and the (c) white light signal, from (i) before and (ii) after washing. (d) Bar chart comparing the fluorescence intensity from the DiI emission window before and after washing (normalised to before washing) at the (green) OLI-MB shell and in the (grey) solution, measured from the area indicated by the white dotted square. All fluorescent images were contrast enhanced equally.

Figure 6.20 shows images from before and after washing of mechanical agitation MBs formed from a mix of two squalane POPC-PEG LONDS solutions, loaded with either DiO or DiI. Here again it can be seen that the MB retained its fluorescence after washing, indicating that the oil portion was stable. A bright fluorescent circle can also be seen directly above the trapped MB after washing. This was thought to be a large oil droplet that also became trapped around the stagnant MB, hence fully fluorescent.

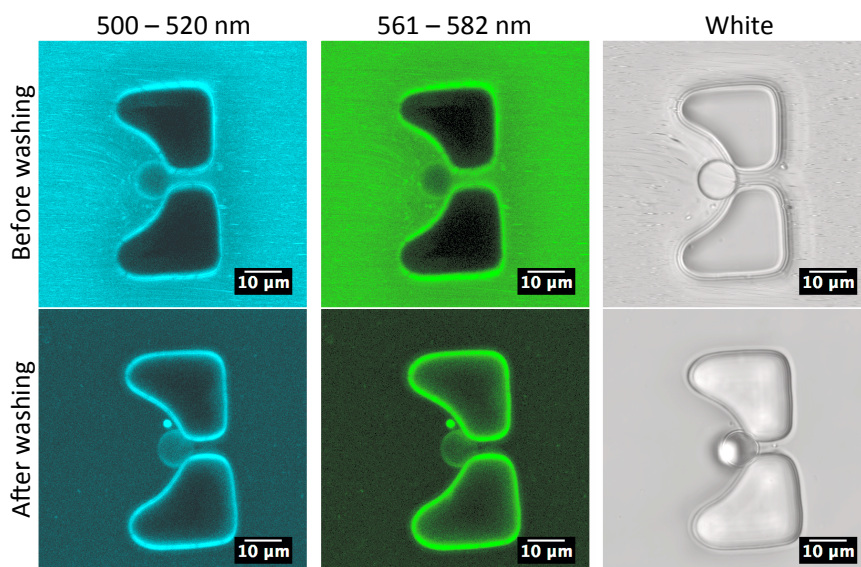


Fig. 6.20. Washing of mechanical agitation LOND shelled MBs formed from a mix of two squalane POPC-PEG LOND solutions, loaded with either DiO or DiI, presented as in the POPC OLI-MBs in Figure 6.19.

6.5.2. Microfluidic OLI-MB formation

This section presents the results concerning the formation of MBs from LOND solution through FF microfluidics in a monodisperse regime. LOND core oils used here were squalane, squalene, and tripropionin.

6.5.2.1. Squalane OLI-MBs

The microfluidic LOND assembly and spreading route for the formation of OLI-MBs was most extensively developed using POPC squalane LONDS. This was due to squalane being a strongly hydrophobic oil and so being good as a model for the mechanism (as well as a potential agent as a drug carrier).

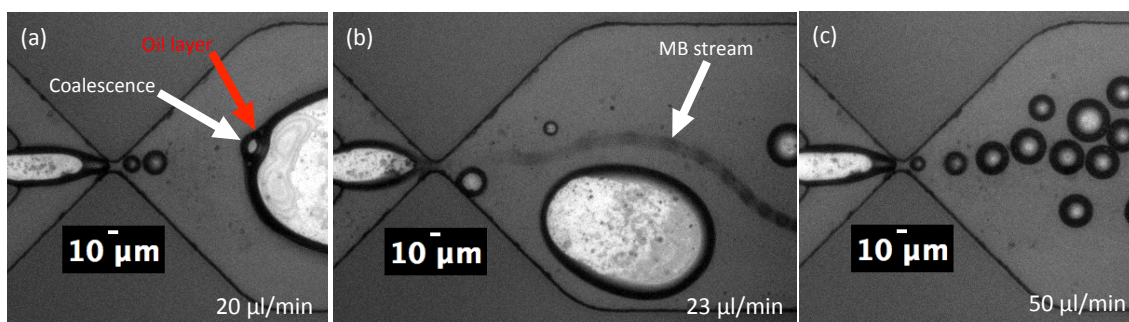


Fig. 6.21. Two-phase FF MB production using POPC squalane LOND solution diluted 1 in 10 in BB flown at (a) 20, (b) 23, and (c) 50 $\mu\text{l}/\text{min}$. Gas pressure of 3 psi used.

Figure 6.21 shows images of attempts to form OLI-MBs from POPC squalane LOND solution diluted to 10^{12} LONDS/ml in BB. A MB stream (which is typically observed for controlled FF non-oil-MB production) was able to be formed over a small range of flow rates (~ 5 $\mu\text{l}/\text{min}$) with optimal conditions at 23 $\mu\text{l}/\text{min}$ LOND solution and 3 si gas. However the MB formation stream was highly unstable and difficult to control. Additionally, coalescence was often observed leading to large gas pockets coated in an oil layer (Figure 6.21a). Post-production imaging showed no evidence of MBs remaining after any sample production.

Previous work has reported that, during the FF formation of lipid stabilised MBs, using higher concentrations of glycerol in the lipid solution phase (10-30 vol%) allows for the stabilisation of a higher concentration of MBs.²⁶⁰ As such, the POPC squalane LOND solution was diluted in BB containing 10 vol% glycerol in order to assess if this improved control over the production and MB stability for off-chip imaging.

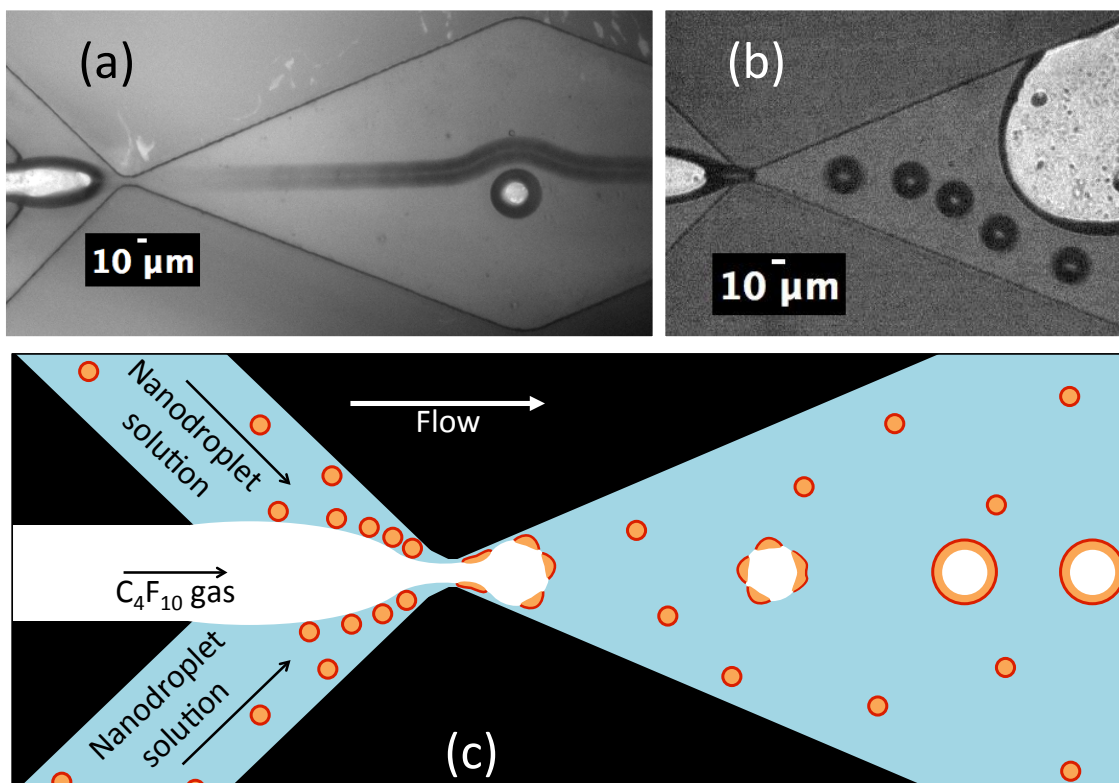


Fig. 6.22. (a) Two-phase FF MB production using POPC squalane LOND solution diluted 1 in 10 in 10 vol% glycerol BB, with (b) high frame rate imaging. C₄F₁₀ gas 4 psi, LOND solution 27 μl/min. (c) A schematic is shown for the proposed mechanism of LOND self-assembly, spreading, and merging, into an oil layer in order to stabilise the bare aqueous-gas interface.

Figure 6.22 shows OLI-MB formation from POPC squalane LONDS diluted to 10^{12} LONDS/ml in 10 vol% glycerol BB. It was observed that gas pressures as low as 3 psi could be used to form MBs, however MB formation rate was low at ~400 MBs/s. At 5 psi, a large proportion of the MBs coalesced just past the nozzle. These large MBs then became trapped in the 25 μm deep outlet, leading to further coalescing. This could be due to the MBs being formed at a high rate with insufficient time for the LONDS to adsorb and rupture at the gas-aqueous interface in order to stabilise the MBs. Optimal production occurred when using 4 psi and 26-28 μl/min LOND solution, giving MB streams in a highly repeatable manner, with production rates of $\sim 5 \times 10^3$ MBs/s, and on-chip MB size of 9 ± 2 μm (SD 3 μm).

Figure 6.23 shows OLI-MBs in microfluidic traps after washing steps, and their fluorescence from DiI loaded into the oil phase. These three MBs are from different formation repeats. The persistent fluorescent halo shows that, like the mechanical agitation OLI-MBs, the oil component was stable against shear forces and the removal of excess oil and lipid from the surrounding solution. Some of the OLI-MBs showed a fluorescent outside only (Figure 6.23cii), however more commonly OLI-MBs showed

more complex structuring at the shell consisting of a fluorescent outside plus a smaller fluorescent circular structure at a point on the MB shell (Figure 6.23aii-bii). These circles were thought to be oil lenses. The appearance of both the fluorescent outside and the lens suggests that the during OLI-MB formation, the LONDS spread into pseudo-partial wetting films.^{261,262}

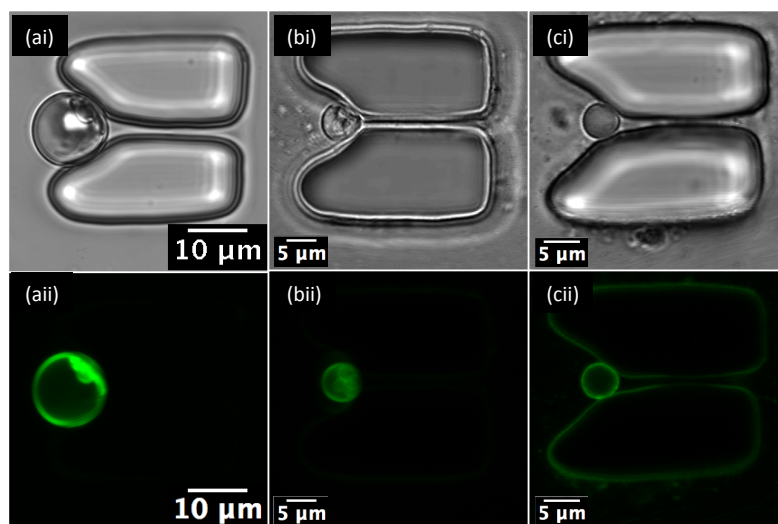


Fig. 6.23. Microfluidic, DiI encapsulated, POPC squalane OLI-MBs after trapping and washing steps form three different samples. (ai-ci) White light and (aii-cii) DiI fluorescence shown.

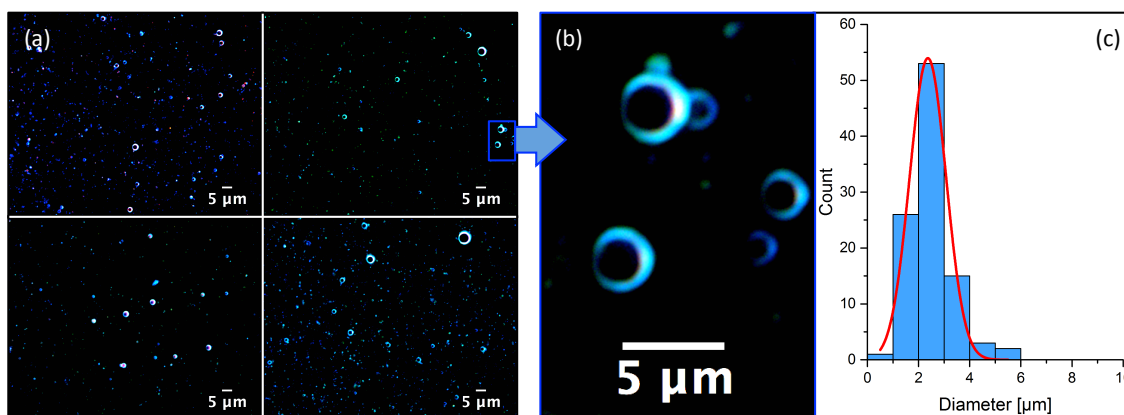


Fig. 6.24. Sizing images and results from microfluidic, POPC squalane OLI-MBs, formed using 4 psi gas and 24 $\mu\text{l}/\text{min}$ LOND solution, showing (a) dark-field images taken after production, (b) with a zoomed in section, and (c) a histogram of OLI-MB sizes.

Figure 6.24 shows off-chip imaging of microfluidic POPC squalane OLI-MB solution, for size distribution and concentration analysis. These MBs had diameters of $2.4 \pm 0.3 \mu\text{m}$ (SD $1.6 \mu\text{m}$) with a concentration of $6.2 \pm 0.8 \times 10^6$ MBs/ml. This was a reduction in size to ~ 0.27 times the on-chip size. This size change was most probably due to gas leakage from the interior of the MBs after production. A MB's diameter effectively stabilises when the lipid shell concentrates from an equilibrium state to being close

packed at the collapse pressure. This effect has been shown previously on DPPC:DPPA:DPPE-PEG5000 MBs formed using FF devices, where MBs shrank to 0.39 times their initial size.¹⁸⁰ The same effect would be expected to be observed from OLI-MBs due to the outer lipid shell.

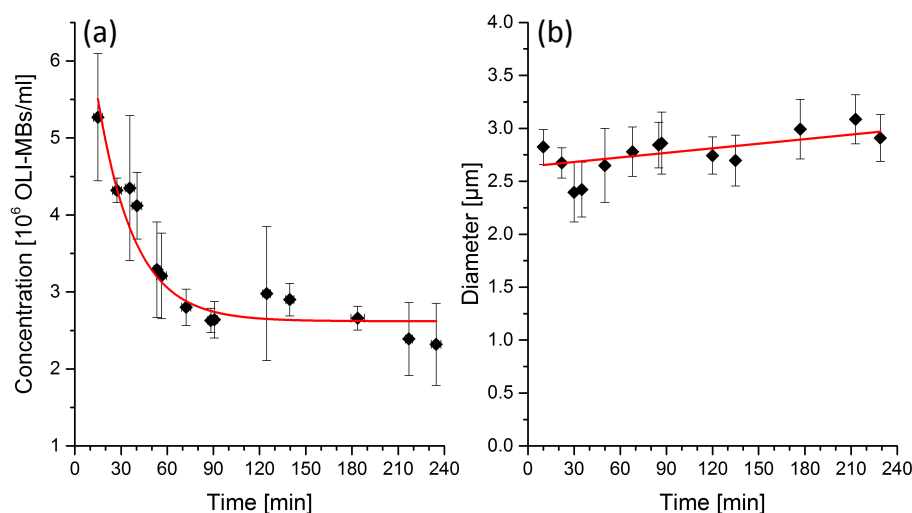


Fig. 6.25. (a) Concentration and (b) diameter of microfluidic squalane OLI-MBs as a function of time, at $\sim 25^\circ\text{C}$. The data presented represents the average of two MB production runs. Each run averaged from three sample aliquots.

Figure 6.25 shows the changes in diameter and concentration of microfluidic squalane OLI-MB over time. The concentration over time showed an exponential decrease, with a sharp initial decrease in concentration over the first 90 minutes, after which the MB concentration appeared stable for the duration of the measurement. During this period the MB population showed a modest increase in size, presumably due to Ostwald ripening.⁹⁰ Figure 6.26 shows a comparison of both the concentration of the mechanical agitation and microfluidic squalane OLI-MBs, both normalised to 100% when $t = 0$ min. Even though the average MB size was significantly different, both OLI-MB production routes showed very similar concentration decay mechanics, especially over the first 60 min. Eventually the two routes stabilised at 26% and 33% of their original concentration for mechanical agitation and microfluidic samples respectively, though as can be seen, the differences were generally within error between the two routes. The high similarity in concentration decay between the two routes suggested that the LONDS had stabilised both MB samples in the same way. This is because MBs stabilised with different shells would be expected to have significantly different lifetime characteristics (dependant on: shell surface tension, gas diffusion rate across the shell, etc., see Theory Chapter 3.2.3, p 41-44).

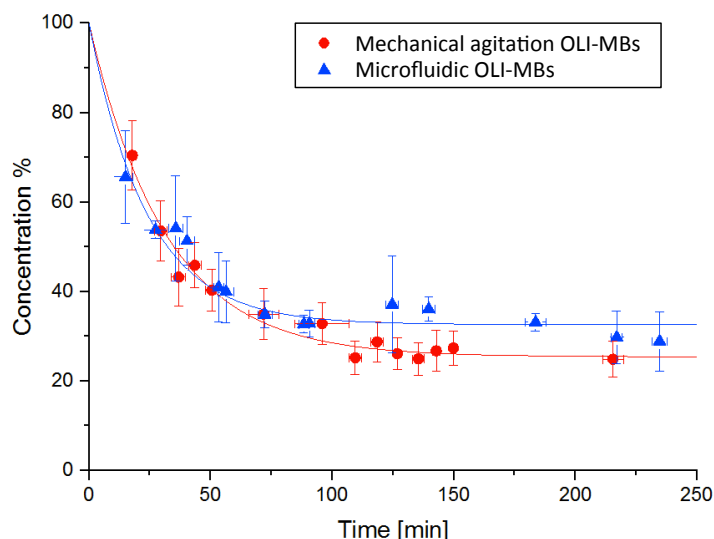


Fig. 6.26. Concentration over time for both the mechanical agitation (red circle) and microfluidic (blue triangle) POPC squalene OLI-MB samples. For both data sets, the exponential fits have been normalised to 100% at $t = 0$ min.

6.5.2.2. Squalene OLI-MBs

After the successful production of monodisperse squalene OLI-MBs, squalene OLI-MBs were formed to be used in later intrinsic oil fluorescence work (see section 6.7). Here, the optimal production was again found, followed by wash steps.

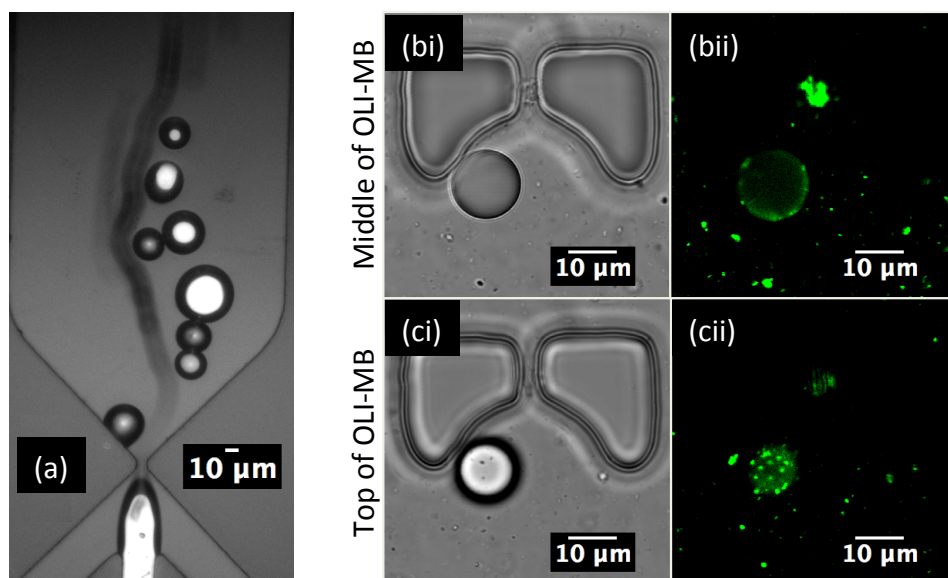


Fig. 6.27. (a) Two-phase FF OLI-MB formation using POPC squalene LOND solution diluted 1 in 10 in 10 vol% glycerol BB. C_4F_{10} gas 4 psi, LOND solution 23 $\mu\text{l}/\text{min}$. (b-c) A POPC squalene OLI-MB is then shown after microfluidic trapping and washing. (i) Brightfield and (ii) fluorescence from DiI loaded into the oil is shown, where the focal plane is (b) through the center and (c) at the top surface of the OLI-MB.

Figure 6.27a shows the optimal FF production found for forming OLI-MBs from POPC squalene LONDS diluted to 10^{12} LONDS/ml in 10 vol% glycerol BB. Optimal production occurred at 4 psi C_4F_{10} and 23-25 $\mu\text{l}/\text{min}$ LOND solution. Formation of MBs from squalene LOND solution was found to be less stable than that using squalane LONDS. This may have been due to the high proportion of unsaturated double bonds in squalene compared to squalane (which is fully saturated), presenting a weaker hydrophobic driving for LOND assembly and spreading at the gas-aqueous interface. As such the concentration and monodispersity of squalene OLI-MBs were expected to be lower than squalane OLI-MBs. Since the intended use of these MBs was for single MB analysis (Raman section 6.7), that was not a factor for this project, however it should be noted that due to this squalene OLI-MBs would not be of practical use for drug delivery. Figure 6.27b-c shows one of these squalene OLI-MBs after trapping and washing steps, where the imaging focal plane was placed either through the OLI-MB centre or at the top of the OLI-MB. Here it can be seen that the OLI-MB had a ‘patchy’ surface of high fluorescence, surrounded by a full MB shell of lower fluorescence. This was another suggestion of a pseudo-partial wetting oil layer around the MB (where the higher fluorescence would indicate a higher proportion of fluorophore and so a thicker oil structure at those locations), however, unlike the squalane OLI-MBs which appeared to have one concentrated oil lens, here there are many smaller lenses across the MB shell.

6.5.2.3. Tripropionin OLI-MBs

Extending the successful formation technique of the microfluidic OLI-MB production to tripropionin oil would allow for the encapsulation of less hydrophobic, but still poorly water soluble drugs. Therefore, formation was also trialled with POPC tripropionin LONDS.

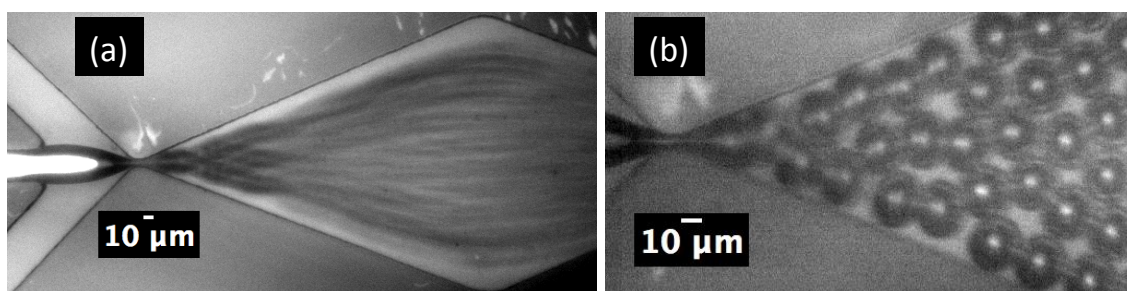


Fig. 6.28. Two-phase FF MB production using tripropionin POPC LOND solution diluted 1 in 10 in tripropionin saturated 10 vol% glycerol BB, with (a) standard and (b) high frame rate imaging. Gas (a) 4 and (b) 6 psi, LOND solution 23 $\mu\text{l}/\text{min}$.

Figure 6.28 shows OLI-MB formation from POPC tripropionin LONDS diluted to 10^{12} LONDS/ml in 10 vol% glycerol BB that had been pre-saturated with tripropionin. In general, microfluidic OLI-MB formation using POPC tripropionin LONDS was vastly superior to that using squalane or squalene POPC LONDS. MB formation from any other LOND solution or non-oil-lipid solution used throughout this project was only ever observed to form MBs with enough control to give a single MB stream. Using tripropionin POPC LONDS, MBs were formed and stabilised rapidly enough to allow MBs to close pack without coalescing as they were flowing through the outlet. This gave the appearance of multilayered MB steams, some of which were close packed enough to fill the entire outlet channel (seen in Figures 6.28a and 6.28b). The implication of these results suggested two important features to the tripropionin OLI-MBs;

- 1) The stabilisation of the OLI-MBs by the accumulation and spreading of the tripropionin LONDS occurred at a far faster rate than either squalane LONDS or non-oil-lipid structures found in standard lipid solution (monomers, micelles, etc)
- 2) The addition of the tripropionin oil led to the OLI-MBs' effective gas-oil-lipid-water interface shell having a dramatically reduced surface tension compared to OLI-MBs formed from squalane LONDS and MBs formed from lipid alone.

Both of these features would be required from the MB shell to prevent coalescence and allow formation to occur at this high rate.

When using 3 psi gas, the on-set of rapid coalescence was found to occur when using LOND solution flow rates above 35 $\mu\text{l}/\text{min}$. This indicated that as the flow rate increased, the LONDS were not having sufficient time to stabilise the OLI-MBs inbetween pinching-off from the main gas bulb and contact with another OLI-MB. Due to this, lower flow rates were preferred until coalescence was not observed in the outlet. Optimal production was found at 4-5 psi C_4F_{10} and $\sim 25 \mu\text{l}/\text{min}$ LOND solution, giving MB formation rates of $35 \pm 10 \times 10^3$ MBs/s, seven times higher than that using POPC squalane LOND solution.

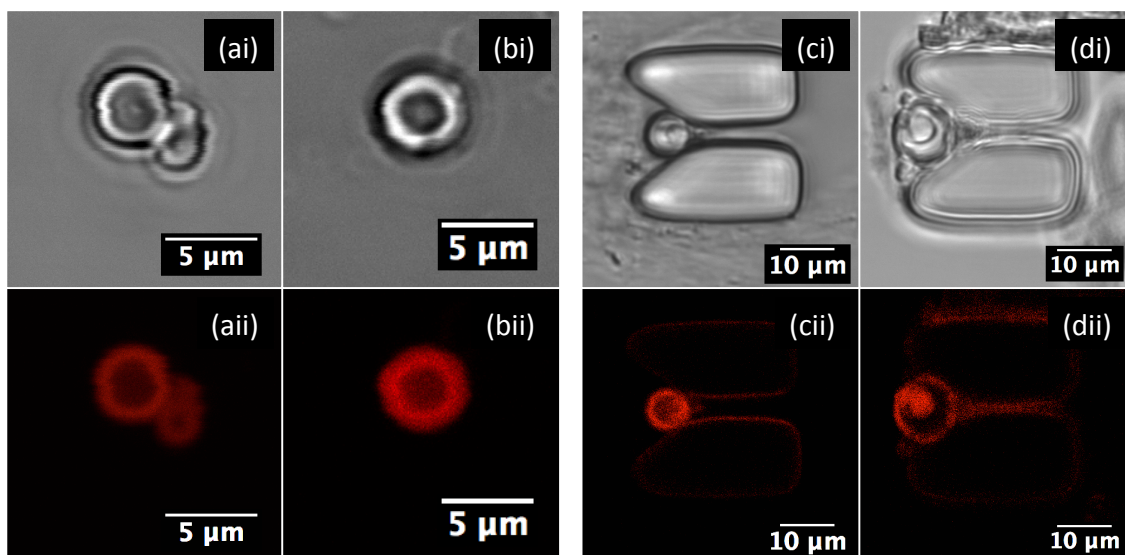


Fig. 6.29. Microfluidic tripropionin OLI-MBs, formed as in Figure 6.28 using optimal production rates. (a-b) OLI-MB solution placed inside a 50 μm chamber and (c-d) after microfluidic trapping and washing steps. Imaging by confocal microscope under (i) white light and (ii) fluorescence from Nile red that had been solubilised into the tripropionin before LOND formation.

Figure 6.29 shows examples of the microfluidic POPC tripropionin OLI-MBs imaged in 50 μm chambers (Figure 6.29a-b), and microfluidic traps after wash steps (Figure 6.29c-d). In the 50 μm chambers, the OLI-MBs were found to have a thick fluorescent layer, suggesting the presence of an oil shell (Figure 6.29a-b). The oil shell thickness was potentially exaggerated due to the OLI-MBs sitting and being deformed against the glass surface, with the gas core being more buoyant than the oil layer. The 50 μm chamber OLI-MBs were found to have an average size of 4.8 ± 0.3 (SD 0.7) μm , with an apparent oil layer thickness of 1.1 ± 0.1 (SD 0.2) μm . For the OLI-MBs washed in microfluidic traps, the fluorescent oil portion was observed to remain around the OLI-MBs' shell (Figure 6.29c-d). Again evidence was given of pseudo-partial wetting in the form of fluorescent circles (with white light contrast) at the OLI-MBs' shell in addition to the OLI-MBs' fluorescent shell.

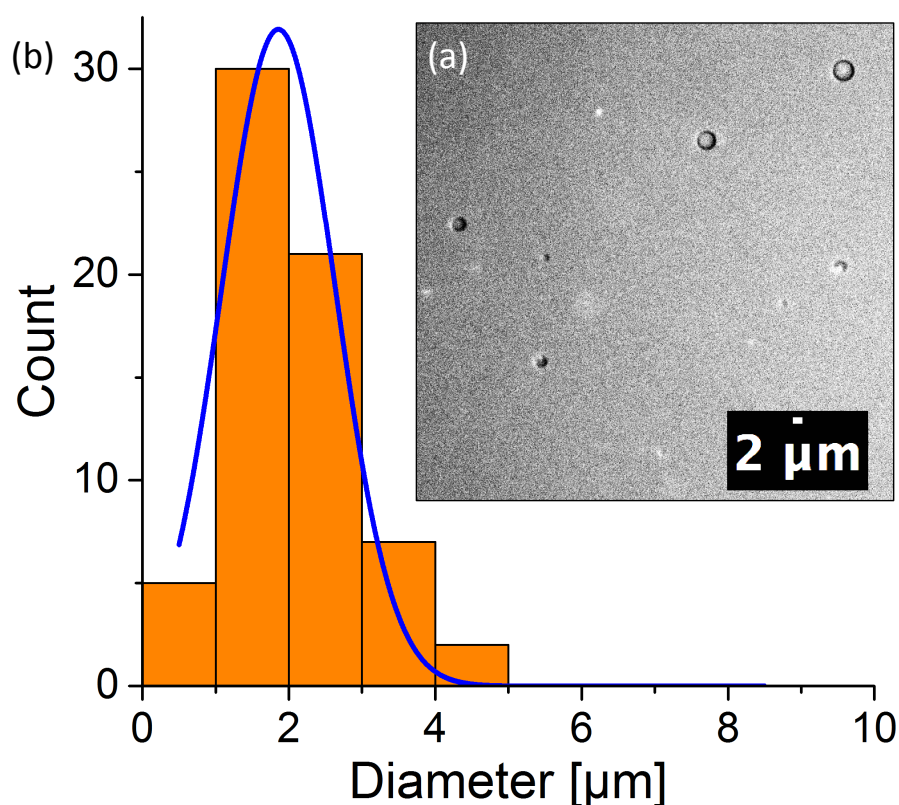


Fig. 6.30. (a) Sizing image and (b) resulting sizing histogram from microfluidic POPC tripropionin OLI-MBs, formed using gas 4 psi and LOND solution 25 $\mu\text{l}/\text{min}$. For imaging, the OLI-MB solution was placed in a 'non-microfluidic flow cell' (Experimental Chapter 4.3, p 71).

Figure 6.30 shows an image of the tripropionin OLI-MBs off-chip and the resulting size distribution measured. Even though the tripropionin OLI-MBs were formed at a high rate on-chip, off-chip the OLI-MBs concentration was found to be very low. Therefore, the MB sample was imaged in one of the large volume $\sim 500\text{ }\mu\text{m}$ deep non-microfluidic flow cells and the MBs allowed to float to the surface. The MBs were found to have an average diameter of $2.1 \pm 0.1\text{ }\mu\text{m}$ (SD $0.8\text{ }\mu\text{m}$), at a concentration magnitude of 10^5 OLI-MBs/ml. Surprisingly, even though the on-chip production rate was seven times faster than when using squalane LONDS, the off-chip concentration was found to be an order of magnitude less. This means that the tripropionin OLI-MBs were less stable to the changes in shear forces when transferring from on-chip, to the OLI-MBs collection point, or simply less stable over time. Figure 6.31 shows size and concentration changes over time for two samples. At least over the first two hours of measurement the size of the OLI-MBs was stable. However, the concentration over time did not show an exponential decay as expected. Over the first ~ 90 min both samples increased in concentration, after which the concentration of first sample began to decrease, as expected, whilst the second sample continued to increase. This indicated that the rise time of the MBs was longer than expected, taking at least 90 min. Tripropionin is more

dense than water whilst C_4F_{10} gas is less dense. This meant that all of the structures floating to the top surface must have been at least part gas due to buoyancy. For a 2 μm MB with a tripropionin shell to take on average 90 min to rise the chamber depth, the gas core diameter would need to be 0.86 μm with a 0.57 μm thick oil shell (tripropionin oil would make up 92% of the total OLI-MB volume). This total OLI-MB diameter to oil layer thickness ratio roughly agrees with that found for the OLI-MBs seen in Figure 6.29 (where tripropionin oil would make up 84% of the total OLI-MB volume). However, for a MB to have zero buoyancy in water the gas core diameter would need to be 0.81 μm with a 0.59 μm thick oil shell (93 vol% tripropionin). Clearly a very small change in oil layer thickness would have a dramatic impact on the buoyancy of the tripropionin OLI-MBs. This might explain why samples 1 and 2 seen in Figure 6.31 showed different concentration profiles.

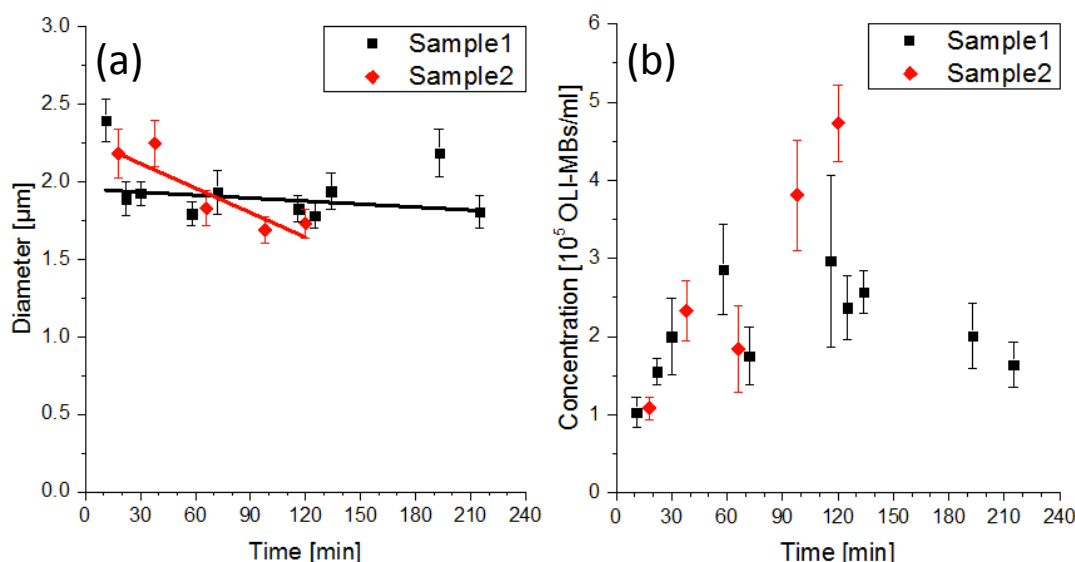


Fig. 6.31. (a) Concentration and (b) diameter of microfluidic tripropionin OLI-MBs as a function of time, at ~ 25 °C. Two sample runs are shown, where each sample was averaged from three aliquots.

6.5.3. Microfluidic spray production

The production of OLI-MB samples by the microfluidic monodisperse regime gave concentrations of 10^6 and 10^5 OLI-MBs/ml when using squalane or tripropionin POPC LOND solutions respectively. 10^6 MBs/ml was the minimum concentration required for our set-up to determine US characteristics (see section 6.8). In order to have any repeats and more reliable measurements at individual frequencies, concentrations of 10^7 - 10^8 OLI-MBs/ml were required. Gaining this higher concentration was also deemed necessary for their clinical application. The microfluidic formation of lipid shelled MBs via FF designs in the monodisperse regime has previously been shown to form MBs at a

concentration that is too low for clinical application.⁴³ In Leeds, this problem was solved by using the ‘microspray’ regime. Here, MBs were readily formed at 10^8 to 10^9 MBs/ml. Though the polydispersity index was higher, the average diameter was $\sim 2 \mu\text{m}$ and with few MBs larger than $4 \mu\text{m}$.⁴³ Attempts to use that microspray regime for OLI-MB formation unfortunately were not successful.

The tripropionin sample did show successful formation of a population of MBs, averaging $2.9 \pm 0.1 \mu\text{m}$ (SD $1.0 \mu\text{m}$) at $3.4 \pm 0.5 \times 10^5$ MBs/ml. However, the concentration was found to be only 14% higher than that of the monodisperse regime production. Further, a bimodal distribution of MBs was found with the second distribution averaging $23 \pm 1 \mu\text{m}$ (SD $5 \mu\text{m}$) at $1.3 \pm 0.1 \times 10^5$ MBs/ml. Table 6.1 presents how the microspray formation compared to the monodisperse formation.

Tab. 6.1. Size and concentration results from MB formation in the monodisperse and microspray regimes, using squalane and tripropionin POPC LONDS.

	Diameter [μm]	Error	SD	Concentration [MBs/ml]	Error
Squalane monodisperse	2.4	0.3	1.6	6.2E+06	8E+05
Squalane microspray	MBs were not found to be stable off-chip				
Tripropionin monodisperse	2.1	0.1	0.8	3.0E+05	6E+04
Tripropionin microspray	2.9	0.1	1.0	3.4E+05	5E+04
	22.8	1.1	5.3	1.3E+05	1E+04

These results showed that microspray production did not achieve the higher concentration samples that were desired. Moving forward, OLI-MBs were formed for further analysis from either the microfluidic monodisperse regime or mechanical agitation methods (since the mechanical agitation OLI-MBs were larger, they were used both as a preliminary tool to the analysis of the microfluidic OLI-MBs, and for greater resolution during fluorescence imaging of the OLI-MB shell).

6.6.LOND introduction to stable MBs

In the previous sections OLI-MBs had been formed using POPC LOND solutions. The hypothesis was that LONDS adsorbed at the air-water interface and formed a lipid-oil lens or a continuous oil layer during formation. An important aspect of this hypothesis was that during formation the freshly formed MB surface would not yet be stabilised by lipid, so would have a high surface tension.

Here, a study is presented of LOND interactions with stabilised lipid MBs. The LONDS were flown past the stabilised MBs and fluorescence observations were made to assess if the oil portion transferred into the MB shell. Lipid stabilised MBs were formed using a two-phase FF microchip, under a microfluidic monodisperse regime, from 4 psi C_4F_{10} gas and 20 $\mu\text{l}/\text{min}$ DPPC-PEG lipid solubilised in 10 vol% glycerol BB. Off-chip sizing, showed that the MBs were formed at $12.3 \pm 0.5 \mu\text{m}$ (SD 2.6 μm). These MBs were trapped in a microfluidic trap device and washed with PBS. DiI POPC squalane LONDS were flown past the MBs, after which the MBs were washed again with PBS until no background fluorescence was observed (indicating the removal of excess LONDS).

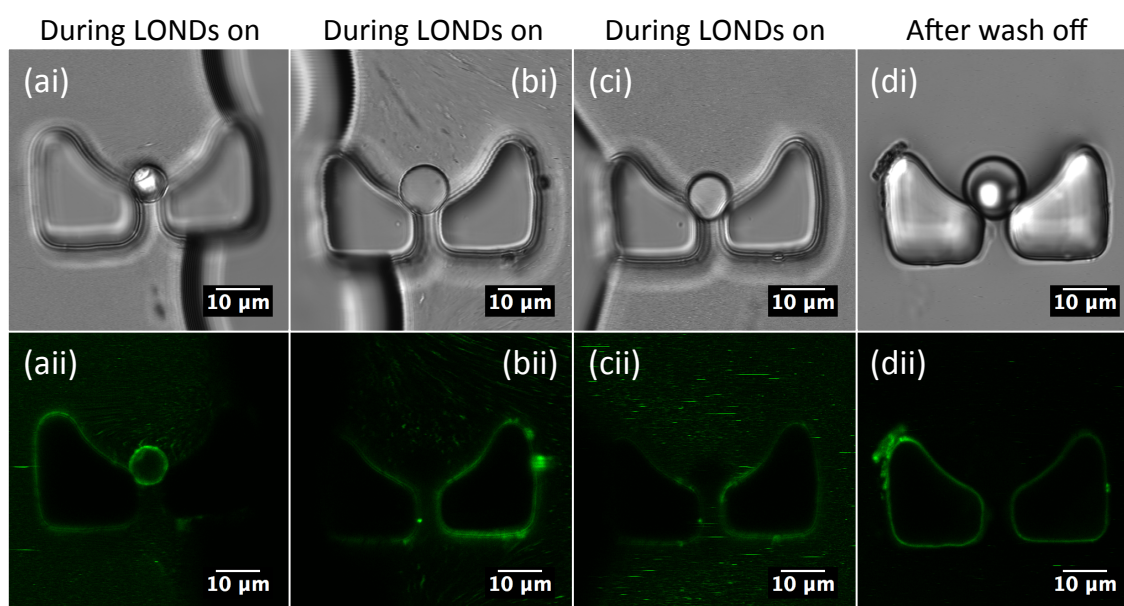


Fig. 6.32. DPPC-PEG MBs trapped and washed, followed by (a-c) the addition of DiI POPC squalane LONDS into the trapping chamber, and then (d) washing of the MBs to remove the excess LONDS. (i) White light and (b) DiI fluorescence emission window are shown. All flow at 10 $\mu\text{l}/\text{min}$.

Figure 6.32 shows the fluorescence signal from DiI encapsulated into POPC squalane LONDS as the LONDS were flown past multiple DPPC-PEG MBs (Figure 6.32a-c), and then after the excess LONDS have been removed by a washing step (Figure 6.32d). Most MBs remained non-fluorescent (as they were before LOND introduction). Figure 6.32a shows that a small fraction of the MBs were seen to become fluorescent during the LOND introduction step, however after washing none of them remained fluorescent. These results showed that LONDS could adhere to the MB shell intact, but that the binding was non-specific, and that the LONDS could not have merged with the MB shell. These results agreed with those seen in the LB trough experiment and confirmed that LONDS cannot form OLI-MBs from MBs that are already fully stabilised by DPPC-PEG lipid shells.

6.7. Using FRET to assess LOND rupture at a MB surface

In this section OLI-MBs were produced from LONDS that were formed with the specific intention of having FRET capabilities. This was done to assess whether POPC shelled LONDS led to the formation of OLI-MBs (with a complete oil layer or oil lenses) and whether POPC-PEG shelled LONDS led to the formation of MBs stabilised by intact LOND shells. The experimental concept was to form two sets of LOND solutions, one encapsulating a FRET donor, the other the FRET acceptor, and then mix them. If the LONDS ruptured at an aqueous-gas interface, this would lead to mixing of the oil cores loaded with the FRET fluorophores, and thus allow for the production of FRET signal. On the other hand if the LONDS remained intact, fluorescence would be observed but no FRET.

6.7.1. Assessment of FRET fluorophores

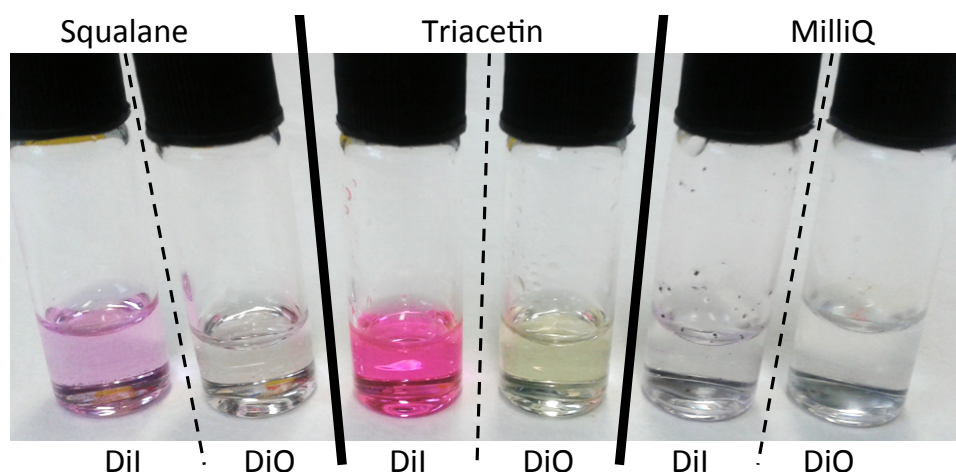


Fig. 6.33. DiO and DiI, FRET donor and acceptor respectively, dissolved in squalane and triacetin at 15 $\mu\text{g}/\text{ml}$. The fluorophores did not dissolve in MilliQ.

Figure 6.33 shows DiO and DiI fluorophores at 15 $\mu\text{g}/\text{ml}$ in ~ 1 ml of squalane oil, triacetin, and MilliQ. Successful solvation was indicated by colouration of the liquid phase. This was achieved for both squalane and triacetin. Solubilisation in MilliQ was unsuccessful, where aggregates of the fluorophores could be seen to have remained against the glass vial walls, which was expected due to the strong hydrophobic nature of the DiO and DiI.

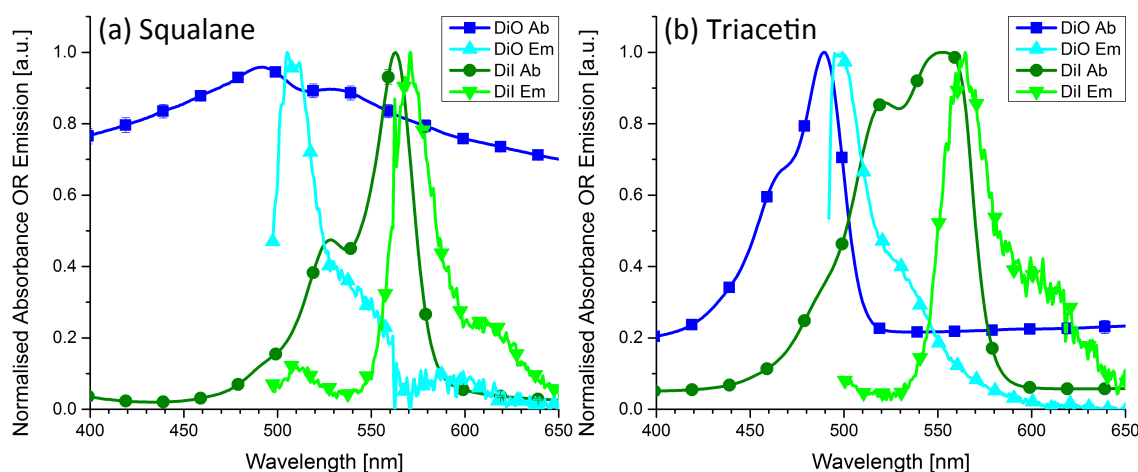


Fig. 6.34. Excitation and emission spectra of DiO and DiI in (a) squalane and (b) triacetin. The graphs were corrected for oil's background, and their maximum value was normalised to 1. A 488 nm laser was used as the excitation source for all emission recordings.

Figure 6.34 shows the excitation and emission spectra of squalane and triacetin loaded with DiO or DiI. For both oils a significant spectral overlap was present between the donor (DiO) emission and acceptor (DiI) excitation spectra. This is one of the requirements for FRET to be able to occur (Theory Chapter 3.4, p 48-50). Tripropionin oil was used as a direct means of improving LOND solutions formed by triacetin oil due to its lower water solubility (results for triacetin LONDS are not shown). However, squalane oil had previously been shown to form more consistent LOND solutions, in regards to oil droplet size and concentration. Therefore, squalane oil was chosen as the primary oil carrier for the DiO and DiI fluorophores during the following FRET experiments.

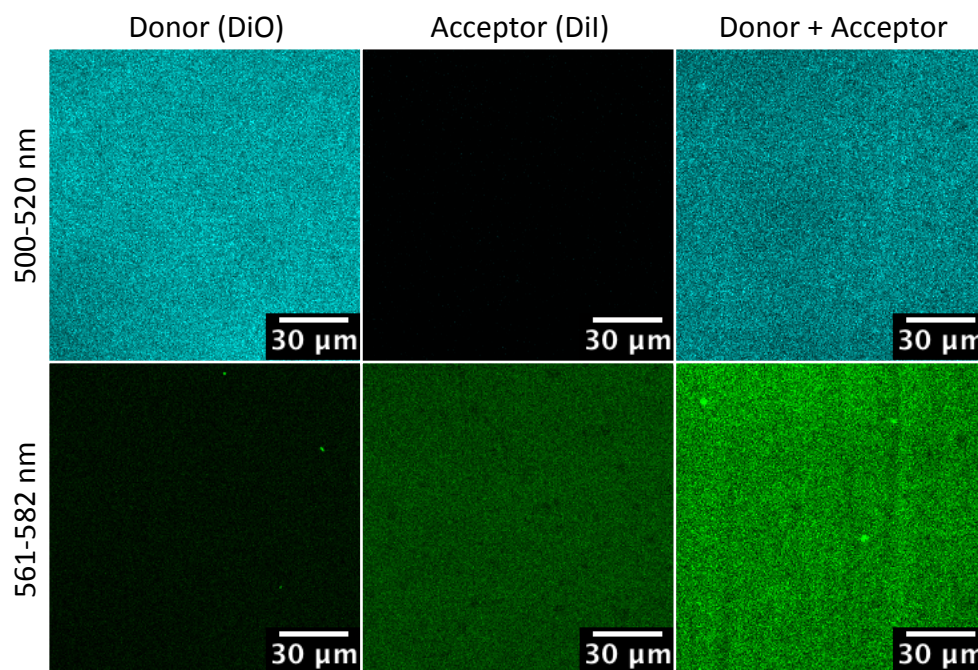


Fig. 6.35. Confocal images of squalane oil in a 50 μm chamber loaded with DiO, DiI or both, where the concentration of each fluorophore was 30 $\mu\text{g}/\text{ml}$. All samples imaged in both the donor and acceptor emission windows, 500-520 nm and 561-582 nm respectively.

Figure 6.35 shows confocal images of the donor and acceptor emission window signals from squalane oil solutions loaded with DiO, DiO, or with a mix of both fluorophores. Figure 6.36 shows how the intensity varied across the pixels of these images. When both fluorophores were together the intensity of the donor emission window was found to be less than when DiO was without the DiI. This indicated that FRET was taking place as a portion of the energy from the DiO was being transferred to the DiI acceptor rather than being emitted. When both fluorophores were together the acceptor emission window intensity was found to be greater than the sum of the intensities from both the separate donor and acceptor images. The sum of the images was the intensity that was expected if the fluorophores emitted independent of each other without FRET occurring. Any intensity above this was therefore determined to be the FRET portion of the signal, which was seen in the signal from the donor + acceptor image. Since the intensity across each image was recorded as a distribution of pixel intensities, in reality this method may have discounted a portion of the FRET signal where there was overlap between the donor and acceptor sum distribution and the donor + acceptor distribution. However any pixels found to have intensities in this overlap region could not be defined as FRET occurring or not occurring, so could not be used as evidence of FRET, and therefore was disregarded.

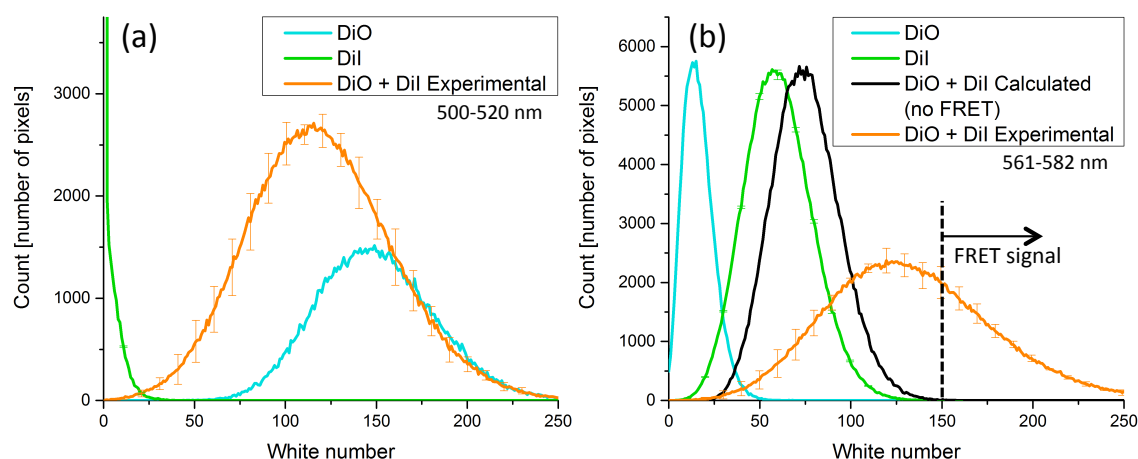


Fig. 6.36. Histograms of the intensity (white number) from the images in Figure 6.35. Showing the distribution of intensities from the images acquired using the (a) 500-520 nm donor and (b) 561-582 nm acceptor emission windows. For the acceptor emission window distributions, a (black) calculated distribution is shown of the addition of the (DiO) donor and (DiI) acceptor signals, which would be expected if FRET did not occur, and (orange) the experimental signal from the (DiO + DiI) donor + acceptor sample, where (dotted line) the higher intensity portion of the signal that can be attributed to FRET is indicated.

Figure 6.37 shows the emission spectra from POPC squalane LONDS loaded with either DiO or DiI fluorophores and a spectra from a solution where both LOND types were mixed. The concentration for each LOND type was kept constant. Since the aim was to use the mixed LOND samples for forming MBs where they would rupture and mix, it was important that the LONDS did not spontaneously coalesce prior to MB formation. If spontaneous coalescence did occur, FRET would be enabled, and observed as an increase in the DiI peak emission intensity. The emission spectra for the mixed LONDS sample was compared to a calculation of the sum of emissions from the separate DiO and DiI LOND samples (Figure 6.37b, black trace). It can be seen that the experimental recording was equivalent to the calculated one, especially and importantly at the DiI emission peak wavelength. This result confirmed that the LONDS were not spontaneously rupturing, coalescing and mixing their oil cores as FRET had not occurred.

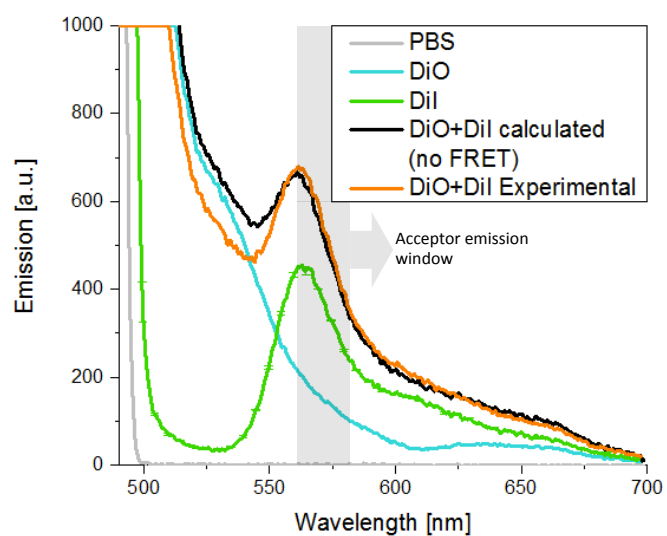


Fig. 6.37. Emission signal from separate and mixed samples of DiO and DiI POPC squalane LONDS. Each LOND concentration was 10^{11} LONDS/ml the signal result of the sum of the DiO and DiI signals is shown in black, and corresponds to what would be expected if FRET did not occur.

6.7.2. FRET at model MB air-water interfaces

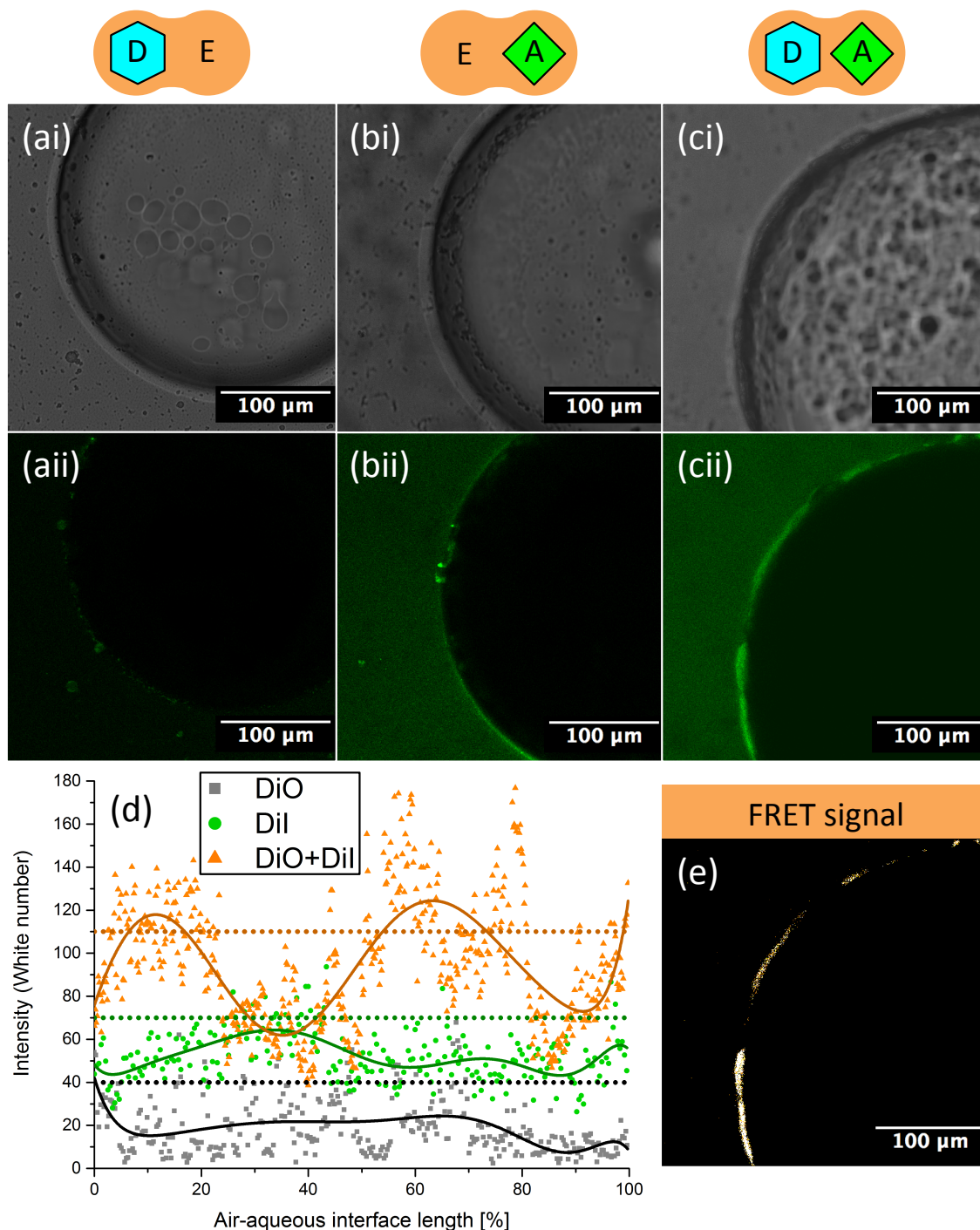


Fig. 6.38. Large air bubbles immobilised in 50 μm chambers by POPC squalane LOND solution containing mixes of donor (D), acceptor (A), and non-fluorescent/empty (E) LONDS. (i) White light and (ii) acceptor emission window fluorescence (561-582 nm) shown. (d) White number intensity at the bubble surfaces, from images *a*ii-*c*ii, is shown with 9th order polynomial fits to each data set (full lines) and a line to indicate the maximum fluorescence recorded from the DiO and DiI samples (dotted black and green lines) (single point noise was discounted) and a sum of two maximum fluorescence values (dotted orange line) to indicate the threshold for identification as FRET signal (as calculated using Equation 4.17, p 96). (e) The DiO+DiI fluorescence image, *c*ii, is then shown with the FRET threshold value removed.

Figure 6.38 shows the experimental acceptor emission following the trapping of large air bubbles by squalane POPC LONDS containing DiO donor, DiI acceptor, and no fluorophore. FRET was shown to occur at the fresh (not yet stabilised) gas-aqueous interface. This provides evidence that the LONDS adsorbed and ruptured at the interface, where the oil, and loaded fluorophores, from both LOND populations, mixed together allowing the FRET to occur. However the FRET signal was seen to be non-uniform along the surface, suggesting more oil at some locations compared to others. This implied the partial wetting of the air-water interface by the oil. The FRET image was calculated by taking the maximum fluorescence at the gas-aqueous interface from the donor + empty and empty + acceptor images (not including random point sources). This will likely have led to the FRET image to not include any of the thinner oil portions at the gas-aqueous interface, even though FRET may still have occurred there. Therefore, (Figure 6.38e) the FRET image seeming to show that FRET only occurred as lenses is likely an artefact of the image manipulation.

6.7.3. FRET to confirm OLI-MB formation

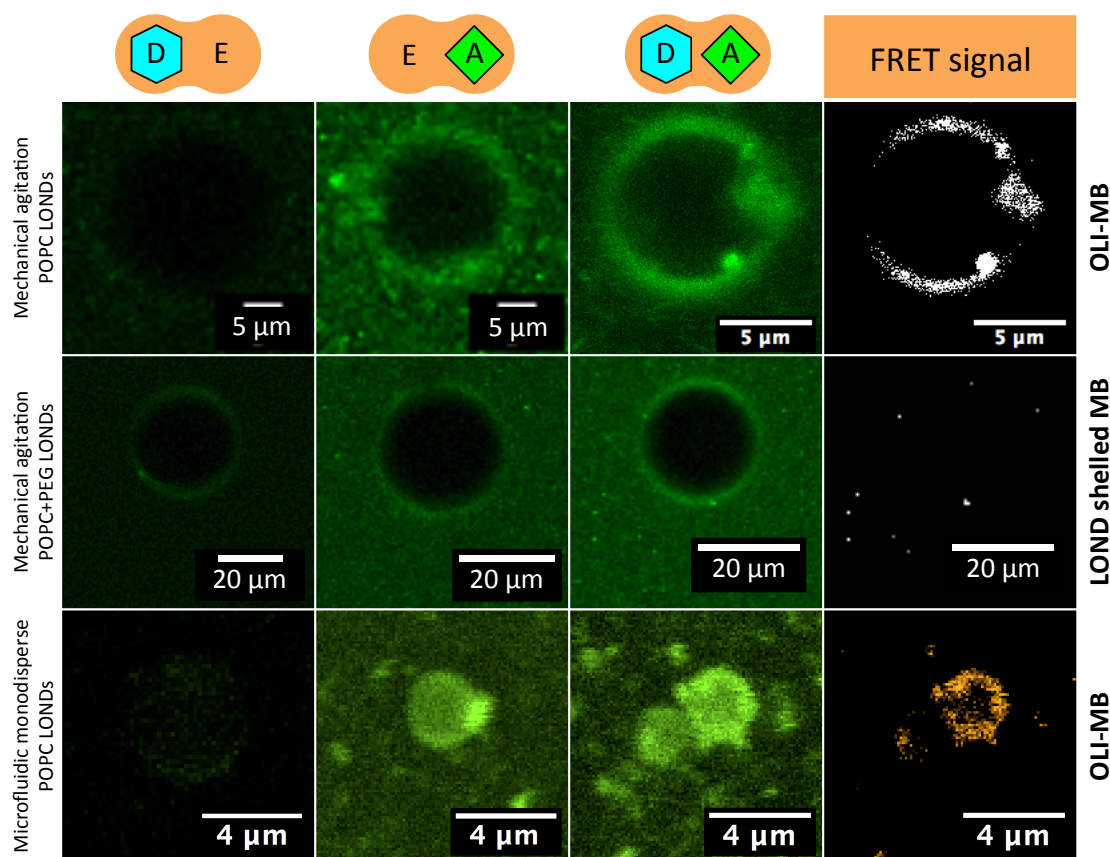


Fig. 6.39. Mechanical agitation and microfluidic monodisperse MBs formed from POPC squalane LOND solution containing mixes of donor (D), acceptor (A), and non-fluorescent/empty (E) LONDS. Acceptor emission window (561-582 nm) fluorescence shown. FRET images calculated as in Figure 6.38.

Figure 6.39 shows the FRET experiment using MBs formed from the POPC squalene LOND solutions. Mechanical agitation and microfluidic monodisperse MBs (formed as in sections 6.5.1 and 6.5.2.1 respectively) are shown, with the former also being stabilised by POPC-PEG LONDS. FRET occurred at the MB surface for both formation techniques when using POPC LONDS. This confirmed that both formation techniques successfully formed OLI-MBs. Irregular fluorescence was seen around the shells, suggesting that the shell was not a simple uniform oil layer. For the microfluidic OLI-MB FRET signal image, it can be seen that one of the MBs had this irregular but almost full shell FRET, whereas the other was lacking FRET across almost the entire shell. This suggested that the oil portion could vary from OLI-MB to OLI-MB. When repeating this experiment with POPC-PEG LONDS, FRET was not observed. Here, the fluorescence at the MB shells from the donor + acceptor sample was found to be slightly lower than the sum of the shell fluorescence from the donor + empty and empty + acceptor samples. This agreed with the LOND fluorescence emission results found in Figure 6.37, where the mixed LOND samples had not yet merged. Since a high MB shell fluorescence was still observed the MBs must have been stabilised by the LONDS, but the lack of FRET showed that the LONDS remained intact, forming a shell of LONDS.

6.8. Native oil fluorescence as an alternative to fluorescent oil-loading

Much of the work covered in the previous sections of this chapter used fluorescence as a marker for oil, to prove the formation of MBs with oil portions, including OLI-MBs. This was accepted as a method since the fluorophores used were known to be hydrophobic, solubilised well in to the oils used, and had previously been used in literature as drug mimics entrapped in micelle hydrophobic cores.²³⁰ However, since lipids have hydrophobic tails, even if very unlikely, it could be speculated that there would be the possibility for MBs to be stabilised by LONDS through a process of the LONDS supplying the MB surfaces with lipid and the loaded fluorophore, but no oil. Almost every section of this chapter holds evidence that disagrees with this as a possible mechanism of stabilisation. As a further confirmation that oil had been loaded into the OLI-MBs, microfluidic and mechanical agitation POPC squalene OLI-MBs were formed and tested for fluorescence intrinsic to the oil without loading any fluorophore into any phase.

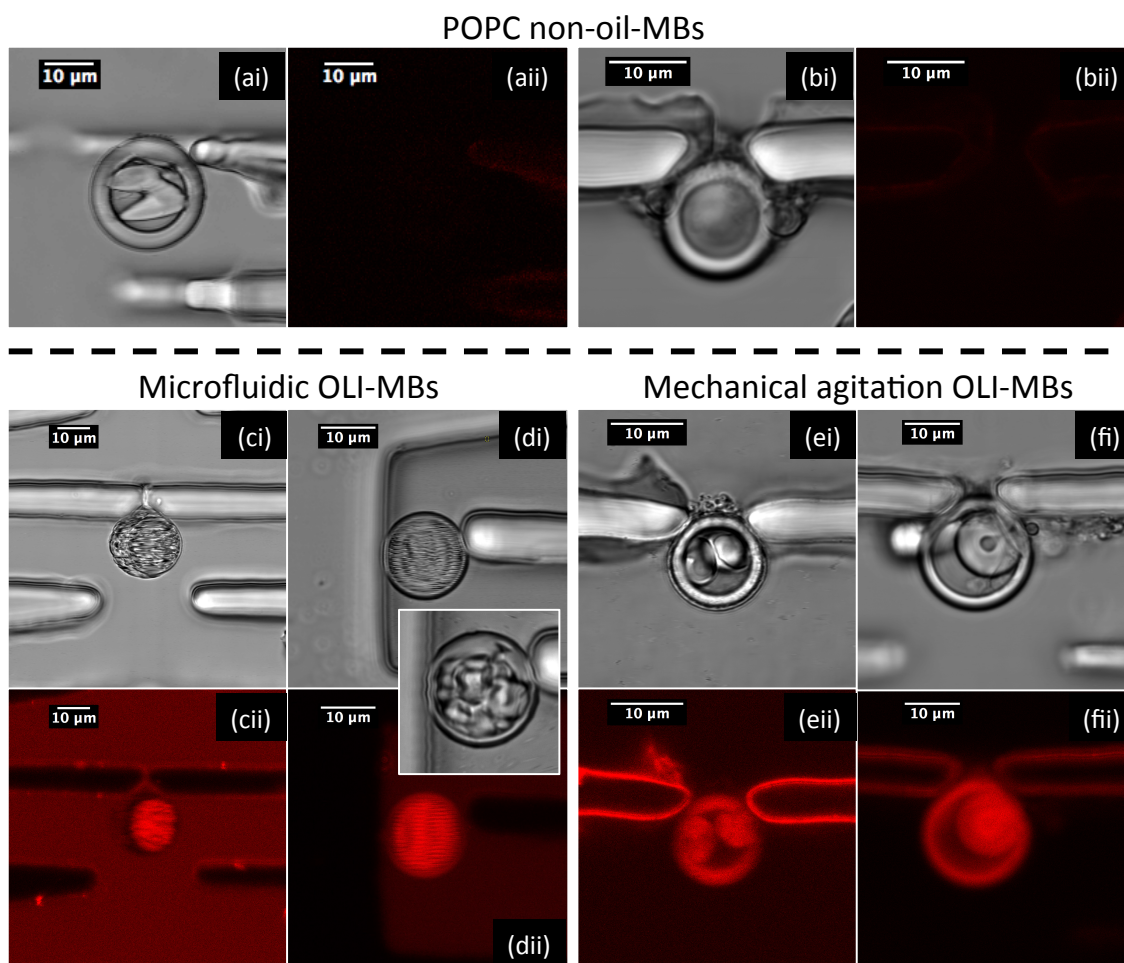


Fig. 6.40. Three samples of MBs, trapped and washed, including (a-b) mechanical agitation POPC non-oil-MBs, (c-d) microfluidic monodisperse POPC squalene OLI-MBs, and (e-f) mechanical agitation POPC squalene OLI-MBs. Two MBs are shown for each formation type, both imaged by (i) white light and (ii) 500 - 794 nm fluorescence, using a 488 nm excitation laser source (5% power, 750 V gain). Fluorescence intensity in the background trap device was indicative of the degree of washing, with (cii, eii) high background intensity images indicating LONs remaining in the surrounding solution, and (dii, fii) low background intensity images indicating a total removal of excess LONs. Whilst washing (a, c, and d) many of the MBs rotated. (Inset in d) An inset is shown of a rapidly acquired snap shot from one of the spinning MBs.

Figure 6.40 shows the intrinsic fluorescence from POPC lipid stabilised non-oil-MBs and POPC squalene OLI-MBs, formed by both monodisperse regime microfluidics and mechanical agitation, during and after washing. Fluorescence was observed in both of the squalene OLI-MB types but not for the non-oil-MBs. Since all MB shells contained POPC, the fluorescence must have originated from the squalene oil. For both of the squalene OLI-MB types, the fluorescence was non-uniform over the MB area. Most OLI-MBs showed fluorescent rings around their perimeter with at least one fluorescent ‘island’ closer to the middle. Presumably these islands were thicker oil patches,

containing more fluorescent material. The fluorescent rings suggested the presence of complete oil layers, whilst the fluorescent islands presented evidence of oil lenses, together providing further evidence of pseudo-partial wetting.

6.9. Echogenicity of LOND formed OLI-MBs

US scattering measurements were taken of the mechanical agitation and microfluidic monodisperse regime POPC squalane OLI-MBs. Since both sample concentrations were close to the concentration limit of our set-up for measuring US scatter response, these results are preliminary and the OLI-MB concentrations should be improved before more reliable US studies are performed. The experiments in this section were performed by Dr. James McLaughlan.

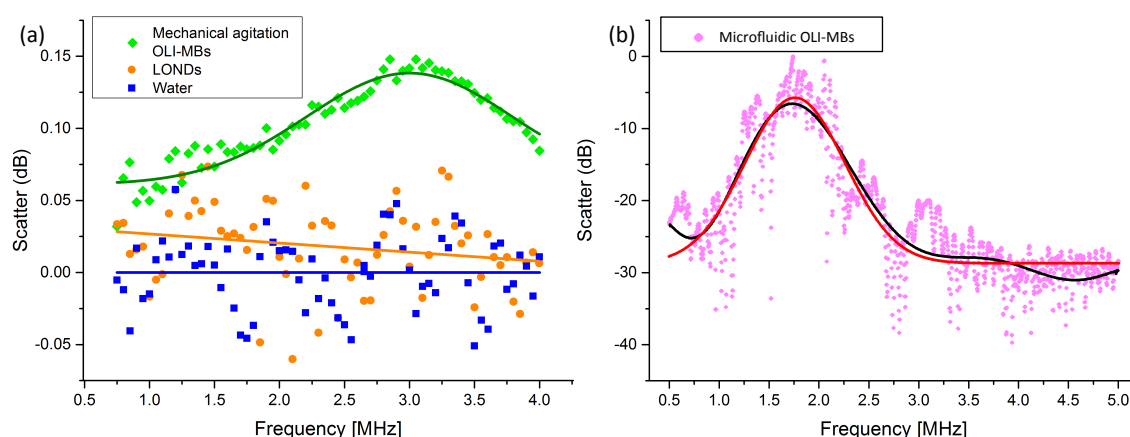


Fig. 6.41. Ultrasound scatter response from unwashed POPC squalane OLI-MBs formed by (a, green) mechanical agitation and (b, pink) monodisperse regime microfluidics. Responses are also given for POPC squalane LOND solution (orange), and a control response from the water container used to hold a sample during measurement (blue). All measurements shown are background corrected to a fitting of the raw water signal and removing that from all of the raw data. Fittings shown are gaussians (dark green and red), a 7th order polynomial (black), linear (orange line), and the water gaussian after background correction (blue line).

Figure 6.41 shows the US scattering from POPC squalane LONDs and OLI-MBs in the presence of excess LONDs. The OLI-MBs were formed through mechanical agitation and monodisperse regime microfluidics. During measurement, the mechanically agitated and microfluidic OLI-MBs were diluted to 10^4 and 10^5 OLI-MBs/ml respectively (due to the measurements taking place in a MilliQ filled 100 ml and 10 ml chamber respectively). As such, the intensity of the scatter should not be compared between the two samples. The resonant frequency should be unaffected by the OLI-MB dilution. The LOND solution did not show significant scattering above the signal from

the water chamber used for measurement. As such, any scatter from the OLI-MB samples can therefore be attributed fully to the MBs and not to the surrounding excess LONDS. The mechanical agitation and monodisperse OLI-MB samples had peak scatter responses at 3.0 and 1.8 MHz, with FWHMs of 1.9 and 1.2 MHz respectively. The broader width of the resonance from the mechanical agitation OLI-MBs is attributed to the broader size range in comparison to the microfluidic OLI-MBs, which had standard deviations of 11 and 1.6 μm respectively. From theory, assuming that each OLI-MB had one complete oil layer shell (between 20 and 500 nm thick), the mechanical agitation OLI-MBs (averaging 20 μm) and the microfluidic OLI-MBs (averaging 2.4 μm) were expected to have resonant frequencies centred on 0.3 and 4.1-4.3 MHz respectively (Chapter 3.2.2, page 40). The resonance expected from theory and the experimental results disagreed significantly. If the mechanical agitation OLI-MBs were resonating as lipid stabilised MBs (as though the oil layer were effectively invisible, or 0 nm thick, in regards to the effect on oscillations), the acquired peak resonance of 3.0 MHz would predict MB diameters averaging 3 μm . On the other hand, if the mechanical agitation OLI-MBs were resonating as MBs in a continuous oil phase (as though the oil layer were effectively of infinite thickness, with a single gas-oil shell, where $\chi = 0 \text{ N/m}$ and $\gamma_{\text{O-A}} = 28 \text{ mN/m}$), the acquired peak resonance of 3.0 MHz would predict MB diameters averaging 2 μm . In either of the above cases, which together cover MBs without any oil and OLI-MBs with thick oil shells, the mechanical agitation OLI-MBs were experimentally measured as significantly larger than this (averaging 20 μm). A similar result is seen for the microfluidic OLI-MBs. Here, the acquired peak resonance of 1.8 MHz would predict lipid MBs and MBs in a continuous oil phase of 4.5 and 3.6 μm respectively, both predictions being larger than the measured microfluidic OLI-MBs (averaging 2.4 μm). There was the possibility of measuring subharmonic and harmonic resonance frequencies from the OLI-MBs during these experiments. However, no lower harmonics were apparent for the mechanical agitation OLI-MBs, and the microfluidic OLI-MBs were exposed to US of the predicted resonance frequency with no resonance being recorded other than that region. Therefore, it can be assumed that the observations were not subharmonic and/or harmonic. Perhaps more importantly though, the smaller microfluidic OLI-MBs resonated at a lower resonant frequency compared to the larger mechanical agitation OLI-MBs that resonated at a higher resonant frequency. Since this disagrees with the well-known property that smaller MBs resonate at higher frequencies (see Theory Chapter 3.2.2, p 41-42), this result heavily suggested that the mechanical

agitation OLI-MBs and microfluidic OLI-MBs had fundamentally different acoustic responses to US.

6.10. Conclusion

In this chapter the experiments aimed to gain control over how the gas, oil, lipid and aqueous phases were introduced to each other through compartmentalising the oil phase into LONDS and by microfluidics. The former aided by controlling the amount of oil meeting the gas surface and the position of the lipid, while the latter reduced chaotic turbulence and pushed the system into a controlled laminar flow between each phase as they were introduced to one another.

Squalane LONDS were found to have peak diameters of 140-190 nm and concentrations of $1\text{--}6 \times 10^{13}$ LONDS/ml. LONDS were found to be stable in size for at least 25 days (potentially over 8 months), and remained at 10^{13} LONDS/ml at least for 4 months. No differences were found between squalane and squalene LONDS, whilst the size distribution of tripropionin LONDS was found to be larger. This is thought to be due to tripropionin's far higher solubility in water, 3.07 mg/ml at 37 °C.⁹⁶

Introducing POPC squalane LONDS to glass saw the LOND solution spontaneously spread across 'fresh' glass surfaces. Observations of the glass surface from where the solution had been displaced showed that a randomly packed array of ~ 1 μm diameter oil patches had been deposited. This was the first indication that the LONDS could be induced to spread into either oil lenses or a complete oil layer. QCM-D experiments looked deeper at the mechanisms of LOND adsorption and spreading. When POPC squalane LONDS were introduced to hydrophobic QCM-D surfaces evidence was given that they adhered, followed by rupturing into an oil layer between 10 and 20 nm thick. Therefore, it was estimated that the POPC squalane LONDS would form OLI-MBs with oil layer thickness of 10s of nanometres. In comparison, POPC and POPC-PEG squalane LONDS were found to bind intact to hydrophilic QCM-D surfaces, and not be removed by washing. A weaker attachment was seen when the POPC-PEG LONDS were introduced to a hydrophobic QCM-D surface.

The effect that LONDS have on the surface tension of air-lipid/water interfaces was studied using an LB trough. By fully compressing a POPC model MB monolayer, introducing POPC squalane LONDS directly underneath, then expanding the monolayer, the surface pressure was recorded as the LONDS were allowed to enter the monolayer. This study revealed that the LONDS did not enter the fully compressed monolayer, but as the surface pressure was reduced entered when the surface pressure was between 8

and 15 mN/m. These results indicated that once a model MB surface had a fully compressed monolayer, LOND entry to the air-water interface was not possible, but that at a lower monolayer concentration, for example when a MB is being formed, LONDS could enter and rupture. Studies where LONDS were allowed to interact with static DPPC model MB monolayers, compressed to different initial surface pressures, revealed the time scale for the LONDS to enter and change the surface pressure. The results showed that no matter the initial monolayer compression, all of the surfaces showed exponential increases to the surface pressure up to a similar end value. For the final surface pressures to all be the same, the same interfaces had to be present in every sample regardless of the initial monolayer compression. The only effect that the initial compression had was on the time-scale for surface pressure change up to this final value, with higher initial compressions requiring less time. For an air-water surface with no monolayer and a monolayer at ESP, 75% of the final surface pressure value was reached after 26 and 10 min respectively. This suggested a limit imposed on the monolayer that once it became 'full', from either lipids or a mixture of lipids and intact LONDS, interactions would stop. If the LONDS adhered to the air-water surface intact, this would require that a monolayer with a higher initial compression be filled with less LONDS when 'full'. The only way for all of the interfaces to be equivalent and for the surface to have this limiting capacity was in the case that the LONDS spread. This would create two interfaces; water/lipid-oil and oil-air, where LONDS would continue to enter and spread until the combined lipids shells would fill the water/lipid-oil interface, while their oil cores would merge together, contributing thickness to an oil layer, where the amount of oil present would play no role in determining the effective surface pressure from the two interfaces.

OLI-MBs were formed successfully from POPC LOND solutions by both mechanical agitation and monodisperse regime microfluidics using squalane, squalene, and tripropionin oils. Microspray microfluidics were unsuccessful at MB formation from POPC squalane LONDS but did work for tripropionin OLI-MBs, though without improving the yield as desired. Mechanical agitation POPC squalane OLI-MBs and POPC-PEG squalane LOND shelled MBs were formed at $20 \pm 6 \mu\text{m}$ (SD 11) μm and $1.7 \pm 0.5 \times 10^6$ OLI-MBs/ml, and $26 \pm 3 \mu\text{m}$ (SD 16) μm and $2 \pm 1 \times 10^6$ MBs/ml respectively. Lifetime studies showed that these squalane OLI-MBs took 35 min to halve in concentration and had a stable size for the initial 60 min. Microfluidic monodisperse POPC squalane OLI-MBs and POPC tripropionin OLI-MBs were formed at $2.4 \pm 0.3 \mu\text{m}$ (SD 1.6) μm and $6.2 \pm 0.8 \times 10^6$ OLI-MBs/ml, at a rate of 5×10^3 MB/s,

and $2.1 \pm 0.1 \mu\text{m}$ (SD $0.8 \mu\text{m}$) and 10^5 OLI-MBs/ml, at a rate of 35×10^3 MB/s, respectively. Lifetime studies showed that the squalane OLI-MBs took 35 min to halve in concentration with a very similar lifetime relationship to their mechanical agitation counterparts. After formation by either method, using POPC or POPC-PEG LONDS, all MBs showed fluorescent shells, indicating successful oil portion integration into the MB shell. The POPC LOND formed OLI-MBs often showing non-uniform fluorescence around the shell, either as a thicker or more intense fluorescent region. These regions could often be seen as surface morphology in corresponding white light images. These findings led to the conclusion that the OLI-MBs were stabilised by pseudo-partial wetting films.

FRET work using squalane LONDS confirmed the conclusion made from the previous LB trough and QCM-D sections, showing that POPC LONDS merged as they stabilised MBs, resulting in the formation of OLI-MBs. On the other hand FRET was not observed for the fluorescent MBs stabilised by POPC-PEG LONDS, confirming that they remained intact as a LOND shell. Observations of OLI-MBs formed from squalene LONDS allowed observations to be made of fluorescence intrinsic to the oil, rather than needing to use a fluorophore loaded into the oil phase. It was confirmed that the oil portion had successfully been integrated into the OLI-MB shell. Irregular fluorescent structures were observed which translated to the white light images.

US scatter measurements of the POPC squalane LONDS, monodisperse microfluidic OLI-MBs, and mechanical agitation OLI-MBs showed no scatter response above the noise, a peak resonant frequency at 1.8 MHz (FWHM 1.2 MHz) and a broader peak resonant frequency at 3.0 MHz (FWHM 1.9 MHz) respectively. The larger resonant frequency distribution was expected from the mechanical agitation OLI-MBs due to their larger size distribution compared to the monodisperse microfluidic OLI-MBs. However, the resonant frequency of the monodisperse microfluidic OLI-MBs was lower than that expected from theory for $2.4 \mu\text{m}$ OLI-MBs, resonating either as lipid MBs (4.1 MHz), OLI-MBs with 20-500 nm thick oil layers (4.1-4.3 MHz), or MBs in a continuous oil phase (2.7 MHz). Similarly, the resonant frequency of the mechanical agitation OLI-MBs was far too high for that expected from theory for $20 \mu\text{m}$ OLI-MBs, resonating either as lipid MBs (0.3 MHz), OLI-MBs with 20-500 nm thick oil layers (0.3 MHz), or MBs in a continuous oil phase (0.3 MHz). These results suggested that neither OLI-MB was resonating as expected based on theory, but also that the two OLI-MB populations were not resonating in the same manner, otherwise at least an inverse relationship between resonance and OLI-MB size should have been followed.

This chapter confirmed that OLI-MBs could be formed within clinical sizes from POPC LONDS of squalane, squalene and tripropionin. The former two oils would be possible carriers for highly hydrophobic drugs, whilst the latter would be a possible carrier for poorly water-soluble drugs. Many of the results showed that the OLI-MB oil portion would be an oil layer of 10s of nanometres, while indications were made that oil lenses were also present. This led to the conclusion that the OLI-MBs were stabilised by pseudo-partial wetting films. The surface tension of the OLI-MB shell was found to be the same as non-oil-MBs when at rest, but lower, and so more energetically favourable, when the MB shell was expanded, as it would be during clinical use if undergoing pressure drops from flow or US exposure. The OLI-MBs were found to take ~30 min to halve in concentration, meaning that for clinical use they would need to be formed on-site and used immediately, or the lifetime needs to be improved by changing the gas core or lipid shell. However, changing the lipid shell to be more stable could inhibit the LONDS from spreading and forming the oil layer (see Conclusion Chapter 9, p 254, for a future experiment, using Diacetylene in the LOND shell that after OLI-MB formation could be activated into a cross-linked state, giving LONDS of a similar stability to the work in this chapter, but OLI-MBs with greater stabilising shells). US scatter responses revealed that the OLI-MBs did still have an acoustic response with the oil portion, however their response was not what was expected from theory. As such, more work needs to be done to characterise the OLI-MBs acoustic properties before work can be progressed to *in vitro* drug delivery analysis, and eventually *in vivo* work.

7. Results: Co-flow controlled, three-phase FF pinch-off

Chapter 5 established that the formation of clinically relevant OLI-MB structures would require high levels of control over how the gas, oil, and aqueous phases were introduced to one another. This chapter evaluates the use of three-phase FF microfluidics to produce OLI-MB structures. Figure 7.1 shows a schematic of a gas bulb, held at a three-phase FF nozzle, coated by a thin oil layer, surrounded by the aqueous phase. This was the idealised on-chip phase geometry that this project aimed to achieve. It was hypothesised that this would then enable the pinch-off of gas-in-oil simultaneously with oil-in-aqueous. In order to retain the fine control over the oil phase thickness at the nozzle, the oil and aqueous were introduced up-stream of gas phase in a co-flow regime where the oil layer could be finely controlled. The work performed in this chapter aimed to improve work presented by Hettiarachchi *et al.* (2009), Kendall *et al.* (2012), and Shih *et al.* (2013).^{31,94,95} The microfluidic systems used in this chapter were designed by, and later in collaboration with, Dr. S. A. Peyman.

The results in this chapter cover:

- 1) Observations of the oil layer thickness during oil-aqueous co-flow in the co-flow channel prior to pinch-off. The aim here was to determine which oils gave the greatest control over the oil layer thickness.
- 2) Characterisation of two-phase FF pinch-off of gas-in-oil and oil-in-aqueous in order to determine if flow conditions exist that would enable both pinch-offs to occur simultaneously in a three-phase pinch-off system.
- 3) Three-phase OLI-MBs pinch-off trials with aqueous surfactant solutions of lipid, pluronic, Triton, and BSA.

All on- and off-chip imaging during this chapter used the upright microscope (Chapter 4.1, p 60).

All of the experiments in this chapter dealt with microfluidics. Four three-phase microfluidic designs were used throughout the work of this chapter; 5C1, 3C1, 3C2, and 3C3. For more information on each design, refer to the Experimental Chapter 4.2.2 (p 64-66). In brief; all of these designs brought the three input phases of gas, oil, and aqueous to one single FF nozzle region. Either all phases were introduced together, leading to a five channel system at the nozzle, '5C', or the oil and aqueous phases were

introduced upstream of the gas phase in a co-flow channel, leading to a three channel system at the nozzle, '3C'. The last number (1-3) refers to the design number. 3C1 was the base design. For 3C2 the outlet was made thinner. For 3C3 the angle of incidence between the oil to aqueous phase inlets in the co-flow channel was reduced and the oil inlet was made thinner.

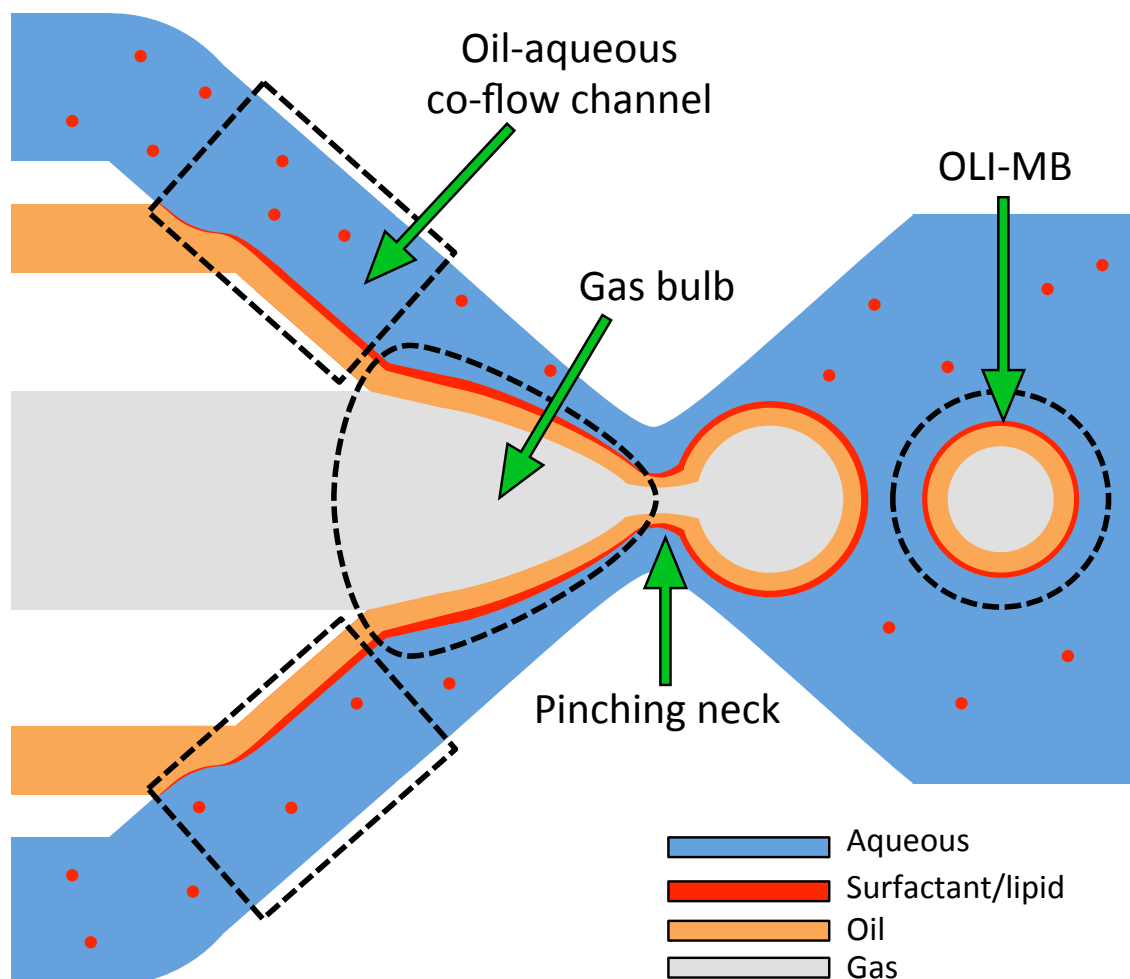


Fig. 7.1. Schematic of OLI-MB pinch-off in the 3C1 microfluidic device with the regions of interest marked by black dotted lines and naming terms given for each marked.

7.1. Forming a thin oil layer under oil-aqueous co-flow

In this section of work, during flow of standard lipid solution, oil, and gas phases through the 3C1 microfluidic device, the oil-aqueous co-flow channel was observed in order to assess the degree of control that could be obtained over the co-flow oil layer formed there. The main observations were of average oil layer thickness and the uniformity along the channel. This was important as a uniform, thin oil layer was desired to coat the gas bulb at the nozzle, and as such, a higher degree of control over the oil layer thickness upstream of the nozzle was thought to be important to facilitate

this. During this work oil and lipid solution flow rates were varied whilst gas pressure was kept constant at 3 psi (20.7 kPa).

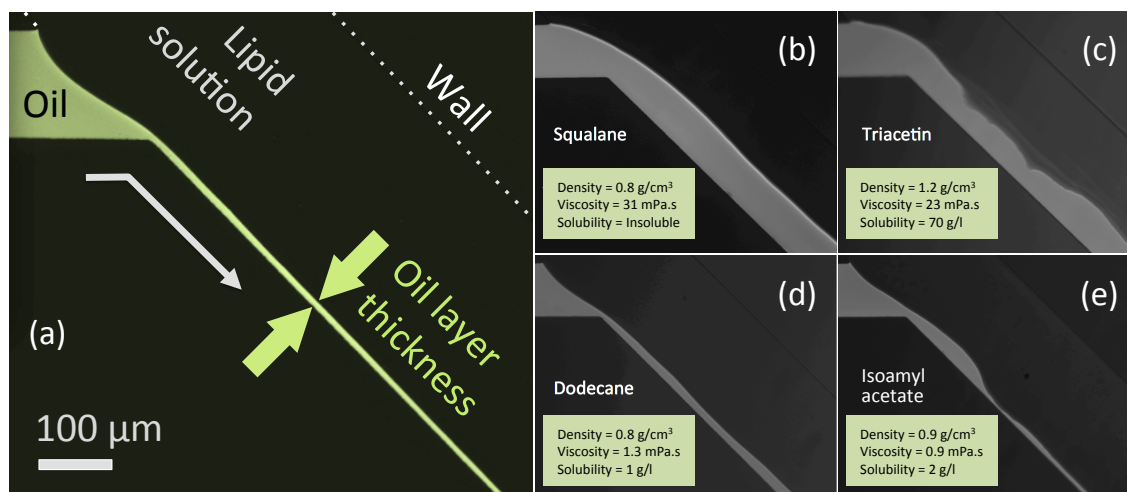


Fig. 7.2. Fluorescence images used to measure the oil layer thickness given in the co-flow channels of the 3C1 microfluidic devices, by varying the oil to standard lipid solution flow rates. (a) Nile red in dodecane oil measurement image is shown. This indicates how the phases flowed, what was measured, and where the device boundaries were. This is followed by images using (b) squalane, (c) triacetin, (d) dodecane, and (e) isoamyl acetate, where all images were at 3 psi C_3F_8 gas and 0.5 $\mu\text{l}/\text{min}$ oil, with (a) 28 or (b-e) 16 $\mu\text{l}/\text{min}$ lipid solution.

Figure 7.2 shows example images of the oil-aqueous co-flow channel during flow of oil and standard lipid solution. For the same flow rates, squalane and triacetin both showed a much thicker oil layer compared to dodecane and isoamyl acetate. This was expected from their higher viscosity. However, squalane and dodecane both showed a far more uniform thickness along the co-flow channel compared to triacetin and isoamyl acetate. This was important as it identified that the latter two oils may be less likely to break-up before arrival at the nozzle. Figure 7.3 shows how the oil layer thickness changed over a range of oil to lipid solution flow rate ratios and how the gradients of these relationships related to the oil viscosity. All four oils showed a linear relationship between the oil layer thickness and the flow rate ratios, where the gradient of the relationship was strongly dependant on the oil viscosity, correlating well ($R^2 = 0.999$) to an exponential relationship. For squalane and isoamyl acetate, the relationship fitted well to an intercept through 0, whereas for triacetin and dodecane did not. It is likely that this was due to some property of the oil or interaction of the oil with the lipid solution, however this could not be attributed to the oil viscosity, density, or surface tension.

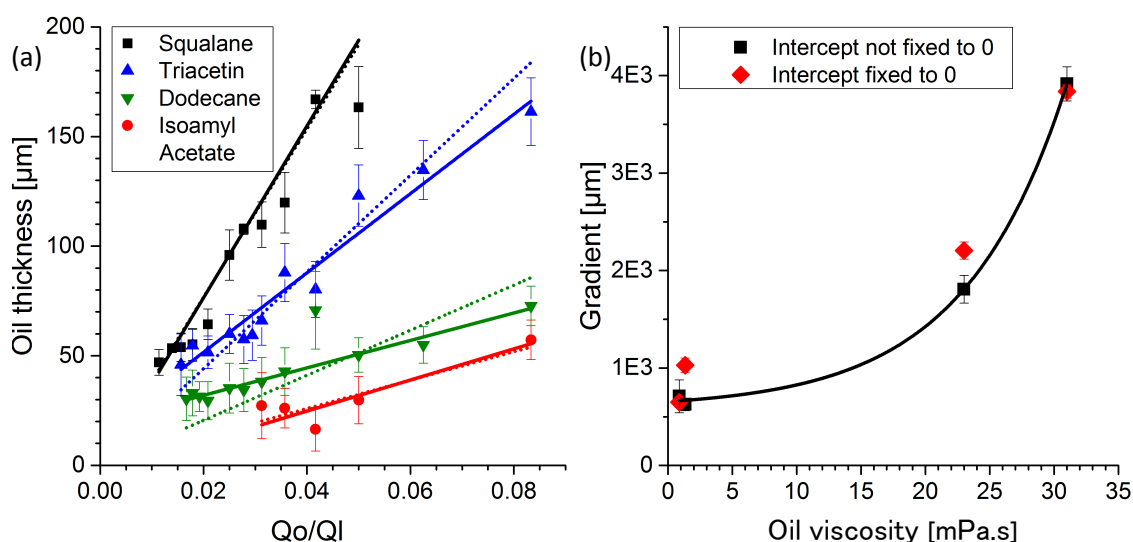


Fig. 7.3. (a) Oil layer thickness given in the 3C1 co-flow channel, measured as in Figure 7.2, dependant on the ratio of (Q_o) oil to (Q_l) lipid solution flow rate. Constant gas pressure (3 psi) and oil flow rate ($Q_o = 0.5 \mu\text{l/min}$). Errors shown are the standard deviation of the oil layer thickness down the co-flow channel. Linear fits are shown with (dotted) and without (solid) the intercept fixed to 0. (b) The gradients of these fits are then shown verses the oil viscosity.

Figure 7.4 shows flow of a squalane oil layer after passing into the thinner portion of the 3C1 co-flow channel, just prior to the nozzle. A schematic is given to explain how the oil is thought to be flowing. This type of flow pattern was seen to occur with all of the oils trialled. The oil layer would partially dewet from the channel wall, sometimes passing into the middle of the channel or fully to another wall. This flow pattern occurred more often when the oil to lipid solution flow rate ratio and the oil flow rate itself were both low. It is expected that this occurred in the thinned co-flow due to the increase in fluid velocity, providing a higher degree of shear forces at the oil-aqueous interface. These flow patterns did not appear to affect the coating of the gas bulb, as the oil was often seen to pass back onto the gas bulb at the nozzle (as can be seen in the bottom right corner of Figure 7.4a). However, if the oil stream had remained against the original flow wall until contacting the gas phase, it can be assumed that no lipids would have stabilised the oil-wall interface, allowing the oil to easily wet the gas on contact. On the other hand, by passing from one wall to another, all sides of the oil stream may have become at least partially stabilised by lipid. This could prevent the oil layer from wetting the gas bulb, or at least make the wetting less efficient. This type of flow pattern was seen to be significantly reduced when updating the microfluidic devices from the 3C1 (and 3C2) design to the 3C3 design, where the angle of incidence for the introduction of the oil and aqueous phases was reduced, allowing for lower flow rates to be used more reliably.

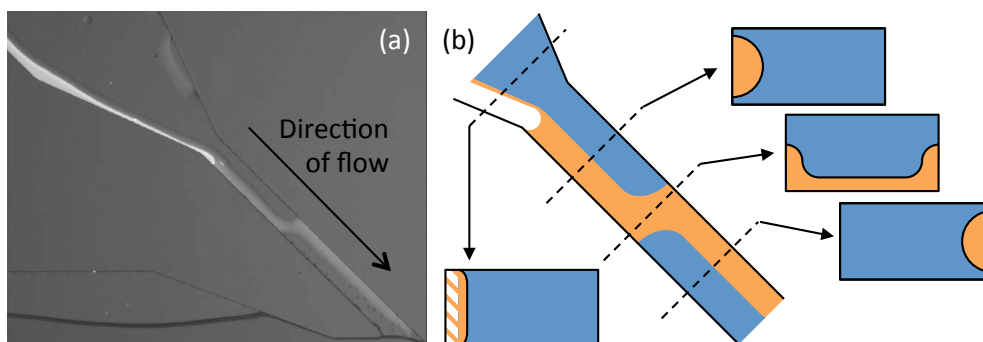


Fig. 7.4. (a) Experimental image of the thinned co-flow region of the 3C1 device during three phase flow of 3 psi C_3F_8 gas, 0.1 $\mu\text{l}/\text{min}$ squalane oil, and 15 $\mu\text{l}/\text{min}$ standard lipid solution. This image presents an example of how when the oil stream was controlled to become thinner, eventually it would stop co-flowing in contact with the entire depth of the microfluidic channel, and often flow around the device channel. (b) A schematic is given to show what is thought to have been occurring.

From the results shown in Figures 7.2 and 7.3 squalane and dodecane were chosen as the main candidate oils going forward. This was because, at least in Figure 7.2, they both showed a higher degree of oil layer thickness uniformity along the co-flow channel, and because squalane and dodecane would allow for coarse and finer changes to the oil layer thickness during three-phase pinch-off trials. Importantly, this work informed on what should be expected during the three-phase trials in terms of how the oil layer would be presented at the nozzle and its dependance on changes to the flow rate and oil type.

7.2. Mapping flow rate ratios to facilitate three-phase FF pinch-off

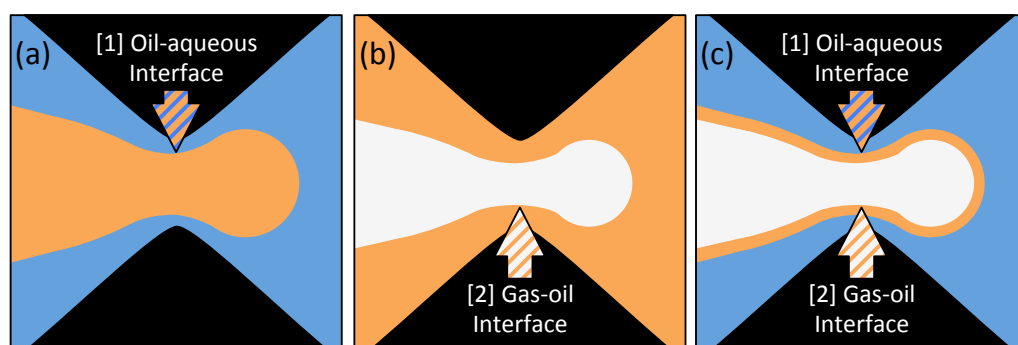


Fig. 7.5. Schematics of (a-b) two-phase and (c) three-phase nozzles, mid-pinch-off of gas (white) oil (orange), and aqueous (blue) phases, indicating the two interfaces where enough shear force needs to be applied for pinch-off to occur. This schematic serves as an illustration of (a-b) the two two-phase pinch-offs that were examined in order to measure the oil velocities required at the two interfaces and to estimate flow conditions that would allow the two-phase pinch-offs to occur simultaneously in (c) three-phase pinch off.

Two-phase pinch-off of oil-in-aqueous and gas-in-oil was studied to define the flow parameters that would allow the two-phase pinch-offs to occur. The volumetric flow rate of the oil phase was then converted into a flow velocity for the two experiments. This was done so that it could be assessed if there are oil velocity ranges that would facilitate both two-phase pinch-offs to occur simultaneously. This would then allow for an estimation of the conditions that would allow for three-phase pinch-off to occur. Figure 7.5 shows schematics of the two two-phase experiments and how they relate to three-phase pinch-off, including the interfaces where the oil velocity had to match the conditions to allow for two-phase pinch-off. This study worked under the assumptions that the two-phase gas and oil bulbs pinched with a similar geometry and that during three-phase pinch-off the oil layer would be negligibly thin relative to the rest of the phase geometry at the nozzle. Work was performed using two-phase FF microfluidics (detailed in Chapter 4.2.2, p 61), C₄F₁₀ gas, squalane, triacetin, dodecane, and isoamyl acetate oils, with standard lipid solution and 1 vol% Triton solution aqueous phases.

7.2.1. Oil droplet pinch-off in water/surfactant

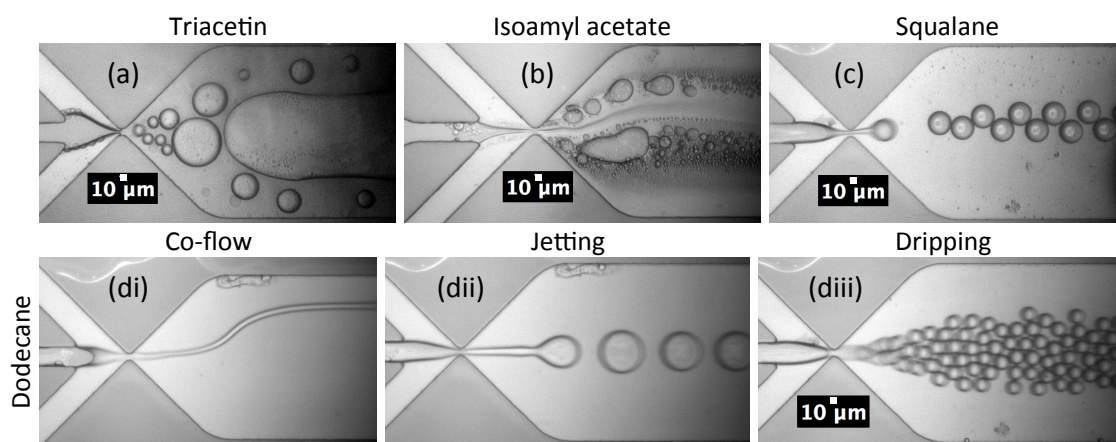


Fig. 7.6. FF pinch-off trials of (a) triacetin-, (b) isoamyl acetate-, and (c) squalane oil-in-1 vol% Triton solution. Triton solution flow rates were ~ 0 , 1, and 3 $\mu\text{L}/\text{min}$, with oil flow rates of ~ 0 , 0.1, and 0.01 $\mu\text{L}/\text{min}$ respectively. Triacetin pinch-off only occurred briefly under inertial flow, after active flow had been stopped. Pinch-off regimes are also shown for (d) dodecane oil-in-Triton solution, showing (di) co-flow, (dii) jetting, and (diii) dripping, at Triton solution flow rates of 5, 10, and 1 $\mu\text{L}/\text{min}$, with oil flow rates of 1.0, 0.5, and 0.5 $\mu\text{L}/\text{min}$ respectively.

Figure 7.6 shows examples of attempted pinch-off of triacetin and isoamyl acetate, and successful pinch-off of squalane and dodecane in 1 vol% Triton solution. It also shows examples of co-flow and jetting for dodecane oil. Pinch-off of all four oils in standard

lipid solution was trialled, but no successful pinch-off was found for any flow ratio including flow that would have led to $Ca \ll 0.1$, where displacement of the oil bulb became so slow that the oil syringe pump led to a pulsatile flow that on average appeared stationary. Immediately this brought into question the capability of three-phase pinch-off in lipid solution as the oil-aqueous interface of an oil droplet or a gas MB coated in oil is the same. For 1 vol% Triton solution, (Figure 7.6d) dodecane oil could easily be transitioned through co-flow, jetting, and dripping regimes, at progressively lower aqueous and oil flow rates. (Figure 7.6c) Squalane oil also achieved pinch-off at low flow rates, but only ever in a jetting-dripping cross-over type of regime, where the oil bulb elongated for a few tens of micrometres into the outlet, but on pinch-off only left an oil bulb typical of a dripping regime. (Figure 7.6a) Triacetin was only seen to achieve pinch-off under limited inertial flow in the microfluidics, after the flow rates had been manually set to 0 $\mu\text{l}/\text{min}$. However, this pinch-off occurred as aqueous-in-oil. (Figure 7.6b) At low flow rates, isoamyl acetate jetted into the outlet and partially solubilised into the aqueous phase.

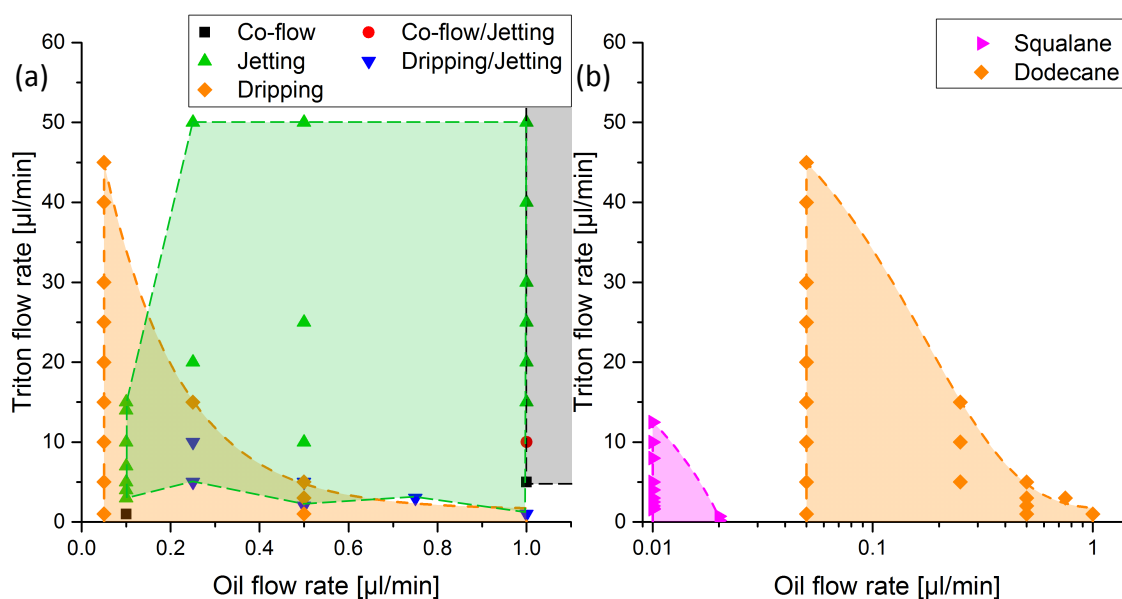


Fig. 7.7. Mapping of the pinch-off regimes for dodecane and squalane oil-in-1 vol% Triton solution. For dodecane oil, (a) the different pinch-off regimes that were observed at specific oil against Triton solution flow rates are indicated, with semitransparent shapes indicating the regions where (orange) dripping, (green) jetting, and (black) co-flow were observed. (b) The flow rates where dripping was observed are then compared for both oils.

Figure 7.7 indicates which pinch-off regime (if any) was observed at specific volumetric flow rates for oil and Triton solution at a two-phase FF nozzle. It then compares the flow conditions that facilitated dripping pinch-off for squalane and dodecane. The semi-

transparent coloured shapes give the rough limits of each pinch-off regime. Achieving the dripping pinch-off regime was less dependant on the flow rate ratio between the two phases than it was on the combined flow rate throughout the chip. In other words, the most effective way to transition the system into the dripping regime was to keep the flow rate ratio the same whilst lowering the combined flow rate. This agrees with Ca theory (see Theory Chapter 3.1.2, p 35-36). Dripping became the most prominent pinch-off regime when the flow rates of both phases were reduced, which would have led to a reduction in both phases' Ca . However, there was significant overlap between the flow conditions that would allow for either jetting or dripping pinch-off to occur. Both pinch-off regimes were highly stable, meaning the once the system had achieved one of the flow regimes it remained in that regime until the flow rate of either or both of the phases was changed enough to transition the pinch-off into the other regime, at which point that regime would be highly stable in the overlap region. This agreed with Ca theory, which predicts a transition zone able to give both types of pinch-off regime for the same flow velocities. Squalane oil was only observed to give dripping pinch-off at flow rates far below that of dodecane. Squalane pinch-off in the dripping regime was only achieved up to ~ 0.02 times the oil flow rate and ~ 0.28 times the Triton solution flow rate. The necessary reduction to the oil flow rate was expected, due to Ca theory, in order to balance the ~ 23 times higher oil viscosity. The Triton solution was the same for both oils, meaning its viscosity was constant. Therefore, due to the remaining reduction to the oil flow rate and the reduction to the triton solution flow rate, it can be concluded that the interfacial tension for the Triton-squalane interface must have been lower than that of the Triton-dodecane interface during flow through the nozzle. These results estimate that the Triton-squalane interfacial tension must have been ~ 3 times lower than that of the Triton-dodecane interfacial tension at the nozzle.

7.2.2. MB pinch-off in oil

The flow rates needed for MB formation in oil in a FF microchip were mapped, with analysis of the MB sizes formed at given volumetric flow rate. Experimentally this work was undertaken with triacetin, squalane, and isoamyl acetate, however, since the previous section (7.2.1) showed that pinch-off of oil-in-aqueous was only effective with dodecane oil, a focus on dodecane oil is given here.

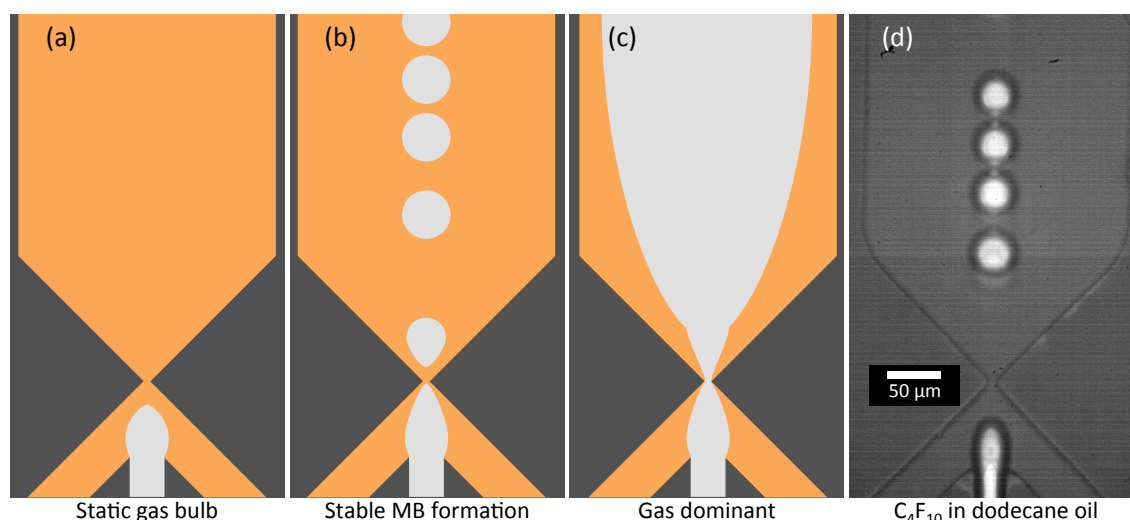


Fig. 7.8. C_4F_{10} gas (light grey) pinch-off in dodecane oil (orange). Schematics are shows of (a) oil dominant flow where the gas phase is held as a static bulb, (b) stable MB formation, and (c) gas dominant flow. (d) An experimental pinch-off image is given where the oil flow rate and gas pressure are 40 $\mu\text{l}/\text{min}$ and 2 psi respectively. No surfactant was present.

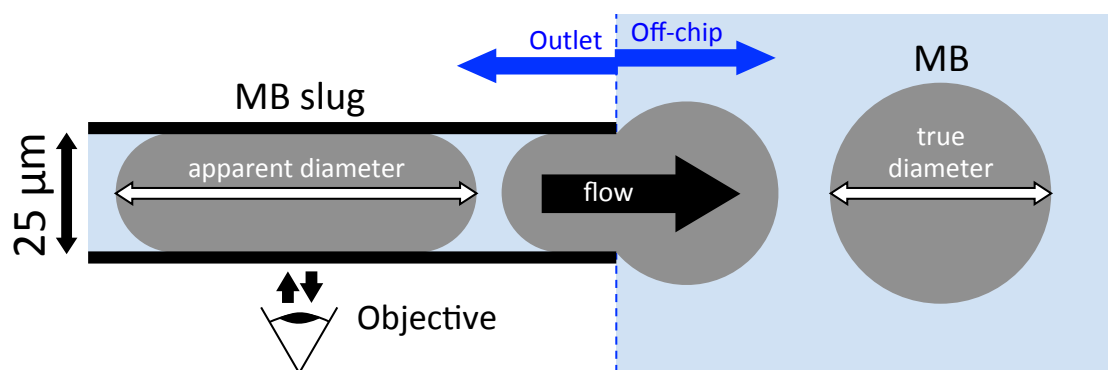


Fig. 7.9. Schematic cross-section of a microfluidic outlet where a MB with a diameter $> 25 \mu\text{m}$ is squashed within the outlet's depth of $25 \mu\text{m}$, giving a MB slug. The diameter of the MB slug is observed, giving an apparent MB diameter that would give an overestimation of the total MB volume if the on-chip MB was assumed spherical. A comparison is given to the real MB diameter once the MB moves off-chip.

Figure 7.8 shows schematics of the flow regimes when MB pinch-off is achieved (Figure 7.8b), and when either the oil (Figure 7.8a) or gas (Figure 7.8c) phases are dominant, preventing pinch-off. An example image for C_4F_{10} MB formation in dodecane oil is also shown. In order to map the flow conditions that led to MB formation, the gas was set to a given pressure, then the oil flow rate was increased over a range of flow rates. Flow rates were noted where the gas phase transitioned from gas dominant, to MB formation with immediate coalescence, to stable MB formation, and then to a static gas bulb. MBs were seen to form on-chip with an apparent diameter of

30-61 μm . Figure 7.9 shows a schematic explaining how a MB that is observed in a channel that is thinner than its diameter off-chip will form a MB slug with an apparent diameter that is larger than the MB's real diameter. Simplifying the MB slug to a cylindrical volume, the apparent diameter can be used to calculate the MB's real diameter. Due to the MB slug's edge curvature, this estimation becomes less accurate for MB slugs with apparent diameter closer to the channel depth. Hence, the recorded MB diameter was always the smallest out of the measured apparent diameter and the calculated real diameter. Therefore, the real MB diameter was estimated as $\sim 30\text{-}52\ \mu\text{m}$. The large MB size was likely due to the lack of any surfactant in the oil phase. While the oil and gas were both hydrophobic, a surface tension will have still existed at the interface between them. An amphiphilic surfactant will not have decreased the surface tension as efficiently as for a hydrophilic-hydrophobic interface, but any surface active particles able to close pack at the surface (e.g. solid particles, hydrophobic-hydrophilic-hydrophobic tri-block copolymers, etc.) could have stabilised the MBs to some degree, likely allowing for smaller MBs to be formed.

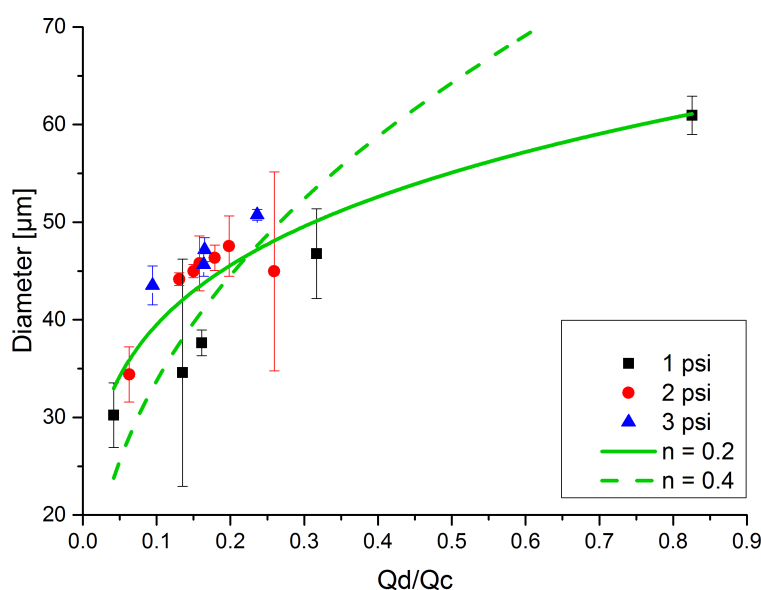


Fig. 7.10. Apparent MB diameter formed at given flow rate ratios between the discontinuous C_4F_{10} gas phase and the continuous dodecane oil phase (Q_d/Q_c). MBs measured from the gas-in-oil pinch-off images presented in Figure 7.8. The gas volumetric flow rate was calculated from the average MB volume and formation rate, knowing the chamber height was $25\ \mu\text{m}$. The lines of fit (green) are $y = ax^n$ power relationships, fit to all of the data with an equal weighting between different data sets, where the power (n) is noted.

Figure 7.10 shows the apparent MB diameters formed across a range of volumetric flow rate ratios between the gas and oil phases. Power relationships were fitted to the data,

with comparison to the literature scaling law for MB pinch-off (Equation 3.8). The device used in this study was a planar FF design with a short nozzle, which Garstecki *et al.* (2005) found to have a scaling law power of $n = 0.4$ (Figure 7.10d, dashed green line).¹⁵⁹ However these studies followed a power of $n = 0.2$. Fitting a power relationship to each gas pressure data set showed a similar power value for each curve where the MB diameter was larger for higher gas pressures, even though the ratio of flow rates was the same. The larger MB size was likely due to the higher flow velocity delaying pinch-off relative to the amount of gas entered into the MB. Similar pinch-off in squalane, triacetin, and isoamyl acetate gave powers of 0.5, 0.1, and 0.3 respectively (data not shown). There was no apparent correlation between MB diameter and the viscosity, density, or surface tension of the relevant oils.

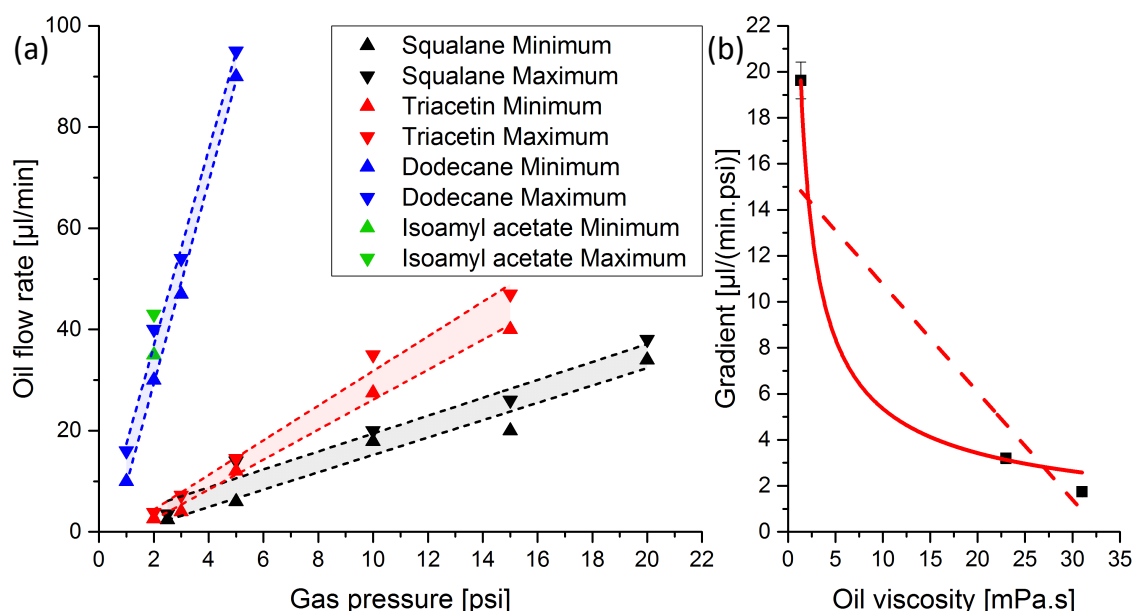


Fig. 7.11. (a) Oil flow rates and C_4F_{10} gas pressures capable of forming gas-in-oil MBs without surfactant (colour filled strips). The maximum (down arrow) and minimum (up arrow) oil flow rates are indicated at set gas pressures. Formation regions are shown for squalane (black), triacetin (red), and dodecane (blue). Isoamyl acetate (green) only showed successful pinch-off at 2 psi gas. (b) A graph is given comparing the oil viscosities to the associated gradients seen in graph a, with both a power (line) and linear (dashed) fit..

Figure 7.11 shows the range of oil flow rates, at set gas pressures, that facilitated pinch-off of C_4F_{10} MBs in squalane, triacetin, dodecane, and isoamyl acetate. For all oils, the range of oil flow rates found to allow for stable MB pinch-off were found to be limited. For squalane, triacetin, dodecane, and isoamyl acetate the oil flow rate ranges were 4 ± 1 , 4 ± 1 , 7 ± 1 , and $8 \mu\text{l}/\text{min}$ respectively at each gas pressure. The lowest gas pressure given for each oil data set was the minimum gas pressure limit that allowed for MB

formation, under which only oil or gas dominant regime could be achieved. For squalane, triacetin, and dodecane the minimum gas pressures were 2.5, 2, and 1 psi respectively, whereas for isoamyl acetate MBs were only formed at 2 psi. The main oil property that determined what flow ratio facilitated MB formation was the oil viscosity, with a high oil viscosity requiring a lower oil flow rate or higher gas pressure (Figure 7.11b), which was expected from Ca theory (Equation 3.6).

7.2.3. Combining two-phase pinch-off regimes to estimate three-phase pinch-off conditions

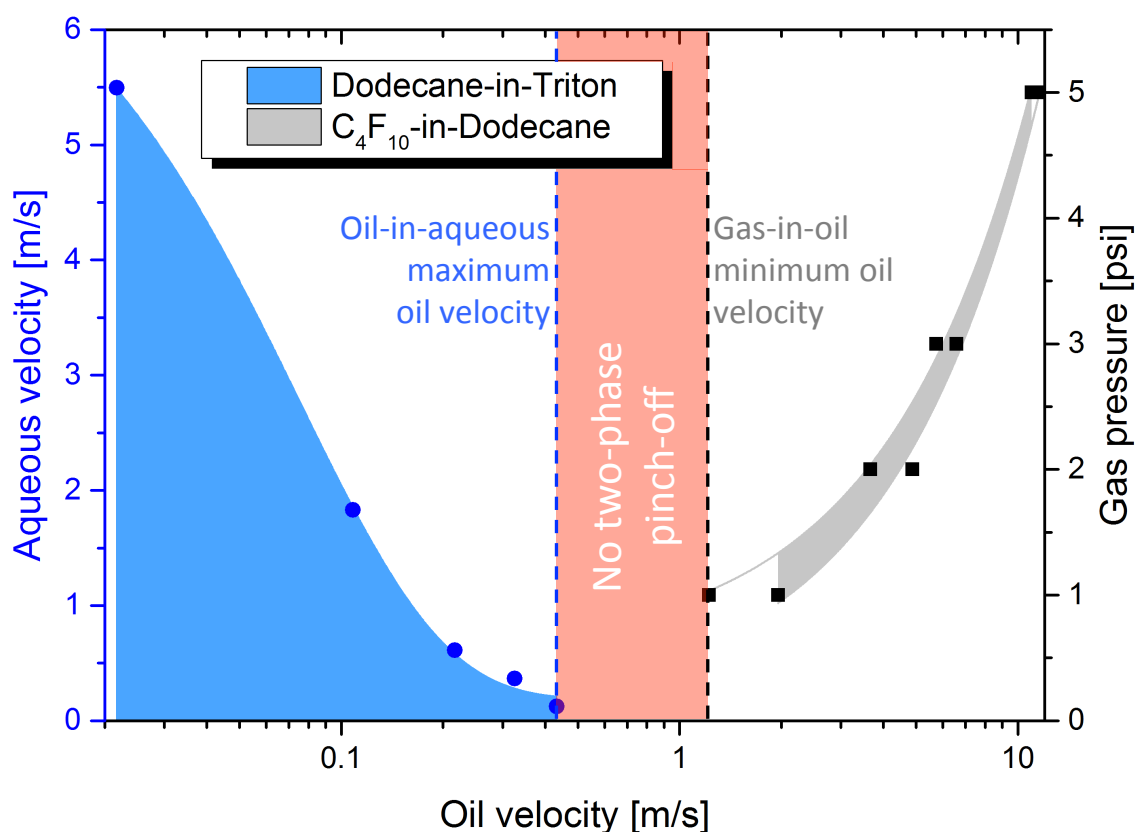


Fig. 7.12. Overlaying the dodecane oil flow velocities that allowed pinch-off to occur during two-phase pinch-off experiments. Assumptions were made (1) that the oil and gas bulbs of oil-in-aqueous and gas-in-oil two-phase pinch-off were of equivalent size and (2) had a diameter of 7 μm (completely filling the thinner dimension of the nozzle), and (3) that the oil layer thickness in the three-phase pinch-off would be negligible.

Figure 7.12 compares the range of dodecane oil velocities shown to give pinch-off at the gas-oil (grey) and oil-aqueous (blue) interfaces from the two-phase mapping experiments in the previous sections. Table 7.1 presents the minimum and maximum flow velocities recorded to achieve C₄F₁₀ gas-in-oil and oil-in-Triton solution pinch-off from the two-phase experiments in the previous sections for both squalane and

dodecane. The velocities given are only estimation for the velocities that would occur in a three-phase nozzle, since it has been assumed that the two-phase gas and oil bulbs were identical and that the three-phase oil layer would be negligibly thin. However it can be assumed that the two interfaces in the three-phase pinch-off would behave the same as in their individual two-phase pinch-off experiments since the phase volume plays no role on influencing the interface's surface tension or Ca .

Tab. 7.1. Dodecane and squalane oil minimum and maximum flow velocities that allow for pinch-off of C_4F_{10} gas-in-oil and oil-in-1 vol% Triton to occur in a two-phase FF device respectively, based on the assumptions defined in Figure 7.12.

Oil	Gas-oil Vmin [m/s]	Oil-aqueous Vmax [m/s]
Dodecane	1.2	0.4
Squalane	0.3	0.009

Figure 7.12 and Table 7.1 presented strong evidence to suggest that the pinch-off of OLI-MBs was not possible from a gas bulb coated with squalane or dodecane oil, using Triton solution, in the FF geometries used. However, if the act of thinning the oil to a negligible thickness meant that both the oil and gas phases' pinch-off was dependant on the aqueous phase's velocity, then theoretically pinch-off could still be possible based on estimated flow conditions. As an example, a dodecane oil flow velocity of 0.045 m/s would pinch-off in Triton solution up to 4 m/s. This aqueous phase velocity then pushing against the gas-oil interface would allow pinch-off to occur at gas pressures of 1.8-2.2 psi. In this case, the full range of possible flow rates to allow OLI-MB pinch-off would be 1.0-2.8 psi C_4F_{10} gas, 0.022-0.14 m/s dodecane oil, and 1.2-5.5 m/s Triton solution. The use of Triton shelled OLI-MBs is limited due Triton's high toxicity towards bilayer membranes, such as the cell wall within the body.^{263,264} However, the results in the oil-in-aqueous pinch-off experiments showed that two-phase pinch-off was not possible in standard lipid solution. This was a strong reason to suspect that an oil-lipid/water interface would also not pinch-off in following three-phase experiments, and was a strong indication that the stable and reliable formation of OLI-MBs would not be possible using the microfluidic in this project.

The work covered in this section of the chapter looked at estimating the flow conditions for successful three-phase pinch-off and so has been presented before the experimental three-phase pinch-off trials. However this work did strongly suggest that as an alternative to lipid stabilised OLI-MB, the formation of Triton stabilised dodecane OLI-

MBs should be trialled as it would be more capable of pinch-off of the oil phase. This work is covered in Table 7.2 and section 7.3.3.

7.3. Three-phase FF trials

A large amount of work was spent on trials of three-phase pinch-off during this project. The ratio between the liquid flow rates and gas pressure were varied for each oil and microfluidic design detailed in the following section. This led to too many flow conditions to detail and explain the differences between in this discussion, when most did not lead to the formation of OLI-MB like structures. As such, presentation of these experiments has been simplified to describe one image of flow between the three phases that was representative of the optimal flow conditions observed for each experiment. Table 7.2 presents a list of the experiments trialled and a summary of what was observed. The results listed in Table 7.2 can be broken down into the four surfactant groups used to stabilise the OLI-MBs; (dark-light blue) lipid, (orange) lipid + pluronic, (orange) Triton, and (green) BSA protein. None of the three-phase FF trials were repeatedly successful at forming a solution of OLI-MBs of clinically relevant sizes at concentrations high enough for any further study.

Tab. 7.2. A list of all three-phase OLI-MB formation trials, dependant on the microchip, oils, surfactant, noting the optimum flow conditions and summary details of the results. Colour bands donate a change in experiment 'type'.

Microfluidic device	Aqueous phase (surfactant)	Oil phase	Optimal flow conditions found			Evidence of OLI-MBs ...		Notes
			Gas [psi]	Oil [μ l/min]	Aqueous [μ l/min]	... on-chip	... off-chip	
3C1	DPPC-PEG	Squalane	1.5	0.1	8	No	No	
		Dodecane	4.5	0.5	50	No	No	
		Triacetin	2	0.05	8	No	No	
		Isoamyl acetate	0.9	0.05	6	Maybe	No	High coalescence on-chip of oil coated MB stream.
3C2	DPPC-PEG	Squalane	3	0.1	25	Yes	No	
		Triacetin	5	0.05	20	Yes	No	
		Isoamyl acetate	3	0.2	40	No	No	
		Squalane	3	0.02	40	Yes	Yes	Very low concentration 5-10 μ m OLI-MBs off-chip, appeared fully fluorescent.
3C3	DPPC-PEG	Triacetin	3	0.05	25	No	No	
		Isoamyl acetate	3	0.05	50	Maybe	No	MB stream on-chip fully coated in oil.
		Squalane	12.5	5	50	No	No	
		Triacetin + 10 vol% Pluronic-F68	3	1.037	30	Yes	Yes	~100 μ m OLI-MBs off-chip, collapsed and ejected oil.
Microspray	DPPC-PEG	Squalane	12.5	5	50	No	No	
3C3	DPPC-PEG + 0.1 vol% Pluronic-F68	Triacetin + 10 vol% Pluronic-F68	5	1.037	20	Yes	No	
		Triacetin + 2 vol% Pluronic-F68	5	0.337	22	Yes	One OLI-MB (remaining oil layer)	Only one ~100 μ m OLI-MB after collapse
		Dodecane	0.9	1	1	No	No	
		Dodecane + 10 vol% Span80	2	0.5	15	Yes	No	Highly stable MB streams on-chip, no coalescence.
3C1	1 vol% Triton	Dodecane	2	3	12	Maybe	No	MB stream on-chip fully coated in oil.
3C3		Dodecane	2	0.02	30	Maybe	No	Very small MBs formed on-chip, all in a stream of oil.
3C3	5 mg/ml BSA	Soybean	3	0.05	5	Yes	One OLI-MB	OLI-MB formation by oil jetting and MB pinch-off in oil.

7.3.1. Lipid shelled OLI-MBs

Following the three-phase FF OLI-MB formation approach, the majority of this work was performed using DPPC-PEG standard lipid solution. Table 7.2 shows that the 3C1, 3C2, 3C3, 5C1, and microspray microfluidic designs were tested here with, with squalane, dodecane, triacetin, and isoamyl acetate oils, all at a large range of flow rates. Figure 7.13 gives the optimal formation flow conditions and off-chip imaging that was observed during all of these trials.

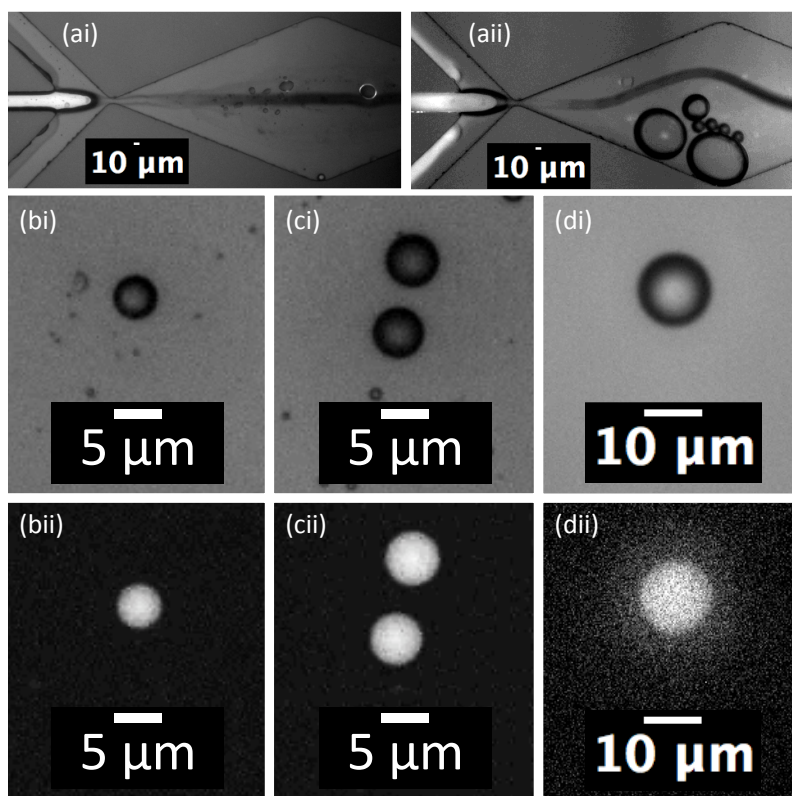


Fig. 7.13. 3C3 microfluidic pinch-off trial of C_4F_{10} gas in squalane oil in DPPC-PEG standard lipid solution. (a) On-chip formation and (b-d) off-chip imaging is shown, with (ii) fluorescence. Gas 3 psi, oil 0.02 $\mu\text{L}/\text{min}$, aqueous 40 $\mu\text{L}/\text{min}$. Images b-c were from the same run as image a, image d was from a different run on a different day with similar on-chip formation.

Figure 7.13 shows pinch-off of C_4F_{10} gas in squalane oil in standard lipid solution through the FF 3C3 nozzle, with off-chip imaging of the sample. The MB streams shown here were very stable over time, which was a vast improvement from the earlier microfluidic 3C1 and 3C2 designs. Only the 3C3 device allowed the oil and aqueous to co-flow into a controlled, thin stream towards the nozzle, whilst forming a stable MB stream past the nozzle. For OLI-MB formation with this method, the most common structure seen off-chip were oil droplets of 1-10 μm , at 10^{5-6} droplets/ml. However, as

shown by Figure 7.13b-d, for roughly half of the experiments runs, a low concentration ($<10^5$ MBs/ml) of 5-10 μm MBs also remained in the solution off-chip. These structures showed white light contrast indicative to that of non-oil-MBs (a thick black outline, as apposed to oil droplets which typically show a thin black outline), but also showed fluorescence across their shell indicating the presence of an oil layer and therefore suggesting the presence of OLI-MBs. These OLI-MB like structures were shown to have fluorescence in their cores, rather than just a fluorescent outside as expected. This may have been a combination of an imaging artefact, due to imaging these structures with fluorescence microscopy that had a long depth of field (rather than confocal imaging), and also due to the thickness of the fluorescent oil layer at the top and bottom of the structure. It is unlikely that this was due to an imaging artefact supplied by the lens resolution since objects down to 1 μm could still be resolved and if the subjects imaged were 5-10 μm oil droplets with central gas cores of ≤ 1 μm , the white light images would be expected to appear more like oil droplets than MBs. As described earlier, this approach lacked reproducibility even when using similar flow conditions. In cases where stable OLI-MBs were observed, non-fluorescent MBs were not. In cases where stable OLI-MBs were not observed, off-chip imaging showed samples consisting of fluorescent oil droplets and non-fluorescent MBs (result not shown), indicating that the MBs had been formed without an oil shell. The conclusion here was that a successful OLI-MB formation could be held stable on-chip. However, once formed the OLI-MBs were unstable, losing their gas core, either to dissolution or collapse, but not to separation and re-stabilisation as separate non-oil-MBs and oil droplets. On the other hand, the FF pinch-off could also be highly stable in its formation of non-oil-MBs and oil droplets, without OLI-MB formation. It is very likely that formation under these two different circumstances looked identical at the microfluidic nozzle.

7.3.2. Pluronic shelled OLI-MBs

Following the work of Shih *et al.* (2013) pluronic-F68 solution (a triblock copolymer, hydrophilic-hydrophobic-hydrophilic chain) was added to the lipid solution and triacetin oil phases.⁹⁵ Shih *et al.* proposed that by adding pluronic to their liquid phases it inhibited coalescence in the outlet, allowing for a higher MB formation rate, and reduced the MB size. Table 7.2 shows that the 3C3 and 5C1 microfluidic designs were tested here, where pluronic was added to the triacetin and lipid solution phases at a concentration of 10 and 0.1 vol%, and 2 and 2vol% respectively. Glycerol concentration was also varied in the lipid solution from 1 to 30 vol%. Figure 7.14 gives the optimal

formation flow conditions and off-chip imaging that was observed during all of these trials.

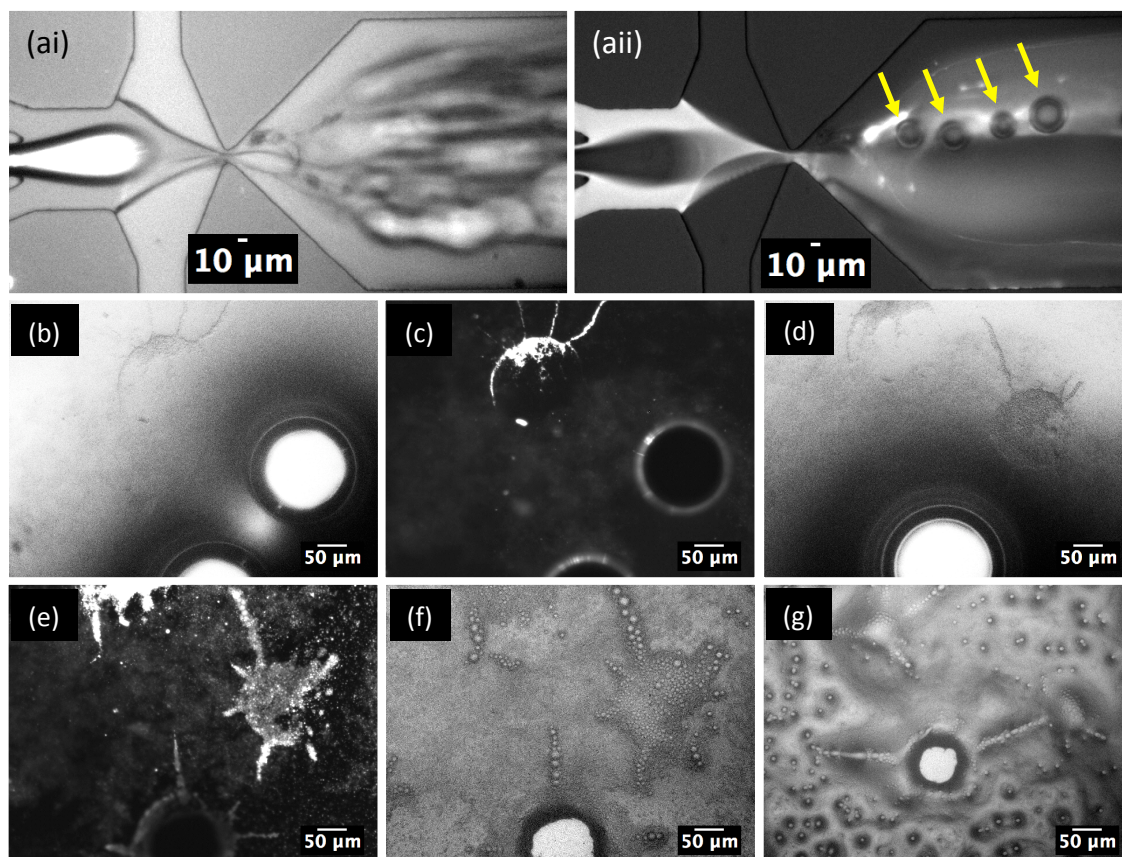


Fig. 7.14. 5C1 microfluidic pinch-off trial of C_4F_{10} gas in triacetin + 10 vol% pluronic in DPPC-PEG standard lipid solution + 0.1 vol% pluronic. (a) On-chip formation, with double layered structures (yellow arrows) noted, and (b-g) off-chip imaging is shown, with (ai, b, d, f, g) brightfield and (aai, c, e) fluorescence. Gas 3 psi, oil 0.02 $\mu\text{l}/\text{min}$, aqueous 40 $\mu\text{l}/\text{min}$. Images *b* to *g* are a timeseries where the time between each image was 5-10 s.

Figure 7.14 shows pinch-off of C_4F_{10} gas in 10 vol% pluronic triacetin oil in 0.1 vol% pluronic standard lipid solution, through the FF 5C1 nozzle, with an off-chip imaging time series (*b* to *g*, 5-10 s between frames) of the sample. Whilst the oil phase had a large volume during flow, it was found that any volumetric flow rate <1 $\mu\text{l}/\text{min}$ caused the oil to be pushed back up the inlet by either the gas or lipid solution phases. During flow, the gas bulb was seen to rapidly displace between the end of its inlet and close to the nozzle. However, as can be seen in Figure 7.14aai, a number of 20-40 μm double-layered structures were successfully formed on-chip. These were formed in the brief moments that the gas bulb was in the region of the nozzle. This indicated the potential for a more stable and repeatable formation regime if the bulb could be held at the nozzle, however a regime like this that successfully showed pinch-off was never achieved.

Figure 7.14b-g shows the resultant solution off-chip. Immediately after sample preparation, $\sim 100\ \mu\text{m}$ MBs were observed. Since the double-layered MBs formed on-chip were $20\text{--}40\ \mu\text{m}$, it is most likely that the off-chip MBs were a result of downstream coalescence. (Figure 7.14b-c) On initial observation, a partial oil ring was observed, with a similar radius of curvature to two neighbouring MBs. Parts of the oil were displaced into the ring and portions of the oil had jetted from the ring into the surrounding solution. (7.14d-e) On further observation of the same area, the two remaining MBs were seen to rapidly go through a gas core collapse, resulting in a similar structure to that of the first oil ring. (Figure 7.14f-g) The remaining oil was then shown to quickly coalesce into larger oil droplets. It is believed that; (1) large OLI-MBs had been successfully stabilised in the solution. After placing the solution, open-topped, on a glass slide, (2) the MBs quickly rose to the surface and began to concentrate at the interface. (3) The water film between the MB interface, of C_4F_{10} gas-oil-lipid/pluronic-water, and the sample meniscus interface, of water-lipid/pluronic-air, progressively became thinner. This continued until (4), akin to how a soap bubble bursts when the water layer between the two soap stabilised surfaces evaporates, the gas core of the MBs became exposed to the air, collapsing inwards due to Laplace pressure. (5) This caused a portion of the oil shell to be dragged inwards, and at the end of MB collapse caused an outward moving shock wave, forcing portions of the oil shell out into the surrounding solution. (6) The freshly formed, unstabilised oil surfaces then began to coalesce. Between OLI-MBs, these events may have occurred around the same time but independently. However, it is also possible that the shockwave generated by MB rupture led to aiding in the destabilisation of the neighbouring MBs.

7.3.3. Triton shelled OLI-MBs

During the studies detailed in section 7.2.3 it was seen that two-phase pinch-off of dodecane oil was possible using Triton solution as the aqueous phase, and estimations were given for flow conditions that could lead to three-phase pinch-off of C_4F_{10} gas in dodecane in Triton solution. Therefore this section of the work looked at using dodecane and Triton solution for OLI-MB formation. Figure 7.15 gives the optimal formation flow conditions and off-chip imaging that was observed during all of these trials.

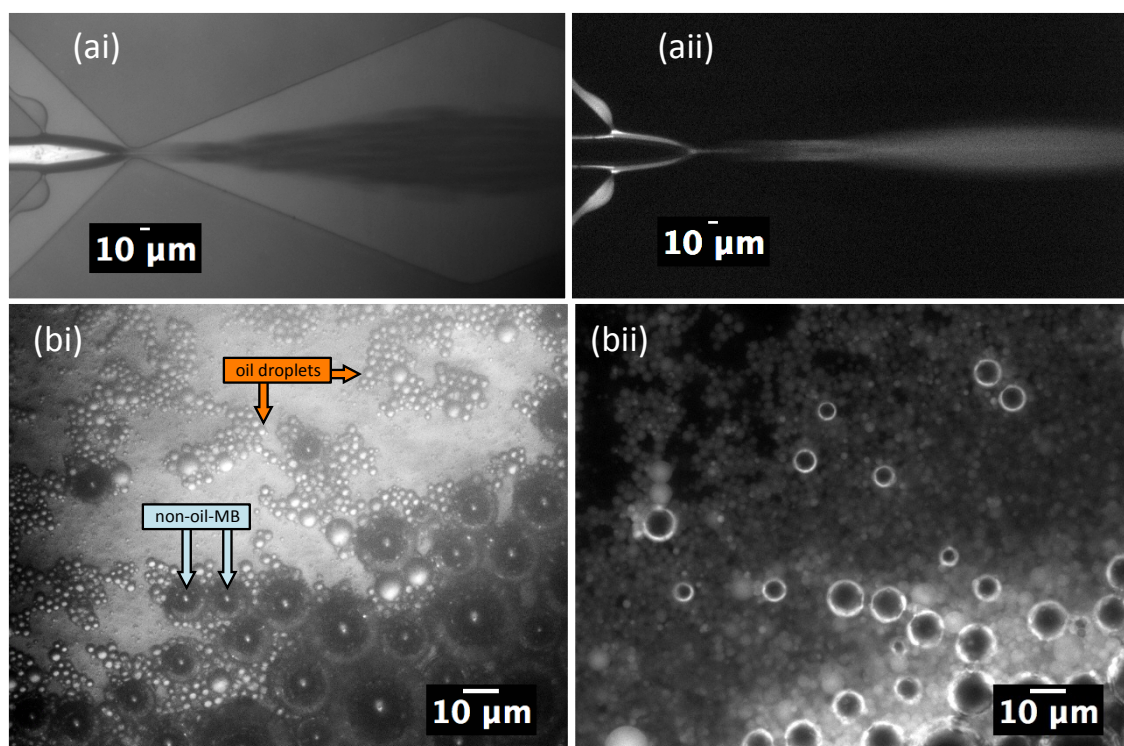


Fig. 7.15. 3C3 microfluidic pinch-off trial of C_4F_{10} gas in dodecane oil + 10 vol% Span80 in MilliQ + 1 vol% Triton. (a) On-chip formation and (b) off-chip imaging is shown, with (ii) fluorescence. Flow of the aqueous phase was set based on information from Figure 7.12. Gas 2 psi, oil 0.5 $\mu\text{l}/\text{min}$, aqueous 15 $\mu\text{l}/\text{min}$ respectively. For off-chip imaging, the MBs and oil droplets were concentrated by adding a droplet of the solution to a glass slide.

Pinch-off of C_4F_{10} gas in dodecane in Triton solution was found to be unsuccessful, leading to a high degree of coalescence on-chip. Therefore, 10 vol% Span80 was added to the oil phase in an attempt to aid stabilisation of the gas-oil interface. Span 80 was used here as it is a common surfactant of choice when forming water droplets where oil is the outer continuous phase.^{156,265–267} Figure 7.15 shows pinch-off of C_4F_{10} gas in dodecane oil + Span80 in Triton solution through the FF 3C3 nozzle, with off-chip imaging of the sample. Flow conditions were set based on the information from Figure 7.12. This led to the rapid formation of highly stable MB streams, allowing for close packing without coalescence. (Figure 7.15aii) Fluorescence was observed around the gas bulb and through the inner close-packed MB streams. This suggested that the oil had successfully coated the gas bulb, but that only a portion of the MBs formed contained oil. When the resultant solution was examined from this experiment, a high concentration of $\sim 3 \mu\text{m}$ oil droplets were observed with a high concentration of MBs that showed inconsistent fluorescence around their shells, thought to be reflections from the oil droplets (in regions of view without droplets, the fluorescence was not observed). No evidence for the formation of stable OLI-MBs was observed. Either OLI-MBs were

formed on-chip but the gas and oil components spontaneously came apart later downstream, or separate MBs and oil droplets were formed on-chip that could not be identified without high frame rate imaging.

7.3.4. BSA shelled OLI-MBs

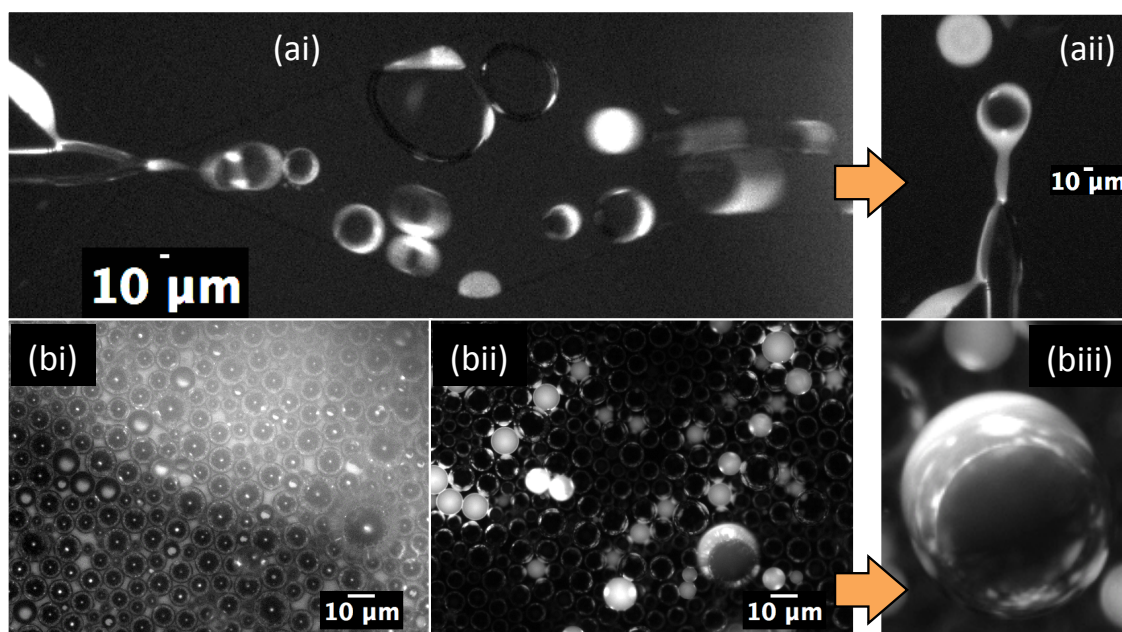


Fig. 7.16. 3C3 microfluidic pinch-off trial of C_4F_{10} gas in soybean oil in BSA solution. (a) On-chip formation and (b) off-chip imaging is shown, with (ai, aii, bii, biii) fluorescence. Gas 3 psi, oil 0.05 $\mu\text{l}/\text{min}$, aqueous 5 $\mu\text{l}/\text{min}$. Focussed regions are shown from (aii) the nozzle during OLI-MB formation, and (biii) a large OLI-MB that was observed off-chip.

Figure 7.16 shows pinch-off of C_4F_{10} gas in soybean oil in BSA solution through the FF 3C3 nozzle, with off-chip imaging of the sample. The on-chip formation of $43 \pm 1 \mu\text{m}$ (SD $6 \mu\text{m}$) OLI-MBs with oil layer thicknesses of $5 \pm 1 \mu\text{m}$ (SD $3 \mu\text{m}$) was regularly observed. Figure 7.16aii, shows a close up of the OLI-MB during pinch-off. The mechanism of formation was as follows: (1) Oil from the gas bulb jetted into the outlet. (2) This was followed by pinch-off of a gas MB, still inside of the oil jet. (3) The whole OLI-MB then pinched off of the bulb completely, allowing the formation of further OLI-MBs to formation to occur. It is most probable that the oil jet pinched off after the formation of the MB due to the momentum of the MB pushing against the oil-BSA interface, with it being more energetically favourable for the gas core to remain inside the oil phase than pass into the aqueous phase and be stabilised by the BSA alone. Off-chip imaging showed a higher number of non-fluorescent MBs and a lower number of fluorescent oil droplets, indicating that stable OLI-MBs had not been formed. The MBs present were observed to reflect the droplet fluorescence. However, one $24.8 \mu\text{m}$ OLI-

MB was observed with a single fluorescent oil lens, 3.6 μm at its thickest point, covering roughly half the of the gas core perimeter. There is a possibility that what occurred here was repeatable BSA shelled OLI-MB formation on-chip, followed by a subsequent de-wetting of the oil layer into separate non-oil-MBs and oil droplets. This effect has been shown in work by Deshpande *et al* (20016).²⁶⁸ They formed $\sim 20\ \mu\text{m}$ double emulsion droplets of water-(1-octanol)-water, using a FF microchip similar to the 5C1 design used in this project, with DOPC, DOPG, and Liss Rhod PE lipid dissolved in the 1-octanol oil phase. In timescales of seconds up to 10 min, they found that the oil portion concentrated to one side of the double emulsion droplet (cf. Figure 7.16biii), whilst leaving behind lipid in the form of a bilayer between the inner and outer water phases. The oil portion then entirely phase separated from the remaining water-(bilayer)-water droplet, a vesicle.

7.4. Conclusion

During this part of the study, the aim was to gain control over how bulk phases of gas, oil, and aqueous interacted with each other in the presence of surfactant (primarily lipids), through the use of microfluidic devices. Flow of the liquid phases was controlled in a co-flow channel, and then the controlled liquid stream was introduced to the gas phase at a FF nozzle. Whilst this control was gained prior to the nozzle, results in this chapter showed that this was not enough to facilitate controlled, repeatable OLI-MB pinch-off formation.

Squalane and dodecane oil were found to give a higher degree of oil layer uniformity when flowing oil and water down a co-flow channel when compared to triacetin and isoamyl acetate. This study found that more viscous oils led to a thicker oil layer for the same oil to lipid solution flow rate ratio. This was expected, but important to verify, as a thin oil layer was desired at the gas bulb of a three-phase FF nozzle between gas, oil, and aqueous phases. Therefore squalane and dodecane were more useful in providing reliable oil layers. Study of parts of the three-phase pinch-off process showed that two-phase pinch-off of squalane, triacetin, dodecane, and isoamyl acetate in lipid solution was not found to occur at any flow rates. Since the oil-lipid/water interface did not pinch-off in these experiments, and this interface also needed to pinch-off in three-phase microfluidics towards the formation of an OLI-MB, this was the first indication that the successful, stable, and repeatable pinch-off of OLI-MBs in lipid solution would not be possible. Pinch-off of the oils in Triton solution was found to be successful for

dodecane and squalane. For dodecane, the pinch-off regime could easily be controlled between co-flow, jetting, and dripping, with dripping occurring up to a maximum of 1 $\mu\text{l}/\text{min}$ oil. For squalane, a regime between dripping and jetting pinch-off occurred up to a maximum of 0.02 $\mu\text{l}/\text{min}$ oil. Pinch-off of C_4F_{10} gas in dodecane formed MBs at a minimum of 30 μm with larger MB sizes following a power relationship scaling law over the ratio between the gas and oil flow rates. Across all MB formation gas pressures, the range of oil flow rates that gave pinch-off was very limited, at 4.2 ± 1 , 4.3 ± 1 , 7.0 ± 1 , and $8.0 \mu\text{l}/\text{min}$ for squalane, triacetin, dodecane, and isoamyl acetate respectively. It was found that an oil with a higher viscosity required a lower flow rate to achieve pinch-off, which agreed with Ca theory. When comparing these two experiments for three-phase pinch off, where the two individual two-phase pinch-offs would need to occur simultaneously, it was found that no overlap existed for the oil velocities of the two two-phase pinch-off regimes. While assumptions were made to come to these findings, they did heavily suggest that stable pinch-off of OLI-MBs from a FF design was not possible. On the other hand, if both the oil and gas phases pinched-off due to shear forces contributed from the aqueous phase, then at least for dodecane oil pinch-off would be possible. For this case, the estimated formation ranges were 1.0-2.8 psi gas, 0.02-0.14 m/s oil, and 1.2-5.5 m/s Triton solution. This led to an estimated Triton solution flow rate of 10-45 $\mu\text{l}/\text{min}$. Later however, OLI-MB formation trials of C_4F_{10} gas in dodecane in Triton solution based on these estimated flow conditions did not provide OLI-MB pinch off, instead leading to a high degree of gas coalescence immediately after pinch-off. Adding Span80 to the dodecane oil prevented coalescence but resulted off-chip in separate oil droplets and non-oil-MBs. At this point the work progressed to trialling three-phase pinch-off of C_4F_{10} gas in the four oils used in this study, in four types of aqueous solution, in a large number of microfluidic FF devices. For more detail on which combinations of oil, aqueous, and microfluidic design were tests and notes on what observed, see Table 7.2. Almost all OLI-MB formation trials using standard lipid solution did not result in OLI-MB formation on-chip. Squalane samples did show off-chip evidence of stable 5-10 μm OLI-MBs. However, only a low concentration of OLI-MBs (< 10) were observed per 70 μl of solution imaged, and only half of the repeats of the flow conditions resulted in OLI-MBs being observed off-chip. After this, the work transitioned to look at forming OLI-MBs without a pure lipid shell. Adding pluronic solution to both the lipid solution and oil phases had some limited success at OLI-MB formation. Using the 5C1 device, 20-40 μm double layered MBs, thought to be OLI-MBs, were formed on-chip. Off-chip imaging showed $\sim 100 \mu\text{m}$ OLI-

MBs that were observed to go through gas collapse. Pinch-off of C₄F₁₀ gas-in-soybean-in-BSA was trialled. Formation in the 3C3 device showed the most promising on-chip OLI-MB formation throughout this chapter. Here, $43 \pm 1 \mu\text{m}$ (SD $6 \mu\text{m}$) OLI-MBs with oil layer thicknesses of $5 \pm 1 \mu\text{m}$ (SD $3 \mu\text{m}$), were formed through a combination of oil jetting, MB pinch-off in the oil jet, and the whole OLI-MB ejecting into the outlet. However, off-chip results showed that the majority of the sample stabilised as 5-10 μm non-oil-MBs and $\sim 10 \mu\text{m}$ oil droplets. One $24.8 \mu\text{m}$ OLI-MB was observed off-chip, with an oil lens, $3.6 \mu\text{m}$ at its thickest, covering half of its perimeter.

During this chapter some evidence for the successful formation of OLI-MBs was given. However, almost always, the introduction of the oil phase to the nozzle was found to destabilise any pinch-off occurring from just the gas and aqueous phases, and if any OLI-MBs were formed on-chip they were not stable to the point of off-chip imaging. This rapid destabilisation, for both scenarios, could indicate that the oil phase was presenting anti- or de-foaming effects (for a description of de-foaming, see Chapter 2.1, p 18). During the experiments in this chapter, only single MBs were created, not foams, but the associated local decreases to the surface tension of the MB shell may have still occurred, which would result in less stable gas-aqueous interfaces with lower MB lifetimes. Those OLI-MBs that were rarely observed off-chip ranged from 20-100 μm , with the squalane DPPC-PEG OLI-MBs being 5-10 μm but at an unusable concentration. The purpose of forming OLI-MBs during this project was to use them as drug delivery agents in the blood stream. This requires that their size be at maximum 8 μm and their concentration be at least 10^6 MBs/ml for any further studies. As such all of the OLI-MBs formed through the methods used in this chapter would be unsuitable for further use. The most promising on-chip formation observed was that of the last study shown of C₄F₁₀ gas-in-soybean-in-BSA solution. This study was only brief and as such could benefit from further work. A potential improvement to this study would be to use both lipid and BSA in the aqueous phase to allow for the formation of OLI-MBs with a hybrid shell, capable of on-chip pinch-off due to the use of the BSA, but also capable of functionalisation with PEG lipid chains, for use of the OLI-MBs in the body without being removed by the immune system, and targeting molecules, for targeting to specific problem sites. It was also suggested that the apparent high rate of OLI-MB formation on-chip followed by lack of OLI-MBs off chip could be due to phase-separation post-formation, as seen by Deshpande *et al.* (2016) for similarly formed water-(1-octanol)-water double emulsion droplets.²⁶⁸ They claim that a crucial step to the success of their

formation was controlling the on-chip channel hydrophobicity/hydrophilicity, where the post-nozzle outlet was treated to be hydrophilic with PVA in order to prevent the adsorption of their droplets immediately after formation.

8. Results: Activation of perfluorocarbon-in-oil-in-aqueous double emulsion droplets into OLI-MBs

Chapter 5 established that the formation of clinically relevant OLI-MB structures requires high levels of control over how the gas, oil, and aqueous phases are introduced. Instead of attempting to form an oil coated MB directly, this chapter studied the formation of oil coated liquid perfluorocarbon (PFC) double emulsion droplets and the potential to activate the liquid PFC into gas, forming an OLI-MB, as a second step. A benefit to this approach was that the dissolution time of liquid PFC is far lower than that of gas PFC, giving these a greater lifetime. This was appealing as it gave the prospect of forming long-life double emulsion droplets, with the ability for storage, and activation into OLI-MBs at the moment they were needed. However, a drawback to this approach was the volume expansion that occurs when a liquid converts into a gas. For a sphere of C_5F_{12} , the liquid to gas diameter expansion is ~ 5 times (see Chapter 3.5.1). In respect to the maximum size limit allowed for drug delivery systems in the blood stream ($8\ \mu\text{m}$), this placed a condition on the double emulsion that the PFC liquid cores could be at maximum $\sim 1.6\ \mu\text{m}$, preferably averaging $\sim 600\ \text{nm}$, with oil loading requiring even smaller liquid PFC core diameters. The work in this chapter is split into two distinct sections. First, formation of single and double emulsion liquid PFC droplets is shown, where the aim was to form droplets that were theoretically within clinical size ranges after activation. Second, different methods of activating the liquid PFC droplets are shown where either the samples' temperature was increased, or a global or local pressure drop was applied within the sample.

8.1. Formation of single emulsion perfluorocarbon droplets

This section of work looked at forming single emulsion PFC droplets without an oil coating. Surfactant shells tested were Triton and DPPC lipid. Formation techniques used consisted of microfluidic and tip sonication formation, which produced microscale and nanoscale PFC emulsions respectively. The nanoscale PFC droplets were formed with the intent of producing clinically relevant sized MBs after activation. However, as discussed in the relevant section of this thesis's theory (Chapter 3.5.2-3), due primarily to Laplace pressure, the smaller the PFC droplet, the more energy that must be supplied

in order to activate it into a gas (given by either an increase in the droplets temperature or decrease in pressure). As such, microscale PFC droplets were formed and used during preliminary testing to see if a particular method could be used for PFC droplet activation. PFC droplets were formed with cores of either C_5F_{12} , C_6F_{14} , or from a mixture of the two PFCs at 40 vol% and 60 vol% respectively (C5:C6).

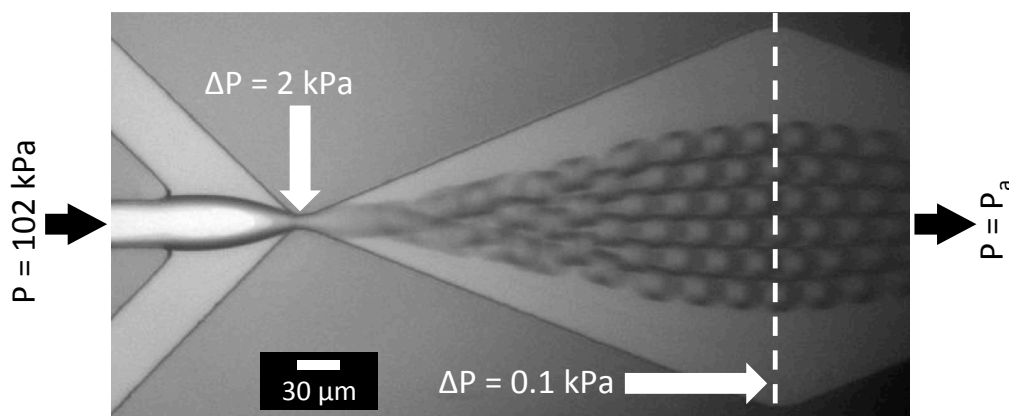


Fig. 8.1. Microfluidic formation of C_5F_{12} droplets in 1 vol% Triton solution, using a two-phase FF device. C_5F_{12} and Triton solutions at 1 and 3 $\mu\text{l}/\text{min}$ respectively. Estimated pressures (P) in and out of the device and pressure drops at specified locations are indicated.

Figure 8.1 shows microfluidic (flow focus) FF formation of C_5F_{12} droplets in 1 vol% Triton solution. Formation of C_6F_{14} and C5:C6 droplets showed equivalent pinch-off mechanics at the same flow rates, and formation with all PFC solutions was very repeatable. Formation was stable enough for the $\sim 20\ \mu\text{m}$ droplets to close pack in the outlet without any observation of coalescence. Optimal formation was found to occur at 1 $\mu\text{l}/\text{min}$ PFC solution and 2-3 $\mu\text{l}/\text{min}$ Triton solution. In order to facilitate pinch-off all flow rates had to be kept low to reduce Ca . It should be noted that as a 1 ml sample was typically desired, formation required 5 h. As such a stable formation that did not require constant attention was highly desirable. Figure 8.2 shows a transition from the PFC phase being in a liquid state to gas state during FF pinch-off. This transition was both occasional (it was not repeatable so no rate could be identified) and short-lived (relative to the whole formation time), though it was observed across all PFC solutions. The transition always originated upstream from the nozzle region. Thorough checks were made to ensure that no gas bubbles had been added to the PFC inlet during experiments, so it can be concluded that this was the PFC liquid phase changing into gas. At the nozzle, in order to phase convert bulk C_5F_{12} , an estimated combined liquid flow rate of 30 $\mu\text{l}/\text{min}$ would be needed to provide the required pressure drop of 17 kPa from atmospheric pressure. The flow rate would need to be increased in the wider parts of the

microfluidics, for PFC at higher molecular weight, and for PFC droplets of smaller size. As such, the phase conversion was occurring without reaching the estimated pressure threshold. Observation of the solution collected immediately after this phase change was observed on-chip showed no MBs off-chip. Either the MBs reverted back to liquid droplets, or the concentration of stable MBs formed was low enough to be negligible to the sample. Importantly the observation of phase transition did show that bulk PFC liquid could be activated into PFC gas with very low flow rates, in the inlet tubing or the larger channels of the microfluidic device, and so at velocities < 2 cm/s.

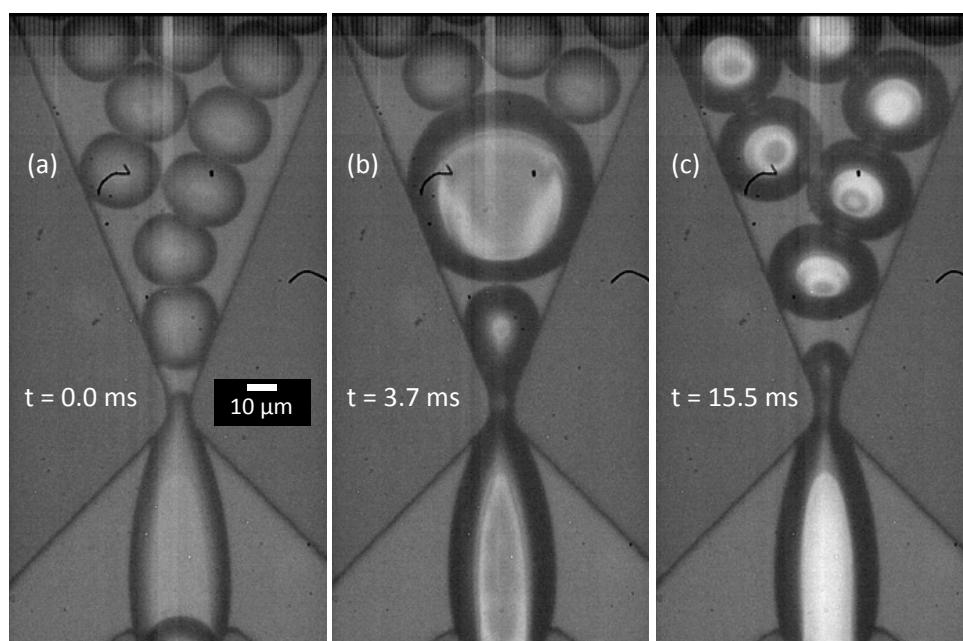


Fig. 8.2. Transition of C5:C6 liquid to gas during pinch-off in 1 vol% Triton solution. C5:C6 and Triton solutions set to liquid flow rates of 1 and 2 $\mu\text{l}/\text{min}$ respectively. High frame rate imaging at 49 kfps.

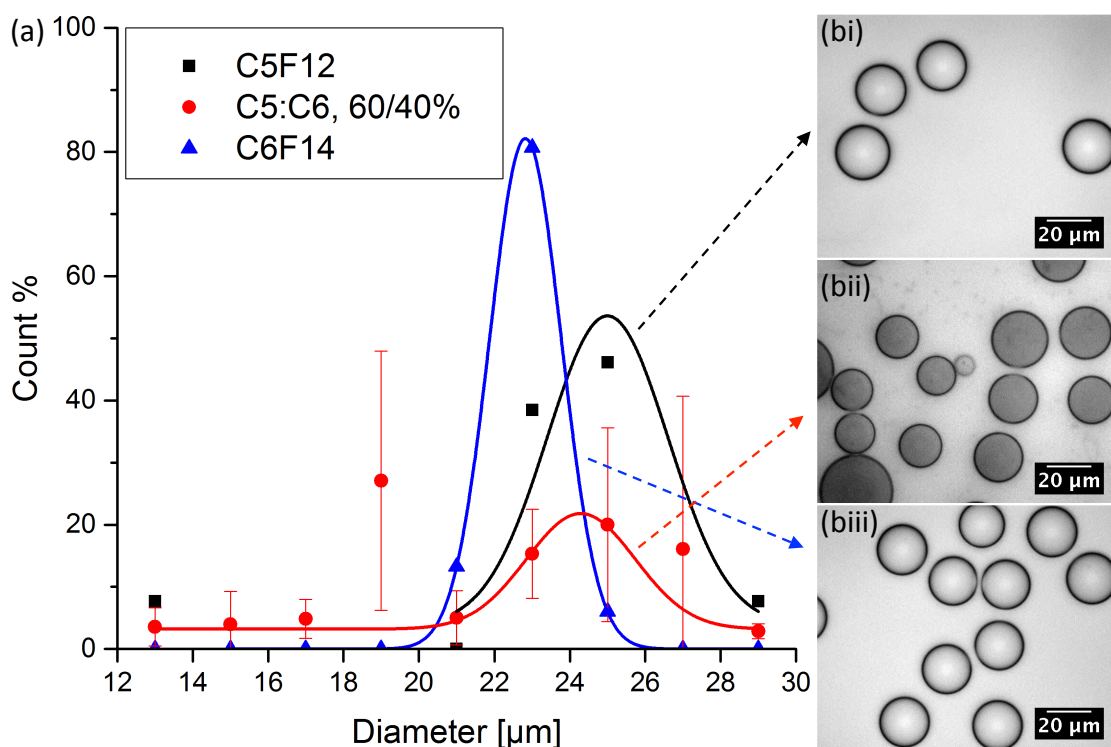


Fig. 8.3. (a) Off-chip sizing of C₅F₁₂ (black), C₅:C₆ (red), and C₆F₁₄ (blue) Triton microfluidic droplets, with (b) example images that the sizing information was measured from. $n \approx 50$.

Figure 8.3 shows sizing histogram data from C₅F₁₂, C₅:C₆, and C₆F₁₄ droplets, which were formed microfluidically in Triton solution, as in Figure 8.1. C₅F₁₂ and C₆F₁₄ droplets showed Gaussian distributions that agreed with the diameter averages, giving peak diameters of 25.0 ± 0.9 (FWHM 3.2) μm and 22.8 ± 0.1 (FWHM 1.9) μm respectively. However, the C₅:C₆ droplets showed a wide distribution of diameters, with a range from 12.3 μm up to 29.9 μm. The average C₅:C₆ droplet diameter was 22.1 ± 1.9 (SD 3.3) μm. Even though C₅F₁₂ and C₆F₁₄ liquids are miscible, each droplet may have been formed with a slightly different volume ratio of C₅:C₆, partly due to the small droplet volume of ~6 pl on-chip. Since C₅F₁₂ is more volatile than C₆F₁₄ this could have led to imbalances between PFC droplets. C₅F₁₂, C₅:C₆, and C₆F₁₄ droplets were formed at concentrations of $1.5 \pm 0.5 \times 10^6$ droplet/ml, $2.4 \pm 0.4 \times 10^7$ droplet/ml, and $9.3 \pm 1.1 \times 10^6$ droplet/ml respectively.

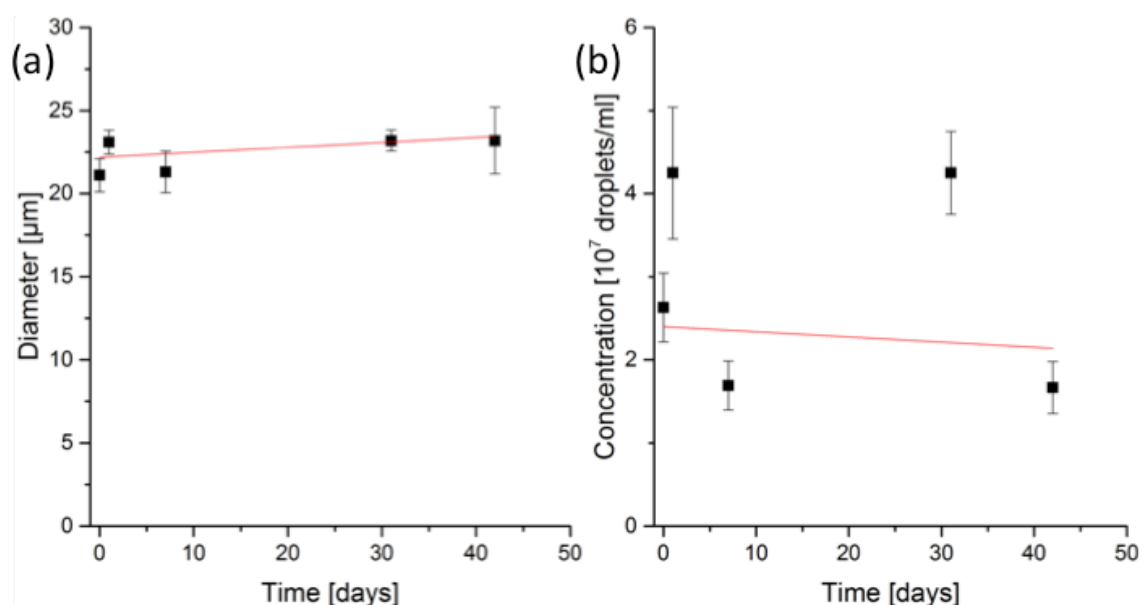


Fig. 8.4. Diameter and concentration measurements of C_5F_{12} Triton microfluidic droplets over 42 days.

Figure 8.4 shows diameter and concentration lifetime measurements from C_5F_{12} microfluidic droplets over a period of 42 days from their formation. Average diameter started at $22.2\ \mu\text{m}$ gradually rising to $23.5\ \mu\text{m}$, a 6% increase. This $1.3\ \mu\text{m}$ increase was within the range of the average error of $1.1\ \mu\text{m}$, so can be assumed to be negligible. The concentration poorly correlated over the 42 days, but remained at 10^7 droplets/ml. PFC droplets of this size were observed to form a pellet out of solution in under 10 s. Therefore, the large variation in the concentration may have been due to the rapid falling out of the droplets immediately after the gentle agitation of the solution in order to extract a sample for sizing and concentration measurement. As the intent was to activate these droplets into MBs, of which typical second generation MBs (consisting of an inert gas core such as PFC) have been suggested to have maximum lifetime of several hours,¹⁸⁶ these results provided the first indication, in this project, that the prospect of forming a long shelf life MB precursor could be achieved using liquid PFC droplets.

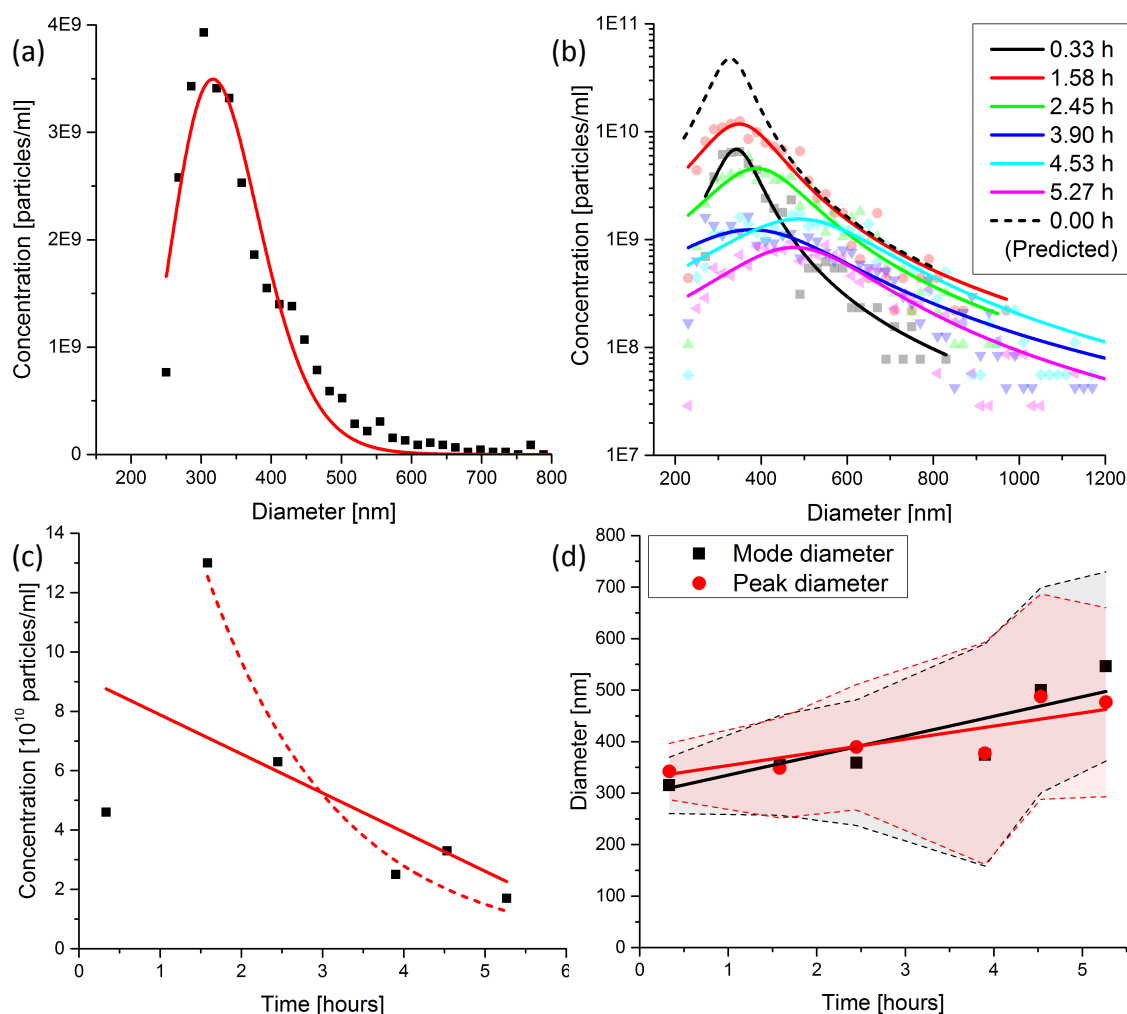


Fig. 8.5. (a) Histogram of 5 min tip sonicated C_5F_{12} -Triton nanoemulsion droplet diameters in respect to concentration and (b-d) lifetime measurements, measured from the same solution, over 5.3 h from the end of nanoemulsion formation. (b) Histogram of droplet diameters in respect to concentration, for each time measurement, with a prediction of the size distribution at 0 h calculated from Figures c-d. (c) Total sample concentration recorded, with a linear fit to all of the data and an exponential fit to all data past the first measurement (the concentration of the first measurement was considered inaccurate – the reason is given in main text). (d) Mode and peak diameters measured from the total sample and the fittings of Figure b, with errors as the FWHM of Figure b.

Figure 8.5 shows diameter and concentration lifetime measurements from 5 min tip sonicated Triton- C_5F_{12} droplets over a period of 5.3 h from their initial formation. Unlike the PFC microemulsion of Figure 8.4, tip sonicated PFC nanodroplets were found to lose concentration and increase in size over the time scale of hours. This was most likely due to the nanoemulsions' higher surface area to volume ratio causing a more rapid Ostwald ripening effect (see Theory Chapter 3.2.3, p 47-48). Calculating the total C_5F_{12} volume at each time point, from the data of Figure 8.5b, revealed that the first recorded time point ($t = 0.33$ h) had only accounted for 1/3 of the total C_5F_{12}

volume in the whole solution (concentration of 5 $\mu\text{l/ml}$). On the other hand each time point following this did account for the entire C_5F_{12} volume, with a following decrease in total volume likely due to dissolution (data not shown). Due to this, the concentration of the first data point was considered to have been measured inaccurately, allowing an exponential to be fit to the data of Figure 8.5c. By the exponential fit, the C_5F_{12} droplets had an initial concentration of $3.4 \pm 0.7 \times 10^{11}$ droplets/ml with a half-life of 1.1 h. For every half-life, the peak diameter of the droplets increased by 35 ± 7 nm ($11 \pm 3\%$ for the initial half-life) and their FWHM distribution increased by 70 nm (69% for the initial half-life). From the concentration, peak size, and distribution data, a predicted 0 h plot was added to Figure 8.5b. During activation of PFC droplets into MBs a large problem that has appeared to plague much of the literature is low activation rates.²⁶⁹ Shpak (2014) claimed that activation of PFC droplets at just 10% would be a relatively high activation, but that due to re-condensation stable MBs could be expected to be around or below 1%.²⁷⁰ As such, it is imperative that a high concentration of precursor droplets are present on activation, and that they are as monodisperse as possible to activate via the same energy provided by a single activation step. As such, the hourly half-life and rapid accumulation of polydispersity found for tip sonicated C_5F_{12} droplets means that they do not have a desired shelf life, and that any use of samples during this project occurred immediately after production, with a fresh formulation for each experiment.

2-3 μm MBs were desired to keep in line with current clinical applications of MBs.^{186,271–275} As such, PFC droplets of 400-600 nm were optimal. A number of nanoemulsions were tested for size based on; PFC core type, lipid or Triton shell, tip sonication times or extrusion formation. 5 min tip sonicated Triton- C_5F_{12} droplets gave the optimal formation of droplets with peak size closest to 400-600 nm, without droplets above 1 μm . However due to the rapid change of sample concentration and size shown in Figure 8.5, any comparison was unreliable without factoring in the time after nanoemulsion formation, and so the data has not been shown.

In this section it was discovered that microfluidically formed PFC microemulsion droplets had the potential for monthly if not yearly shelf life. However, these droplets were too large for clinical use, especially with further liquid to gas expansion. On the other hand, tip sonicated PFC nanoemulsion droplets could be formed at clinically relevant sizes, but their hourly half-life meant that they did not have a desirable shelf life and should be used immediately after formation.

8.2. Formation of double emulsion perfluorocarbon-in-oil droplets

This section of the work looked at forming double emulsion droplets of C_5F_{12} encapsulated in an oil layer, encapsulated in an aqueous solution with some surfactant layer. Oils tested were soybean, isoamyl acetate, triacetin, dodecane, and squalane. Surfactants studied were Span 80, Triton, BSA protein. The first set of experiments detail the success of a two-step method of forming a stable emulsion of C_5F_{12} droplets in oil, then passing this through FF microfluidics to encapsulate the emulsion. The second set of experiments cover a simultaneous encapsulation of C_5F_{12} in oil and oil in BSA solution by mechanical agitation, the findings of this method with different oils in terms of the droplet sizes and oil layer to total size ratio, and optimising control over these aspects of the droplets by varying the concentration of each phase.

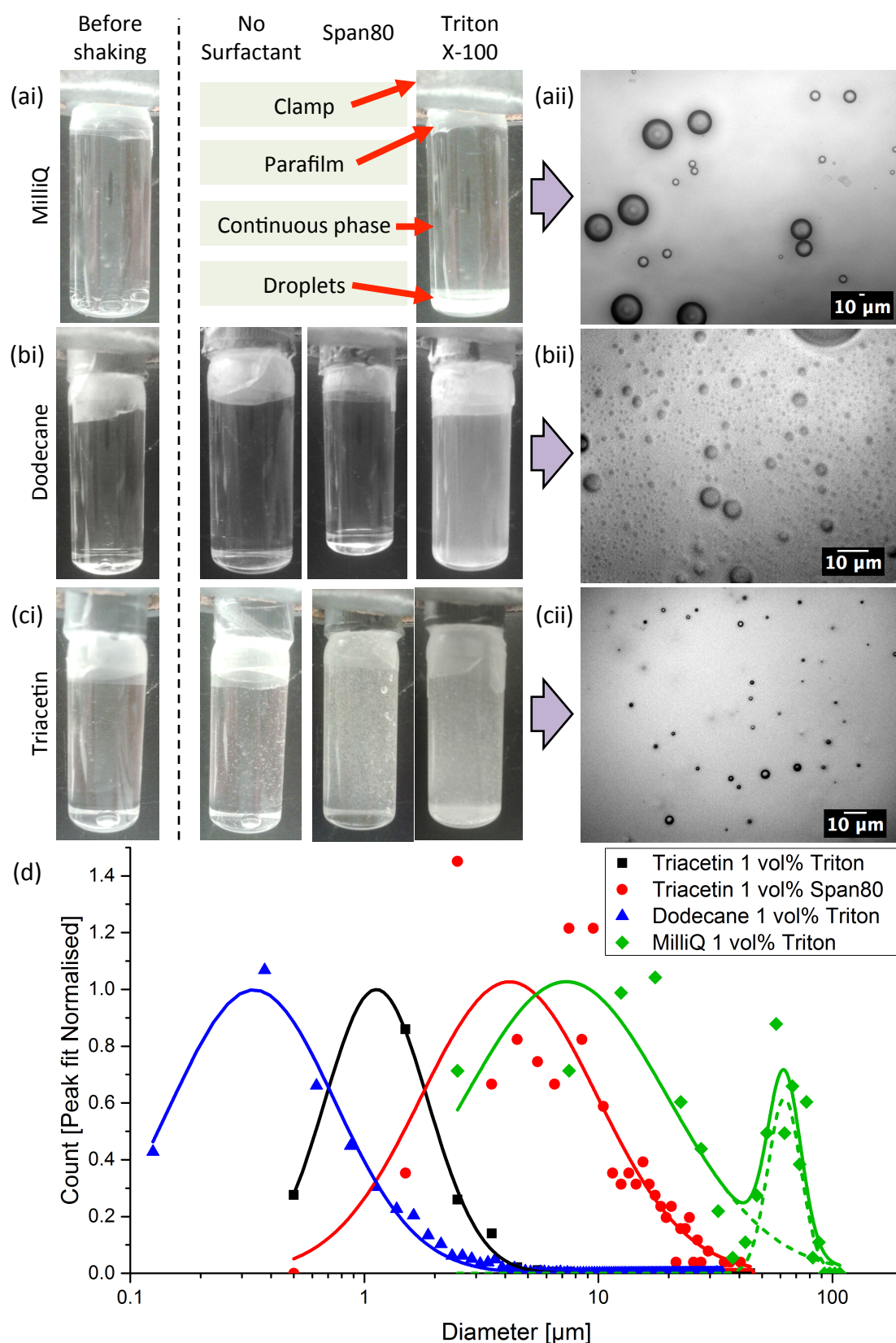


Fig. 8.6. Mechanical agitation formation and sizing of C_5F_{12} droplets in (a) MilliQ, (b) dodecane, and (c) triacetin, using no surfactant, 1 vol% Span80, and 1 vol% Triton. (i) Vials filled with 1 vol% C_5F_{12} in the continuous aqueous or oil phases are shown before and after 45 s of mechanical agitation, with (ii) example images shown of post-formation droplets, and (d) sizing histograms measured from those images.

Figure 8.6 shows vials filled with C_5F_{12} in MilliQ, dodecane, or triacetin, where no surfactant, Span 80, or Triton X-100 was solubilised into the continuous phase, before and after mechanical agitation (45 s agitation as in MB formation, Experimental Chapter 4.4, p 71). It then shows post-agitation example images of the droplet emulsions stabilised by Triton solution, followed by comparative histograms of the droplet diameters measured from all of the samples that showed a stable droplet emulsion. Squalane and isoamyl acetate samples were tested alongside the other oils, but neither showed any stable emulsion. Peak sizes were recorded as 1.5 ± 0.1 (FWHM 1.4) μm , 8.8 ± 0.9 (FWHM 10.1) μm , and 0.6 ± 0.1 (FWHM 0.7) μm for C_5F_{12} in triacetin + Triton, triacetin + Span80, and dodecane + Triton emulsions. C_5F_{12} droplets in MilliQ Triton showed a bimodal distribution with peaks at 64 ± 2 (FWHM 25) μm and 20 ± 5 (FWHM 22) μm . Since for clinical use, droplets with a desired average and maximum allowed size were 200-600 nm and 1.6 μm respectively, only the C_5F_{12} in dodecane + 1 vol% Triton emulsion had an acceptable size distribution for further encapsulation (this sample's size distribution still had droplets $> 1.6 \mu\text{m}$, which might have meant that this emulsion would be clinically unviable, but they were of a low concentration). Figure 8.7 shows on-chip FF pinch-off of the C_5F_{12} -dodecane + Triton emulsion in MilliQ + 1 vol% Triton solution. Example images are shown from observations of the resultant emulsion off-chip. Histogram size distributions are presented of the droplet diameters recorded on- and off-chip. Droplets were recorded on- and off-chip at 25.5 ± 0.1 (FWHM 1.2) μm and 2.5 ± 0.7 (FWHM 13.6) μm respectively. (Figure 8.7bii) Fluorescence showed that a small number of droplets contained cores with decreased fluorescence, indicating a double emulsion structure. However, the large majority of droplets were fully fluorescent. The reduction in droplet diameter, increase in size distribution, and only a fraction of the droplets retaining C_5F_{12} cores, together suggested that a high proportion of the double emulsion droplets had been activated but left no stable MBs. The activation would have expanded the C_5F_{12} portions, potentially forcing the oil shells to break apart into smaller droplets, as is suggested by the off-chip images. One solution to the problem of premature activation would be to use a C_6F_{14} core emulsion. However, the on-chip droplet size, which would be retained in the off-chip droplet size if premature activation did not occur, was more than 3 times the allowed maximum drug carrier diameter for clinical use. As such, this double emulsion formation technique stopped here.

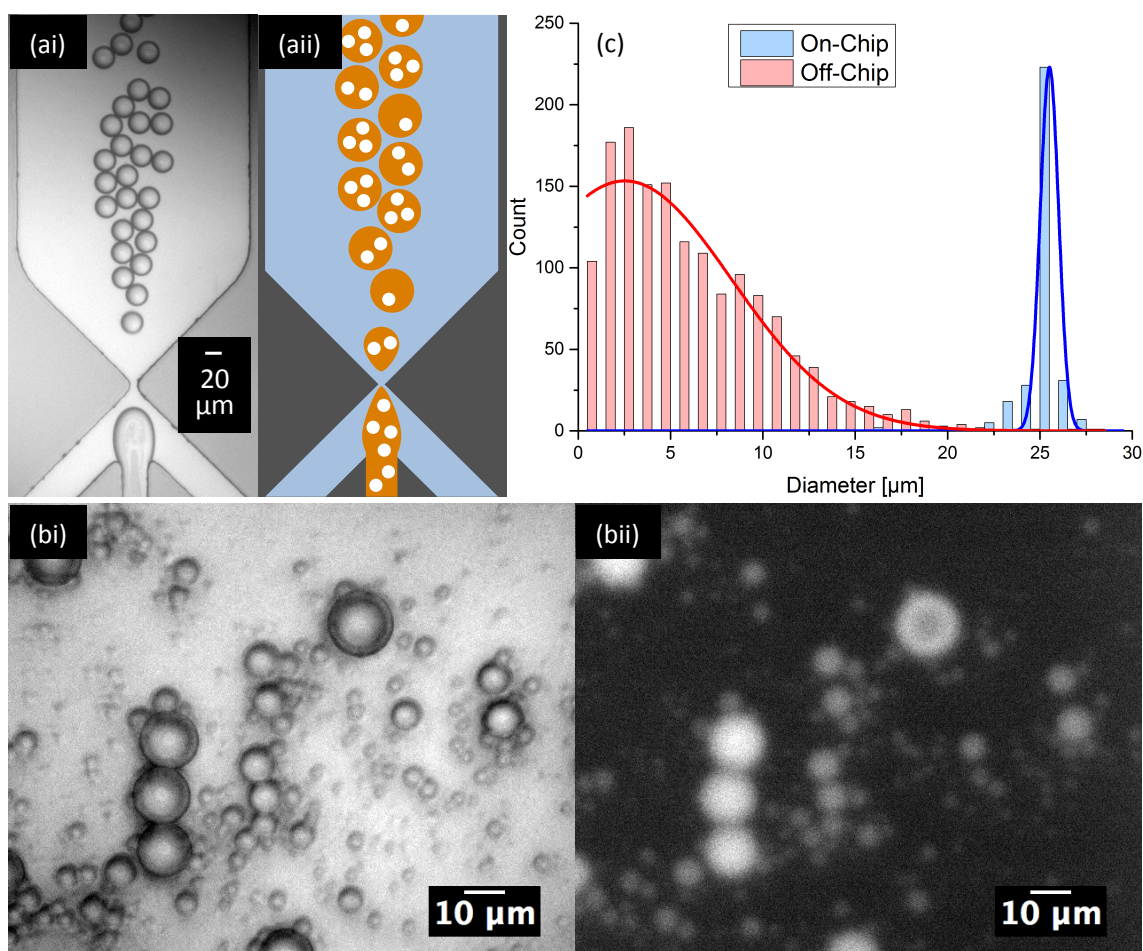


Fig. 8.7. (ai) Experimental image and (aai) schematic of pinch-off of C_5F_{12} (white) in dodecane + 1 vol% Triton (orange) emulsion in MilliQ + 1 vol% Triton solution (blue), at 1 and 2 $\mu\text{l}/\text{min}$ respectively. (b) Off-chip imaging of resulting droplet solution. (c) Sizing histograms of droplets formed on-chip and resultant droplet solution off-chip.

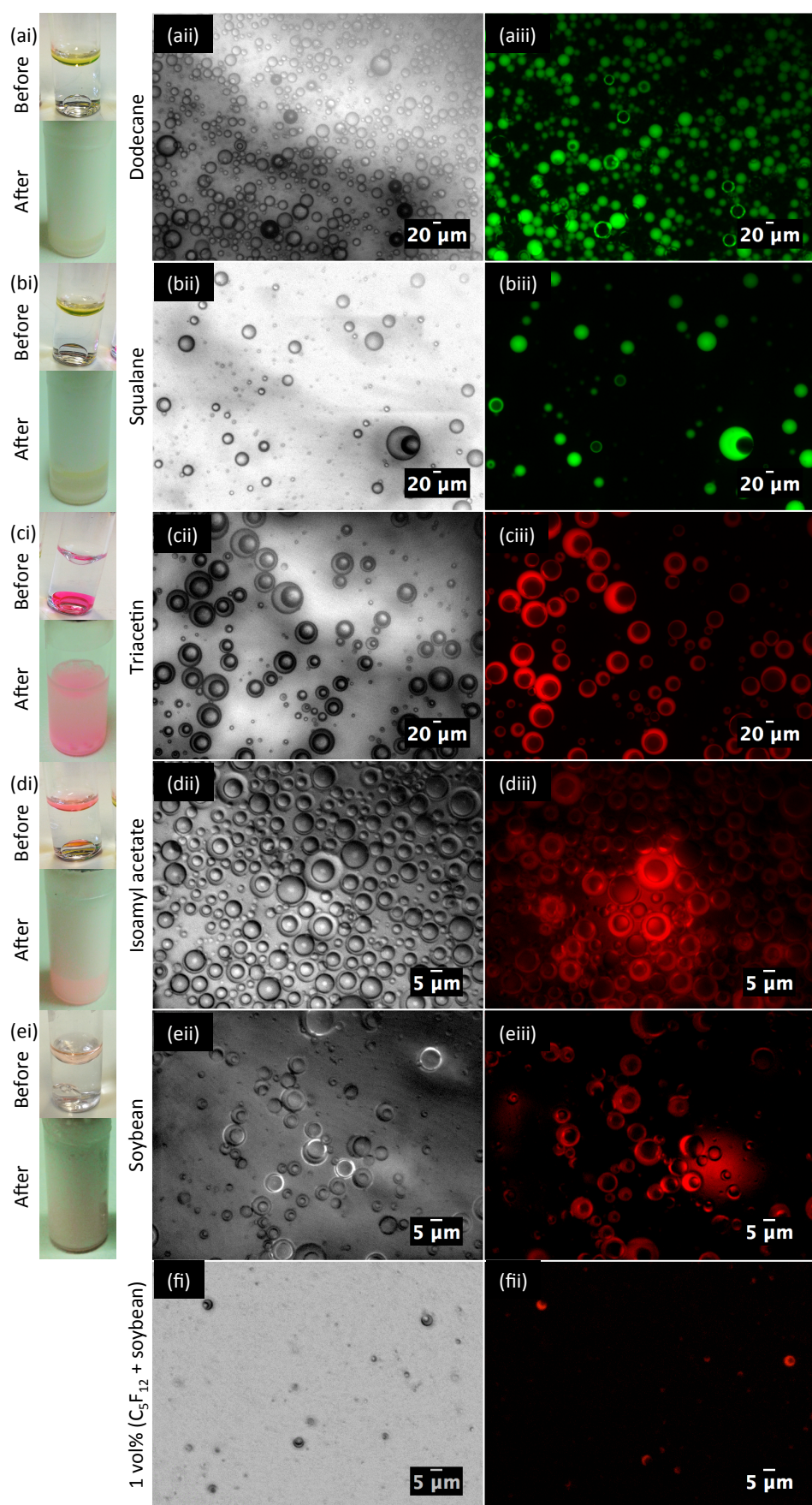


Fig. 8.8. Mechanical agitation formation of C_5F_{12} -oil-BSA double emulsion droplets. (ai-ei) Vials of 10 vol% C_5F_{12} + 10 vol% oil in 4 mg/ml BSA solution before and after agitation. Imaging of the resultant droplet solution by (a(ii)-e(ii)) white light and (a(iii)-e(iii)) fluorescence from Nile red in the oil phase.

Figure 8.8 shows vials of 10 vol% C_5F_{12} + 10 vol% oil in BSA solution before and after mechanical agitation, and gives example images of the remaining post-agitation solution. Dodecane, squalane, triacetin, isoamyl acetate, and soybean were tested. An example is also shown for soybean and C_5F_{12} at 1 vol%. Apart from the triacetin sample, all samples formed large foams with $\sim 100\text{--}500\ \mu\text{l}$ of remaining solution. The triacetin sample did also form MBs that floated to the top of the vial, however it retained almost all of its solution. It is most probable that the majority of these foams were due to high shear stress activation of the non-emulsified C_5F_{12} liquid, since similar mechanical agitation of BSA solution in the presence of PFC gas regularly forms a cloudy solution of MBs without this degree of foaming. Dodecane and squalane samples showed a small proportion of double emulsion droplets, but most droplets were either single emulsion C_5F_{12} or oil droplets, as defined by either no fluorescence (potentially reflecting fluorescence) or fully fluorescent cores. Triacetin, isoamyl acetate, and soybean all showed successful double emulsion formation with few to no droplets observed as single emulsions. Determining which oils showed successful double emulsion formation could not be attributed to the oil viscosity, solubility, or oil-water surface tension. The density of both squalane and dodecane is lower than the other three oils, but given the relative densities of the successful oils to water, this did not seem to play any role in the success or fail of double emulsion formation. Figure 8.9 shows histograms of the double emulsion droplet sizes measured from the Figure 8.8 and how the total droplet radius related to the C_5F_{12} core radius. Only data from the four successful formation samples (as defined above) are shown. All samples showed a clustering of the ratio between the core and total radius over the total droplet diameter, with no apparent relationship between the two aspects. Table 8.1 shows how the peak droplet diameter and the average ratio of core to total droplet radius compared for each sample. Triacetin double emulsion droplets were found to be larger than the other oil samples, at $34.5\ \mu\text{m}$. This may have been due to triacetin's higher solubility than dodecane or soybean, at $70\ \text{g/l}$.⁹⁶ During break-up of the bulk oil, the surface to volume ratio will have greatly and rapidly increased. This will have allowed for rapid solubilisation of the new triacetin surfaces, likely leading to a slower stabilisation of surfaces, and so a greater potential for coalescence of the C_5F_{12} and oil emulsions. Both the isoamyl acetate and 10 vol% soybean samples showed smaller droplet peak sizes at 7.7 and $5.3\ \mu\text{m}$ respectively, though both samples had droplets above the clinical size limit before activation. As such, the 1 vol% soybean sample was also studied to see if

the total droplet diameter could be decreased whilst keeping the core to total droplet radius ratio constant. The 1 vol% soybean sample did decrease the peak droplet size to 3.3 μm , and gave a more monodisperse peak size sample, but the spread of the core to total droplet radius ratio was increased. Attempts to control the droplet size and radius ratio are continued in Figure 8.10.

Tab. 8.1. C_5F_{12} -oil-BSA, mechanical agitation, double emulsion peak droplet diameter, average value of the droplets' C_5F_{12} core radius divided by the radius of the whole droplet, and droplet concentration.

	Oil and C_5 vol%	Diameter [μm]	FWHM [μm]	Radius of C_5 core / total droplet	Stdev	Concentration [droplets/ml]
Triacetin	10	34.5 ± 3.3	47.4	0.68 ± 0.02	0.15	$4.2\text{E}+06$
Isoamyl acetate	10	7.7 ± 0.4	5.8	0.69 ± 0.01	0.09	$2.5\text{E}+08$
Soybean	10	5.3 ± 0.6	5.7	0.68 ± 0.01	0.10	$1.2\text{E}+08$
	1	3.3 ± 0.1	1.8	0.59 ± 0.02	0.11	$1.8\text{E}+07$

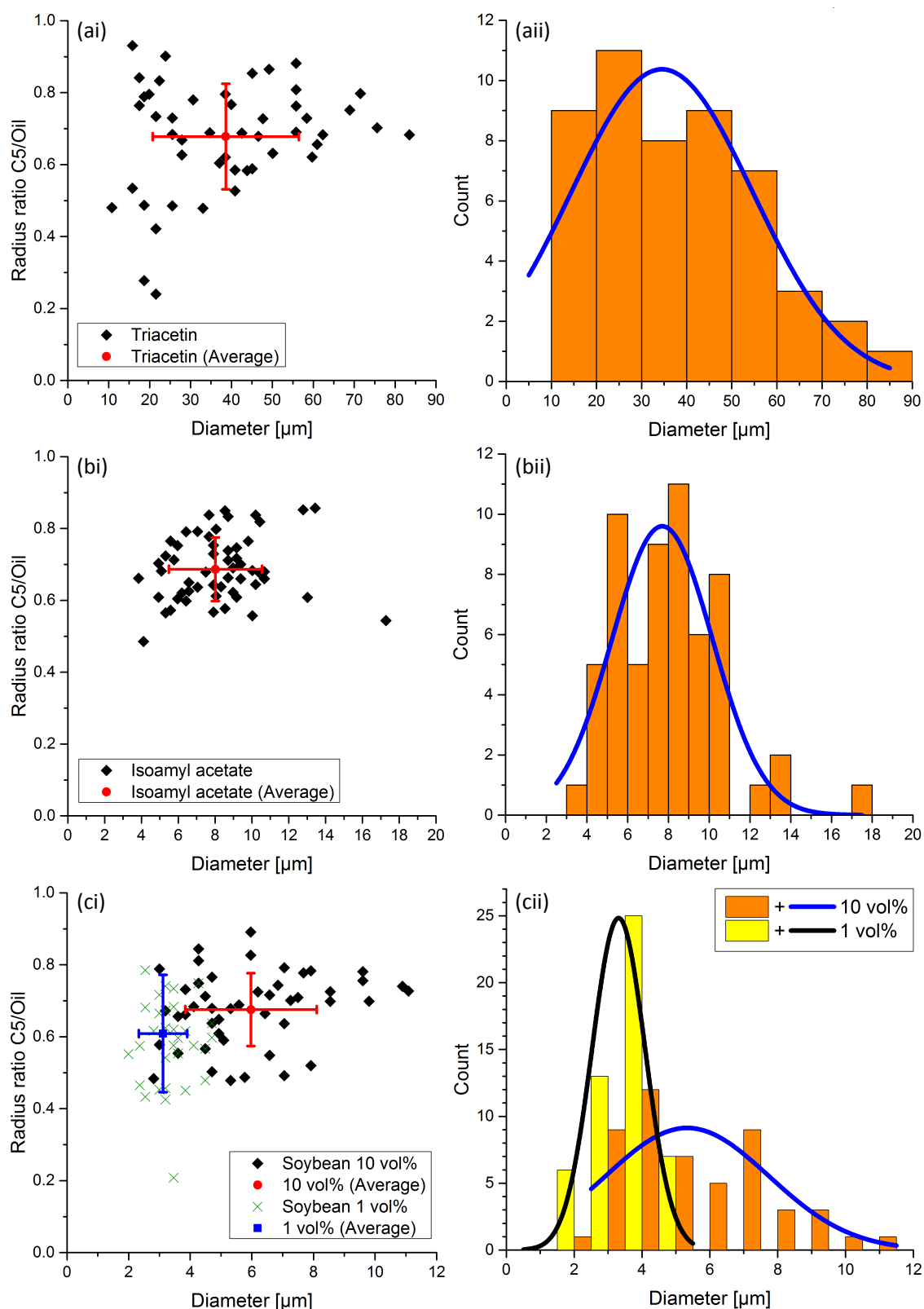


Fig. 8.9. Sizing measurements of C_5F_{12} -oil-BSA double emulsion droplets, using (a) triacetin, (b) isoamyl acetate, and (c) soybean oil. C_5F_{12} and oil phases both at 10 vol% with soybean also at 1 vol%. (i) Measurements of droplet diameter against the radius of the C_5F_{12} core divided by the radius of the whole C_5F_{12} -oil double emulsion droplet (as a radius ratio). (ii) Sizing histograms of the whole droplet diameters.

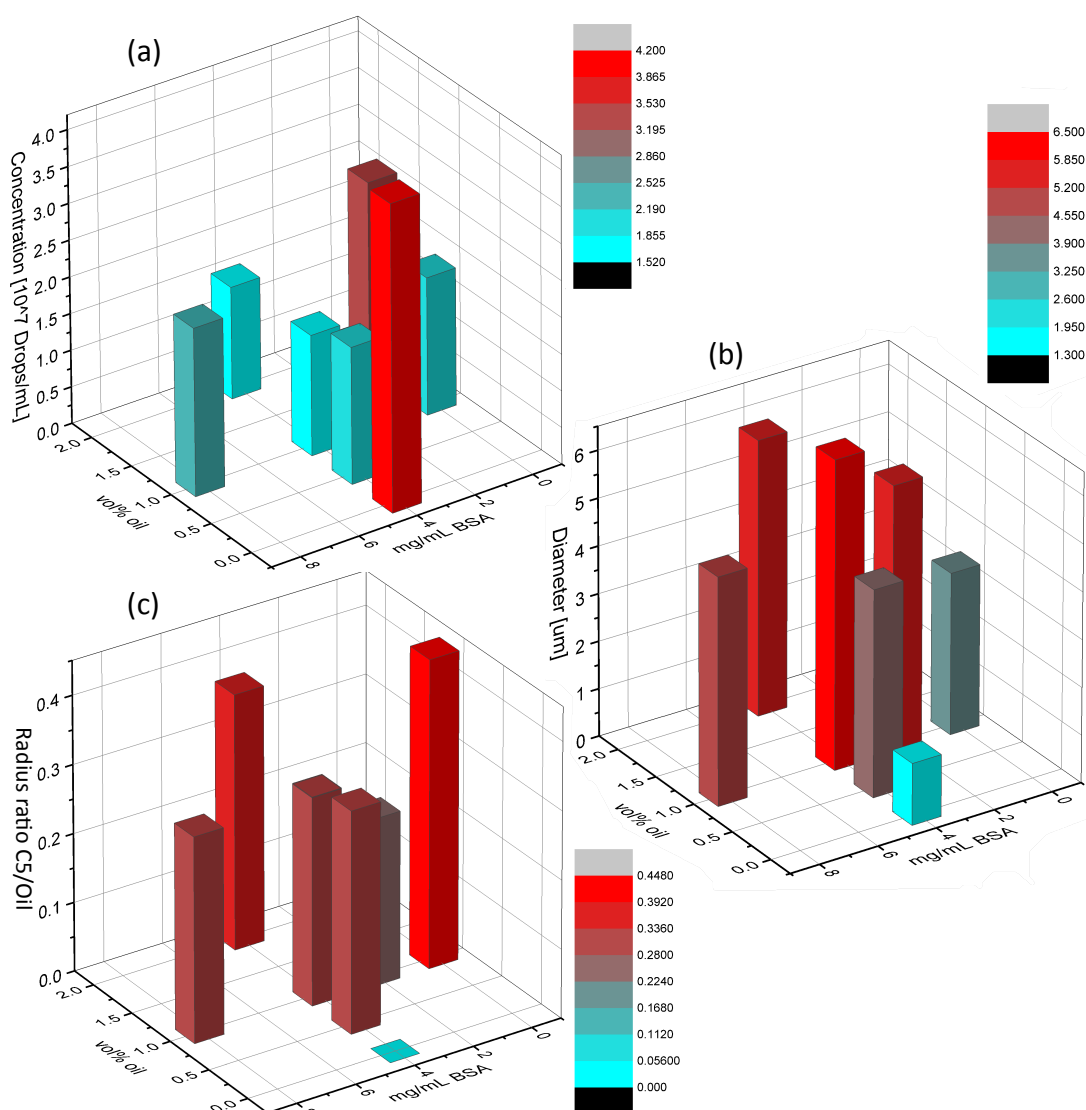


Fig. 8.10. Sizing data from C₅F₁₂-soybean-BSA double emulsion droplets with constant 1 vol% C₅F₁₂ when varying oil and BSA concentration. Average droplet (a) concentration, (b) diameter, and (c) the radius of the C₅F₁₂ core divided by the radius of the whole C₅F₁₂-oil double emulsion droplet (as a radius ratio).

Figure 8.10 shows the average concentration, diameter, and ratio of core to total droplet radius measured for double emulsion C₅F₁₂-soybean-BSA droplets, due to varying the oil and BSA concentration whilst keeping the C₅F₁₂ concentration constant at 1 vol%. It was expected that increasing the oil concentration would decrease the core to total droplet radius ratio and increase the droplet size, or increase droplet concentration. However, overall no systematic control was gained over the droplets size, concentration, or ratio of core to total droplet radius over the oil and BSA concentration ranges tested. It should also be noted that the repeat results from Figures 8.9 and 8.10 did not agree with one another, showing large batch variability. This all suggests that the mechanical agitation method for forming C₅F₁₂-oil-BSA droplets does not have room for any

greater level of control. It is understood that this is most probably due to the chaotic nature of phase break-up by the mechanical agitation method.

Tip sonication of C_5F_{12} , soybean oil, and BSA solution was studied as another technique for double emulsion formation since it had been shown to provide size control over single emulsion PFC droplet by sonication times in section 8.1. However, the results were inconclusive (results not shown) showing a bimodal distribution, with peak diameter at 0.6 and 2.2 μm , and little indication that C_5F_{12} had been encapsulated into the oil phase.

In this section the formation of double emulsion PFC-oil-aqueous droplets were studied. Encapsulating a PFC-oil precursor emulsion in aqueous was found to be successful on-chip using dodecane oil. However the total droplet diameter formed on-chip was too large for clinical application, and at some point after on-chip formation to off-chip observation, the droplets were found to activate, leaving a highly polydisperse sample of oil droplets with a negligible concentration of double emulsion droplets remaining. Mechanical agitation of PFC, oil, and BSA solution was found to form the double emulsion for a number of the oils tested. Initially, the total droplet size was reduced by reducing the concentration of PFC and oil from 10 vol% to 1 vol%. However, deeper studies of the approach gave little control over the total droplet or PFC core size. During the activation trials detailed in the following sections, all experiments using the PFC-oil double emulsion droplets used the 10 vol% emulsion due to the larger size requiring a lower energy for activation.

8.3. Activation of single and double emulsion droplets

In this section, the single and double emulsion PFC droplets that had been formed in sections 8.1-8.2 were put through phase-change activation trials. These included increases to the temperature, to approach and pass the droplets' boiling point, and decreases to the pressure, to approach and pass the droplets' vapour pressure and nucleate phase-change.

8.3.1. Thermal activation

This section deals with the thermal activation trials. The temperature of PFC droplet micro- and nanoemulsions was gradually increased. Observations were made of the microemulsion solution by eye, focusing on solution turbidity, of the microscale

droplets by direct observation, and of the nanoscale droplets through DLS size measurements over time.

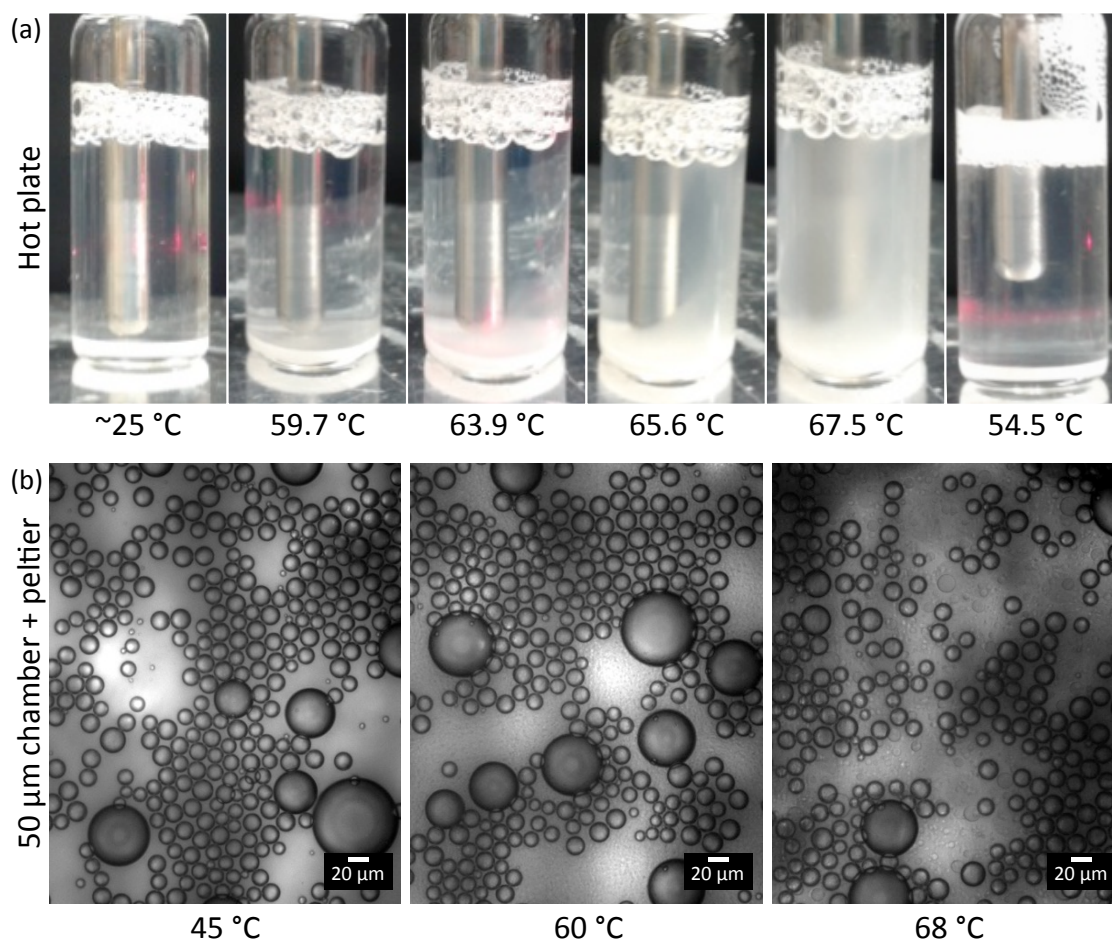


Fig. 8.11. C_5F_{12} -Triton microemulsion, in a (a) vial and (b) $50\ \mu\text{m}$ chamber, during heating to 68°C , either from a hot plate or Peltier heater respectively.

Figure 8.11 shows microfluidically formed C_5F_{12} -Triton droplet solution, both at the bottom of a vial on a hot plate and in a $50\ \mu\text{m}$ deep chamber contacting a Peltier heater, on thermal ramp up to 70°C . Due to the droplets' size, as recorded in Figure 8.3, and an estimation of the C_5F_{12} -Triton-MilliQ interfacial tension being between 10 to $50\ \text{mN/m}$ (this value was unknown partly due to the change in temperature), these droplets were expected to cross the boiling point and phase change between 30 to 32°C . If the droplets in the vial activated into MBs, they were expected to float to the surface and increase solution turbidity due to the presence of larger particles and higher refractive index difference between water- C_5F_{12} gas compared to water- C_5F_{12} liquid. As can be seen for both experiments, none of the droplets were seen to activate. Approaching 64°C , the solution in the vial began to become turbid. In the chamber, this was accompanied by droplets nucleating in the solution at 60°C with a different contrast to

the C_5F_{12} droplets. However, this was not due to the C_5F_{12} . Instead it was the Triton cloud point, which has been well covered in literature and quoted to occur around 64 to 67 °C, where the Triton molecules become insoluble in the aqueous phase and fall out of solution.^{276,277} Allowing the solution to cool back to below 60 °C reversed clouding. Figure 8.12 shows the results of a similar experiment where the size of tip sonicated nanoemulsion C_5F_{12} DPPC and Triton droplets was recorded by DLS as the emulsion temperature was controlled. Due to the droplets' initial peak and Z-average size (at 25 °C), and estimation interfacial tension (10-50 mN/m), the DPPC and Triton droplets were expected to cross the boiling point and phase change between 42 to 117 °C and 39 to 108 °C, with peak activation at ~68 and ~65 °C respectively. If activation had occurred, ~1.4-3.6 μm MBs would have been formed, which would have heavily contributed to solution polydispersity and turbidity. Since DLS is incapable of measuring turbid solutions, the recorded size after activation would have been large with high error. This was observed after 65 and 60 °C for the C_5F_{12} Triton droplets and control Triton solution respectively, most probably due to the Triton cloud point. C_5F_{12} DPPC droplets did not show any evidence of activation. Even though this study was only performed up to just past the expected peak activation for both samples (and kept there for 15-30 min), it was expected that even a small fraction of activated droplets would cause a dramatic shift in the diameter recorded due to how DLS is more sensitive to larger particles.

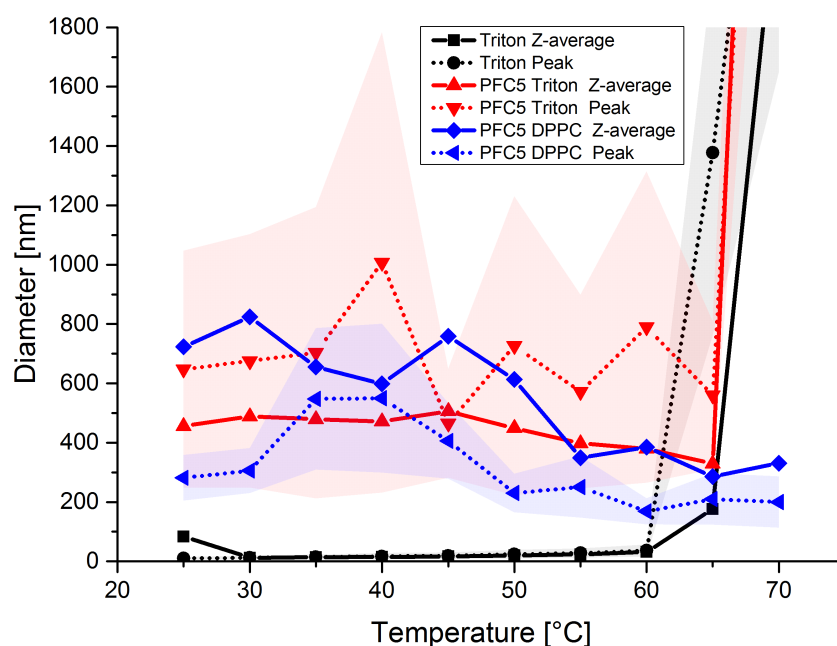


Fig. 8.12. Z-averages and diameter distribution peaks from C_5F_{12} nanoemulsion droplets stabilised by Triton (red) and DPPC lipid (blue) during heating to 70 °C. A control of 1 vol% Triton solution (black) is also shown.

The findings in this section showed that if PFC droplets were placed in an environment above their boiling point, this did not necessarily mean they would phase change into gas. Therefore, these results suggest that there must be an additional energy barrier that had to be overcome to cause gas nucleation, suggested as over 40 °C of thermal energy for the ~25 µm microemulsion droplets. Once one droplet nucleated, the rapid volume increase could have supplied enough kinetic energy to the surrounding droplets to push them over their energy barrier, allowing for a chain reaction of droplet nucleations. An energy barrier such as this has been discussed in literature before, however the theory and experimental results surrounding it are in disagreement. Evans *et al.* (2006) described that in order to phase-change a liquid droplet, enough energy must be supplied to take the liquid over the phase boundary (at an elevated temperature due to droplet confinement), but also to account for the increase in surface area due to the liquid expanding into a gas.¹⁹⁷ However, they also stated that in an open, thermally heated system (such as that used in the above experiments), the energy required for the surface area increase would be accounted for, and therefore would not increase the droplet's boiling point. Rapoport *et al.* (2007) showed that when PEG-PCL, C₅F₁₂ droplets, averaging 428 nm, were heated to 37 °C, they phase converted into MBs.¹⁴⁵ Apposed to this, Schad *et al.* (2010) showed that when larger cholesterol (35 mol%), lecithin (65 mol%), C₅F₁₂ droplets, averaging 1.8-8.3 µm were placed at 37 °C, they remained as droplets and did not activate.¹⁴² For interfacial tensions from 10 to 50 mN/m, the lowest theoretical boiling point for the 428 nm droplets is ~50 °C, and the highest theoretical boiling point for the 8.3 µm droplets is ~35 °C. This means that the former and latter droplets would be expected to remain as droplets and phase convert respectively at 37 °C, which disagrees with the above literature results. During the Figures 8.11 and 8.12 experiments, adding any additional thermal energy over what was already used in this work would have led to boiling of the continuous aqueous phase before droplet activation. As such, activation trials moved onto pressure drop methods. It was expected that this energy barrier would effect droplet activation by pressure drop to vapour pressure in a similar manner.

8.3.2. Activation by pressure drop

This section of work studied activation of the PFC micro and nanodroplets into MBs by decreasing the pressure surrounding the droplets, pushing the liquid phase beyond its

vapour pressure. Many of these experiments included heating the samples to lower the energy requirement needed for pressure decrease.

8.3.2.1. On-chip flow induced pressure drop

Kripfgans *et al.* (2004) discussed how phase change can be induced by pulling a droplet away from a surface or when under flow of 14-23 m/s in a small tunnel.¹²⁹ It is understood that the flow velocity puts the droplet in a pressure drop environment, and the shear forces induce a nucleation point for phase conversion from liquid PFC into gas, causing activation of the whole droplet into a MB. This method is promising for clinical use as a PFC droplet solution could be injected through a custom syringe filter outfitted with wide pores for the purpose of flow pressure drop and shear force activation, allowing one-step activation and injection with less concern for MB lifetime. This method was studied here, where 200 $\mu\text{l}/\text{min}$ through a microfluidic two-phase FF nozzle achieved a flow velocity of 19 m/s at the thinnest point. Figure 8.13 shows C_5F_{12} -Triton microemulsion droplets being passed through the nozzle region of a two-phase FF device and a microspray device. If activation occurred, the $\sim 25\ \mu\text{m}$ droplets were expected to form $\sim 125\ \mu\text{m}$ MBs. In the two-phase FF device $\sim 60\ \mu\text{m}$ MBs were observed around the nozzle region, however these types of MBs are often seen to form when water alone is flowed at that rate as gases dissolved in the water phase cavitate out of the solution. Additional to this, PFC droplets were observed past the nozzle, as is shown in Figure 8.13a, with a droplet circulating around an eddy. The microspray device had an extra depth step in the outlet that should have led to a greater pressure drop and shear force across the nozzle region, however PFC droplets were still seen to pass through the nozzle without any indication of activation (Figure 8.13b).

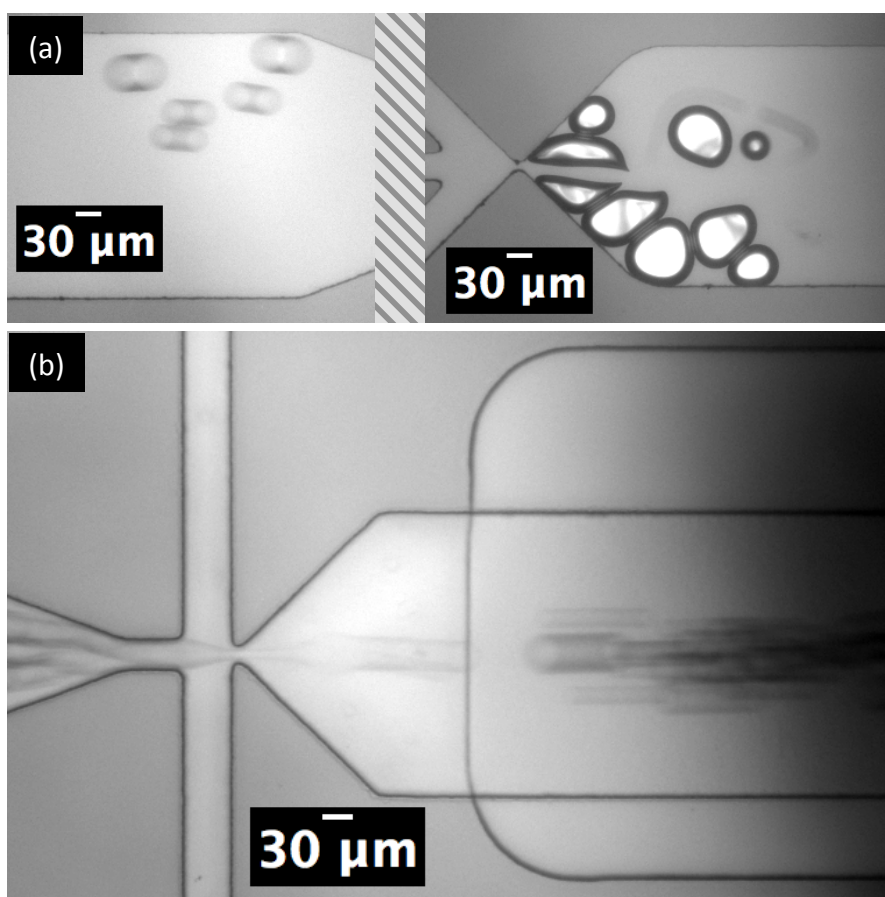


Fig. 8.13. Microfluidic C₅F₁₂ Triton droplets passing through microfluidic nozzles of a (a) two-phase FF and (b) microspray design. Outer phase is 1 vol% Triton solution. All flow is at (a) 100 and (b) 200 µl/min respectively.

25 µm C₅F₁₂ droplets require a pressure drop of ~19 kPa to cross their vapour pressure into the gaseous phase (see Theory Chapter 3.5.3, p 58-59). Since the FF nozzle was so thin (7 µm x 25 µm), the minimum volumetric flow rate required to give this pressure drop was only ~33 µl/min. A flow rate of 200 µl/min would have supplied a pressure drop of ~115 kPa. Therefore, the high flow rates used in this study were far in excess to place the droplets in a pressure drop environment to facilitate phase change activation. However, the droplets will have only experienced this pressure drop for ~0.8 µs, through the nozzle. After this, the remaining outlet channel pressure drop was only ~34 kPa. Still above the C₅F₁₂ droplet pressure drop threshold, but far less in excess. Whilst the shear forces in the outlet channel will have been reduced relative to the nozzle region, shear was expected to remain high due to the 25 µm channel depth being roughly equal to the droplet diameters. However, droplet activation was still never observed during these studies, even though all of the theory heavily suggested that it should have.

8.3.2.2. Hypobaric activation

Hypobaric activation was presented for activation of PFC droplets by Forsberg *et al.* (1998), involves rapidly forcing the expansion of a container (a syringe in the literature and during these experiments) filled with a PFC emulsion roughly 7.5 times its initial volume, holding the expanded volume for a few seconds, and then allowing elasticity to collapse the volume back down.²³⁶ The expansion places the PFC droplets under a pressure drop for a few seconds, presumably activating a proportion of the droplets into MBs. The following rapid decrease of the volume then sends a shockwave through the solution. This shockwave breaks apart many of the MBs into smaller fragments. If any droplets are still within the energy region for activation, the shockwave may also induce further nucleation, allowing further droplet activation, either from the force of the oncoming half of the wave, or the pressure drop due to the tail half of the wave. During these experiments single microemulsion C₅F₁₂, C₆F₁₄, and C5:C6 Triton droplets, and double emulsion C₅F₁₂-soybean-BSA droplets were put through tests of hypobaric activation.

Figure 8.14 shows example images of C₅F₁₂, C₆F₁₄, and C5:C6-Triton microdroplets before and after activation, and the MBs that were formed. Before activation, the droplets were allowed to settle in their vial, 90% of the Triton solution was aspirated off and replaced with fresh MilliQ, and the resultant solution was thoroughly mixed. This dilution was performed twice, which was found to prevent the formation of MBs from control Triton solution that lacked PFC. Table 8.2 presents the average measurements of the solutions' droplet and MB diameter and concentration before and after activation. After activation all samples saw a reduction in droplet diameter, for C₅F₁₂ and C5:C6 samples, to ~10 % of the initial droplet diameter, and an order of magnitude increase to concentration. This was the result of the shock wave fragmenting the emulsion either as droplets or MBs (in the case of the latter, with MB condensation back to droplets). Respectively, the C₅F₁₂, C5:C6, C₆F₁₄ samples resulted in MBs with 58, 112, and 154% of the initial droplet diameters, and 221, 61, and 14% the initial droplet concentrations. The higher content C₅F₁₂ MBs may have been smaller due to a faster dissolution rate than the larger C₆F₁₄ gas molecules, and will have had a higher concentration due to the lower energy requirement for phase conversion. All of the C₆F₁₄ MBs were coated in a layer of non-activated liquid C₆F₁₄, which did not appear to change for at least 10 min. The stable existence of contacting PFC gas and liquid simultaneously was important as it showed that PFC phase changes from liquid to gas and from gas to liquid must have energy landscapes that are different from one another. Otherwise, all discrete C₆F₁₄

volumes would only have been able to be in one phase or another at one time. These findings are expected to be true for all PFC molecules. After activation, PFC MBs are expected to remain as gas due to the increase in their particle diameter and subsequent change to Laplace pressure, however this new finding (of coexistence and contacting liquid PFC and gas PFC) adds to the stability against PFC MBs from returning to their original phase once the source of activation returns to ambient conditions.

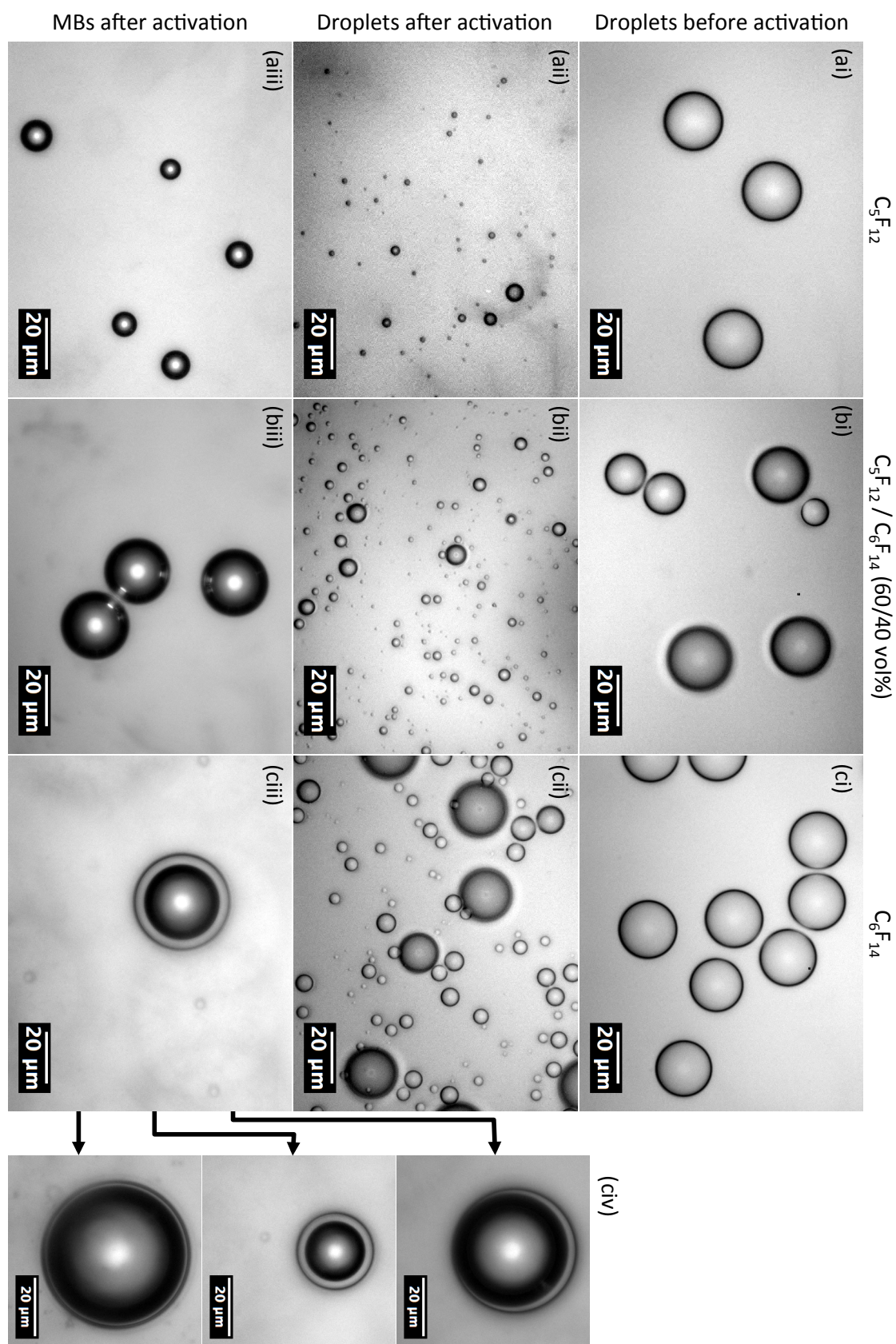


Fig. 8.14. Hypobaric action of microfluidic PFC Triton droplets. (a) C_5F_{12} , (b) $C_5:C_6$, and (c) C_6F_{14} (i-ii) droplets and the resultant (iii) MBs formed are shown from (i) before and (ii-iii) after activation. (civ) Further C_6F_{14} MBs are shown.

Tab. 8.2. Average droplet and MB sizes and concentrations measured from the images presented in Figure 8.14 during hypobaric activation studies.

Sample	C5F12			C5F12 + C6F14			C6F14		
	Diameter [μm]	StDev [μm]	Concentration [particles/ml]	Diameter [μm]	StDev [μm]	Concentration [particles/ml]	Diameter [μm]	StDev [μm]	Concentration [particles/ml]
Droplets pre-activation	23.3 ± 0.4	3.4	9.9E+06	22.7 ± 1.3	6.2	2.8E+06	22.1 ± 0.4	2.9	5.9E+06
Droplets post-activation	2.2 ± 0.03	1.2	1.6E+08	2.7 ± 0.1	1.8	5.1E+07	9.1 ± 0.4	6.0	2.6E+07
Bubbles post-activation	13.6 ± 0.7	9.3	2.2E+07	25.5 ± 2.3	8.1	1.7E+06	34.1 ± 4.6	11.5	8.4E+05

Figure 8.15 shows C₅F₁₂-soybean-BSA droplets in a chamber upon heating to 50 °C, then undergoing the hypobaric activation method with the shockwave passing through the chamber from the inlet. Hypobaric activation trials of double emulsion droplets off-chip (results not shown) in a ~25 °C syringe had not resulted in MB formation, instead giving an apparent slight reduction in the C₅F₁₂ core volume per droplet, with no overall change to solution concentration or morphology. The Figure 8.15 experiment aimed to observe the double emulsion droplets through the activation process by high frame rate imaging. The hypobaric image shown (Figure 8.15d) was during the shockwave portion of the process, after the initial volume increase, hence the displacement of droplets from the previous images (Figures 8.15a-c). The temperature increase during the experiment should have lowered the energy requirement for activation. However, even though the test fluid was displaced, no change to the morphology of any of the double emulsion droplets was observed.

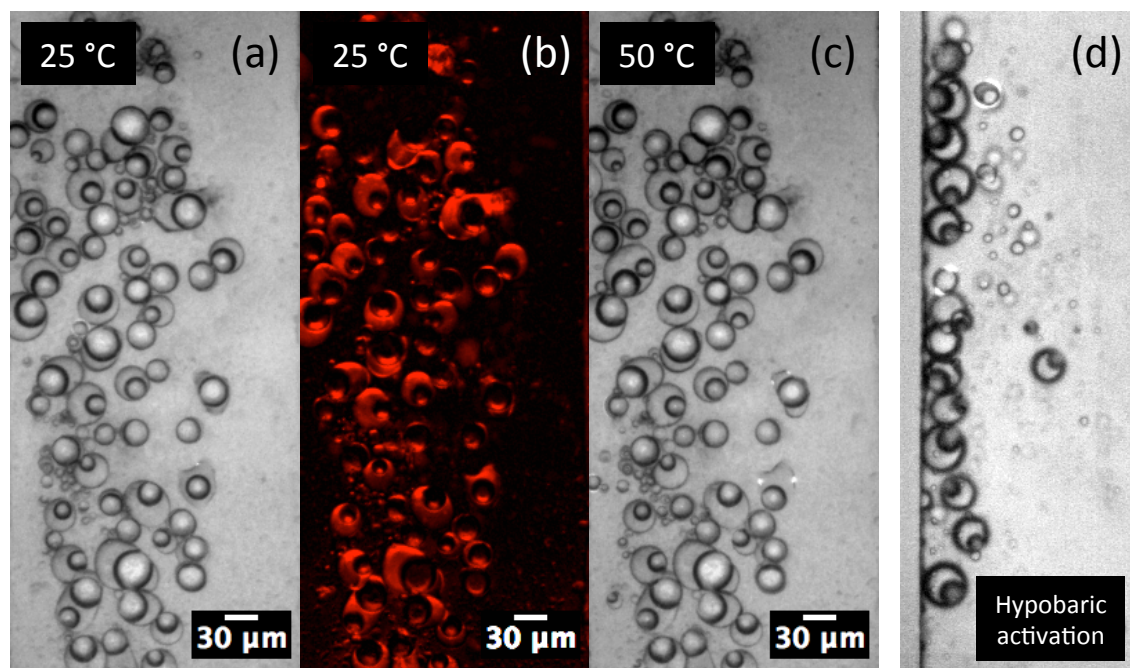


Fig. 8.15. On-chip heating and subsequent hypobaric activation trial of C₅F₁₂-soybean-BSA droplets.

Hypobaric activation of single emulsion droplets was highly efficient, leading to twice as many C_5F_{12} MBs as precursor droplets. However, translating this to the double emulsion C_5F_{12} -soybean droplets did not provide any activation. The pressure drop that both droplet types experienced were roughly the same (the method was user controlled, so would not be identical), however the oil layer may have acted to attenuate the shock wave before interaction with the PFC core. Added to this, the oil layers' higher viscosity, 40.5 mPa.s,²⁰⁵ compared to water, and stiffness differences between a BSA protein-oil and Triton shell may have contributed to a damping effect against increases to the droplet volume, providing a higher energy requirement for activation.

8.3.2.3. Ultrasound activation

In this section of work, activation of PFC single and double emulsion droplets by US was addressed through methods of ADV that were introduced in the Context and Background chapter (Chapter 2.3, p 24-27). Activation of bulk samples is first presented by low frequency US (45 kHz), followed by more clinically relevant frequencies (1.1 MHz), then activation of single droplets of PFC-oil was examined with the use of high frame rate imaging.

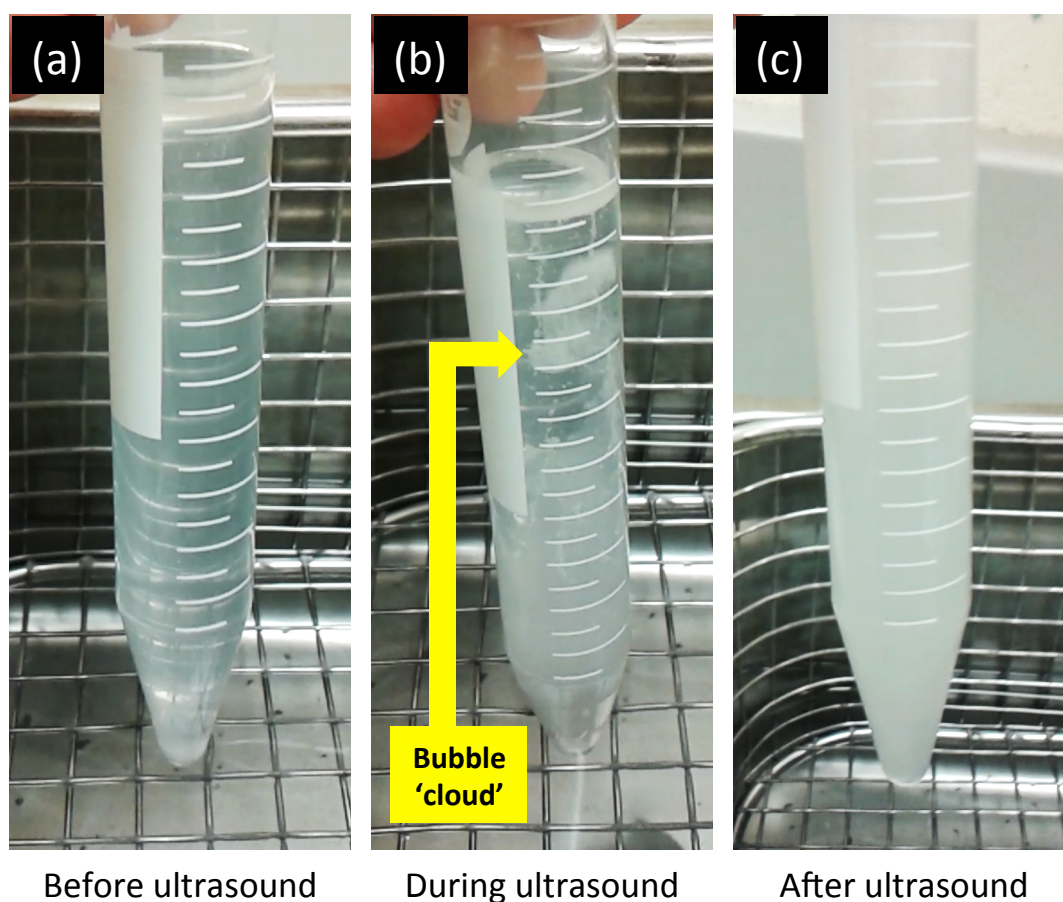


Fig. 8.16. Exposure of dilute microemulsion C_5F_{12} Triton droplets to ~ 5 s of continuous wave 45 kHz ultrasound.

Figure 8.16 shows a falcon tube filled with a dilute solution of $\sim 25 \mu m$ C_5F_{12} Triton microfluidic droplets, where the droplets were allowed to settle to the bottom of the tube as a pellet, before, during, and after immersion of the droplet portion in a 45 kHz US bath. This was a preliminary experiment of PFC droplet activation. The low US frequency was used due to PFC activation work presented by Rapoport *et al* (2009) (see Context and Background Chapter 2.3, p 28).¹⁴³ After exposure of ~ 2 s, a large (relative to the initial droplet pellet) white volume was seen to rapidly rise to the top of the tube and then, after ~ 5 s of the turbulent movement, led to the entire solution becoming turbid. This was an indication of droplet to bubble activation, likely of MBs at least $125 \mu m$ in diameter, since the droplets and bubbles would be more and less dense than the Triton solution respectively. Exposure of Triton solution, without PFC, to 45 kHz US showed no bubble formation (both by eye and microscopic observation). This method was repeated and more thoroughly examined using tip sonicated C_5F_{12} Triton nanoemulsions. Figure 8.17 shows light microscopy example images of the nanoemulsion before and after ~ 20 s of 45 kHz sonication, and the MBs that were formed. ‘Before sonication’ images involved gentle agitation of 1 ml of the PFC

nanoemulsion solution and extraction of a 70 μl sample for imaging. Activation then took place, after which the sample was agitated and 70 μl extracted again for ‘after images’. Histogram size distributions are given and Table 8.3 lists the size and concentration averages (measured from the microscope images) of the droplets (as point sources since their size was below optical limits) and MBs before and after activation respectively. Activation of C_5F_{12} droplets into MBs was successful, however the MBs that were observed were 9.6 times larger (peak size) than expected from theory (see Chapter 3.5.1, p 54-56). Previous literature on PFC activation size increase would suggest this was due to a three-step system of (1) activation, (2) coalescence, and (3) diffusion of gasses from the solution into the newly formed MBs (this theory was introduced in Context and Background Chapter 2.3, p 24).¹²³ However, due to the monodispersity of the MB sample (PDI ~ 0.2) it is most likely that coalescence played a small role, if any, in size expansion, otherwise a more polydisperse sample would be expected. Looking at the concentrations, the droplet point sources appeared to decrease by an order of magnitude, further suggesting that the MBs had been formed due to the droplets and not from gases dissolved in the solution. Knowing that the nanoemulsion was on the order of 5×10^{10} droplets/ml before activation (from qNano measurement, Figure 8.5b), if coalescence is disregarded as a reason for over-sized expansion, only ~ 1 in 10^4 droplets activated. The end result was a monodisperse, 10^6 MBs/ml solution, potentially high enough for further US echogenicity studies, but where activation efficiency was extremely poor and the MBs were too large for clinical application.

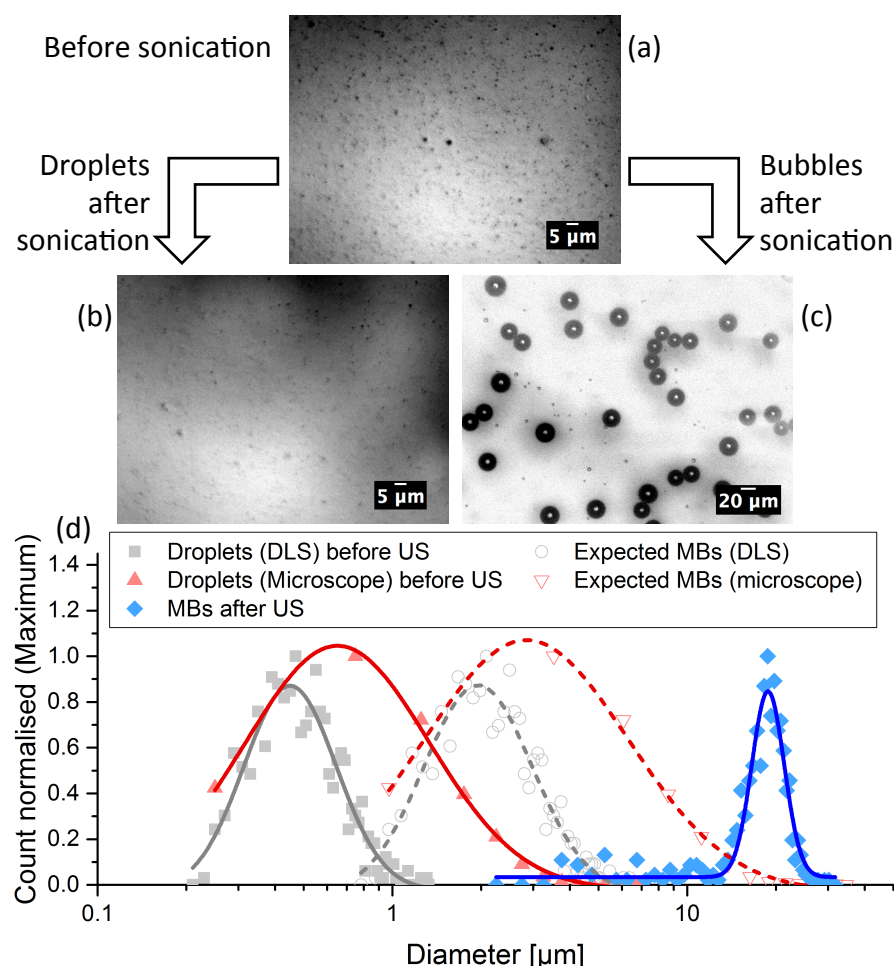


Fig. 8.17. Images of C_5F_{12} -Triton nanoemulsion (a-b) droplets and (c) MBs (a) before and (b-c) after exposure to ~ 5 s of continuous wave 45 kHz ultrasound, with (d) sizing histograms from these samples.

Tab. 8.3. Average droplet and MB sizes and concentrations from the C_5F_{12} Triton nanoemulsion samples of Figure 8.17, before and after exposure to ~ 5 s of continuous wave 45 kHz ultrasound.

	Diameter [μm]	StDev [μm]	Concentration [particles/ml]
Droplets pre-activation	1.2 ± 0.02	0.7	$1.0\text{E}+10 \pm 7\text{E}+06$
Droplets post-activation	1.1 ± 0.03	0.8	$1.67\text{E}+09$
Bubbles post-activation	18.0 ± 0.2	4.2	$7.9\text{E}+06 \pm 8\text{E}+05$

Since the activation efficiency of Figure 8.17 was so poor, a further study was done where the droplet solution was first diluted 1 in 100 in Triton solution. It was thought that there could be a maximum concentration of MBs allowed before the activation energy of the US wave was absorbed and shielded from the droplets. Figure 8.18 presents this further study and shows measurements of the droplet and MB size and concentration over total sonication times, where samples were removed at the time

points given (this solution was not allowed to settle before US exposure). The droplet size (microscope measurement) did not change. The droplet concentration was found to decrease over 20 s, after which it remained constant, indicating that all droplets that would activate had after the first 20 s. The MB size appeared to increase up to 30 s, and then began to decrease. The MB concentration had a high error up to 30 s, with some samples showing MBs and some not at all (zero MBs at 20 s, single MBs at 30 s). From 40 s the MB concentration was consistent at $\sim 2 \times 10^5$ MBs/ml. The concentration results suggest that activation by this method was unreliable. The appearance, disappearance, and then re-appearance of MBs could have suggested that activation was occurring on large groups of droplets at once, which were then removed from the solution by the continued US or floatation, followed by the next set of droplets. The sizing results suggest that post-activation, the continued US caused the MBs to rapidly loose their volume. This was most likely due to US driven oscillations decreasing shell stability, increasing gas dissolution. The initial droplet dilution increased activation efficiency to ~ 1 in 10^3 droplets, though this was still a very poor activation efficiency, and the MB size was increased from 18 μm to 30-55 μm , likely due to the higher concentration ratio of gases dissolved in solution to MBs.

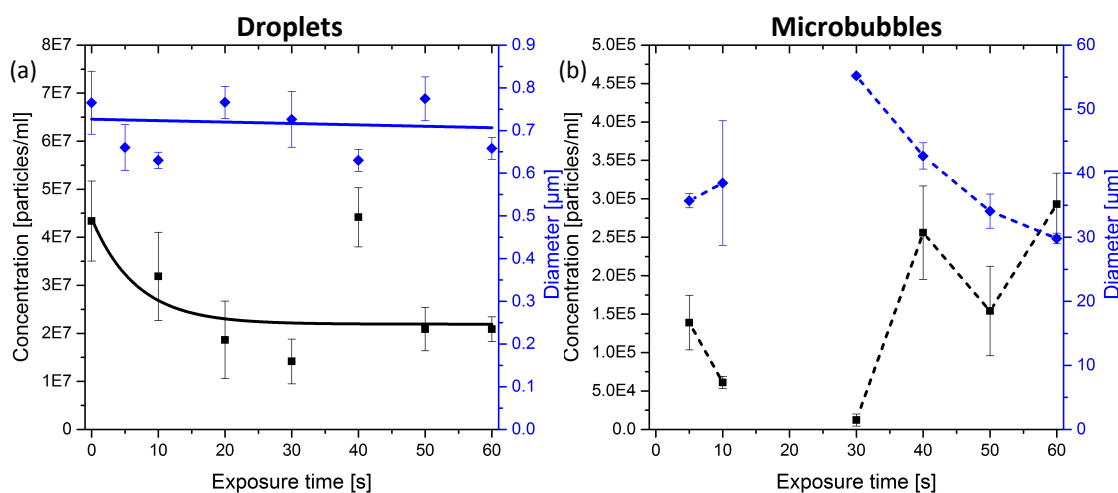


Fig. 8.18. C₅F₁₂-Triton (a) nanoemulsion droplet and (b) MB sizes and concentrations after exposure to continuous wave 45 kHz ultrasound over times given.

Figure 8.19 shows soybean and triacetin C₅F₁₂-oil double emulsion droplets before and after exposure to the 45 kHz US. No successful MB formation was observed. Instead, for the both samples, the C₅F₁₂ volumes were removed from almost all droplets and reduced in any droplets still loaded with C₅F₁₂. This suggested that activation of the C₅F₁₂ did occur, but that the newly formed MBs were not stabilised, leading to rapid dissolution or coalescence and removal by floatation, importantly without the oil

portions. Since larger oil droplets were not observed after activation compared to before, this did confirm that coalescence of the oil portions did not occur.

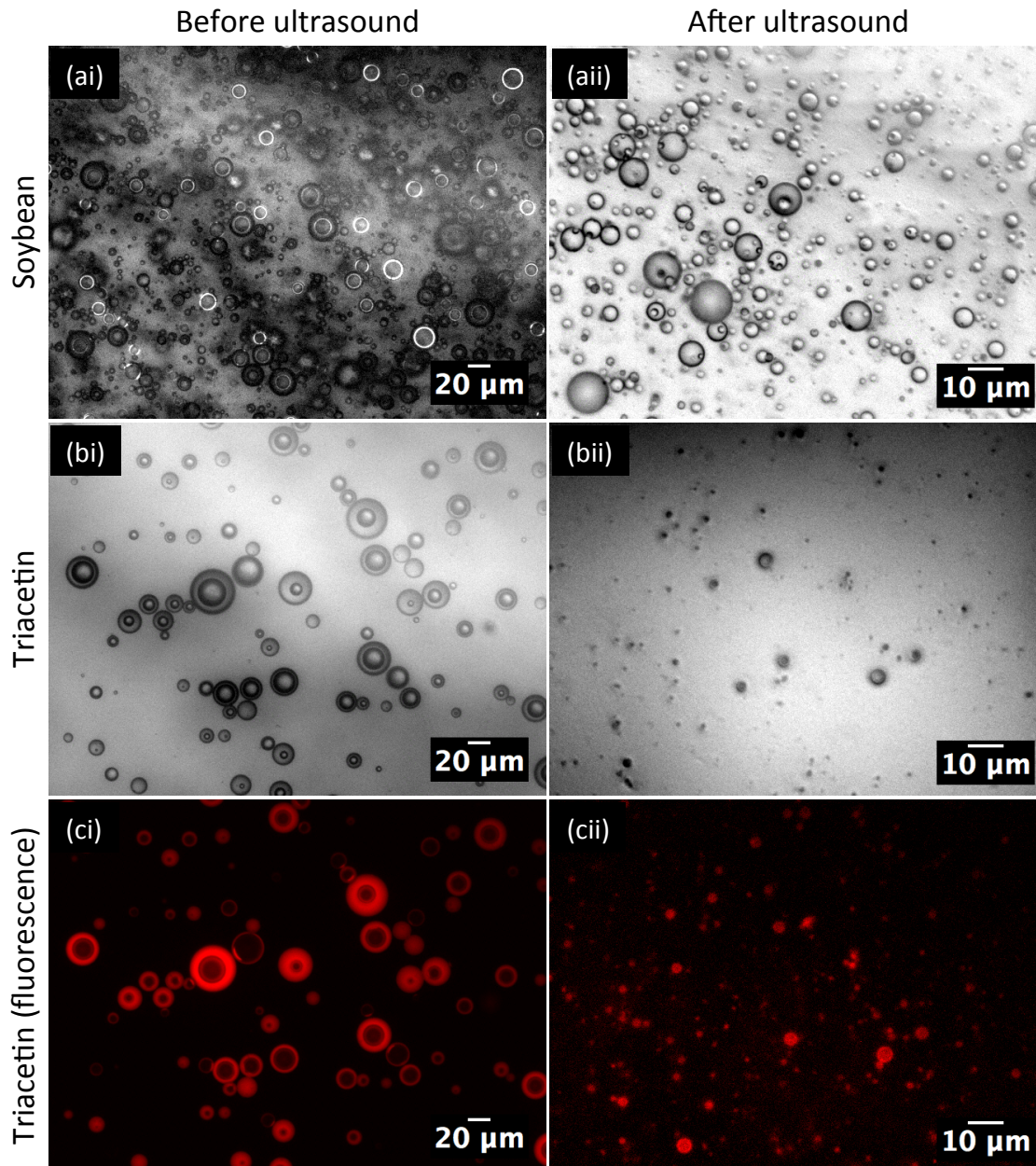


Fig. 8.19. Images of C_5F_{12} -oil-BSA droplets (i) before and (i) after exposure to ~ 5 s of continuous wave 45 kHz ultrasound. (a) Soybean and (b-c) triacetin samples are shown, with (c) fluorescence for the latter.

The previous experiments looked at applying 45 kHz US to the PFC droplets at room temperature. The work below looked at applying more clinically applicable US of 1.1 MHz to PFC droplets around body temperature.

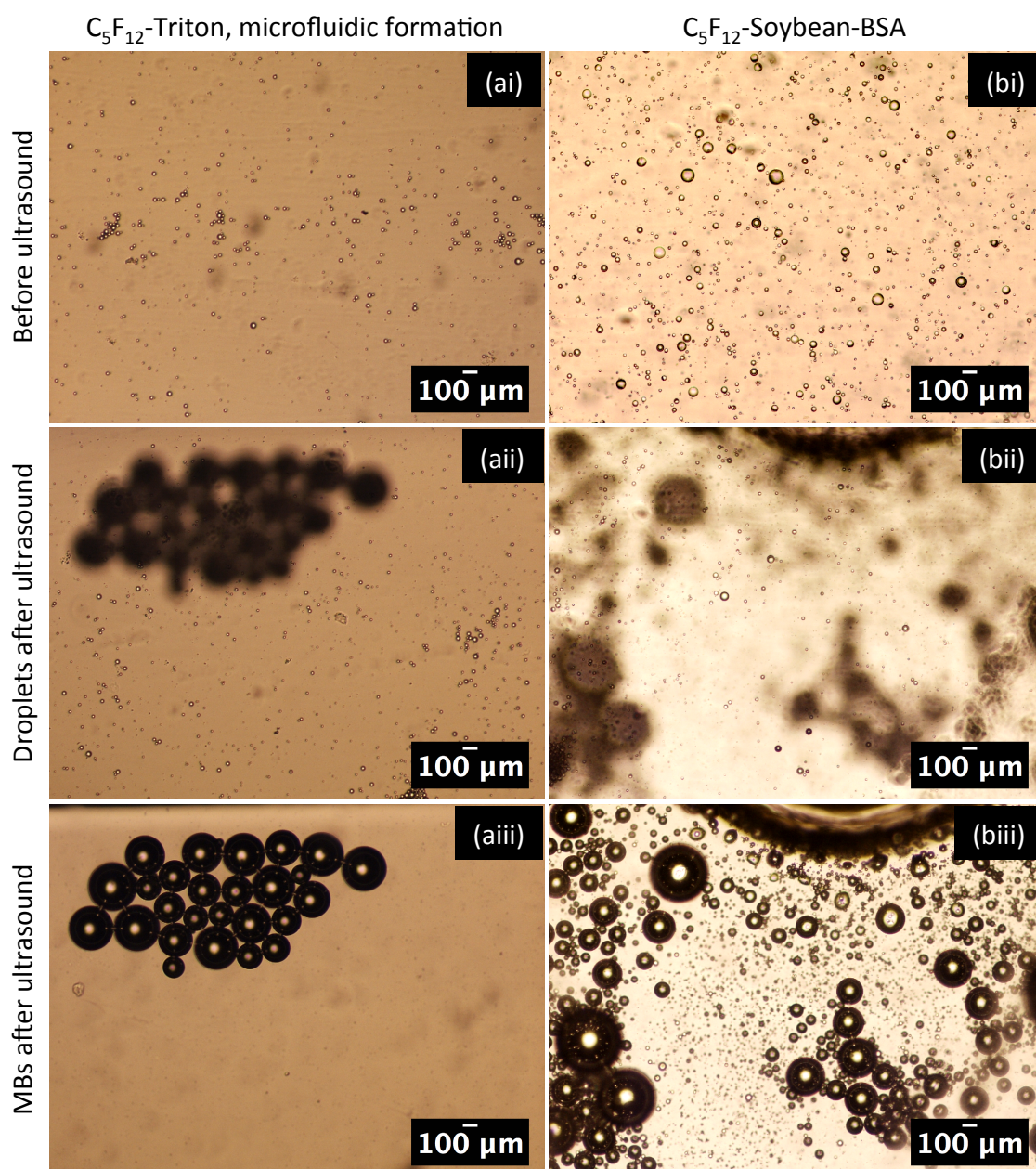


Fig. 8.20. (a) Microemulsion C_5F_{12} -Triton and (b) C_5F_{12} -soybean-BSA (i-ii) droplets and (iii) MBs, in an Ibidi chip at 34 °C, (i) before and (ii-iii) after exposure to ≤ 1 s, DC 20%, 1.1 MHz, 12 ms prf, 3.5 MPa US. No MBs were observed before US exposure.

Figure 8.20 shows C_5F_{12} -Triton single emulsion microfluidic droplets, C_5F_{12} -soybean-BSA double emulsion droplets, and the MBs formed before and after exposure to 1.1 MHz US. Table 8.4 gives the average diameters and concentrations measured from the Figure 8.20 images. The double emulsion was compared to the C_5F_{12} -Triton microemulsion, rather than the nanoemulsion, due to the size differences giving less difference to the energy requirement for activation between the two samples. For both samples, the droplets reduced by $\sim 9\%$ diameter during US, suggesting more rapid dissolution. However, whilst the concentration of the C_5F_{12} -Triton microemulsion remained the same, indicating poor activation efficiency, the C_5F_{12} -soybean-BSA

concentration was reduced by ~ 5 times, suggesting far more efficient activation. The concentration of MBs post-activation (ignoring if coalescence occurred) agreed with this with only 6% of the C_5F_{12} -Triton droplets activating, up to 64% of the C_5F_{12} -soybean-BSA droplets. This indicated that the oil layer aided droplet activation, likely by lowering the energy requirement. The major difference between the two samples was the polydispersity of MBs formed from activation. The C_5F_{12} -Triton droplets formed MBs 16.6 times larger than their initial size with a PDI of 0.2, whereas, whilst the C_5F_{12} -soybean-BSA MBs were on average 3.1 times larger than their initial droplet diameter, their PDI was 4.8, with MBs 100s of micrometres large and one bubble appearing to be on the millimetre scale. A 3.0 times expansion was expected for the C_5F_{12} -soybean-BSA droplets (on the basis that their oil volume would remain constant). These results suggest that gas diffusion into the C_5F_{12} -soybean-BSA MBs did not occur but played a large role in C_5F_{12} -Triton MB expansion, whereas, coalescence played a small role in C_5F_{12} -Triton MB expansion but played an important role in the resulting large C_5F_{12} -soybean-BSA MBs and led to a highly polydisperse sample. The inclusion of the thick BSA-oil layer may have prevented gas diffusion across the MB shell far greater than the thin Triton shell, but the oil layer may also have allowed for far greater coalescence due to requiring more time for stabilisation of the oil-BSA/water interface on expansion of the C_5F_{12} core.

Tab. 8.4. Average droplet and MB sizes and concentrations from the microfluidic C_5F_{12} -Triton and C_5F_{12} -soybean-BSA samples of Figure 8.20, before and after exposure to ≤ 1 s, DC 20%, 1.1 MHz, 12 ms prf, 3.5 MPa US.

	C5-Triton, Microfluidic formation			C5-Soybean-BSA		
	Diameter [μm]	StDev [μm]	Concentration [particles/ml]	Diameter [μm]	StDev [μm]	Concentration [particles/ml]
Droplets before US	14.4 \pm 0.6	11.4	1.2E+05	15.6 \pm 0.4	13.9	3.3E+05
Droplets after US	12.9 \pm 0.6	10.8	1.8E+05	14.3 \pm 1	16.2	6.8E+04
Bubbles after US	238.7 \pm 11	58.4	7.7E+03	48.7 \pm 2	53.1	2.1E+05

The last part of this section studied focused US activation of single C_5F_{12} -soybean-BSA double emulsion droplets under observation with high frame rate microscopy. The aim here was to observe how the C_5F_{12} core expanded, including uniformity in all directions, how the oil was displaced during activation, including if the C_5F_{12} and oil components remained together or spontaneously came apart, and if coalescence occurred.

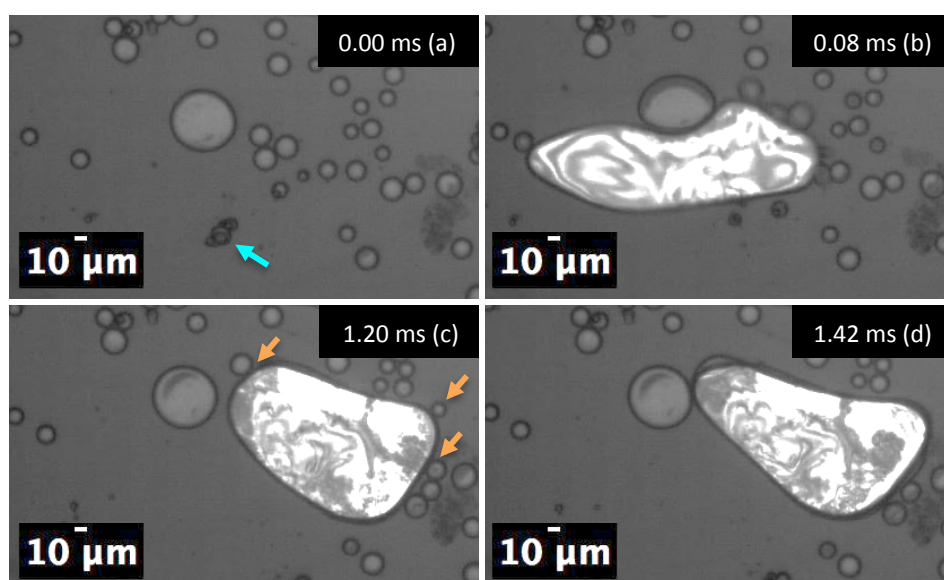


Fig. 8.21. High frame rate imaging of activation of a single C_5F_{12} -soybean-BSA droplet by focused 3.5 MHz, continuous wave (DC 100%), ~ 1 MPa US, at $\sim 37^\circ\text{C}$. Arrows indicate the droplet that activated (blue), one frame before activation, and oil droplets that on the next image have coalesced with the activated gas bubble (orange).

Figure 8.21 shows activation of one C_5F_{12} -soybean-BSA double emulsion droplet by continuous wave, 3.5 MHz US. Activation to full MB size was seen to occur over less than 80 μs . During expansion, the oil that had encapsulated the C_5F_{12} core was not seen to separate from the C_5F_{12} portion. Instead it rapidly thinned out, and over the next 2 ms, surrounding oil droplets were acquired and then merged with the shell of the newly formed MB. Since no surrounding oil droplets, which lacked C_5F_{12} cores, were seen to coalesce with each other, it can be concluded that the merging was only due to the unstable, newly formed MB surface. This surface was formed so rapidly through expansion that the initial droplet's pre-existing oil layer likely did not coat the entire MB surface. If a bulk sample was activated in a similar way, and two newly activated MBs both merged with one oil structure (or the oil layer from another oil coated MB), bridging the MBs together, this would be expected to allow for the MB gas cores to contact without stabilising surfactant, and so cause coalescence of the gas cores.

Figure 8.22 looked at this potential further by observing activation of a more concentrated area of C_5F_{12} -soybean-BSA droplets. The DC here was reduced from 100% to 10% in an effort to bring the US towards clinical viability (DC $\leq 1\%$ is used with tissue to prevent heating)^{131,136}. The US focal point was of the order of 1 mm^2 , meaning that the entire area observed (0.4 mm^2) was expected to have been exposed to the US wave. Droplets were seen to activate in a stochastic manner, which agrees with claims in literature on single emulsion PFC droplets,²⁷⁸ at an estimated rate of 4

droplets/ms, rather than all at once, over the area observed. After activation of a C_5F_{12} double emulsion droplet, surrounding droplets were seen to be displaced by the expanding gas volume, rather than coalesce immediately on contact. When merging did occur (after ~ 1 ms), if the displaced droplet contained a liquid C_5F_{12} core, immediately on contact of the liquid and gas C_5F_{12} portions, the liquid core activated into further gas, causing another rapid expansion and the potential for further coalescence with surrounding droplets. After 9.9 ms it can be seen that almost all of the activated droplets had merged into one large gas pocket, and that the rapid displacement of the gas surfaces had led portions of the merged oil to break up into a polydisperse distribution of oil droplets. Towards 35.6 ms the main gas pocket merged with further C_5F_{12} droplets outside of the area of focus, with the main volume being displaced towards them. This allowed observations of the high degree of oil droplet break up that had occurred.

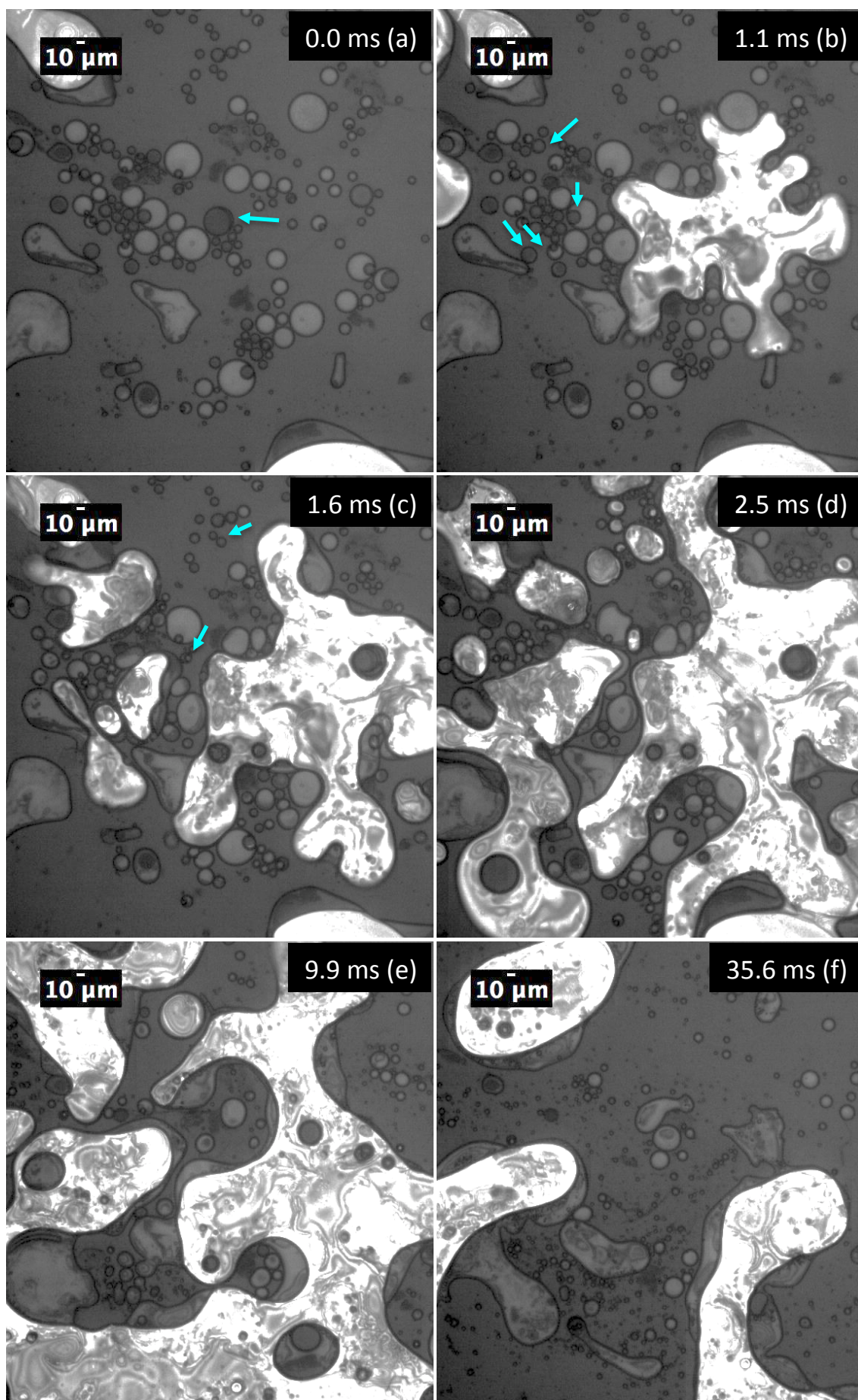


Fig. 8.22. High frame rate imaging of activation of C_5F_{12} -soybean-BSA droplets by focused 3.5 MHz, DC 10%, ~ 1 MPa US, at $\sim 37^\circ\text{C}$. Arrows indicate droplets that by the next image had activated (blue).

The main features that were observed during these high frame rate activation experiments were that droplets activated in a stochastic manner, that on activation the expansion was rapid, and that surface stability was low, leading to the high potential for coalescence. All of these features would be problematic for activating a solution on mass for clinical use. Due to the stochastic activation, a high US exposure time would be required in order to activate enough droplets effectively, which clinically would mean a higher potential for damage to the patient from the US exposure. The rapid expansion on activation followed by the continued gas surface displacement from US (whilst activating more droplets) could lead to damaging shear stresses and mechanical forces on surrounding vasculature. The dramatic decrease to surface stability on activation and subsequent coalescence could easily lead to the formation of gas pockets and droplets of oil big enough to cause damaging vasculature occlusion.

8.4. Conclusion

During this chapter, the aims were to form liquid PFC-in-oil double emulsion precursors and assess their ability to be activated into OLI-MBs. There was a significant focus during this chapter on forming the emulsion so that after activation it would theoretically be of a sufficient size and concentration for clinical use, and on observing the conditions during activation to evaluate their suitability towards clinical application. The sections of work firstly look at forming single emulsion PFC droplets as a micro- and nanoemulsion, followed by the formation of double emulsion PFC-oil droplets. The work then progressed to study a few different methods for activation that could be suitable for activation either outside (heat, on-chip pressure drop, and hypobaric activation) or inside (US) the body.

Single emulsion PFC droplets were formed with cores of C_5F_{12} , C_6F_{14} , and a mix of both PFCs (C5:C6). These were formed on the micro- and nanoscale, by microfluidic FF pinch-off and tip sonication respectively. Microscale C_5F_{12} and C_6F_{14} droplets were formed with Triton shells at 25.0 ± 0.9 and 22.1 ± 1.9 μm respectively. Kept at 4 °C, the C_5F_{12} droplets showed a 6% diameter increase and negligible concentration change over 42 days. As such, these PFC droplets showed a long shell life, very suitable for clinical application, though their size was far too large (> 8 μm) for injection into the blood stream. Nanoscale C_5F_{12} droplets were formed with Triton shells at 327 ± 2 nm with

droplets up to 600 nm. At 4 °C, this nanoemulsion had a short half-life of 1.1 h. Over the first half life the droplets had an $11 \pm 3\%$ increase in their diameter, up to $50 \pm 10\%$ over 5 h. This meant that any further study performed with the PFC nanoemulsions would have to be performed as soon as possible on the day of formation, and that these nanoemulsions are not suitable for storage before any intended clinical use. At this point the experiments studied the formation of double emulsion PFC-oil droplets. Mechanical agitation formation of single emulsion C_5F_{12} droplets in surfactant/oil solutions was studied with the aim to use FF microfluidic to pinch-off the PFC-oil emulsion into droplets in an aqueous phase. Dodecane and triacetin both showed successful encapsulation of C_5F_{12} when mechanically agitated with 1 vol% Triton in the oil phase and triacetin was also successful when using 1 vol% Span80 in place of Triton. The dodecane emulsion had droplets of 638 ± 9 (FWHM 583) nm. Attempted encapsulation of the C_5F_{12} -(dodecane+Triton) emulsion into droplets on-chip using Triton aqueous solution gave monodisperse PFC-oil droplets on-chip of 26 μm . Off-chip the size dropped to 2.5 μm with a wide size distribution (FWHM 13.6 μm). It is believed that during the transition from on-chip to off-chip imaging a high proportion of the PFC cores phase converted into gas, expanding and breaking the thick oil shells apart into smaller oil droplets. As such, this formation route was unusable for further activation studies during this project, but would be worth revisiting in the future for further study. Formation of double emulsion PFC-oil droplets was possible through mechanical agitation of 10 vol% C_5F_{12} , 10 vol% oil, and BSA solution using triacetin, isoamyl acetate, and soybean oil, where droplets were given at 35 ± 3 (FWHM 47), 7.7 ± 0.4 (FWHM 5.8), and 5.3 ± 0.6 (FWHM 5.6) μm respectively. For soybean, dropping the C_5F_{12} and oil to 1 vol% showed a reduction in droplet size to 3.3 ± 0.1 (FWHM 1.8) μm , however further variation of the oil and BSA concentrations were not found to give any further control over the droplet size, concentration, or oil fraction for each droplet. For all 10 vol% (oil and C_5F_{12}) samples, on average the droplets were found to have a C_5F_{12} core that was 0.68 times (SD 0.11) the total droplet diameter. This dropped to 0.59 times (SD 0.11) for the 1 vol% soybean sample. This disagreed with literature on the same C_5F_{12} -soybean-BSA mechanically agitated droplet formation technique presented by Fabiilli *et al.* (2010), where they found that 12 vol% droplets had C_5F_{12} cores ~ 0.4 times the total droplet diameter.¹³⁸

Activation studies showed that none of the PFC droplet samples showed any activation into MBs on heating up to 50 °C. Pressure drop supplied by high flow rates through an on-chip nozzle was not found to activate any droplet emulsions either. Hypobaric

activation did show success at activating the C₅F₁₂, C₆F₁₄, and C₅:C₆ microemulsions. All samples showed a dramatic decrease in droplet size after activation, caused by the activation method's shock wave breaking apart the droplets. The C₅F₁₂ microemulsion gave MBs that were the smallest, at 13.6 ± 0.7 (SD 9.3) μm , and the highest concentration, at 2.2×10^7 MBs/ml, 220% of the initial droplet concentration. However, C₅F₁₂-soybean-BSA double emulsion droplets were not seen to activate by hypobaric activation, even after heating to 50 °C on-chip. Continuous wave, 45 kHz US was observed to activate the C₅F₁₂ microemulsion in under 5 s. 45 kHz US applied to the C₅F₁₂ nanoemulsion showed MB formation at 18 ± 0.2 (SD 4.2) μm and 7.9×10^6 MBs/ml. However, the efficiency of activation was low at around 1 in 10^4 droplets. Diluting the bulk nanoemulsion 1 in 100 showed an increase in activation efficiency to 1 in 10^3 droplets, but increased MB size to 30-55 μm . Attempting to activate the C₅F₁₂-soybean-BSA double emulsion using 45 kHz US gave a post-US sample where the PFC core was significantly reduced if not removed from all droplets, with no OLI-MBs. Activation of single and double emulsion C₅F₁₂-Triton and C₅F₁₂-soybean-BSA droplets by 1.1 MHz US in a 37 °C Ibidi chip showed a drop in droplet diameter for both samples by ~9%. However, where as the concentration of the C₅F₁₂-Triton droplets remained roughly the same, the concentration of the C₅F₁₂-soybean-BSA droplets showed a 5 times reduction, suggesting a greater activation efficiency. This means that while the oil layer had retarded activation in the hypobaric studies, the oil layer had aided activation in the 1.1 MHz US studies. The C₅F₁₂-Triton and C₅F₁₂-soybean-BSA 1.1 MHz US activated MBs were formed at 240 ± 10 (SD 60) μm and 49 ± 2 (SD 53) μm respectively, equating to an average diameter increase of 16.6 times and 3.1 times the initial average diameter respectively, and at 10^3 and 10^5 MBs/ml respectively. From theory, the C₅F₁₂-Triton and C₅F₁₂-soybean-BSA droplets were expected to expand in diameter by 5 times and 3.0 times respectively during activation into MBs. This led to the conclusion that on activation, the larger expansion of the monodisperse C₅F₁₂-Triton MBs was driven by the diffusion of gases in from the surrounding solution, while the high polydispersity of the C₅F₁₂-soybean-BSA MBs, which expanded as theory dictated without regarding diffusion, was driven by coalescence. The higher degree of coalescence was likely caused by the surfactants being less efficient at stabilising the water-oil interface than they would be at stabilising a water-gas interface. This problem of the oil layer causing a far greater coalescence of the PFC MBs was later confirmed when observing activation of single C₅F₁₂-soybean-BSA droplets by high frame rate microscopy using 3.5 MHz US. Observing a single droplet undergo activation showed

that the full MB diameter was achieved in less than 80 μ s. Observing multiple droplets showed significant coalescence over the area of activation, eventually forming a large gas pocket, surrounded by a thick oil layer, covering most of the 0.4 mm² observed area. For the US used, activation occurred at a rate of \sim 4 droplets/ms over the 9×10^{-3} mm³ volume observed rather than all of the droplet activating at once. Similarly, Fabiilli *et al.* (2010) have previously shown that they could only achieve \sim 5% activation for C₅F₁₂-soybean-BSA droplets of 2 μ m through US activation.¹³⁸

These last two US studies brought serious concerns to the future prospects of double emulsion PFC-in-oil droplets for clinical use. The rapid expansion during activation could cause damage to tissue surrounding the droplet/MB through the shear forces and mechanical pressure it could impart on vasculature walls. The low rate of activation would require a long US exposure to be used in order to activate enough droplets. This would prolong exposure to the patient and could result in damage to healthy tissue. Alternatively, a higher concentration of drug-loaded droplets could be delivered to the patient to alleviate the need for a higher proportion of droplets activated into MBs. However, this would greatly increase the required total dosage of drug delivered into the patient and the remaining drug left over after activation, reducing bioavailability. Lastly, the far greater degree of coalescence observed with oil coated PFC droplets increases the danger that large pockets of gas or droplets of oil could be formed in the blood stream during activation, leading to blood flow problems that could have serious impact on patient health.

9. Conclusions

The primary, overarching goal of this thesis project was to develop a reliable and simple method for the formation of MBs with a thin oil layer coating (OLI-MBs) of clinically relevant size and concentration. With that aim in mind, the energetic favourability of different conformations of gas, oil, and lipid/aqueous phases was studied with a view to see if the OLI-MB structure would be expected to be able to be formed, and then after formation if the structure would be stable. It was concluded that the formation of OLI-MBs would be possible, and that they could be stable after formation, but that only with direct control over how the phases were allowed to meet could a sample be produced at a high concentration, with control over the average OLI-MB size, uniformity of the oil layer thickness between OLI-MBs, and a lack of pure oil droplets and non-oil-MBs. This thesis then presented three possible routes for the formation of OLI-MBs under controlled conditions; three-phase pinch-off through a single FF microfluidic nozzle, formation of double emulsion liquid PFC-oil droplets to be used as precursors for activation into gas filled OLI-MBs, and oil nanodroplet self-assembly and spreading into a thin oil layer at newly formed MB surfaces. The three-phase pinch-off route had previously been shown to be possible by Hettiarachchi *et al.* (2009), Kendall *et al.* (2012), and Shih *et al.* (2013),^{31,82,94,95} though in the last publication they had admitted that collection of a sufficient OLI-MB sample off-chip was not possible. During the studies of this thesis we were never able to replicate the on-chip MB formation results. This may have been due to limitations in the apparatus used. For example using microfluidics formed from different materials as the above publications, leading to changes to the wall rigidity and interfacial tension with the gas, oil, and aqueous phases, or the pump systems not supplying sufficient control over the interaction of these phases. The liquid PFC-oil precursor route was first presented by Fabiilli *et al.* (2010).¹³⁸ Since the method of formation was mechanical agitation, a chaotic route, work in this thesis looked to optimise the formation process, in order to form a more monodisperse sample, by varying the concentrations of the droplet components. However, batch variation both in and between samples remained high. Activation by US then shed new light on the clinical potential for these structures. Compared to non-oil-PFC droplets, the oil-PFC droplets showed a far greater potential for coalescence. Whilst on average OLI-MBs were formed only 3 times larger than the precursor microdroplets, the sample polydispersity was large, forming many MBs 100s of μm in

diameter, even up to millimetres in scale. Stable particles of this size could easily occlude the vasculature, leading blood flow to stop, potentially causing serious damage to a patient. Observing activation at high frame rate showed that the full MB volume was achieved in under 80 μs , which has the potential for damaging shear forces and mechanical stresses if activation were to occur *in vivo*. The last study also confirmed that, like non-oil-PFC droplets,²⁷⁸ activation of the PFC-oil droplets was stochastic, which would require long US exposure times for adequate droplet activation efficiency. These findings bring serious questions to the clinical viability of liquid PFC-oil double emulsion droplets as precursors for *in vivo* activation. Use of oil nanodroplets for microfluidic FF formation of OLI-MBs was a route novel to this thesis. OLI-MBs were successfully formed from squalane, squalene, and tripropionin oil, with POPC shells. Extending formation to these three oils has resulted in extending the capabilities of the OLI-MB structure. Highly hydrophobic payloads can be loaded into the squalane and squalene, whilst low water solubility payloads can be loaded into the tripropionin. Squalane and tripropionin OLI-MBs were formed at 2.4 ± 0.3 (SD 1.6) μm and 2.1 ± 0.1 (SD 0.8) μm respectively, meaning that they have been formed at size for further clinical interest. Off-chip, OLI-MB samples only reached concentrations of 10^6 and 10^5 OLI-MBs/ml respectively and samples halved in concentration after ~ 35 min. This concentration and lifetime must be improved upon if the OLI-MB structures are to be considered for further clinical application. While OLI-MBs showed US response, indicating the presence of a gas core, the frequency at resonance was unexpected. Large ~ 20 μm OLI-MBs showed a wide resonance, with a centre at 3 MHz, where as the smaller microfluidic 2.4 μm OLI-MBs showed a lower resonance at 1.8 MHz. According to theory, smaller MBs should show higher resonance frequencies. As such, further US work needs to be done to address how the OLI-MBs were oscillating under the US exposure, and the effect the oil layer gave to damping oscillations.

In terms of future work, the three-phase FF studies could be improved by looking at surface treatment of the microfluidic walls and use of more reliable fluid inlet pumps. Work by Deshpande *et al.* (2016) looked at forming water-oil-water emulsions in a similar three-phase microfluidic nozzle design to that used during this project.²⁶⁸ They claimed that without surface treatment of microfluidic device to be hydrophobic before the nozzle and hydrophilic after the nozzle, and the use of fluid pumps more reliable than syringe drivers, pinch-off of water-oil-water droplets was not possible. The same pinch-off limitations are likely to also apply to the formation of gas-oil-water emulsions

(OLI-MBs). For the LOND formed OLI-MBs, the most important future steps are to study the US response further, look into OLI-MB drug loading capacity and drug release, and to try to improve OLI-MB concentration and lifetime. Traditionally, MB concentration and lifetime can be improved by increasing the stability of the MB shell. A problem with using this method for OLI-MB stability is that the shell comes from the precursor LONDS, which if too stable, will not spread. Therefore, a method needs to be used in which the OLI-MB shell can be further stabilised after formation of the thin oil layer. One candidate material for this would be diacetylene molecules. MBs have previously been formed with lipid-diacetylene shells. After exposure to ultraviolet light, these MBs were shown to have significantly increased lifetime due to the diacetylene molecules cross-linking with one another within the lipid shell.²¹⁴ Using this method, LONDS could be formed with POPC-diacetylene shells, remain non-cross-linked, and be used for the formation of OLI-MBs. After formation, these OLI-MBs could then be exposed to ultraviolet light, cross-linking the shell, extending their lifetime. Figure 9.1 shows a schematic of a more efficient system, where a serpentine could be added to the microfluidic outlet with the ultraviolet light being shone through it. This would allow the OLI-MBs time to form, stabilise, and be exposed to the ultraviolet light all on-chip. This method could potentially have the very desirable effect of increasing the off-chip OLI-MB concentration towards the far higher concentration of OLI-MBs predicted from on-chip observations.

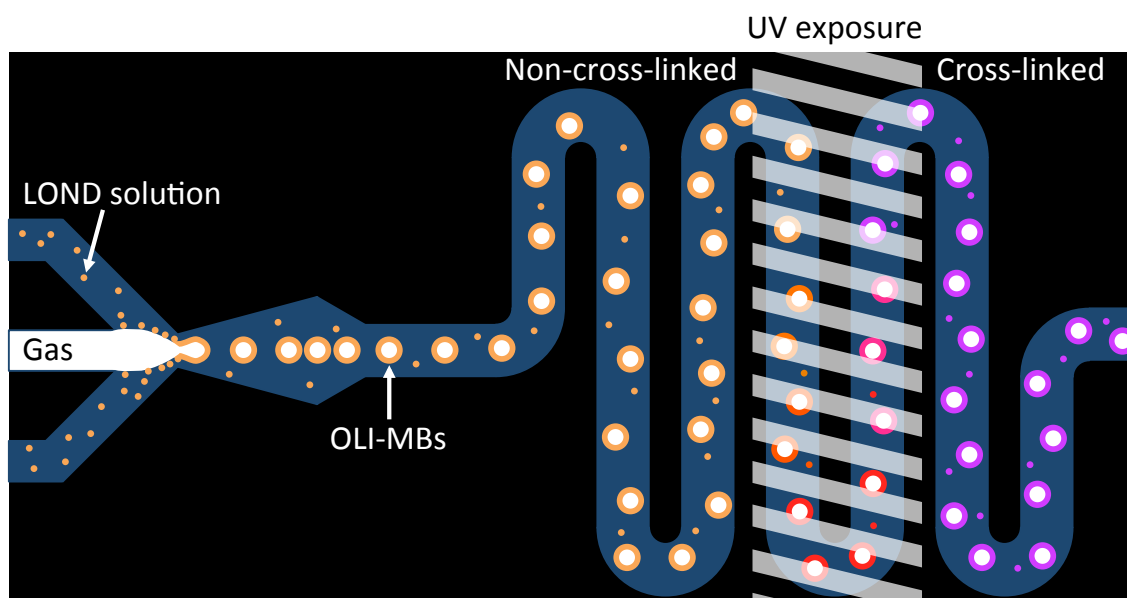


Fig. 9.1. Schematic of the microfluidic formation of OLI-MBs from lipid-diacetylene LONDS (orange), followed by an on-chip serpentine to allow OLI-MB stabilisation time and a further ultraviolet light exposure step to cross-link the diacetylene molecules in the shell (purple). MB outline represents the entire lipid-diacetylene and oil shell, even though only the outer lipid-diacetylene portion becomes cross-linked.

References

1. World Health Organization (WHO/Europe). Cancer. (2017). Available at: <http://www.euro.who.int/en/health-topics/noncommunicable-diseases/cancer>. (Accessed: 23rd August 2017)
2. Cancer Research UK. Cancer Research UK. Available at: <https://www.cancerresearchuk.org/>. (Accessed: 23rd August 2017)
3. Schluep, T. *et al.* Pharmacokinetics and tumor dynamics of the nanoparticle IT-101 from PET imaging and tumor histological measurements. *Proc. Natl. Acad. Sci. U. S. A.* **106**, 11394–9 (2009).
4. Thakor, A. S. & Gambhir, S. S. Nanooncology: The future of cancer diagnosis and therapy. *CA. Cancer J. Clin.* **63**, 395–418 (2013).
5. Slingerland, M., Guchelaar, H. J. & Gelderblom, H. Liposomal drug formulations in cancer therapy: 15 years along the road. *Drug Discov. Today* **17**, 160–166 (2012).
6. Mico, V. *et al.* Evaluation of lipid-stabilised tripropionin nanodroplets as a delivery route for combretastatin A4. *Int. J. Pharm.* **526**, 547–555 (2017).
7. Rogstad, D. K. *et al.* Chemical decomposition of 5-aza-2'-deoxycytidine (Decitabine): Kinetic analyses and identification of products by NMR, HPLC, and mass spectrometry. *Chem. Res. Toxicol.* **22**, 1194–1204 (2009).
8. Mitragotri, S., Burke, P. A. & Langer, R. Overcoming the challenges in administering biopharmaceuticals: formulation and delivery strategies. *Nat. Rev. Drug Discov.* **13**, 655–72 (2014).
9. Allen, T. M. & Cullis, P. R. Drug delivery systems: entering the mainstream. *Science* **303**, 1818–22 (2004).
10. Song, B., Wu, C. & Chang, J. Controllable delivery of hydrophilic and hydrophobic drugs from electrospun poly(lactic-co-glycolic acid)/mesoporous silica nanoparticles composite mats. *Journal of Biomedical Materials Research - Part B Applied Biomaterials* **100B**, 2178–2186 (2012).
11. Straub, J. A. *et al.* Intravenous hydrophobic drug delivery: A porous particle formulation of paclitaxel (AI-850). *Pharm. Res.* **22**, 347–355 (2005).
12. Darrat, Y. *et al.* *Tubular Nanocontainers for Drug Delivery, in Materials Nanoarchitectonics*. (Wiley-VCH Verlag GmbH & Co. KGaA, 2018). doi:10.1002/9783527808311.ch4
13. Aliabadi, H. M. *et al.* Encapsulation of hydrophobic drugs in polymeric micelles

- through co-solvent evaporation: The effect of solvent composition on micellar properties and drug loading. *Int. J. Pharm.* **329**, 158–165 (2007).
14. Sharma, M. & Sharma, R. Implications of designing a bromelain loaded enteric nanoformulation on its stability and anti-inflammatory potential upon oral administration. *RSC Adv.* **8**, 2541–2551 (2018).
 15. Allen, T., K. Cheng, W., Hare, J. & Laginha, K. Pharmacokinetics and Pharmacodynamics of Lipidic Nano-Particles in Cancer. *Anticancer. Agents Med. Chem.* **6**, 513–523 (2006).
 16. Lotem, M. *et al.* Skin Toxic Effects of Polyethylene Glycol–Coated Liposomal Doxorubicin. **136**, (2017).
 17. Chan, A., Shih, V. & Kian, T. C. Liposomal doxorubicin-associated acute hypersensitivity despite appropriate preventive measures. *J. Oncol. Pharm. Pract.* **13**, 105–107 (2007).
 18. Lindenberg, M., Kopp, S. & Dressman, J. B. Classification of orally administered drugs on the World Health Organization Model list of Essential Medicines according to the biopharmaceutics classification system. *Eur. J. Pharm. Biopharm.* **58**, 265–278 (2004).
 19. Hite, M., Turner, S. & Federici, C. Part 1: Oral Delivery of Poorly Soluble Drugs. *Samedan* (2003).
 20. Kawabata, Y., Wada, K., Nakatani, M., Yamada, S. & Onoue, S. Formulation design for poorly water-soluble drugs based on biopharmaceutics classification system: Basic approaches and practical applications. *Int. J. Pharm.* **420**, 1–10 (2011).
 21. Savjani, K. T., Gajjar, A. K. & Savjani, J. K. Drug solubility: importance and enhancement techniques. *ISRN Pharm.* **2012**, 195727 (2012).
 22. Sareen, S., Mathew, G. & Joseph, L. Improvement in solubility of poor water-soluble drugs by solid dispersion. *Int J Pharm Investig* **2**, 12–17 (2012).
 23. Miyako, Y., Khalef, N., Matsuzaki, K. & Pinal, R. Solubility enhancement of hydrophobic compounds by cosolvents: Role of solute hydrophobicity on the solubilization effect. *Int. J. Pharm.* **393**, 48–54 (2010).
 24. Serajuddin, A. T. M. Salt formation to improve drug solubility. *Adv. Drug Deliv. Rev.* **59**, 603–616 (2007).
 25. Jain, P. & Yalkowsky, S. H. Solubilization of poorly soluble compounds using 2-pyrrolidone. *Int. J. Pharm.* **342**, 1–5 (2007).
 26. Liu, R. *Water-insoluble drug formulation*. (CRC Press, 2008).

27. Kwon, H. C. & Kwon, J. H. Measuring aqueous solubility in the presence of small cosolvent volume fractions by passive dosing. *Environ. Sci. Technol.* **46**, 12550–12556 (2012).
28. Gupta, S. *et al.* Designing and Testing of an Effective Oil-in-Water Microemulsion Drug Delivery System for In Vivo Application. *Drug Deliv.* **12**, 267–273 (2005).
29. Ganta, S., Devalapally, H., Shahiwala, A. & Amiji, M. A review of stimuli-responsive nanocarriers for drug and gene delivery. *Journal of Controlled Release* **126**, 187–204 (2008).
30. Muller, R. H., Mader, K. & Gohla, S. Solid lipid nanoparticles (SLN) for controlled drug delivery - a review of the state of the art. *Eur. J. Pharm. Biopharm.* **50**, 161–177 (2000).
31. Hettiarachchi, K., Lee, A. P., Zhang, S., Feingold, S. & Dayton, P. a. Controllable microfluidic synthesis of multiphase drug-carrying lipospheres for site-targeted therapy. in *Biotechnology Progress* **25**, 938–945 (2009).
32. Stride, E. & Saffari, N. Microbubble ultrasound contrast agents: a review. *Proc. Inst. Mech. Eng. H.* **217**, 429–47 (2003).
33. Miller, A. P. & Nanda, N. C. Contrast echocardiography: new agents. *Ultrasound Med. Biol.* **30**, 425–34 (2004).
34. Sirsi, S. & Borden, M. Microbubble Compositions, Properties and Biomedical Applications. *Bubble Sci Eng Technol.* **1**, 3–17 (2009).
35. Hettiarachchi, K. & Lee, A. P. Polymer-Lipid Microbubbles for Biosensing and the Formation of Porous Structures. *J. Colloid Interface Sci.* **344**, 521–527 (2010).
36. Thomson, L. M., Polizzotti, B. D., McGowan, F. X. & Kheir, J. N. Manufacture of Concentrated , Lipid-based Oxygen Microbubble Emulsions by High Shear Homogenization and Serial Concentration. *J. Vis. Exp.* **87**, (2014).
37. Chuang, E. Y. *et al.* Self-assembling bubble carriers for oral protein delivery. *Biomaterials* **64**, 115–124 (2015).
38. Swanson, E. J., Mohan, V., Kheir, J. & Borden, M. A. Phospholipid-Stabilized Microbubble Foam for Injectable Oxygen Delivery. *Langmuir* **26**, 15726–15729 (2010).
39. Pinchasik, B., Möhwald, H. & Skirtach, A. G. Mimicking Bubble Use in Nature: Propulsion of Janus Particles due to Hydrophobic-Hydrophilic Interactions. *Small* **10**, 2670–2677 (2014).

40. TETTEH, E. K. & RATHILAL, S. Evaluation Of The Coagulation Flootation Process For Industrial Mineral Oil Wastewater Treatment Using Response Surface Methodology (rsm). *Int. J. Environ. Impacts* **1**, 491–502 (2018).
41. Dalla Palma, L. & Bertolotte, M. Introduction to ultrasound contrast agents: physics overview. *Eur. Radiol.* **9**, S338–S342 (1999).
42. Chatterjee, D. & Sarkar, K. A Newtonian rheological model for the interface of microbubble contrast agents. *Ultrasound Med. Biol.* **29**, 1749–1757 (2003).
43. Peyman, S. A. *et al.* Expanding 3D geometry for enhanced on-chip microbubble production and single step formation of liposome modified microbubbles. *Lab Chip* **12**, 4544 (2012).
44. Liu, J., Liu, Y., Huang, J., Huang, L. & Zhao, P. Real-time monitoring of contrast-enhanced ultrasound for radio frequency ablation. *Open Med.* **12**, 474–480 (2017).
45. Hernot, S. & Klibanov, A. L. Microbubbles in ultrasound-triggered drug and gene delivery. *Advanced Drug Delivery Reviews* **60**, 1153–1166 (2008).
46. Pitt, W. G., Hussein, G. a & Staples, B. J. Ultrasonic drug delivery – a general review. *Expert Opin. Drug Deliv.* **1**, 37–56 (2004).
47. Lentacker, I., De Smedt, S. C. & Sanders, N. N. Drug loaded microbubble design for ultrasound triggered delivery. *Soft Matter* **5**, 2161 (2009).
48. Squires, T. & Quake, S. Microfluidics: Fluid physics at the nanoliter scale. *Rev. Mod. Phys.* **77**, 977–1026 (2005).
49. van Wamel, A. *et al.* Vibrating microbubbles poking individual cells: Drug transfer into cells via sonoporation. *J. Control. Release* **112**, 149–155 (2006).
50. Ibsen, S., Schutt, C. E. & Esener, S. Microbubble-mediated ultrasound therapy: a review of its potential in cancer treatment. *Drug Des. Devel. Ther.* **7**, 375–388 (2013).
51. Reeve, D. M. *Diagnostic Ultrasound: Physics and Equipment*. Cambridge University Press (Cambridge University Press, 2010). doi:doi:10.2967/jnumed.112.105395
52. Stride, E. & Edirisinghe, M. Novel microbubble preparation technologies. *Soft Matter* **4**, 2350 (2008).
53. van Rooij, T. *et al.* Viability of endothelial cells after ultrasound-mediated sonoporation: Influence of targeting, oscillation, and displacement of microbubbles. *J. Control. Release* **238**, 197–211 (2016).
54. Khayamian, M. A., Baniassadi, M. & Abdolahad, M. Monitoring the effect of

- sonoporation on the cells using electrochemical approach. *Ultrason. Sonochem.* **41**, 619–625 (2018).
55. Chen, H., Kreider, W., Brayman, A. A., Bailey, M. R. & Matula, T. J. Blood vessel deformations on microsecond time scales by ultrasonic cavitation. *Phys. Rev. Lett.* **106**, 1–4 (2011).
 56. Thanou, M. *Theranostics and Image Guided Drug Delivery*. (Royal Society of Chemistry, 2018).
 57. Prentice, P., Cuschieri, A., Dholakia, K., Prausnitz, M. & Campbell, P. Membrane disruption by optically controlled microbubble cavitation. *Nat. Phys.* **1**, 107–110 (2005).
 58. Saleki-haselghoubi, N. & Dadvand, A. Simulation of bubble dynamics oscillating near a circular aperture made in a curved rigid plate using boundary element method. *Ocean Eng.* **151**, 12–22 (2018).
 59. Huang, S. L. Liposomes in ultrasonic drug and gene delivery. *Adv. Drug Deliv. Rev.* **60**, 1167–1176 (2008).
 60. Couture, O., Foley, J., Kassell, N. F., Larrat, B. & Aubry, J. Review of ultrasound mediated drug delivery for cancer treatment: updates from pre-clinical studies. **3**, 494–511 (2014).
 61. Unger, E. C., Hersh, E., Vannan, M., Matsunaga, T. O. & McCreery, T. Local drug and gene delivery through microbubbles. *Prog. Cardiovasc. Dis.* **44**, 45–54 (2001).
 62. Liu, Y., Miyoshi, H. & Nakamura, M. Encapsulated ultrasound microbubbles: Therapeutic application in drug/gene delivery. *Journal of Controlled Release* **114**, 89–99 (2006).
 63. Vannan, M. *et al.* Ultrasound-mediated transfection of canine myocardium by intravenous administration of cationic microbubble-linked plasmid DNA. *J. Am. Soc. Echocardiogr.* **15**, 214–218 (2002).
 64. Christiansen, J. P., French, B. A., Klibanov, A. L., Kaul, S. & Lindner, J. R. Targeted tissue transfection with ultrasound destruction of plasmid-bearing cationic microbubbles. *Ultrasound Med. Biol.* **29**, 1759–1767 (2003).
 65. Taylor, S. L., Rahim, A. A., Bush, N. L., Bamber, J. C. & Porter, C. D. Targeted retroviral gene delivery using ultrasound. *J. Gene Med.* **9**, 77–87 (2007).
 66. Ferrara, K., Pollard, R. & Borden, M. Ultrasound Microbubble Contrast Agents: Fundamentals and Application to Gene and Drug Delivery. *Annu. Rev. Biomed. Eng.* **9**, 415–447 (2007).

67. Lum, A. F. H. *et al.* Ultrasound radiation force enables targeted deposition of model drug carriers loaded on microbubbles. *J. Control. Release* **111**, 128–134 (2006).
68. Kheirrolomoom, A. *et al.* Acoustically-active microbubbles conjugated to liposomes: Characterization of a proposed drug delivery vehicle. *J. Control. Release* **118**, 275–284 (2007).
69. Geers, B. *et al.* Self-assembled liposome-loaded microbubbles: The missing link for safe and efficient ultrasound triggered drug-delivery. *J. Control. Release* **152**, 249–256 (2011).
70. Luan, Y. *et al.* Acoustical Properties of Individual Liposome-Loaded Microbubbles. *Ultrasound Med. Biol.* **38**, 2174–2185 (2012).
71. Raymond, J. L. *et al.* Loss of gas from echogenic liposomes exposed to pulsed ultrasound. *Phys. Med. Biol.* **61**, 8321–8339 (2016).
72. Shekhar, H. *et al.* In vitro thrombolytic efficacy of echogenic liposomes loaded with tissue plasminogen activator and octafluoropropane gas. *Phys. Med. Biol.* **62**, 517–538 (2017).
73. Huang, S. L. & MacDonald, R. C. Acoustically active liposomes for drug encapsulation and ultrasound-triggered release. *Biochim. Biophys. Acta - Biomembr.* **1665**, 134–141 (2004).
74. Klegerman, M. E. *et al.* Ultrasound-enhanced bevacizumab release from echogenic liposomes for inhibition of atheroma progression. *J. Liposome Res.* **26**, 47–56 (2016).
75. Teupe, C. *et al.* Vascular gene transfer of phosphomimetic endothelial nitric oxide synthase (S1177D) using ultrasound-enhanced destruction of plasmid-loaded microbubbles improves vasoreactivity. *Circulation* **105**, 1104–1109 (2002).
76. Zhao, Y. Z., Liang, H. D., Mei, X. G. & Halliwell, M. Preparation, characterization and in vivo observation of phospholipid-based gas-filled microbubbles containing hirudin. *Ultrasound Med. Biol.* **31**, 1237–1243 (2005).
77. Eriksson, M., Taskinen, M. & Leppä, S. Mitogen Activated Protein Kinase-Dependent Activation of c-Jun and c-Fos is required for Neuronal differentiation but not for Growth and Stress Repose in PC12 cells. *J. Cell. Physiol.* **207**, 12–22 (2006).
78. Phillips, L., Klivanov, A. L., Wamhoff, B. & Hossack, J. Localized Ultrasound Enhances Delivery of Rapamycin from Microbubbles to Prevent Smooth Muscle

- Proliferation. *J. Control. Release* **154**, 42–49 (2011).
79. Mico, V. Developing Microbubble-Nanodroplet Composites for Enhanced Hydrophobic Drug Delivery. PhD Dissertation. (University of Leeds, 2017).
 80. Unger, E. C., McCreery, T. P., Sweitzer, R. H., Caldwell, V. E. & Wu, Y. Acoustically active lipospheres containing paclitaxel: a new therapeutic ultrasound contrast agent. *Invest. Radiol.* **33**, 886–92 (1998).
 81. Kooiman, K. *et al.* Oil-filled polymer microcapsules for ultrasound-mediated delivery of lipophilic drugs. *J. Control. Release* **133**, 109–118 (2009).
 82. Hettiarachchi, K., Lee, A. P., Feingold, S. G., Sheeran, P. S. & Dayton, P. a. Ultrasonic analysis of precision-engineered acoustically active lipospheres produced by microfluidic. in *Proceedings - IEEE Ultrasonics Symposium* 1302–1305 (Ieee, 2009). doi:10.1109/ULTSYM.2009.5441565
 83. May, D. J., Allen, J. S. & Ferrara, K. W. Dynamics and fragmentation of thick-shelled microbubbles. *IEEE Trans. Ultrason. Ferroelectr. Freq. Control* **49**, 1400–1410 (2002).
 84. Fang, J., Hung, C., Liao, M.-H. & Chien, C.-C. A study of the formulation design of acoustically active lipospheres as carriers for drug delivery. *Eur. J. Pharm. Biopharm.* **67**, 67–75 (2007).
 85. Kooiman, K. *et al.* Ultrasound-triggered local release of lipophilic drugs from a novel polymeric ultrasound contrast agent. *J. Control. Release* **132**, e41–e42 (2008).
 86. Kooiman, K. *et al.* Oil-filled polymeric ultrasound contrast agent as local drug delivery system for lipophilic drugs. *IEEE Int. Ultrason. Symp.* **5000**, 333–336 (2008).
 87. De Aguiar, H. B., De Beer, A. G. F., Strader, M. L. & Roke, S. The interfacial tension of nanoscopic oil droplets in water is hardly affected by SDS surfactant. *J. Am. Chem. Soc.* **132**, 2122–2123 (2010).
 88. Hettiarachchi, K., Talu, E., Longo, M. L., Dayton, P. A. & Lee, A. P. On-chip generation of microbubbles as a practical technology for manufacturing contrast agents for ultrasonic imaging. *Lab Chip* **7**, 463–468 (2007).
 89. Talu, E. *et al.* Tailoring the size distribution of ultrasound contrast agents: Possible method for improving sensitivity in molecular imaging. *Mol. Imaging* **6**, 384–392 (2007).
 90. Talu, E. *et al.* Maintaining monodispersity in a microbubble population formed by flow-focusing. *Langmuir* **24**, 1745–1749 (2008).

91. Andrieux, S., Drenckhan, W. & Stubenrauch, C. Generation of Solid Foams with Controlled Polydispersity Using Microfluidics. *Langmuir* [Epub ahead of print] (2018). doi:10.1021/acs.langmuir.7b03602
92. Ahmad, Z. *et al.* Generation of multilayered structures for biomedical applications using a novel tri-needle coaxial device and electrohydrodynamic flow. *J. R. Soc. Interface* **5**, 1255–1261 (2008).
93. Zhang, H., Meng, H., Sun, Q., Liu, J. & Zhang, W. J. Multi-Layer Microbubbles by Microfluidics. *Sci. Res.* **5**, 146–148 (2013).
94. Kendall, M. R., Bardin, D., Shih, R., Dayton, P. a & Lee, A. P. Scaled-Up Production of Monodisperse, Dual Layer Microbubbles Using Multi-Array Microdic Module for Medical Imaging and Drug Delivery. *Bubble Sci Eng Technol* **4**, 12–20 (2012).
95. Shih, R. *et al.* Flow-focusing regimes for accelerated production of monodisperse drug-loadable microbubbles toward clinical-scale applications. *Lab Chip* **13**, 4816 (2013).
96. Royal Society of Chemistry. ChemSpider. (2015). Available at: <http://www.chemspider.com/>.
97. Leong, T. S. H., Wooster, T. J., Kentish, S. E. & Ashokkumar, M. Minimising oil droplet size using ultrasonic emulsification. *Ultrason. Sonochem.* **16**, 721–727 (2009).
98. Alayoubi, A. Y., Anderson, J. F., Satyanarayanajois, S. D., Sylvester, P. W. & Nazzal, S. Concurrent delivery of tocotrienols and simvastatin by lipid nanoemulsions potentiates their antitumor activity against human mammary adenocarcenoma cells. *Eur. J. Pharm. Sci.* **48**, 385–392 (2013).
99. Alayoubi, A., Alqahtani, S., Kaddoumi, A. & Nazzal, S. Effect of PEG surface conformation on anticancer activity and blood circulation of nanoemulsions loaded with tocotrienol-rich fraction of palm oil. *AAPS J.* **15**, 1168–79 (2013).
100. Contente, T. C., Kretzer, I. F., Filippin-Monteiro, F. B., Maria, D. A. & Maranhão, R. C. Association of daunorubicin to a lipid nanoemulsion that binds to low-density lipoprotein receptors enhances the antitumour action and decreases the toxicity of the drug in melanoma-bearing mice. *J. Pharm. Pharmacol.* **66**, 1698–1709 (2014).
101. Dordević, S. M. *et al.* Experimental design in formulation of diazepam nanoemulsions: Physicochemical and pharmacokinetic performances. *J. Pharm. Sci.* **102**, 4159–4172 (2013).

102. Cortés-Muñoz, M., Chevalier-Lucia, D. & Dumay, E. Characteristics of submicron emulsions prepared by ultra-high pressure homogenisation: Effect of chilled or frozen storage. *Food Hydrocoll.* **23**, 640–654 (2009).
103. Floury, J., Desrumaux, A., Axelos, M. A. V. & Legrand, J. Effect of high pressure homogenisation on methylcellulose as food emulsifier. *J. Food Eng.* **58**, 227–238 (2003).
104. Blanco, E., Shen, H. & Ferrari, M. Principles of nanoparticle design for overcoming biological barriers to drug delivery. *Nat. Biotechnol.* **33**, 941–951 (2015).
105. Ghosh, V., Saranya, S., Mukherjee, A. & Chandrasekaran, N. Cinnamon Oil Nanoemulsion Formulation by Ultrasonic Emulsification: Investigation of Its Bactericidal Activity. *J. Nanosci. Nanotechnol.* **13**, 114–122 (2013).
106. Jing, X. *et al.* A novel polyethylene glycol mediated lipid nanoemulsion as drug delivery carrier for paclitaxel. *Nanomedicine Nanotechnology, Biol. Med.* **10**, 371–380 (2014).
107. Singh, K. K. & Vingkar, S. K. Formulation, antimalarial activity and biodistribution of oral lipid nanoemulsion of primaquine. *Int. J. Pharm.* **347**, 136–143 (2008).
108. Gianella, A. *et al.* Multifunctional nanoemulsion platform for imaging guided therapy evaluated in experimental cancer. *ACS Nano* **5**, 4422–4433 (2011).
109. Deshpande, D., Janero, D. R. & Amiji, M. Engineering of an omega-3 polyunsaturated fatty acid-containing nanoemulsion system for combination C6-ceramide and 17beta-estradiol delivery and bioactivity in human vascular endothelial and smooth muscle cells. *Nanomedicine* **9**, 885–894 (2013).
110. Hak, S., Garaiova, Z., Olsen, L. T., Nilsen, A. M. & De Lange Davies, C. The effects of oil-in-water nanoemulsion polyethylene glycol surface density on intracellular stability, pharmacokinetics, and biodistribution in tumor bearing mice. *Pharm. Res.* **32**, 1475–1485 (2015).
111. Hak, S. *et al.* The effect of nanoparticle polyethylene glycol surface density on ligand-directed tumor targeting studied in vivo by dual modality imaging. *ACS Nano* **6**, 5648–5658 (2012).
112. Wooster, T. J., Golding, M. & Sanguansri, P. Ripening Stability. *Langmuir* **24**, 12758–12765 (2008).
113. Dickinson, E., Murray, B. S. & Stainsby, G. Coalescence stability of emulsion-sized droplets at a planar oil-water interface and the relationship to protein film

- surface rheology. *J. Chem. Soc. Faraday Trans. 1* **84**, 871 (1988).
114. Koczó, K., Lobo, A. & Wasan, D. Effect of Oil on Foam Stability : Aqueous Foams Stabilized by Emulsions in an aqueous solution. *J. Colloid Interface Sci.* **150**, 492–506 (1992).
 115. Hotrum, N. E., van Vliet, T., Cohen Stuart, M. A. & van Aken, G. A. Monitoring Entering and Spreading of Emulsion Droplets at an Expanding Air/Water Interface: A Novel Technique. *J. Colloid Interface Sci.* **247**, 125–131 (2002).
 116. Bunqay, H. R. Handling of Antifoam Oils for Fermentations *. *J. Biochem. Microbiol. Technol. Eng.* **11**, 143–155 (1960).
 117. Darling, D. F. Recent advances in the destabilization of dairy emulsions. *Journal of Dairy Research* **49**, 695 (1982).
 118. Heller, W. & Peters, J. Mechanical and Surface Coagulation. *J. Colloid Interface Sci.* **32**, 592–605 (1970).
 119. Mulder, H. & Walstra, P. *The milk fat globule : emulsion science as applied to milk products and comparable foods*. (Commonwealth Agricultural Bureaux, 1974).
 120. Schmidt, D. G. & van Hooydonk, A. C. M. A scanning electron microscopical investigation of the whipping of cream. *Scan. Electron Microsc.* 653–658 (1980).
 121. Graf, E. & Müller, H. R. *Fine structure and whippability of sterilized cream*. **41**, (Carl, 1965).
 122. Life Technologies. Pluronic® F-68 Non-ionic Surfactant (100X). Available at: <http://www.lifetechnologies.com/order/catalog/product/24040032>. (Accessed: 16th August 2014)
 123. Rapoport, N. Phase-Shift, Stimuli-Responsive Perfluorocarbon Nanodroplets for Drug Delivery to Cancer. *Wiley Interdiscip Rev Nanomed Nanobiotechnol* **45**, 492–510 (2012).
 124. Iyer, A. K., Khaled, G., Fang, J. & Maeda, H. Exploiting the enhanced permeability and retention effect for tumor targeting. *Drug Discov. Today* **11**, 812–818 (2006).
 125. Campbell, R. Tumor Physiology and Delivery of Nanopharmaceuticals. *Anticancer. Agents Med. Chem.* **6**, 503–512 (2006).
 126. Hobbs, S. K. *et al.* Regulation of transport pathways in tumor vessels: Role of tumor type and microenvironment. *Proc. Natl. Acad. Sci. U. S. A.* **95**, 4607–12 (1998).
 127. Kripfgans, O. D., Fowlkes, J. B., Miller, D. L., Eldevik, O. P. & Carson, P. L.

- Acoustic droplet vaporization for therapeutic and diagnostic applications. *Ultrasound Med. Biol.* **26**, 1177–1189 (2000).
128. Fabiilli, M. L. *et al.* Ultrasonic delivery of a chemotherapeutic agent using Acoustic Droplet Vaporization (ADV). in *Proceedings - IEEE Ultrasonics Symposium* 101–103 (2009). doi:10.1109/ULTSYM.2009.5442058
 129. Kripfgans, O. D., Fabiilli, M. L., Carson, P. L. & Fowlkes, J. B. On the acoustic vaporization of micrometer-sized droplets. *J. Acoust. Soc. Am.* **116**, 272–281 (2004).
 130. Apfel, R. Activatable infusible dispersions containing drops of a superheated liquid for methods of therapy and diagnosis. (1998).
 131. Kripfgans, O. D. *et al.* Acoustic droplet vaporization for temporal and spatial control of tissue occlusion: A kidney study. *IEEE Trans. Ultrason. Ferroelectr. Freq. Control* **52**, 1101–1108 (2005).
 132. Kripfgans, O. D., Fowlkes, J. B., Woydt, M., Eldevik, O. P. & Carson, P. L. In vivo droplet vaporization for occlusion therapy and phase aberration correction. *IEEE Trans. Ultrason. Ferroelectr. Freq. Control* **49**, 726–738 (2002).
 133. Miller, D. L. & Song, J. Lithotripter shock waves with cavitation nucleation agents produce tumor growth reduction and gene transfer in vivo. *Ultrasound Med. Biol.* **28**, 1343–1348 (2002).
 134. Miller, D. L., Kripfgans, O. D., Fowlkes, J. B. & Carson, P. L. Cavitation nucleation agents for nonthermal ultrasound therapy. *J. Acoust. Soc. Am.* **107**, 3480 (2000).
 135. Fabiilli, M. L. *et al.* The role of inertial cavitation in acoustic droplet vaporization. *IEEE Trans. Ultrason. Ferroelectr. Freq. Control* **56**, 1006–1017 (2009).
 136. Lo, A. H., Kripfgans, O. D., Carson, P. L. & Fowlkes, J. B. Spatial control of gas bubbles and their effects on acoustic fields. *Ultrasound Med. Biol.* **32**, 95–106 (2006).
 137. Lo, A. H., Kripfgans, O. D., Carson, P. & Fowlkes, J. B. Acoustic droplet vaporization: Effects of ultrasound contrast agent and attenuation. *Int. Symp. Ther. Ultrasound* **54**, in press (2007).
 138. Fabiilli, M. L. *et al.* Delivery of chlorambucil using an acoustically-triggered perfluoropentane emulsion. *Ultrasound Med. Biol.* **36**, 1364–1375 (2010).
 139. Fabiilli, M. L., Lee, J. A., Kripfgans, O. D., Carson, P. L. & Fowlkes, J. B. Delivery of water-soluble drugs using acoustically triggered perfluorocarbon double emulsions. *Pharm. Res.* **27**, 2753–2765 (2010).

140. Zhang, M. *et al.* Initial Investigation of Acoustic Droplet Vaporization for Occlusion in Canine Kidney. *Ultrasound Med. Biol.* **36**, 1691–1703 (2010).
141. Wong, Z. Z., Kripfgans, O. D., Qamar, A., Fowlkes, J. B. & Bull, J. L. Bubble evolution in acoustic droplet vaporization at physiological temperature via ultra-high speed imaging. *Soft Matter* **7**, 4009 (2011).
142. Schad, K. C. & Hynynen, K. In vitro characterization of perfluorocarbon droplets for focused ultrasound therapy. *Phys. Med. Biol.* **55**, 4933–4947 (2010).
143. Rapoport, N. Y., Elfros, A., Christensen, D., Kennedy, A. & Nam, K. H. Microbubble Generation in Phase-Shift Nanoemulsions used as Anticancer Drug Carriers. *Bubble Sci Eng Technol* **1**, 31–39 (2009).
144. Gao, Z., Kennedy, A. M., Christensen, D. a. & Rapoport, N. Y. Drug-loaded nano/microbubbles for combining ultrasonography and targeted chemotherapy. *Ultrasonics* **48**, 260–270 (2008).
145. Rapoport, N., Gao, Z. & Kennedy, A. Multifunctional nanoparticles for combining ultrasonic tumor imaging and targeted chemotherapy. *J. Natl. Cancer Inst.* **99**, 1095–1106 (2007).
146. Rapoport, N. *et al.* Ultrasound-mediated tumor imaging and nanotherapy using drug loaded, block copolymer stabilized perfluorocarbon nanoemulsions. *J. Control. Release* **153**, 4–15 (2011).
147. Rapoport, N. Y., Kennedy, A. M., Shea, J. E., Scaife, C. L. & Nam, K. H. Controlled and targeted tumor chemotherapy by ultrasound-activated nanoemulsions/microbubbles. *J. Control. Release* **138**, 268–276 (2009).
148. Rapoport, N., Christensen, D. a., Kennedy, A. M. & Nam, K. H. Cavitation Properties of Block Copolymer Stabilized Phase-Shift Nanoemulsions Used as Drug Carriers. *Ultrasound Med. Biol.* **36**, 419–429 (2010).
149. Dayton, P. A. *et al.* Application of Ultrasound to Selectively Localize Nanodroplets for Targeted Imaging and Therapy. *Mol Imaging* **5**, 160–174 (2006).
150. Fang, J., Hung, C., Hua, S. & Hwang, T. Acoustically active perfluorocarbon nanoemulsions as drug delivery carriers for camptothecin: Drug release and cytotoxicity against cancer cells. *Ultrasonics* **49**, 39–46 (2009).
151. Purcell, E. Life at low Reynolds number. *American Journal of Physics* **45**, 3 (1977).
152. Dean, R. B. Reynolds Number Dependence of Skin Friction and Other Bulk Flow Variables in Two-Dimensional Rectangular Duct Flow. *J. Fluids Eng.* **100**,

215 (1978).

153. Peyman, S. A. Magnetic Forces for Surface-Based Bioanalysis in Microfluidic Devices. (University of Hull, 2010).
154. Gravesen, P., Branebjerg, J. & Jensen, O. S. Microfluidics-a review. *J. Micromechanics Microengineering* **3**, 168–182 (1993).
155. Tice, J., Song, H., Lyon, A. & Ismagilov, R. Formation of droplets and mixing in multiphase microfluidics at low values of the Reynolds and the capillary numbers. *Langmuir* 9127–9133 (2003).
156. Nunes, J. K., Tsai, S. S. H., Wan, J. & Stone, H. a. Dripping and jetting in microfluidic multiphase flows applied to particle and fibre synthesis. *J. Phys. D. Appl. Phys.* **46**, 114002 (2013).
157. Utada, A., Fernandez-Nieves, A., Stone, H. & Weitz, D. Dripping to Jetting Transitions in Coflowing Liquid Streams. *Phys. Rev. Lett.* **99**, 94502 (2007).
158. Gupta, A. & Kumar, R. Flow regime transition at high capillary numbers in a microfluidic T-junction: Viscosity contrast and geometry effect. *Phys. Fluids* **22**, 122001 (2010).
159. Garstecki, P., Gañán-Calvo, a M. & Whitesides, G. M. Formation of bubbles and droplets in microfluidic systems. *Bull. Polish Acad. Sci.* **53**, 361–372 (2005).
160. Hoeve, W. van. Fluid Dynamics at A Pinch ; Droplet and Bubble Formation in Microfluidic Devices. *University of Twente University* (University of Twente, 2011). doi:10.3990/1.9789036531610
161. Fukai, J. *et al.* Wetting effects on the spreading of a liquid droplet colliding with a flat surface : Experiment and modeling Wetting effects on the spreading of a liquid droplet surface : Experiment and modeling colliding with a flat. **236**, (2007).
162. Gañán-Calvo, a M. & Gordillo, J. M. Perfectly monodisperse microbubbling by capillary flow focusing. *Phys. Rev. Lett.* **87**, 274501 (2001).
163. Garstecki, P., Fuerstman, M. J., Stone, H. A. & Whitesides, G. M. Formation of droplets and bubbles in a microfluidic T-junction—scaling and mechanism of break-up. *Lab Chip* **6**, 437 (2006).
164. Castro-Hernández, E., van Hoeve, W., Lohse, D. & Gordillo, J. M. Microbubble generation in a co-flow device operated in a new regime. *Lab Chip* **11**, 2023 (2011).
165. Azhari, H. *Basics of Biomedical Ultrasounds for Engineers*. (John Wiley & Sons, Inc., 2010).

166. Freitas, R. *Nanomedicine, Volume I: Basic Capabilities*. **I**, (Landes Bioscience, 1999).
167. Tente, R. *Microbubbles and Ultrasound*. (Lap Lambert Academic Publishing GmbH KG, 2011).
168. Raisinghani, A. & DeMaria, A. N. Physical principles of microbubble ultrasound contrast agents. *Am. J. Cardiol.* **90**, 3–7 (2002).
169. Kabalnov, A., Klein, D., Pelura, T., Schutt, E. & Weers, J. Dissolution of multicomponent microbubbles in the bloodstream: 2. experiment. *Ultrasound Med. Biol.* **24**, 751–760 (1998).
170. Walton, C. B., Anderson, C. D., Boulay, R. & Shohet, R. V. Introduction to the ultrasound targeted microbubble destruction technique. *J. Vis. Exp.* (2011). doi:10.3791/2963
171. Bekeredjian, R., Grayburn, P. a & Shohet, R. V. Use of ultrasound contrast agents for gene or drug delivery in cardiovascular medicine. *J. Am. Coll. Cardiol.* **45**, 329–35 (2005).
172. Marmottant, P. *et al.* A model for large amplitude oscillations of coated bubbles accounting for buckling and rupture. *J. Acoust. Soc. Am.* **118**, 3499 (2005).
173. van der Meer, S. M. *et al.* Microbubble spectroscopy of ultrasound contrast agents. *J. Acoust. Soc. Am.* **121**, 648–656 (2007).
174. van Rooij, T. *et al.* Non-linear Response and Viscoelastic Properties of Lipid-Coated Microbubbles: DSPC versus DPPC. *Ultrasound Med. Biol.* **41**, 1432–1445 (2015).
175. McLaughlan, J. R. *et al.* Characterisation of Liposome-Loaded Microbubble Populations for Subharmonic Imaging. *Ultrasound Med. Biol.* **43**, 346–356 (2017).
176. Morgan, K. E. *et al.* Experimental and Theoretical Evaluation of Microbubble Behaviour: Effect of Transmitted Phase and Bubble size. *IEEE Trans. Ultrason. Ferroelectr. Freq. Control* **47**, 1494–1509 (2000).
177. Leighton, T. G. *The Acoustic Bubble*. Elsevier (Elsevier, 1994). doi:10.1121/1.410082
178. Klibanov, A. L. Ligand-carrying gas-filled microbubbles: ultrasound contrast agents for targeted molecular imaging. *Bioconjug. Chem.* **16**, 9–17 (2005).
179. Häbich, A., Ducker, W., Dunstan, D. E. & Zhang, X. Do stable nanobubbles exist in mixtures of organic solvents and water? *J. Phys. Chem. B* **114**, 6962–6967 (2010).

180. Segers, T., De Rond, L., De Jong, N., Borden, M. & Versluis, M. Stability of Monodisperse Phospholipid-Coated Microbubbles Formed by Flow-Focusing at High Production Rates. *Langmuir* **32**, 3937–3944 (2016).
181. Borden, M. A. & Longo, M. L. Dissolution behavior of lipid monolayer-coated, air-filled microbubbles: Effect of lipid hydrophobic chain length. *Langmuir* **18**, 9225–9233 (2002).
182. Dayton, P. & Klibanov, A. Acoustic radiation force in vivo: a mechanism to assist targeting of microbubbles. *Ultrasound Med. Biol.* **25**, 1195–1201 (1999).
183. Shortencarier, M. J. *et al.* A Method for Radiation-Force Localized Drug Delivery Using Gas-Filled Lipospheres. *Trans. Ultrason. Ferroelectr. Freq. Control* **51**, 822–831 (2004).
184. Gref, R., Lück, M. & Quellec, P. ‘Stealth’corona-core nanoparticles surface modified by polyethylene glycol (PEG): influences of the corona (PEG chain length and surface density) and of the. *Colloids Surfaces B ...* **18**, 301–313 (2000).
185. Immordino, M. L. & Cattel, L. Stealth liposomes : review of the basic science , rationale , and clinical applications , existing and potential. 297–315 (2006).
186. Sarkar, K., Katiyar, A. & Jain, P. Growth and dissolution of an encapsulated contrast microbubble: effects of encapsulation permeability. *Ultrasound Med. Biol.* **35**, 1385–96 (2009).
187. Wagner, C. Theorie der Alterung von Niederschlägen durch Umlösen (Ostwald-Reifung). *Zeitschrift für Elektrochemie, Berichte der Bunsengesellschaft für Phys. Chemie* **65**, 581–591 (1961).
188. Tadros, T., Izquierdo, P., Esquena, J. & Solans, C. Formation and stability of nano-emulsions. *Advances in Colloid and Interface Science* **108–109**, 303–318 (2004).
189. Israelachvili, J. *Intermolecular and Surface Forces*. Academic Press (2011). doi:10.1016/C2009-0-21560-1
190. Robinson, J. V. & Woods, W. W. A method of selecting foam inhibitors. *J. Soc. Chem. Ind.* **67**, 361–365 (1948).
191. Sirks, H. A. *Verslag Rijks-Landbouwproefstation*. (Hoorn, 1938).
192. Schokker, E. P., Bos, M. A., Kuijpers, A. J., Wijnen, M. E. & Walstra, P. Spreading of oil from protein stabilised emulsions at air/water interfaces. *Colloids Surfaces B Biointerfaces* **26**, 315–327 (2002).
193. King, N. *The Milk Fat Globule Membrane and Some Associated Phenomena*.

(Lamport Gilbert, 1955).

194. Helms, V. *Principles of computational cell biology : from protein complexes to cellular networks*. (Wiley-VCH, 2008).
195. Olympus Microscopy Resource Center. Fluorescence Resonance Energy Transfer (FRET) Microscopy - Introductory Concepts. Available at: <http://www.olympusmicro.com/primer/techniques/fluorescence/fret/fretintro.html>. (Accessed: 11th June 2017)
196. Periasamy, A. & Day, R. N. *Molecular Imaging: FRET Microscopy and Spectroscopy*. Elsevier (Published for the American Physiological Society by Oxford University Press, 2011). doi:doi:10.1117/1.2388275
197. Evans, D. R., Parsons, D. F. & Craig, V. S. J. Physical properties of phase-change emulsions. *Langmuir* **22**, 9538–9545 (2006).
198. Linstrom, P. J. & Mallard, W. G. NIST Chemistry WebBook. *National Institute of Standards and Technology* (2010). Available at: <http://webbook.nist.gov/chemistry/>.
199. Kohler, S. P. K., Reed, S. K., Westacott, R. E. & McKendrick, K. G. Molecular dynamics study to identify the reactive sites of a liquid squalane surface. *J. Phys. Chem. B* **110**, 11717–11724 (2006).
200. Fowkes, F. M., Riddle, F. L., Pastore, W. E. & Weber, A. A. Interfacial interactions between self-associated polar liquids and squalane used to test equations for solid-liquid interfacial interactions. *Colloids and Surfaces* **43**, 367–387 (1990).
201. Bascom, W. D., Cottington, R. L. & Singleterry, C. R. Dynamic surface phenomena in the spontaneous spreading of oils on solids. *Contact Angle, Wettability, Adhes.* **43**, 355–379 (1964).
202. Saecker, M. E., Govoni, S. T., Kowalski, D. V, King, M. E. & Nathanson, G. M. Molecular Beam Scattering from Liquid Surfaces. *Science (80-.)*. **252**, 1421–1424 (1991).
203. Phillips, L. F. A Geometrical Explanation for the Enhanced Small-Scale Roughness of a Liquid Surface. *J. Phys. Chem. B* **108**, 1986–1991 (2004).
204. NIH U.S. National Library of Medicine. ChemIDplus: Tripropionin. Available at: <https://chem.nlm.nih.gov/chemidplus/rn/139-45-7>. (Accessed: 7th July 2017)
205. Diamante, L. M. & Lan, T. Absolute Viscosities of Vegetable Oils at Different Temperatures and Shear Rate Range of 64 . 5 to 4835/s. *J. Food Process.* **2014**, 1–6 (2014).

206. ChemicalBook. SOYBEAN OIL. Available at: http://www.chemicalbook.com/ProductChemicalPropertiesCB2703220_EN.htm. (Accessed: 7th July 2017)
207. Bhattacharya, S. Plasma bonding of poly(dimethyl)siloxane and glass surfaces and its applications to microfluidics. *A Thesis in Mechanical Engineering* (Texas Tech University, 2013). doi:10.1017/CBO9781107415324.004
208. Elveflow. How to choose the right plasma cleaner for the PDMS bonding of you microfluidic chip? (2015). Available at: <http://www.elveflow.com/microfluidic-tutorials>. (Accessed: 20th May 2017)
209. Hede, P. D., Bach, P. & Jensen, A. D. Two-fluid spray atomisation and pneumatic nozzles for fluid bed coating/agglomeration purposes: A review. *Chem. Eng. Sci.* **63**, 3821–3842 (2008).
210. Xu, X., Sarder, P., Li, Z. & Nehorai, A. Optimization of microfluidic microsphere-trap arrays. *Biomicrofluidics* **7**, 1–16 (2013).
211. Kheirrolomoom, A. *et al.* Acoustically-active microbubbles conjugated to liposomes: Characterization of a proposed drug delivery vehicle. **118**, 275–284 (2007).
212. Seo, M., Gorelikov, I., Williams, R. & Matsuura, N. Microfluidic assembly of monodisperse, nanoparticle-incorporated perfluorocarbon microbubbles for medical imaging and therapy. *Langmuir* **26**, 13855–13860 (2010).
213. Peyman, S. A., Abou-Saleh, R. H. & Evans, S. D. Microbubbles for therapeutic delivery. *Ther. Deliv.* **4**, 539–542 (2013).
214. Park, Y. *et al.* Tunable diacetylene polymerized shell microbubbles as ultrasound contrast agents. *Langmuir* **28**, 3766–3772 (2012).
215. Peyman, S. A. *et al.* High production rates of stable drug-loadable microbubbles toward targetted, triggered drug delivery. in *17th international conference on miniaturized systems for chemistry and Life Sciences* 521–523 (2013).
216. Parrales, M. a, Fernandez, J. M., Perez-Saborid, M., Kopechek, J. a & Porter, T. M. Acoustic characterization of monodisperse lipid-coated microbubbles: Relationship between size and shell viscoelastic properties. *J. Acoust. Soc. Am.* **136**, 1077 (2014).
217. Abou-Saleh, R. H. *et al.* The influence of intercalating perfluorohexane into lipid shells on nano and microbubble stability. *Soft Matter* **12**, 7223–7230 (2016).
218. Bois, A. . & Albon, N. Equilibrium spreading pressure of l- α -dipalmitoyl lecithin below the main bilayer transition temperature: Can it be measured? *J. Colloid*

Interface Sci. **104**, 579–582 (1985).

219. Tadmor, R. Line Energy and the Relation between Advancing , Receding , and Young Contact Angles. *Langmuir* **186**, 7659–7664 (2004).
220. Malvern Instruments (UK). Nanoparticle Tracking Analysis. Available at: <http://www.malvern.com/en/products/technology/nanoparticle-tracking-analysis/default.aspx>. (Accessed: 14th May 2017)
221. Izon science. Tunable Resistive Pulse Sensing Brochure. 1–4 (2015). Available at: <http://www.izon.com/assets/SideColumnPDFs/TRPS-Brochure-April-15.pdf>. (Accessed: 14th May 2017)
222. Sauerbrey, G. Verwendung von Schwingquarzen zur Wägung dünner Schichten und zur Mikrowägung. *Zeitschrift für Phys.* **155**, 206–222 (1959).
223. Vogt, B. D., Lin, E. K., Wu, W. I. & White, C. C. Effect of film thickness on the validity of the sauerbrey equation for hydrated polyelectrolyte films. *J. Phys. Chem. B* **108**, 12685–12690 (2004).
224. Liu, S. X. & Kim, J. T. Application of Kevin-Voigt Model in Quantifying Whey Protein Adsorption on Polyethersulfone Using QCM-D. *J. Lab. Autom.* **14**, 213–220 (2009).
225. Nadermann, N. K., Chan, E. P. & Stafford, C. M. Bilayer mass transport model for determining swelling and diffusion in coated, ultrathin membranes. *ACS Appl. Mater. Interfaces* **7**, 3492–3502 (2015).
226. Kankare, J. Sauerbrey equation of quartz crystal microbalance in liquid medium. *Langmuir* **18**, 7092–7094 (2002).
227. Voinova, M. V, Rodahl, M., Jonson, M. & Kasemo, B. Viscoelastic Acoustic Response of Layered Polymer Films at Fluid-Solid Interfaces: Continuum Mechanics Approach. *Phys. Scr.* **59**, 391–396 (1999).
228. Cho, N. J., Kanazawa, K. K., Glenn, J. S. & Frank, C. W. Employing two different quartz crystal microbalance models to study changes in viscoelastic behavior upon transformation of lipid vesicles to a bilayer on a gold surface. *Anal. Chem.* **79**, 7027–7035 (2007).
229. Clift, R. (Roland), Grace, J. R. & Weber, M. E. *Bubbles, drops, and particles*. (Dover Publications, 2005).
230. Chen, H. *et al.* Release of hydrophobic molecules from polymer micelles into cell membranes revealed by Forster resonance energy transfer imaging. *Proc. Natl. Acad. Sci.* **105**, 6596–6601 (2008).
231. Zou, P., Chen, H., Paholak, H. J. & Sun, D. Noninvasive fluorescence resonance

- energy transfer imaging of in vivo premature drug release from polymeric nanoparticles. *Mol. Pharm.* **10**, 4185–4194 (2013).
232. Sengupta, P., Holowka, D. & Baird, B. Fluorescence Resonance Energy Transfer between Lipid Probes Detects Nanoscopic Heterogeneity in the Plasma Membrane of Live Cells. *Biophys. J.* **92**, 3564–3574 (2007).
 233. Aguilar-Castillo, B. A. *et al.* Nanoparticle stability in biologically relevant media: influence of polymer architecture. *Soft Matter* **11**, 7296–7307 (2015).
 234. Xia, Z. & Liu, Y. Reliable and global measurement of fluorescence resonance energy transfer using fluorescence microscopes. *Biophys. J.* **81**, 2395–2402 (2001).
 235. Shubhra, Q. T. H., Tóth, J., Gyenis, J. & Feczkó, T. Surface modification of HSA containing magnetic PLGA nanoparticles by poloxamer to decrease plasma protein adsorption. *Colloids Surfaces B Biointerfaces* **122**, 529–536 (2014).
 236. Forsberg, F. *et al.* Conventional and hypobaric activation of an ultrasound contrast agent. *Ultrasound Med. Biol.* **24**, 1143–1150 (1998).
 237. Grayburn, P. Perflenenapent Emulsion (EchoGen(R)): A New Long-Acting Phase-Shift Agent for Contrast Echocardiography. *Clin. Cardiol.* **20**, 12–18 (1997).
 238. Sontum, P. *et al.* Acoustic Cluster Therapy (ACT) - A novel concept for ultrasound mediated, targeted drug delivery. *Int. J. Pharm.* **495**, 1019–1027 (2015).
 239. Guntupalli, R. *et al.* Phage Langmuir monolayers and Langmuir-Blodgett films. *Colloids Surfaces B Biointerfaces* **82**, 182–189 (2011).
 240. Griffith, E. C., Guizado, T. R. C., Pimentel, A. S., Tyndall, G. S. & Vaida, V. Oxidized aromatic-aliphatic mixed films at the air-aqueous solution interface. *J. Phys. Chem. C* **117**, 22341–22350 (2013).
 241. Silva, E. A. da, Oliveira, V. J. R. de, Braunger, M. L., Constantino, C. J. L. & Olivati, C. de A. Poly(3-octylthiophene)/stearic Acid Langmuir and Langmuir-Blodgett Films: Preparation and Characterization. *Mater. Res.* **17**, 1442–1448 (2014).
 242. Yun, H., Choi, Y. W., Kim, N. J. & Sohn, D. Physicochemical properties of phosphatidylcholine (PC) monolayers with different alkyl chains, at the air/water interface. *Bull. Korean Chem. Soc.* **24**, 377–383 (2003).
 243. Winterhalter, M., Bürner, H., Marzinka, S., Benz, R. & Kasianowicz, J. J. Interaction of poly(ethylene-glycols) with air-water interfaces and lipid monolayers: investigations on surface pressure and surface potential. *Biophys. J.*

- 69**, 1372–1381 (1995).
244. Duncan, S. L. & Larson, R. G. Comparing experimental and simulated pressure-area isotherms for DPPC. *Biophys. J.* **94**, 2965–2986 (2008).
 245. McConlogue, C. W. & Vanderlick, T. K. A Close Look at Domain Formation in DPPC Monolayers. *Langmuir* **13**, 7158–7164 (1997).
 246. Domènech, Ò., Sanz, F., Montero, M. T. & Hernández-borrell, J. Thermodynamic and structural study of the main phospholipid components comprising the mitochondrial inner membrane. *Biochim. Biophys. Acta(BBA)-Biomembranes* **1758**, 213–221 (2006).
 247. Sarangi, N. K., Ayappa, K. G., Viswewariah, S. S. & Basu, J. K. Nanoscale dynamics of phospholipids reveals optimal assembly mechanism of pore-forming proteins in bilayer membranes. *Phys. Chem. Chem. Phys.* **18**, 29935–29945 (2016).
 248. Merino, S. *et al.* Surface thermodynamic properties of monolayers versus reconstitution of a membrane protein in solid-supported bilayers. *Colloids Surfaces B Biointerfaces* **44**, 93–98 (2005).
 249. Domenech, O. *et al.* Surface thermodynamics study of monolayers formed with heteroacid phospholipids of biological interest. *Colloids Surfaces B Biointerfaces* **41**, 233–238 (2005).
 250. Pownall, H. J., Pao, Q., Brockman, H. L. & Massey, J. B. Inhibition of lecithin-cholesterol acyltransferase by diphytanoyl phosphatidylcholine. *J. Biol. Chem.* **262**, 9033–9036 (1987).
 251. Smith, E. C., Crane, J. M., Laderas, T. G. & Hall, S. B. Metastability of a supercompressed fluid monolayer. *Biophys. J.* **85**, 3048–3057 (2003).
 252. Tseng, F. G., Huang, C. Y., Chieng, C. C., Huang, H. & Liu, C. S. Size effect on surface tension and contact angle between protein solution and silicon compound, PC, and PMMA substrates. *Microscale Thermophys. Eng.* **6**, 31–53 (2002).
 253. Arya, S. K. *et al.* Application of octadecanethiol self-assembled monolayer to cholesterol biosensor based on surface plasmon resonance technique. **69**, 918–926 (2006).
 254. Cras, J. J., Rowe-taitt, C. A., Nivens, D. A. & Ligler, F. S. Comparison of chemical cleaning methods of glass in preparation for silanization. *Biosens. Bioelectron.* **14**, 683–688 (1999).
 255. Diamanti, E. *et al.* The effect of top-layer chemistry on the formation of supported lipid bilayers on polyelectrolyte multilayers: primary versus quaternary

- amines. *Phys. Chem. Chem. Phys.* **18**, 32396–32405 (2016).
256. Richter, R. P. & Brisson, A. R. Following the Formation of Supported Lipid Bilayers on Mica: A Study Combining AFM, QCM-D, and Ellipsometry. *Biophys. J.* **88**, 3422–3433 (2005).
 257. Dixon, M. C. Quartz crystal microbalance with dissipation monitoring: Enabling real-time characterization of biological materials and their interactions. *Journal of Biomolecular Techniques* **19**, 151–158 (2008).
 258. Keller, C. A. & Kasemo, B. Surface Specific Kinetics of Lipid Vesicle Adsorption Measured with a Quartz Crystal Microbalance. *Biophys. J.* **75**, 1397–1402 (1998).
 259. Hotrum, N. E., Cohen Stuart, M. A., van Vliet, T. & van Aken, G. A. *Food Colloids, Biopolymers and Materials: Entering and Spreading of Protein-Stabilized Emulsion Droplets at the Expanding Air-Water Interface*. (Royal Society of Chemistry, 2003).
 260. Abou-Saleh, R. H., McLaughlan, J. R., Freear, S., Evans, S. D. & Thomson, N. Glycerol interaction with phospholipid molecules: Impact on microbubble physical, mechanical and acoustic properties [In preparation]. (2017).
 261. Wilkinson, K. M., Bain, C. D. & Matsubara, H. Wetting of Surfactant Solutions by Alkanes. *ChemPhysChem* **6**, 547–555 (2005).
 262. Du, L., Bodiguel, H., Cottin, C. & Colin, A. Dynamics of liquid–liquid menisci in pseudo-partial wetting. *Chem. Eng. Process.* **68**, 3–6 (2013).
 263. Jahan, K., Balzer, S. & Mosto, P. Toxicity of nonionic surfactants. *WIT Trans. Ecol. Environ.* **110**, 281–290 (2008).
 264. Koley, D. & Bard, A. J. Triton X-100 concentration effects on membrane permeability of a single HeLa cell by scanning electrochemical microscopy (SECM). *Proc. Natl. Acad. Sci. U. S. A.* **107**, 16783–7 (2010).
 265. Smith, B. J. & Gaver, D. P. Agent-based simulations of complex droplet pattern formation in a two-branch microfluidic network. *Lab Chip* **10**, 303–12 (2010).
 266. Huang, S.-H., Tan, W.-H., Tseng, F.-G. & Takeuchi, S. A monolithically three-dimensional flow-focusing device for formation of single/double emulsions in closed/open microfluidic systems. *J. Micromechanics Microengineering* **16**, 2336–2344 (2006).
 267. Hashimoto, M. *et al.* Formation of bubbles and droplets in parallel, coupled flow-focusing geometries. *Small* **4**, 1795–805 (2008).
 268. Deshpande, S., Caspi, Y., Meijering, A. E. C. & Dekker, C. Octanol-assisted

- liposome assembly on chip. *Nat. Commun.* **7**, 10447 (2016).
269. Fabiilli, M. L. Ultrasound-triggered drug delivery using acoustic droplet vaporization. *Proquest* (The University of Michigan, 2010).
 270. Shpak, O. Acoustic Droplet Vaporization. (University of Twente, 2014). doi:10.3990/1.9789036537230
 271. Choi, J. *et al.* Noninvasive and Transient Blood-Brain Barrier Opening in the Hippocampus of Alzheimer's Double Transgenic Mice Using Focused Ultrasound. *Ultrasound Imaging* **30**, 189–200 (2008).
 272. Sirsi, S., Feshitan, J., Kwan, J., Homma, S. & Borden, M. Effect of microbubble size on fundamental mode high frequency ultrasound imaging in mice. *Ultrasound Med. Biol.* **36**, 935–48 (2010).
 273. Dicker, S., Mleczko, M., Schmitz, G. & Wrenn, S. P. Size distribution of microbubbles as a function of shell composition. *Ultrasonics* **53**, 1363–7 (2013).
 274. Schutt, E. G., Klein, D. H., Mattrey, R. M. & Riess, J. G. Injectable microbubbles as contrast agents for diagnostic ultrasound imaging: The key role of perfluorochemicals. *Angew. Chemie - Int. Ed.* **42**, 3218–3235 (2003).
 275. Tu, J., Guan, J., Qiu, Y. & Matula, T. J. Estimating the shell parameters of SonoVue microbubbles using light scattering. *J. Acoust. Soc. Am.* **126**, 2954–62 (2009).
 276. Almgren, M. *et al.* The effect of different alcohols and other polar organic additives on the cloud point of Triton X-100 in water. *Desalination* **36**, 1–8 (2001).
 277. Bordier, C. Phase separation of integral membrane proteins in Triton X-114 solution. *J. Biol. Chem.* **256**, 1604–1607 (1981).
 278. Sheeran, P. S. *et al.* Decafluorobutane as a Phase-Change Contrast Agent for Low-Energy Extravascular Ultrasonic Imaging. *Ultrasound Med. Biol.* **37**, 1518–1530 (2011).